FIELD EMISSION ELECTRIC PROPULSION THRUSTER MODELING AND SIMULATION

by

Anton Sivaram VanderWyst

A dissertation submitted in partial fulfillment
of the requirements for the degree of
Doctor of Philosophy
(Aerospace Engineering)
in The University of Michigan
2006

Doctoral Committee:

Professor Iain D. Boyd, Co-Chairperson
Professor Wei Shyy, Co-Chairperson
Assistant Professor Andrew J. Christlieb
Assistant Research Scientist Michael Keidar

ACKNOWLEDGEMENTS

I would like to offer my sincere appreciation for other people who have been crucial to the success of this project. I would like to thank my advisor, Prof. Iain D. Boyd. You have always been willing to talk, have supported my efforts through the years, have had a major impact in my presentation style and substance, have cleared innumerable barriers in my path, and had the confidence in me to trust that I would present you with worthwhile research plans, tasks and accomplishments. For all of these things and many more, I am greatly indebted to your supervision and aid. Thanks are due for consistent and ongoing research aid from Prof. Andrew Christlieb - the technical approach has been vastly refined because of his continuing help, reassurance and ideas on how to improve. As the analysis kept shooting off in different directions, you provided a rein on what could and could not be done, and illuminated possible avenues to study. For riding this bucking beast and talking over countless cups of coffee, you have more than earned all possible thanks I can offer. In addition,

The other members of my committee, Prof. Michael Keidar and Prof. Wei Shyy, have helped me as technical references, pointed out useful independent sources and provided their time and assistance in smoothing this work. Due to their efforts, all errors that remain are my own. In addition, Prof. Shyy was willing to act as co-chair and help shepherd this through administrative hoops.

Three individuals have made notable contributions to specific chapters. Professor

Mark Sussman at Florida State University has significantly aided my computational efforts and thesis grand overview with his level set code and prompt responses to my simulation questions. Professor Stephen Bectel at Ohio State University clarified much of the asymptotic approximation procedure used in Chapter III. Jerry Emhoff provided substantial assistance in understanding 2D Green's functions in cylindrical coordinates for a 2D axisymmetric formulation in Chapter IV.

On a personal front, several people have helped keep me sane and finding my way through the bureaucracy of a major research institution. As the graduate student services coordinator, Margaret Fillion got me through the first few years here; I won't have been able to find my way without her efforts. Jenna and Diane have been a constant sounding board for me while I berated my computer for not producing the results I had expected - it continually responded with what I typed instead. My office mates have patiently put up with me for almost a half decade; thanks Jin, Chunpei and Yongjun. Many around FXB have listened to technical issues and offered unbiased feedback. Michael, Matt, Jerry, Jon, John, Jeremy and Justin (just judiciously justifying their jumbo judgment). A special thanks to Jeremy and Yongjun for selflessly reading over the thesis; your comments improved the flow and tempo of the work. A last minute thanks to Mamagaru and Attagaru for rapid reporting.

Most importantly, a very special thanks to my wife, Saumya for her support while I flailed around, slowly and seemingly randomly making progress until I produced this finished product. I want to let her know I appreciate her being there to listen to me when I was frustrated, to celebrate when things went well, and for showing me the continuing, fulfilling life beyond research.

Funding for this dissertation was provided by the NASA Jet Propulsion Labora-

tory's Graduate Student Research Program (GSRP), the National Science Foundation's Dissertation Enhancement Program (DEP), the Office of Technical Communication and the Department of Aerospace Engineering at the University of Michigan.

TABLE OF CONTENTS

LIST OF FIGURES

Figure

LIST OF TABLES

Table

LIST OF NOMENCLATURE

ACRONYMS

ACTNOW	anti-crossing tracking normal-weighting, a surface connectivity scheme
AMR	adaptive mesh refinement
ARCS	Austrian research center, Seiborsdorf
BEM	boundary element method
DAQ	digital acquisition
DEP	dissertation enhancement program
DOF	degrees of freedom
DSMC	direct simulation Monte Carlo
EADS	European Aeronautic Defense and Space company
EP	electric propulsion
erfc	complementary error function
ESA	European Space Agency
FEEP	field emission electric propulsion
FN	Fowler-Nordheim method
FWHM	full width half maximum
GOCE	gravity field and steady-state ocean circulation explorer, future ESA satellite mission
GCR	gradient conjugate residual
GSRP	graduate student research program
GUEST	Griffith University erosion system template, a hydrological model
IEPC	international electric propulsion conference

LIFET	large indium FEEP endurance testing facility
LMIS	liquid metal ion source
MPD	magnetoplasmadynamic
MTCR	mass to charge ratio
NASA	National Aeronautics and Space Administration
NM	Nelder-Mead, nonlinear function optimization
NSSK	north-south station keeping
PIC	particle-in-cell
PPT	pulsed plasma thruster
QCM	quartz crystal microbalance
RIT	radio-frequency ion thruster
TOF	time of flight
UHV	ultra high vacuum

Constants

amu	atomic mass unit, 1.6606×10^{-27} [kg]
e	electron charge, 1.6022×10^{-19} [C]
ϵ_0	permittivity of free space, 8.8542×10^{-12} $\left[\frac{F}{m}\right]$
g	gravitational acceleration, 9.80665 $\left[\frac{m}{s^2}\right]$
h	Planck's constant, 6.6261×10^{-34} $[J \cdot s]$
k	Boltzmann's constant, 1.3807×10^{-23} $\left[\frac{J}{K}\right]$
m_e	mass of electron, 9.1094×10^{-31} [kg]
μ_0	permeability of free space, 1.2566×10^{-6} $\left[\frac{H}{m}\right]$
R	universal gas constant, 8.314×10^3 $\left[\frac{J}{kg \cdot mole}\right]$

CGS unit system equivalents

charge($\underbrace{q}$) (e)$\times 3 \times 10^9$ [statCoulomb]

current($\underbrace{I}$) (I)$\times 3 \times 10^{9}$ [statAmpere]

density($\underbrace{\rho}$) (ρ)$\times 1 \times 10^{-3}$ $\left[\frac{g}{cm^3}\right]$

electric field($\underbrace{E}$) (E)$\times \frac{1}{3} \times 10^{-4}$ $\left[\frac{statV}{cm}\right]$

mass($\underbrace{amu}$) (amu)$\times 1 \times 10^{3}$ [g]

Variables

a	acceleration $\left[\frac{m}{s^2}\right]$
A	tube area $[mm^2]$
$\overline{a}$	average acceleration $\left[\frac{m}{s^2}\right]$
a_{groove}	needle groove radius [m]
a_i	acceleration of i^{th} droplet $\left[\frac{m}{s^2}\right]$
a_{Sor}	Soret coefficient
A_1	integration constant
α	acceleration value $\left[\frac{m}{s^2}\right]$
α_N	source term for Neumann boundaries
α_{pow}	specific power $\left[\frac{W}{kg}\right]$
b	tube inner radius [m]
B	magnetic field [Weber]
b_i	frequency of droplets in i^{th} histogram bin
$b_{i,e}$	experimental viscous coefficients
c	molar concentration $\left[\frac{mole}{cm^3}\right]$
C	tube capacitance [F]
c_0	initial fluid contamination $\left[\frac{kg}{m^3}\right]$
$C^{[x]}$	panel approximation polynomial, C^0=linear
c_{emp}	fitting constant
c_t	fluid contamination carrying capacity $\left[\frac{kg}{m^3}\right]$

C_{tot}	total capacitance [F]
χ	atomic fraction of each element
χ_i	nondimensional variable
χ_m	merit function, method of steepest descent
$\chi^-(\overrightarrow{x})$	$\begin{cases} 1 & \text{if } \phi(\overrightarrow{x}) \leq 0 \\ 0 & \text{if } \phi(\overrightarrow{x}) > 0 \end{cases}$, characteristic function
d	gap distance [m]
D	diffusion rate $\left[\frac{cm^2}{s}\right]$
D	symmetric part of the velocity gradient
$d(\overrightarrow{x})$	distance function, where d=0 on the boundary. $\min(\lvert\overrightarrow{x} - \overrightarrow{x_I}\rvert)$ for all $\overrightarrow{x_I} \in \partial\Omega$
d_{eff}	effective droplet diameter in 2D axisymmetric coordinates [m]
D_{defm}	rate of deformation tensor
d_{te}	tip-electrode distance [m]
d_{TOF}	distance from needle tip to downstream current collector [m]
$\hat{\delta}(\overrightarrow{x})$	$\nabla H(\phi(\overrightarrow{x})) \cdot \overrightarrow{n}$, Dirac delta function
$\{\}\lvert_\partial$	{ } evaluated on the surface F
E	electric field $\left[\frac{V}{m}\right]$
E_a	activation energy $\left[\frac{J}{mole}\right]$
E_c^0	electric field, Taylor limit $\left[\frac{V}{m}\right]$
e_F	Fermi energy [eV]
E_i	ion evaporation electric field $\left[\frac{V}{m}\right]$
ϵ	order of perturbation expansion
ε	nondimensional variable
η	mass efficiency [%]
η_m	measured mass efficiency [%]
η_{sys}	system efficiency

f	Dirichlet boundary condition
F	force [N]
F	free surface
$f_{[x]}$	largest force, nondimensionalized
$f(x, \alpha)$	spatial distribution function
F_E	electrostatic panel force [N]
F_T	film thickness [m]
g	Neumann boundary condition
G	Green's function
$\breve{\gamma}$	source term for Dirichlet boundaries
h_c	combustion enthalpy $\left[\frac{J}{kg}\right]$
h_{jet}	mini jet protrusion height [m]
$H(\phi)$	$\begin{cases} 0 & \text{if } \phi(\overrightarrow{x}) \leq 0 \\ 1 & \text{if } \phi(\overrightarrow{x}) > 0 \end{cases}$, Heaviside step function
$H(x-c)H(x-d)$	$\begin{cases} 1 & \text{if x} \in [c, d) \\ 0 & \text{otherwise} \end{cases}$, modal Heaviside step function
I	emission current [A]
$\mathbf{I}$	identity matrix
I_C	emitter critical current when droplets first form [μA]
I_e	droplet emitter current [μA]
I_{SP}	specific impulse [s]
$\iota(\zeta)$	experimentally fitted function
J	current density $[\frac{A}{m^3}]$
J_{dif}	total diffusion rate $\left[\frac{mole}{cm^2 \cdot s}\right]$
j_{sc}	maximum current density $\left[\frac{C}{m^3}\right]$
κ	$\nabla \cdot \overrightarrow{N} = \nabla \cdot \frac{\nabla \phi}{\lvert \nabla \phi \rvert}$, mean surface curvature $\left[\frac{1}{m}\right]$

κ_ϕ	ExB sensor peak half-width [V]
L	panel length [m]
L_n	needle length [m]
L_e^B	molar heat of evaporation $\left[\frac{kJ}{mole}\right]$
L_{tot}	length, total [m]
L_1	length between needle and probe [m]
$L_2 = L_4$	length between needle and faceplate [m]
L_3	length of tube [m]
$\lambda_{1,2}$	characteristic fluid evolution times [s]
λ_d	characteristic length of deposition. The distance a particle travels downslope when the particle settles a vertical distance equal to the indium depth [m]
$\lambda(\Delta H_{ij}^{\infty})$	partial enthalpy of solution at infinite dilution of a liquid metal (A) in (B) $\left[\frac{kJ}{mole}\right]$
Λ	time, nondimensional $\frac{\lambda}{t_0}$
Λ_{cm}	length of collimator [m]
Λ_p	length of probe [m]
Λ_{pe}	distance of the probe from the emitter [m]
Λ_{pp}	distance between probe plates [m]
m	mass of atoms [kg]
$\dot{m}$	mass flow rate $\left[\frac{kg}{s}\right]$
$m_{initial}$	mass, system initial [kg]
m_{ion}	mass, ion [kg]
$m_{propellant}$	mass, propellant [kg]
$m_{p,s}$	mass, payload+structure [kg]
Δm	total mass change [kg]
μ	viscosity $\left[\frac{N \cdot s}{m^2} = Pa \cdot s\right]$
N	number of droplets in the tube at one time = 0.5

$\overrightarrow{n}$	$\frac{\nabla\phi}{\lvert\nabla\phi\rvert}$, outward/counterclockwise surface unit normal
$\partial_{\overrightarrow{n}}\{\,\}$	vector normal derivative
ν	molar concentration $\left[\frac{mole}{m^3}\right]$
ν_{feh}	Fehringer velocity $\left[\frac{m}{s}\right]$
$\nu_{10,20}$	molar concentration, relative ratio
$o(\zeta,\varepsilon)$	shank fitted function
$\omega(\zeta)$	experimentally fitted function
Ω	resistance [Ohms]
Ω	surface of shape
Ω_{crit}	critical minimum system resistance [Ohms]
$\partial\Omega$	edge of shape. Location BEM is performed around
$\partial\Omega_D$	Dirichlet boundary
$\partial\Omega_N$	Neumann boundary
p	2D pressure vector
p_a	atmospheric pressure [Pa]
p_{es}	electrostatic pressure [Pa]
P_{jet}	power, jet [W]
P_{sys}	power, system [W]
P_{solar}	power, solar [W]
$P_{\frac{1}{2}}$	Legendre function
ϕ	free surface radius [m]
ϕ	level set function. Positive outside, 0 on the interface, negative inside.
$\nabla\phi$	gradient of the level set function $\left(\frac{\partial\phi}{\partial x},\frac{\partial\phi}{\partial y},\frac{\partial\phi}{\partial z}\right)$
$\Delta\phi_c$	sensor center peak signal location [V]
ψ	degrees probe is off thruster plume centerline [^{0}]
Ψ	rate of deposition $\left[\frac{kg}{m^2\cdot s}\right]$

Ψ	angle off-axis of droplets [^{0}]
q	charge on molecules [C]
q_{flow}	flow rate per unit width $\left[\frac{m^2}{s}\right]$
q_t	time epsilon sensitivity factor
r_c	needle tip radius of curvature [m]
r_i	rate of flow entrainment $\left[\frac{kg}{m^2 \cdot s}\right]$
r_{jet}	mini jet radius [m]
r_T	Taylor cone radius [m]
r(o)	shank fitted function
r_0	needle cylindrical radius [m]
r_1	faceplate hole radius [m]
r_2	exiting hole radius [m]
$\hat{r}$	radial unit vector
$\tilde{r}$	nondimensionalized radius $\frac{r}{r_0}$
ρ	density of fluid $\left[\frac{kg}{m^3}\right]$
ρ_i	density of the impurity i $\left[\frac{kg}{m^3}\right]$
$\breve{\rho}$	areal charge density in fluid. Zero for perfect conductors
s	distance along surface [m]
sgn	one dimensional smeared signum function $\frac{\phi}{\sqrt{\phi^2+(\Delta x)^2}}$
σ	surface tension $\left[\frac{N}{m}\right]$
σ^d	dispersion (nonpolar) component of surface tension $\left[\frac{N}{m}\right]$
$\sigma_{gl,gs,ls}$	surface energy of gas-liquid, gas-solid and liquid-solid surfaces $\left[\frac{N}{m}\right]$
σ_{min}	electrical conductivity, minimum $[\frac{S}{m}]$
σ^p	polar component of surface tension $\left[\frac{N}{m}\right]$
t	time [s]
T	temperature [K]

T_a	atmospheric stress [N]
t_{in}	droplet entering time [s]
t_{out}	droplet leaving time [s]
t_p	trip time [s]
t_{TOF}	droplet time of flight [s]
t_0	time, nondimensional $\frac{z_0}{v_0}$
τ	capacitive tube diameter [mm]
τ_{drop}	total droplet travel time [s]
τ_{LS}	level set surface bandwidth [m]
τ_{work}	material work function [eV]
Δt	time change [s]
θ	droplet impinging angle [^{o}]
θ_{wet}	wetting angle [^{o}]
θ_T	Taylor cone angle [^{o}]
Θ	lateral fluid input source term $\left[\frac{kg}{m^2 \cdot s}\right]$
ϑ	interface velocity $\left[\frac{m}{s}\right]$
$\underline{\mathbf{T}}$	Cauchy stress tensor
u, v	x, y local velocities $\left[\frac{m}{s}\right]$
U	potential [V]
$U(\overrightarrow{x})$	potential at location $\overrightarrow{x}$ [V]
U_N	needle potential [V]
U_a	accelerating voltage [V]
U_p	plate applied voltage [V]
U_0	ion extraction voltage [V]
ΔU	potential drop from electrode to needle [V]
Υ	the mixed flux/potential variable solved for on the panel boundary
v	particle velocity $\left[\frac{m}{s}\right]$

v_c	characteristic velocity $\left[\frac{m}{s}\right]$
v_e	exhaust velocity $\left[\frac{m}{s}\right]$
v_F	Fermi velocity $\left[\frac{m}{s}\right]$
V_F	volume of fluid fraction $\frac{1}{\Delta x \Delta y} \int_\Omega H(\phi(\overrightarrow{x}))\, d\overrightarrow{x}$
v_i	particle fall velocity for size class i $\left[\frac{m}{s}\right]$
v_{jet}	mini jet velocity $\left[\frac{m}{s}\right]$
v_r	radial velocity $\left[\frac{m}{s}\right]$
v_z	axial velocity $\left[\frac{m}{s}\right]$
v_0	characteristic velocity $\left[\frac{m}{s}\right]$
Δv	change in velocity $\left[\frac{m}{s}\right]$
W_a	specific adhesive work $\left[\frac{N}{m}\right]$
$\dot{w}$	weight flow rate $\left[\frac{kg \cdot m}{s^3}\right]$
$\overrightarrow{x}$	(x, y, z) position vector
Δx	change in position [m]
ξ	fractional mass percentage of impurities in stream [%]
ξ_{cl}	height of the collector slit [m]
ξ_{ds}	height of the downstream collimator slit [m]
ξ_f	fluid thickness on needle [m]
ξ_{us}	height of the upstream collimator slit [m]
$\Xi(\alpha)$	flux distribution function $\left[\frac{1}{s}\right]$
Z	geometrical needle impedance [Ω]
z_0	needle length [m]
ζ	nondimensional variable
ζ_{conc}	experimentally determined coefficient raising the tip concentration maximum
ζ_{cl}	amount collector misaligned [m]
ζ_{cm}	amount collimator misaligned [m]

ζ_θ	difference between Greens function angles
$\zeta(E)$	nondimensional droplet axis ratio
$\{\}_t$	time change of { } vector
$\{\}_{x,y}$	spatial change of { } vector

LIST OF APPENDICES

Appendix

CHAPTER I

Introduction

The following introductory sections provide a brief overview to electric propulsion; a discussion of the historical background; operation and types of field emission electric propulsion (FEEP); and the motivation and organization of this thesis.

1.1 Specific impulse and the rocket equation

A space propulsion system accelerates a spacecraft by applying a thrust force. This usually occurs by expelling a propellant mass at high velocity. Electric propulsion (EP) is a form of advanced propulsion that is rapidly becoming the standard choice for positioning satellites and other items launched from Earth. Unlike a chemical rocket, which relies on the stored internal energy in the molecular bonds of its propellant, an electric rocket's energy is obtained from an external power source. No longer limited by chemical reaction energies and instead only by available power, EP has a very high mass efficiency. This efficiency is measured in seconds of specific impulse (I_{SP}); roughly the number of seconds for which one pound of propellant will produce one pound of thrust. Various forms of EP rockets have I_{SP} values of thousands of seconds, compared to standard chemical rockets which have around 400 seconds.

The average exit velocity of the ejected propellant v_e, is directly related to the thrust and mass efficiency, as seen in Eq. (1.1). Here, F is the thrust force and $\dot{m}$ is the mass flow rate, $\dot{m} = \frac{dm}{dt}$.

$$I_{SP} = \frac{\int_0^t F\, dt}{g \int_0^t \dot{m}\, dt} \tag{1.1}$$

If the thrust and mass flow rate are constant over time, then Eq. (1.1) reduces to Eq. (1.2), where v_e is the exhaust velocity.

$$I_{SP} = \frac{F}{\dot{m}g} = \frac{F}{\dot{w}} = \frac{v_e}{g} \tag{1.2}$$

Chemical rockets have an upper limit of exhaust velocity of a few kilometers per second. Due to restrictions of chemical combustion, $v_{e,chemical} \leq \sqrt{\frac{2h_c}{m}}$, where h_c is the combustion enthalpy. To change the motion of body by a given velocity increment Δv requires consuming a certain fraction of the initial mass $m_{initial}$. Rocket performance can be understood using Newton's 3^{rd} Law,

$$m\frac{dv}{dt} = \dot{m}v_e \tag{1.3}$$

where the product of mass and acceleration comes from the product of mass flux and propellant exhaust velocity. Replacing $\dot{m}$ by $\frac{dm}{dt}$ and integrating Eq. (1.4) gives the final relation of exhaust velocity to the mass ratio of the spacecraft [229].

$$\begin{aligned} \int_{v_{initial}}^{v_{final}} \frac{\partial v}{v_e} &= \int_{m_{initial}}^{m_{final}} \frac{\partial m}{m} \\ \frac{m_{final}}{m_{initial}} &= \exp\left(-\frac{\Delta v}{v_e}\right) \end{aligned} \tag{1.4}$$

This result implies that to deliver a useful mass fraction, the exhaust velocity should be on the order of the needed velocity increment Δv [113]. The single stage,

gravity-free version of the Tsiolkovsky "rocket" equation is Eq. (1.5) and it can be seen that at higher specific impulses, the propellant fraction drops drastically due to the exponential term.

$$\frac{m_{propellant}}{m_{initial}} = 1 - \exp\left(-\frac{\Delta v}{g \cdot I_{SP}}\right) \tag{1.5}$$

Here, the initial mass is the sum of the payload, structure and propellant.

$$m_{initial} = m_{p,s} + m_{propellant} \tag{1.6}$$

For example, a change in technology that increases a spacecraft's I_{sp} from 225 seconds to 1,300 seconds could extend the workable lifetime of a north-south station keeping (NSSK) geosynchronous satellite from five to twenty years [19]. With electric propulsion exhaust flows up to 110 km/s, the usefulness of this higher propellant efficiency becomes obvious [250].

1.2 Electric propulsion background

With their specific impulses 1.3 to 30 times greater than chemical propulsion, electric propulsion possesses several notable advantages. For satellites in orbit, the mass of fuel or structures containing that fuel are upwards of 50% of the total orbited mass. The greater efficiency of electric propulsion can drastically reduce the needed volume and mass of that propellant. Therefore, spacecraft can be made much lighter, now fitting in a smaller rocket and resulting in reduced costs. The change in fuel mass could be exchanged for additional payload, making it a more capable satellite. Or, the same configuration could be used, now allowing for a significantly longer traveling range and the consideration of previously impossible missions. In addition to large mass savings, by avoiding combustion electric propulsion does not need an

oxidizer. Finally, by using easily stored inert propellants such as xenon, EP has increased safety margins [34].

The history of EP has spanned over a century and filled with significant discoveries. The benefits of electric over chemical propulsion were first pointed out by Robert Goddard in 1906 [97, 221]. Another EP pioneer was Hermann Oberth in the mid-1940's. His major electric propulsion contributions were not from a specific technical invention, but defining, publicly and unambiguously, EP as a worthwhile endeavor [43]. These men were followed by Ernest St*ü*hlinger in the early 1960's, who wrote one of the definitive books of the time on the field [221] and who recently won the lifetime recognition award from the International Electric Propulsion Conference (IEPC). Detailed analysis of the advantages of electric propulsion technologies can be found in the literature, including other University of Michigan theses [34, 65, 132, 215].

1.2.1 Weaknesses of electric propulsion

It is very important to note, however, that current EP systems are severely restricted in their mass throughput and total impulse because high power demands per kg of propellant reduce the practical mass flow rate and operational lifetime is too short to compensate for this low $\dot{m}$. They produce very little thrust, from μN to 10s of Newtons of force instead of the mega-Newtons some chemical systems produce [35, 2]. This restricts electric propulsion to a role as a *secondary propulsion system*, one that requires standard chemical rockets to get to low Earth orbit.

In addition, since these systems require electrical power, there has to be the corresponding inclusion of electricity-generating apparatus on board. This added power equipment can be quite large, and as specific impulse increases, the power

conditioning mass will grow quite substantially. For the most mass-efficient systems, the power/thrust ratio can be above one million Watts per Newton.

Hofer notes that due to this "power supply penalty" of the mass required to provide the necessary power, a higher specific impulse is not necessarily ideal [113]. In fact, the optimal setup is given by Eq. (1.7)

$$\frac{v_e}{\Delta v} \cdot \exp\left(\frac{\Delta v}{v_e - 1}\right) - \frac{1}{2}\left(\frac{v_c}{v_e}\right) - \frac{1}{2} = 0 \tag{1.7}$$

where v_c is the characteristic velocity given by Eq. (1.8), $\alpha_{pow} = P_{sys}/M_{pp}$ is the specific power, t_p is the mission time and $\eta_{sys} = \frac{1}{2} g I_{sp} \frac{F}{P_{sys}}$ is the system efficiency.

$$v_c = \sqrt{2\alpha_{pow} t_p \eta_{sys}} \tag{1.8}$$

Using today's EP technology, for missions with a total velocity change in the neighborhood of 10 km/s, the ideal main propulsive thruster has an approximate specific impulse of 3,000 seconds.

1.2.2 Types of electric propulsion

Electric propulsion can be broadly divided into three mechanisms through which thrust is produced: electrothermal, electromagnetic and electrostatic devices [122, 132, 221].

Electrothermal Electrothermal electric propulsion devices use electric power to heat a propellant, which is then accelerated through a nozzle to produce thrust. Arc jets, cyclotron resonance thrusters and resistojets are examples of this form of propulsion. Performance is limited by the maximum sustainable temperature of the body or the heating elements. As of 2006, typical systems have specific impulses of 300-600 seconds, thrust of 0.1-1 Newtons and power levels of 0.1-2 kW. Some

researchers have measured arc jet powers up to 100 kW [132]. A schematic of an arc jet is shown in Fig. (1.1).

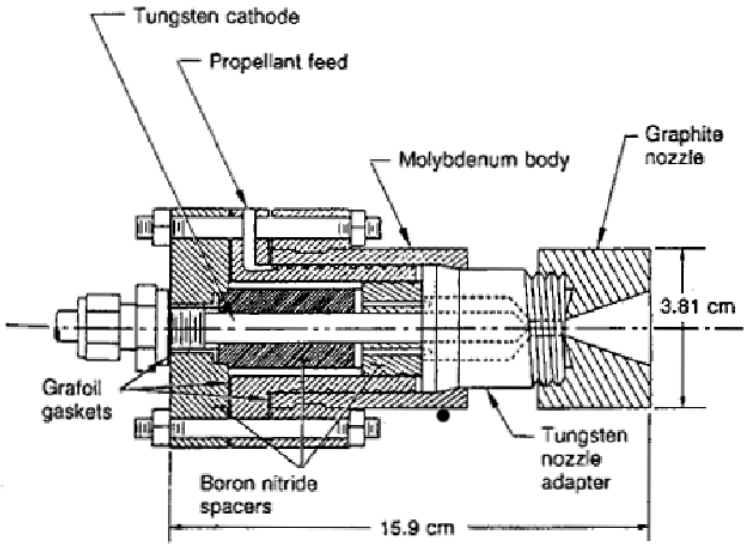

Figure 1.1: Arcjet schematic [89]

Electromagnetic Electromagnetic electric propulsion devices use a combination of electric (E) and magnetic (B) fields to accelerate the propellant. Subject to perpendicular $E \times B$ fields, a plasma current j is created. The plasma typically remains neutral, so space charge limitations are not a concern. The magnetic field is large enough to alter both electron and ion trajectories. Magnetoplasmadynamic (MPD), pulsed plasma thrusters (PPT) and traveling-wave accelerators are examples of electromagnetic force devices. The various implementations of this propulsion method inhabit totally different operation regimes. MPD thrusters run at extremely high power, using over 100 kW steady-state. These theoretically generate relatively large forces of 10-1,000 N with specific impulses of 1,500-8,000 seconds [132]. The PPTs, as the name indicates, utilize pulsed energy from a capacitor bank. They can use a wide range of power rates and generate the corresponding thrust, but suffer from

frozen flow losses and therefore rarely attain even 30% mass efficiency. Figure (1.2) displays a PPT using a block of Teflon as propellant. A capacitor bank discharges, which ablates and accelerates the polyamide, producing μN of force.

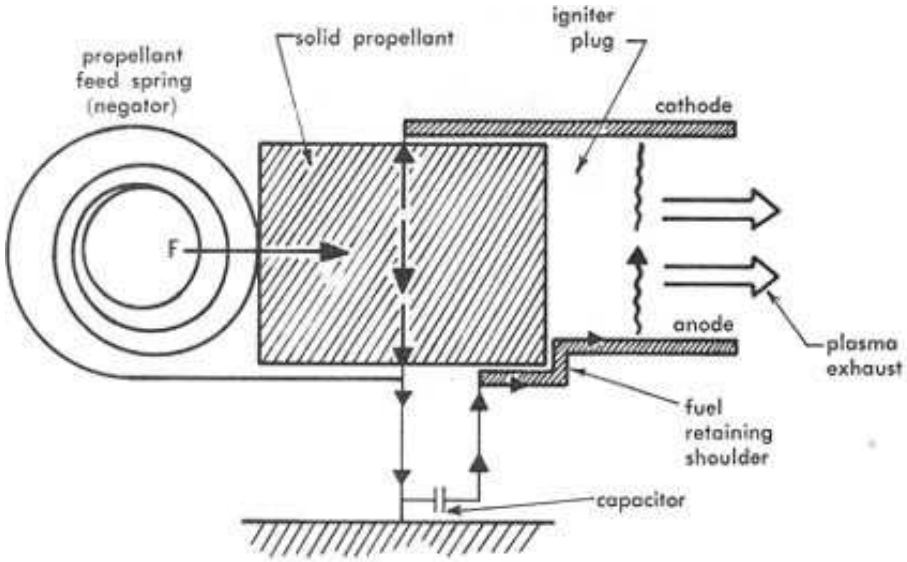

Figure 1.2: Teflon pulsed plasma thruster schematic [17]

Electrostatic Electrostatic electric propulsion devices accelerate charge-carrying propellant particles in a static electric field. An electron source in the near field neutralizes the exhaust after it travels through the nozzle. Ion, Hall and FEEP thrusters are examples of generating force through fields. By using the electric field instead of heat to accelerate the particles, material thermal issues are largely alleviated, resulting in higher performance. Maximum force constraints in ion engines occur because of space-charge limitations, although Hall thrusters are not impacted this way. Child's Law (or the Child-Langmuir Law) gives the maximum space-charge limited current in one dimension as a function of the length and potential difference along that dimension. It assumes that ions fall freely under the influence of the electric field, which is true if ion-neutral collisions are negligible [41]. Across a

surface-electrode gap d_{te}, the maximum current density j_{sc} is given by Eq. (1.9).

$$j_{sc} = \frac{4\epsilon}{9d_{te}^2}\sqrt{\frac{2q_iU^3}{m_i}} \tag{1.9}$$

Typical systems have specific impulses of 2,000-10,000 seconds, thrust of 0.1 μN - 1 N and power draws from 1-5,000 Watts. Figure (1.3) shows a Hall thruster in operation. It uses the Hall effect to trap electrons and which then ionize the propellant. The propellant acceleration occurs from a axial electric field.

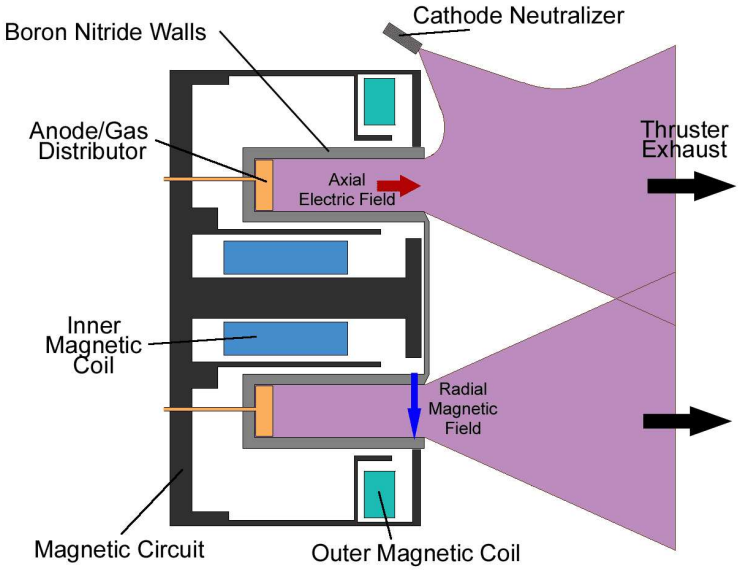

Figure 1.3: Hall thruster schematic [219]

Figure (1.4) displays the relative range of specific impulse and thrust/power for a variety of EP technologies. A particular type of electrostatic space rocket system is called "FEEP", for *f*ield *e*mission *e*lectric *p*ropulsion. This thesis is based on simulating this propulsion system. It will be described in greater detail in Sec. (1.4), but first the basic process and operation will be outlined.

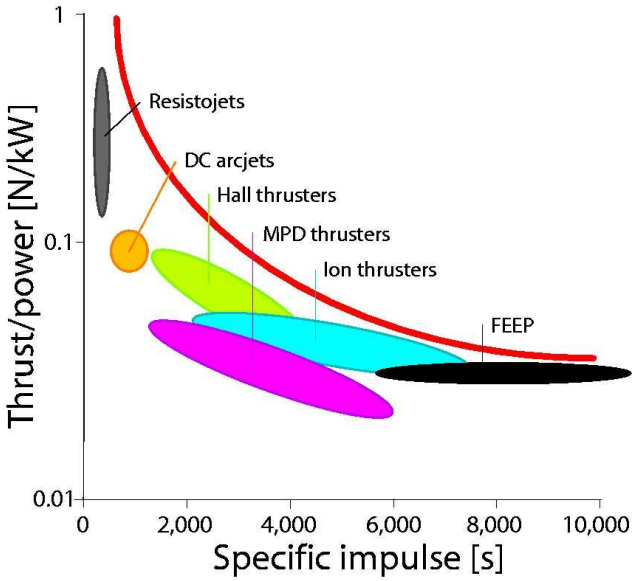

Figure 1.4: Electric propulsion specific impulse and power ranges

1.3 Field emission

Field emission refers to the process of using a strong electric field to produce a spray of charged ions and/or droplets. The potential difference between an electrode and a liquid surface is balanced by the surface tension of the fluid. As a result, the surface deforms to an equilibrium shape of a cone. The strong field intensity at the tip then causes a propellant jet to form, composed of ions and droplets [189]. The phenomenon of ion and droplet evaporation from charged liquid surfaces is of considerable interest in many areas of science and technology. Some of the many realms in which field emission occurs include: electron microscopy [114], data displays [31], carbon nanotube fluorescence [33], ink jets [217] and thermoelectric coolers [47].

Field emission driven by electrostatic forces has been studied for decades [77], first being analyzed by Schottky in 1923 [203]. As in conducting solids [171], ion evaporation from liquids occurs only when surface electric fields are in excess of a critical material-specific threshold [84, 119]. Field-ion emission from metal sur-

faces was examined initially by Tsong and Müller [251]. When used for propulsion, thrusters use the field emission process by accelerating the ions and droplets past an electrode, producing thrust through high velocity expelled mass.

1.3.1 Field emission theory

Fowler-Nordheim (FN) theory describes the field emission process in terms of a tunneling current density J through a potential barrier between a planar surface and a vacuum [80]:

$$J = \frac{e^3 E^2}{8\pi h \tau \iota^2(\zeta)} \exp\left(\frac{-8\pi\omega(\zeta)\sqrt{2m_e\tau_{work}^3}}{3heE}\right) \tag{1.10}$$

where e is the elementary electrical charge, E is the electric field, h is Planck's constant, τ_{work} is the material work function, m_e the mass of the electron, and two empirical functions $\iota(\zeta) = 1 + 0.1107\zeta^{1.33}$ and $\omega(\zeta) = 1 - \zeta^{1.69}$ [108]. Physically, ζ is a material-specific parameter describing relative electron attachment. A larger ζ implies greater charge mobility. For indium with $\tau_{work} = 4.12\,eV$, an electric field of $2.5 \times 10^9\,\frac{V}{m}$ and an emission area of 40 μm^2, $\iota(\zeta)$ =1.02, $\omega(\zeta)$ =0.876 and I=196 μA.

$$\zeta = \frac{1}{\tau_{work}}\sqrt{\frac{e^3 E}{4\pi\epsilon_0}} = 9.212 \times 10^{-6}\sqrt{E} \tag{1.11}$$

However, conventional FN theory does not represent accurately the experimental behavior of field emitters. This deviation is because the emitters are curved, typically with a radius of curvature of around 50 μm. The emission from a sphere mounted on a tapered shank can be calculated by defining non-dimensional variables:

$$\varsigma = \tfrac{\tau_{work}\kappa}{eE}, \quad \chi = r\kappa, \quad \varepsilon = \tfrac{e^2}{8\pi\epsilon_0 r_n \tau_{work}} \tag{1.12}$$

$$\begin{aligned} o(\varsigma,\varepsilon) = &\quad \tfrac{3}{2}\int_{\chi_1}^{\chi_2}\sqrt{1-\tfrac{1}{\varsigma}(1-\tfrac{1}{\chi})-\varepsilon(\tfrac{1}{\chi^2-1}+\tfrac{2}{\chi}-\tfrac{1}{\chi^2})}\,d\chi \\ r(o) = &\quad \tfrac{o(\varsigma,\varepsilon)+2\varsigma\frac{\partial o}{\partial \varsigma}-2\varepsilon\frac{\partial o}{\partial \varepsilon}}{3\varsigma} \end{aligned} \tag{1.13}$$

and using Eq. (1.13) to replace $\iota(\zeta)$ with $r(o)$ and $\omega(\zeta)$ with $\frac{o(\varsigma,\varepsilon)}{\varsigma}$ in Eq. (1.10). The limits χ_1, χ_2 are values of χ, greater than unity, at which the integrand is zero [63]. Substituting the values of Eq. (1.13) into Eq. (1.10) gives a corrected high-curvature current. The new approach accurately matches field emission characteristics for emitters with less than a 20nm radius of curvature [62], while planar approaches over predict the current by over 100%.

1.3.2 Taylor cones

For a fluid assumed to be a perfect conductor (see Sec. 4.1), the conical surface is an equipotential. Therefore to balance the surface tension, the potential gradient must be proportional to $\frac{1}{\sqrt{r}}$. Expressed in polar coordinates, the electric field which satisfies this stress condition has the potential [245]

$$U = U_0 + A_1\sqrt{r}P_{\frac{1}{2}}(\cos\theta) \tag{1.14}$$

where the line $\theta = 0^o$ or $\theta = 180^o$ is the axis of the cone, A_1 is an integration constant and $P_{\frac{1}{2}}$ is the Legendre function of order $\frac{1}{2}$. If $\theta = \theta_0$ is the conical equipotential surface where $U = U_0$, then $P_{\frac{1}{2}}(\cos\theta) = 0$. The only angle within that range at which the forces balance is at $\theta_0 = 49.3^o$ where the forces of electrostatics and surface tension are mathematically in balance [245], as shown in Fig. (1.5). As the potential on the ring electrodes increases, the liquid curvature increases until reaching this half-angle and a *Taylor cone* forms. [84].

However, the space charge effects near an infinitely fine cone point prevent field

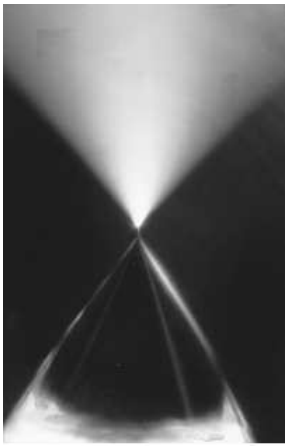

Figure 1.5: Taylor cone spray from a liquid field emitter. The liquid bottom forms a 49^0 angle, while ionic emission occurs in the upper half.

evaporation; this can be avoided by allowing for a small jet on top of the underlying Taylor shape. The size of these small extended jets varies depending on mass flow rates and tip radii of curvature. These protrusions have been observed at approximately 100 nm long and 30 nm in diameter [123, 232, 258]. The fluid velocity, width and height of the jet scale as Eq. (1.15) [257, 259]. The distance from the jet tip to the electrode is labeled d_{te}, while the current is I, the electric field E and the charge q.

$$\begin{aligned} v_{jet}\left[\frac{m}{s}\right] &= \frac{0.01\times E}{\sqrt{8\pi\rho}} \\ r_{jet}[m] &= 0.01\sqrt{\frac{m_{ion}I}{\pi\rho q v_{jet}}} \\ h_{jet}[m] &= 0.01 \times d_{te}\left(\frac{r_{jet}E}{v_{jet}}\right)^2 \end{aligned} \tag{1.15}$$

At the point of jet initiation, field emission occurs around the tip.

1.3.3 Droplet behavior

Droplets as well as ions form from field emitting tips as the emitting current increases. For the Austrian Research Center - Seiborsdorf (ARCS) design, this

changeover occurs above 10 μA [238]. The exact initiation point depends on materials, electrostatic potential and needle radius of curvature. Two different droplet sources are presented in the literature [238, 257, 259]. From a field emitter, either Rayleigh or Faraday droplets can be generated. Rayleigh droplets are generated due to the instabilities of the jet on the tip of the Taylor cone near to where ions are formed [58]. This is the dominant type of droplet for mass efficiencies of 10-100%.

Faraday droplets are bigger in size and are formed on the shank of the Taylor cone via surface wave instabilities [102]. This variety of droplet is primarily found in emitters operating from $0 - 10\%$ mass efficiency. Compared to Rayleigh droplets, when Faraday droplets are the primary type of emitted propellant experiments have observed a flatter current/efficiency relationship [237, 238].

Rayleigh limit

Efforts to determine the minimum mass necessary for a stable droplet began over one hundred years ago. Lord Rayleigh showed that the spherical shape of a drop of radius a, surface tension σ and charge q remains stable as long as the fissility χ does not exceed unity [193].

$$\chi \leq \frac{q^2}{64\pi^2\epsilon_0\sigma a^3} \tag{1.16}$$

Above that point, the repulsive forces between electrons outweigh the attractive force from surface tension. The droplet is now unstable and emits charged microjets to equalize these forces. This emission occurs because smaller droplets remain stable with a greater relative charge due to the smaller radii increasing the surface tension forces. The destruction of the old droplet and formation of multiple smaller droplets is known as Rayleigh discharge or Coulomb fission [127], and is depicted in Fig. (1.6).

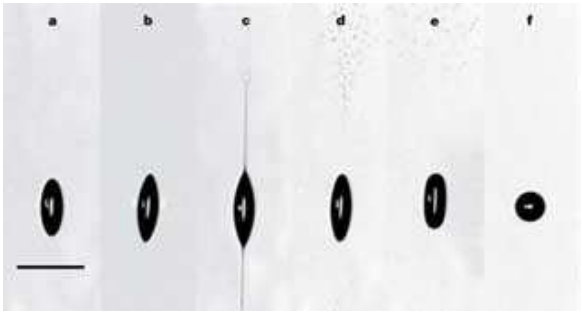

Figure 1.6: Coulomb fission of overcharged droplets [60]

Thompson and Engel rewrote Rayleigh's expression using atomic mass m and density ρ [246]; critical fissility is more easily calculated with this version. The radical equation on the right hand side of Eq. (1.17) provides the minimum mass necessary to retain stability, while the factor 1.15×10^{-6} converts the kg/C of the indium droplet to the number of molecules per free electron.

$$1.148 \times 10^{-6} MTCR \left[\frac{\#\text{ in. atoms}}{e^-}\right] = \frac{m}{q}\left[\frac{kg}{C}\right] \geq \sqrt{\frac{\rho^2 a^3}{36\epsilon_0 \sigma}} \tag{1.17}$$

Figure (1.7a) shows how this critical minimum number of atoms per charge varies as the droplet diameter changes from 0 to 10 μm, while Fig. (1.7b) highlights just the 0 to 1 μm diameter range. Overall, Fig. (1.7) demonstrates that the minimum stable MTCR for a 1 μm diameter droplet is approximately 160,000 indium atoms per free electron. Note that a lower MTCR equates to a relatively higher-charged droplet; any point to the left of the line is stable since the greater curvature of a smaller droplet allows more relative charge.

The largest mass to charge ratio for droplets is harder to pin down. Experimentally, droplets have about 1.5 times the critical Rayleigh limit with a standard deviation of 8% [88]. Based on numerous experimental tests, Gamero-Castañ*o* posits this as a general upward bound for electrospray relative charge variation. Therefore,

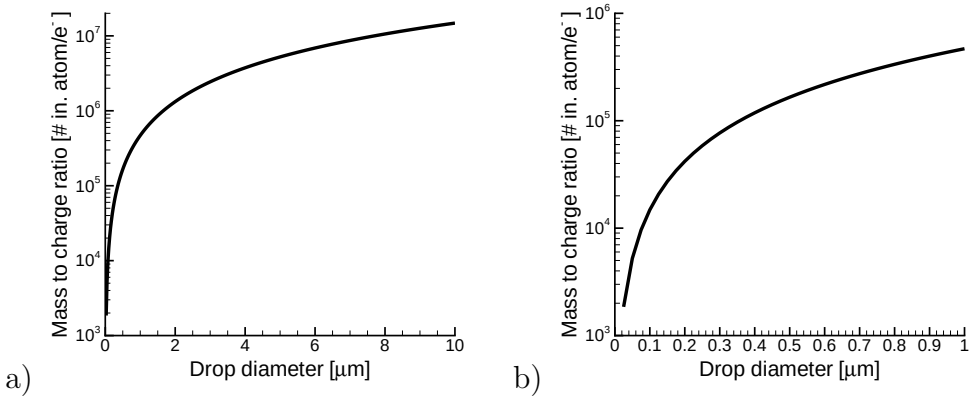

Figure 1.7: The minimum number of molecules per electron before droplets break apart from Coulomb fission and form jets. Shown for the a) 0-10 μm and b) 0-1 μm range

it is reasonable to set the expected droplet charge at the limit. The capacitance can then be used to determine how many charges remain on the surface and the resulting charge density.

Instabilities

According to current theories, Rayleigh droplets are generated if the propellant is not transported rapidly enough to fully replenish the amount emitted. The time to form a droplet is the jet height divided by the velocity, or $t_{jet} = h_{jet}/v_{jet}$. If this time needed to form a droplet is less than that needed for the liquid to flow along the jet, a Rayleigh droplet is produced.

Early experimental [271] and theoretical [184] work showed that neutral droplets symmetrically elongate parallel to the electrical field as polarization-induced charge densities develop at opposite ends of the droplets [106]. The elongating droplets become unstable when the applied electric field reaches a critical limit, E_c^0. This field is known as the *Taylor limit*.

$$E_c^0 = c_{emp}\sqrt{\frac{2\sigma}{8\pi\epsilon_0 r_c}} \tag{1.18}$$

In Eq. (1.18), the fitting constant c_{emp} has been determined theoretically and is 1.625 for liquid droplets in air [245]. Assuming that the droplet remains a spheroid, when $E < 0.55E_c^0$, the resulting function for the major/minor axis ratio of these detached droplets versus electric field $\varsigma(E)$ is given by Eq. (1.19) [201].

$$\varsigma(E) = \left(1 + \frac{9r_c\epsilon_0 E^2}{16\sigma}\right)\left(1 - \frac{9r_c\epsilon_0 E^2}{16\sigma}\right)^{-1} \tag{1.19}$$

Between the Rayleigh charge limit and the Taylor field strength limit is the case of excess electrical pressure. In this realm, the spherical approximation is not correct, since charged droplets are egg- or tear-shaped [3]. For a droplet of charge q, this shape becomes unstable at a critical electric field E_c^q and is characterized by the formation of a single jet from the sharper end [106]. These unstable droplets can form quite a large percentage of the mass flux for the higher mass flow of emitters. The modeling and simulation of these elements in field emission thrusters forms a large portion of this thesis.

Basic droplet model

A basic model for the force on a droplet states that if the surface charge q is uniformly distributed on the surface of a conducting fluid sphere of radius R in an infinite expanse of an ambient dielectric fluid of the same density as the sphere and absent viscous stresses, the pressure inside the sphere p would be related to that outside, p_0, as Eq. (1.20),

$$\begin{aligned} p = &\quad p_0 + \left(\tfrac{2\sigma}{R} - \tfrac{1}{2}\epsilon_0 E_n^2\right) \\ = &\quad p_0 + \left(\tfrac{2\sigma}{R} - \tfrac{1}{2\epsilon_0}\sigma_E\right) \end{aligned} \tag{1.20}$$

where E_n is the normal component of the electric field on the ambient fluid side of the interface, σ is the surface tension, σ_E is the surface charge density and $\sigma_E = \frac{q}{4\pi R^2} = \epsilon_0 E_n$ [282]. This equation makes it clear that increasing the local field strength or the local charge density reduces the electromechanical surface tension of the interface [163].

Conductivity regimes and shear stress

If the drop is a perfect conductor, the entire drop is an equipotential surface and the interior electric field is zero. When the liquid is not a perfect conductor, there is necessarily a difference in potential around the shape. This potential variation ensures the presence of a tangential electric field. Moreover, if the drop is not a perfect insulator, there will be a distribution of free charge on the surface. When an interface supports both a tangential electric field and free surface charge, it is subject to electrical shear stress [201]. In the absence of varying surface tension, such an electrical shear stress can only be balanced by a viscous shear stress exerted by the drop on the surface. For these intermediate conductivity fluids, the shear stresses drive interior bulk circulation, and stabilize the surface during its growth before detachment [282].

1.3.4 Critical current

As noted previously, in addition to ions, field emitters can also produce micro-droplets. Generally, the higher the emission current, the greater the Taylor cone instability that triggers the production of droplets [239]. Theoretically, instabilities

should occur on sharp needles only above the critical current I_C:

$$I_C = \frac{13.4\pi\sigma^2 e\sqrt{\rho}}{E_i m\epsilon_0\sqrt{\epsilon_0}} \tag{1.21}$$

where E_i is the ion evaporation field. Using indium as the liquid, the critical current regime is 12.7-15.8 μA. Note that the expression is only determined by the material properties and the electric field.

1.3.5 Minimum voltage

There is a critical minimum electric field below which ion emission will not occur. Below this field potential, the liquid gradually deforms into a Taylor cone with an apex half angle approaching the critical 49^o as the voltage increases. Experimentally, emission has been demonstrated at an extractor electrode distance of 200 μm and a 10 kV potential, although any combination that develops an electric field of approximately $10^9\, V/m$ causes ions to begin streaming [91] for indium tipped emission. As the tip radius of curvature decreases, the local electric field increases; ion emission occurs at voltage U_0 [152],

$$U_0 = \ln\left(\frac{2d_{te}}{r_c}\right)\sqrt{\frac{r_c\sigma}{\epsilon_0}} \tag{1.22}$$

where r_c is the needle radius of curvature and d_{te} the tip to electrode distance. Figure (1.8) displays the baseline relationships for voltage and needle curvature.

1.4 Description of field emission electric propulsion thrusters

Two examples of field emission thrusters are colloid and field emission electric propulsion thrusters. They have been examined for decades [55, 274] and the ion/droplet plume composition has been investigated [145, 179]. Several scaling laws

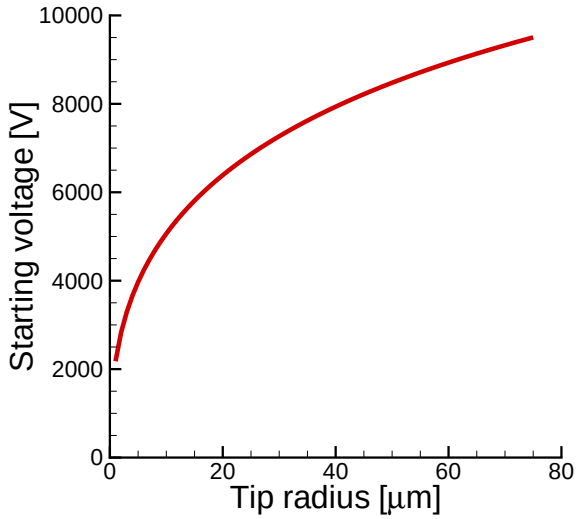

Figure 1.8: Minimum electrode potential vs. needle tip radii of curvature

about current and voltage, droplet size and specific impulse have been developed [36, 243].

FEEP thrusters are currently being considered for a variety of space missions both in the United States and Europe. FEEP thrusters provide a source of high specific impulse, ultra-low impulse bit electrostatic space propulsion. A space-tested indium FEEP has been under development in Austria for over a decade [94]. Such thrusters are appropriate for scientific drag-free missions such as LISA [25], Darwin [124], GOCE [129] and SMART-2 [161].

1.4.1 Thruster description

The liquid metal ion source (LMIS) thruster as built and tested by the ARCS consists of a needle covered in the element indium reacting to an applied electric potential from an extractor ring held at -6 kV [94, 240, 243]. When the field strength at the tip reaches 1 V/nm, a cone of indium is then ionized from the surface and accelerated over a fine tungsten needle that is about 1 cm long and 50 μm wide.

Depending on the mass flow rates, either ions or droplets are observed coming from the tip. Planar and isometric schematics of a FEEP are shown in Fig. (1.9). Figure (1.10) displays some experimental apparatuses for slit [92] and needle field emitters [242].

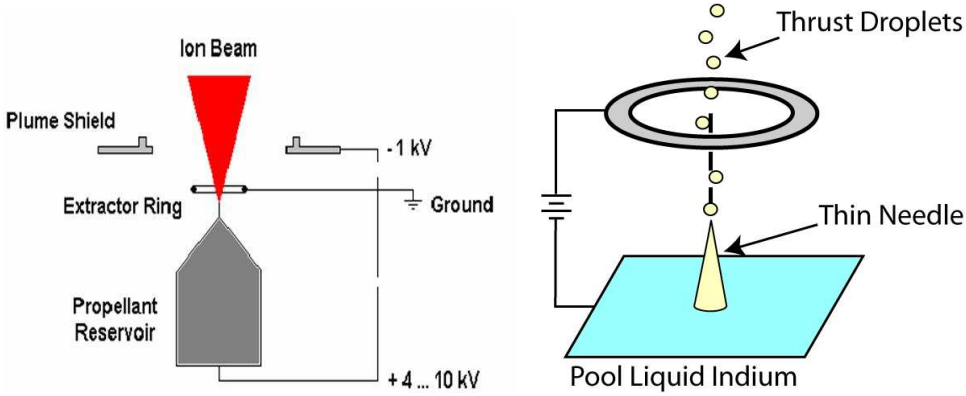

Figure 1.9: Needle FEEP emitting a) ions and b) droplets

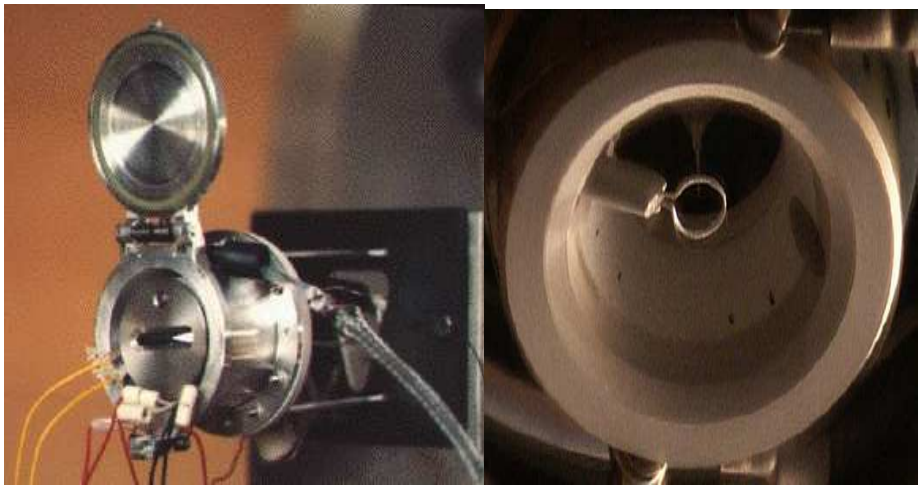

(a) Centrospazio cesium slit FEEP (b) ARCS indium needle FEEP

Figure 1.10: Experimental field emission thrusters

Droplet importance

Experimental efforts indicate that below 20 μA, only ion emission occurs in a wide cross-section of field emission needles [90, 93, 178]. Above that point, at a current that varies based on the thermal and electrical properties of the fluid, periodic stochastic motions of droplet formation and emission interrupt the steady ion stream [238, 258]. For the emitter to be an effective space attitude control thruster, a current of several hundred μA is necessary [94]. At this level of current, significant mass flow rates generate 100s of μN of thrust. The droplet initiation current is thus driven by the properties of the fluid flowing over the tip. As the current increases, ever-increasing mass fractions are emitted as large droplets and less as ions. Due to localized field evaporation on the Taylor cone shank, there is never 100% droplet content.

The existence and corresponding behavior of these droplets is of large practical concern because as more droplets form, operational efficiency decreases, lifetime is limited because drops clog the extractor electrode, and plume divergence is impacted due to non-identical charge distributions in the exhaust stream. Knowledge on how the beam behaves and the ability to manipulate it can be used to improve two performance parameters of the FEEP thruster. First, spacecraft contamination can be significantly reduced through a reduction in beam spreading. Secondly, with this lower spreading rate per μA, a larger current (and therefore thrust) is possible without contamination [86]. In combination, these effects substantially increase the range of missions that can be successfully undertaken by field emission electric propulsion thrusters. Therefore, a numerical investigation into the formation and charge distributions among these expelled droplets is undertaken and described in this thesis.

Potential field

Since field emission predominantly occurs in the areas of maximum electric field, a necessary precursor to this investigation is an awareness of the electrostatic potential field around the needle. The potential field U was determined using Matlab's finite volume numerical Poisson solver on 300x100 rectangular grids. The mixed Dirichlet and Neumann boundary conditions imposed are listed in Eq. (1.23).

$$\begin{aligned}
\text{needle:} \quad & U(0,\, [0\,0.025]) && = -2 \\
\text{base:} \quad & U([0\,0.1],\, 0) && = -2 \\
\text{far edge:} \quad & \tfrac{\partial U}{\partial n}(0,\, [0\,0.05]) && = 0 \\
\text{electrode:} \quad & U([0.01\,0.1],\, 0.05) && = 8,000 \\
\text{gap:} \quad & \tfrac{\partial U}{\partial n}([0\,0.01],\, 0.05) && = 0 \\
\text{axis:} \quad & \tfrac{\partial U}{\partial n}(0,\, [0.025\,0.05]) && = 0
\end{aligned} \tag{1.23}$$

This potential solution indicated that the sharpest potential gradient is located at the tip of the needle, as can be seen in Fig. (1.11). As a result, the droplet emission far from the shank of the needle surface is less prevalent due to the lower electric fields and reduced field emission.

1.4.2 Propellant considerations

Many liquids can be used in a field emitter and several studies have outlined the characteristics of an ideal propellant [160, 168, 169]. Cesium was the initial element chosen [177] decades ago, but re-evaluation points to an improved propellant choice of the element indium due to its high atomic mass, low ionization potential and good wetting properties. An additional strong benefit is that it can be exposed to

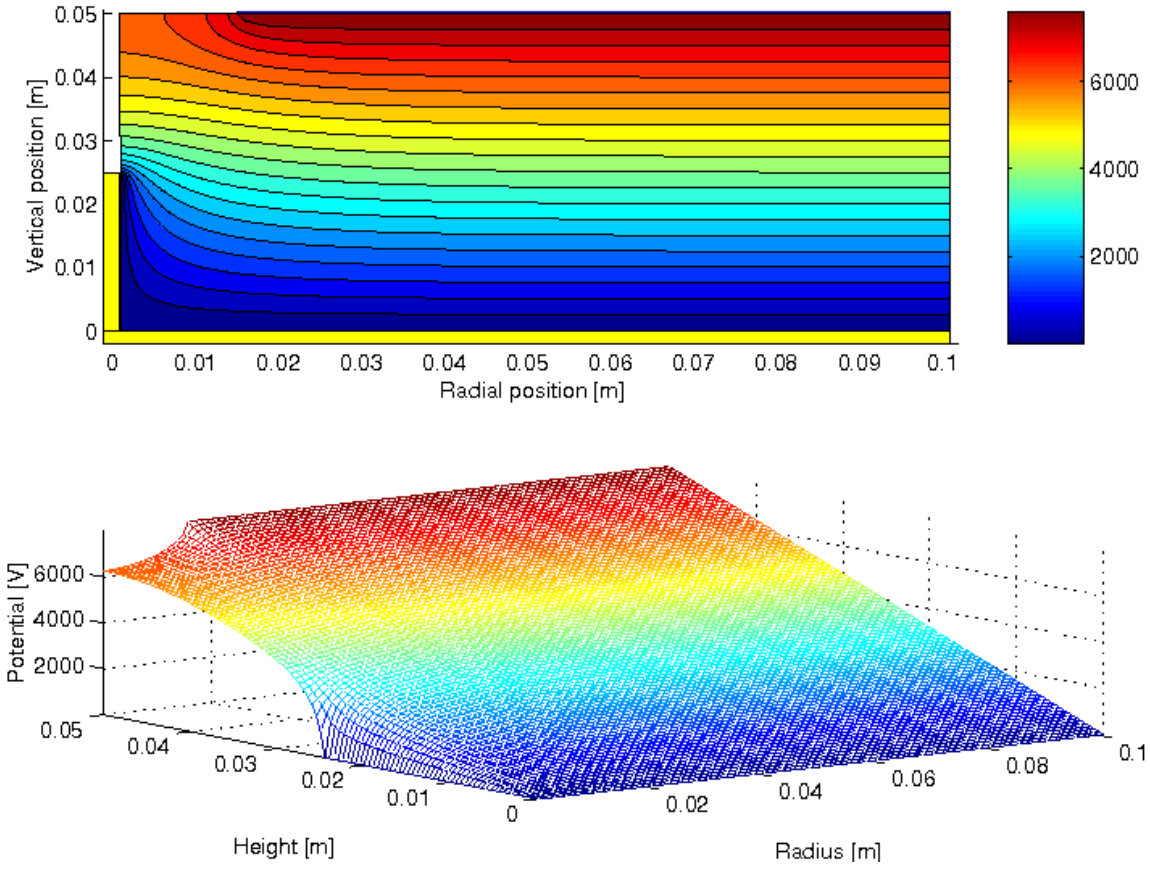

Figure 1.11: Simulation of potential contours for a needle FEEP

air without exploding or dangerously out-gassing.

Atomic mass The heavier the atom, the greater the maximum achievable thrust for a given electric field. Lighter elements and alloys travel faster but impart lower momentum changes to the engine. The minimum acceptable atomic mass for potential propellants was initially defined by an ESA panel in 1980 as that of cesium with a mass of 133 amu, but a lower secondary standard of 100 amu was also adopted [177].

Capillary / needle flow The flow rate along the surface of a needle needs to be large enough to allow constant emission at relatively higher currents of 100 μA. Calculations relating to fluid flow lead to the conclusion that the velocity of the liquid is determined by geometric parameters (e.g. the radius and length of the needle) as well as physical parameters such as viscosity. This is examined in much more detail in Sec. (3.3).

Diffusion rate Based on reservoir leaching contamination in Austria, unwanted tip material buildup and sparking can occur if propellant contamination over 5% by volume occurs [90, 169].

Droplet emission To work as a pure field emitter, the liquid must emit individual ions rather than droplets or clusters when subjected to an intense electric field. One older model of emission characteristics was developed by Crowley that relates the emission of ions to a low value of $\frac{\rho}{\lambda}$, the ratio of the electrical resistivity to the thermal conductivity of the liquid [52]. However, his work originally was established for the case of electrostatic spraying from one single liquid metal cone. In cases

with multiple-tip emitters like the slit emitter that possess a rather low current per emission site, the importance of this criterion may be regarded as somewhat inferior. However, emission with a preponderance of ions is significantly greater for a propellant with a low first and a high second ionization energies, due to the large energy gap between these points.

Environmental concerns The handling and operation of the propellant choice necessitates infrastructure costs and procedures. The choice of a hazardous, toxic, explosive liquid such as cesium for propulsion drastically increases the ground system financial burden to safely handle and contain carcinogens. Future environmental regulations further restricting acceptable exposure to chemicals are predicted to make even this path untenable [214]. Indium avoids many of these concerns, reducing but not eliminating these environmental aspects of propellant selection.

Melting temperature The propellant should melt at temperatures that can be achieved readily in the feeding system without incurring a significant power demand. Commonly, this has been around 100-300 ^0C [71].

Resistance to vacuum breakdown During operation, a possible eventual malfunction of a FEEP thruster due to arcing, sparking or flashover is strongly possible. The physical phenomenon of vacuum breakdown represents the closing of an insulating vacuum gap by a low-voltage, high-current vacuum arc. This breakdown may cause damage to the emitter itself and perhaps to the high-voltage supplies, but the transients accompanying such phenomena also may damage or even destroy the highly sensitive electronic equipment on board a spacecraft due to induced overvoltages. Thus a requirement on the liquid metal propellant requires a resistance against

vacuum breakdown [168].

Vaporization It is desirable that the propellant has a low vapor pressure, for at higher values of vapor pressure the liquid would not be emitted as a focused thrust cone but instead as a non-accelerated mist. This diffusion lowers mass efficiency and increases deposition rates upon the spacecraft itself.

Voltage standoff Physical liquid properties such as work function, ionization energy and surface tension contribute to the initial potential needed to induce field emission. Lower beginning voltages reduce power and secondary equipment mass requirements.

Wetting The propellant should flow readily along capillary feed systems and maintain the liquid films or menisci from which emission occurs. It must therefore be able to wet the reservoir feed system and emitter materials.

Conclusion Among all the requirements for alternative propellants to cesium, reliability seems the most critical. Arcing or flashover may cause irreversible damage to the whole FEEP thruster system, thus influencing the reliability and lifetime. Substantial arguments exist against cesium as a reliable liquid metal propellant. Indium achieves substantial improvements in usability with only mild degradation in performance, and is therefore a better selection.

1.4.3 Droplet vs. ion thrust

One question that often arises is why for a given thruster droplets provide more thrust than ions, even though they move at a slower velocity. The key detail is that satellites have a fixed total power available to the thruster (P_{jet}); it usually comes

from solar panels (P_{solar}) or radioactive decay. Letting $P_{solar} = P_{jet}$ and qE=F=$\dot{m}$a, the final velocity of a particle starting from rest in a constant electric field E traveling over a fixed distance x is $v^2 = 2a\Delta x$, or

$$v = \sqrt{2\frac{q}{m}E\Delta x} \tag{1.24}$$

Therefore, a more highly charged droplet, one with a lower mass to charge ratio (MTCR), moves faster than a lesser charged droplet. With the velocity of the exhaust particle stream $v = g_o I_{SP}$, Eq. (1.25) shows a higher charged droplet has a higher specific impulse.

$$I_{SP} = \frac{1}{g_0}\sqrt{2\frac{q}{m}E\Delta x} \tag{1.25}$$

The jet power and force from the rocket is shown in Eq. (1.26), while the power-to-force ratio is given by Eq. (1.27).

$$\begin{aligned} P_{jet} &= \tfrac{1}{2}\dot{m}v^2 \\ F &= \dot{m}v = \dot{m}gI_{SP} \end{aligned} \tag{1.26}$$

$$P_{jet}/F = \frac{1}{2}v = \frac{1}{2}gI_{SP} \tag{1.27}$$

This gives a relationship stating that as the engine becomes more mass efficient from a higher specific impulse, more power per unit thrust is required. Using Eq. (1.27) with a fixed maximum power supply,

$$\text{const} = F \times I_{SP} \sim \dot{m}I_{SP}^2 \tag{1.28}$$

and therefore higher charged, faster-moving ions produce *less* thrust while using *less* mass from a given power level than the corresponding droplet emission.

1.4.4 Alternative technologies

While the main benefits of field emission electric propulsion include its small impulse bit, high mass efficiency (specific impulse) and low thrust, alternative technologies exist that also provide less than 1 mN of thrust. Colloid thrusters and micro radio frequency ion thrusters (μN-RITs) are two approaches that have lower specific impulse and power requirements than FEEP, but still are in the micro-thruster regime.

Colloid thrusters Colloid thrusters are a design very similar to that of FEEPs. The main difference is that colloids commonly employ organic propellants of low conductivity. The main effect of this lower conductivity (generally under 0.1 S/m) is that charge shielding and the tangential electric field play a large role in the droplet evolution. In addition, generally only droplets are formed during operation. As a result of using long chain hydrocarbons, the thrust is greater per μg, while the necessary power and voltage are lower. Most of the work in the field is termed as electrospraying, since the original use was the formation and mixing of various size and charged droplets. Colloid thruster development can be traced to the early 1960s, but early work generally failed as a result of the poor technical understanding of the physical elements underlying the electrospraying process [5]. Later, an improved understanding came from de la Mora's work in the mid 1990s [73]. This improved insight has allowed the development of microfabricated emitters, as seen in Fig. (1.12). Other versions of colloid emitters are designed to fly on LISA [115].

Micro radio-frequency ion propulsion European research into μ-RIT propulsion was initially conducted in the 1960's by the University of Giessen, Germany. The

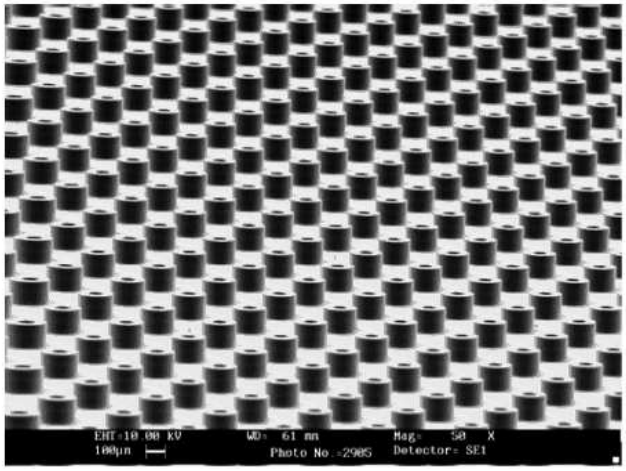

Figure 1.12: Section of a microfabricated silicon wafer containing 20,000 nozzles in a 75 mm diameter area [5].

European Aeronautic Defense and Space Company (EADS) undertook the industrial development. Several thrusters have flown in space since 1992 and have been demonstrated to work for thousands of hours. The design engines for the GOCE mission produce a specific impulse of 3,500 seconds and a thrust of 250 μN from a 1,000 V potential difference [101].

1.5 Motivation

The purpose of the effort reported in this thesis is to theoretically and computationally analyze an indium-fed needle FEEP. Specifically, there is a desire to quantify the number, size and charge of droplet emission from the needle surface and how the various aspects of needle design affect overall performance. Notable questions about thruster performance are analyzed by using a dual approach of theoretical mathematical and computational models.

1.5.1 Experimental results and limitations

Due to the high electrostatic potentials of over 5 kV needed between the electrode and the needle, experimental work on field emitters requires expensive and extensive voltage regulatory equipment. When used as a thruster, there is also a need for a strong vacuum chamber due to rapid background pressure neutralization. The original choice by Centrospazio of the reactive metal cesium as a propellant necessitated significant material-handling restrictions and raised contamination issues [167]. A later switch by ARCS to using the metal indium as the propellant source reduced the hazard associated with inhaling the material, but indium still coats the walls of the experimental vacuum chambers and requires extensive cleanup afterwards [1]. While these hardware difficulties can and have been overcome, it necessitates a significant capital and time investment. Computer simulations of FEEPs can be performed anywhere and may provide a useful complement to measured data.

While meaningful research has been performed on FEEP thrusters, experimental work has been limited in the types of questions that can be addressed. NASA's Jet Propulsion Laboratory (JPL) and ARCS have concentrated on scaling the ion emission to the $150\,\mu N$ thrust range [9, 241]. Earlier testing on droplet size and mass/charge ratios [135] has shown that as the relative charge of the droplets increases toward the Rayleigh limit, droplet breakup is more frequent. In addition, the relative number of large droplets decreased when the source current increased, the reservoir pressure decreased, or the operating voltage increased [160]. What has not been determined is why or how these values change. Modeling presents an alternative approach to studying droplet dynamics and is flexible, rapid, cheap and capable of investigating scenarios outside of the normal experimental realm.

1.5.2 Modeling approaches

To complement experimental studies, a variety of techniques have been used in the modeling of electrostatic droplets. Kaufman's original approach was the basis for nearly all computer models regarding ion propulsion [126]. FEEP simulation started a little later and focused more on ion trajectories than on bulk plasma behavior. Compared to the well-developed chemical propulsion simulations, fewer field emission models have been developed. Some of these approaches include perturbation of an infinite cone [207], marker-and-cell surface tracking [53], repeated coordinate reinitialization for Taylor cones [230], 1-D Laplacian jets [143], particle plume models [233], and microdroplet Rayleigh instabilities [257].

However, none of these attempts to simulate a field emitter provide detailed droplet relative charge after snap-off. To do so, several issues have to be successfully addressed. A full model must account for:

- Accurate force representation in the presence of very large electrostatic gradients
- A rapidly moving surface
- Formation of singularities as a new droplet detaches
- Arbitrary and changing droplet shape
- High-density liquid evolving in a vacuum

The other approaches cannot track the droplet in a reasonable time frame in a dense fluid during a highly charged fission event. Due to the lack of detailed information from both experiments and models of FEEP droplet formation and behavior, the combined approach described hereafter is a new addition to the community.

1.6 Organization

This dissertation is organized into three major parts: background, mathematical analysis and simulation of droplet detachment for a FEEP thruster. Chapter (I) laid out the importance of EP, the base setup of field emission, the functioning of a FEEP thruster, and contribution of this work. The next few chapters provide theoretical tools to study field emission and the effect of varying the initial conditions on produced droplets. Chapter II discusses a parametric evaluation of the needle and propellant composition and introduces new impedance and surface tension models. These models are used to predict the direction and magnitude of the thrust change from varying the experimental setup. Chapter III presents a mathematical asymptotic perturbation analysis of the dominant forces involved in the formation of a FEEP droplet.

The bulk of the dissertation and the majority of the modeling and simulation efforts are discussed in Chapter IV. The level set and boundary element methods are introduced for 2D and 2D axisymmetric configurations, and a number of difficulties encountered are introduced, dissected and solved. Simulation results are shown in Chapter V; they are in line with Chapter II's approach and related to the outcome of Chapter III's perturbations. Here, component properties are varied and the droplet time behavior and mass to charge ratio presented.

The major conclusions from the thesis are summarized and suggestions for future development of the electrostatic drop tracking are proposed in Chapter VI. Finally, the appendices provide details of standard FEEP needle thruster operation, mathematical derivations, sample problems and a full hardware sensor design.

CHAPTER II

Parametric Analysis of FEEP Performance

Prior theoretical and experimental work states that geometrical impedance Z and overall mass efficiency η_m are impacted by efforts to change the film thickness of indium along a field emission electric propulsion needle thruster [156, 151, 238, 261]. Current theory states that droplets begin to form when the velocity of indium being supplied to the tip of the Taylor cone is insufficient to replenish the mass lost through ion emission [143]. This velocity is strongly affected by the needle tip radius of curvature, where the needle's impedance and surface fluid thickness change the width of the Taylor cone [237]. As the film thickness decreases, the fluid velocity, required extractor voltage and mass efficiency increase.

Understanding the related question of how modification of the needle and propellant affects mass efficiency would therefore provide necessary clarification about the interaction between these components. An algorithm is presented on linking flow impedance with mass usage rates and how altering the composition of the propellant stream impacts fluid flux.

2.1 Needle impedance effect on mass efficiency

The current-voltage I-V characteristics of liquid metal ion sources are determined by the combined effects of flow and space charge around the tip of the FEEP needle. However, in situations in which the flow impedance is sufficiently small, the limitation of space charge is the dominant factor controlling the emitted current. The maximum current able to be extracted is limited since the self-shaping nature of the liquid emitter means that even an initially low-impedance source becomes flow-limited due to a decrease in film thickness [156].

If space charge effects at the apex of the Taylor cone alone limited the emission rate, then the current-voltage characteristics would *not* depend on the geometry of the needle. Rather, a current-voltage curve would be dependent only on each metal's Taylor cone. Thus, the observed strong dependence of $\frac{dI}{dV}$ on needle radius and surface roughness [262] demonstrates that the ion current is limited by flow impedance of liquid metal on the needle surface. Further evidence for hydrodynamic limitation is the extremely steep $\frac{dI}{dV}$ curves for nozzle geometry ion sources in which the flow impedance is very small [130]. Therefore, understanding the transition of indium flow between smooth and grooved needles (high and low impedance, respectively) is essential to being able to predict how varying needle geometry impacts mass efficiency.

2.1.1 Impedance models

Across fields as diverse as acoustics, aerospace and electronic circuits, a variety of methods to model fluid impedance have been proposed [46, 156, 157]. On purely physical grounds, the ideal model would include terms describing the material parameters, predicting varying results for smooth versus rough surfaces [156], Taylor

cone width [155] and liquid thickness [154].

In the mid-1980's, the first expression for the current-voltage characteristics of capillary field emission devices was introduced [153, 22] where the current is determined solely through the geometric properties of the Taylor cone base radius r_T and half angle θ_T, the fluid surface tension σ and starting voltage U_0.

$$I = 3\pi\sqrt{\frac{2e}{m}} \cdot \frac{r_T \sigma \cos\theta_T}{\sqrt{V_0}} \cdot \left(\frac{U}{U_0} - 1\right) \tag{2.1}$$

The model agrees well with experimental data for capillary emitters and low-impedance needle emitters, characterized by grooved or well-roughened surfaces [235]. For high impedance needles, Mair modified the formulation as in Eq. (2.2) to include that resistance, Z. [156].

$$I = \left[3\pi\sqrt{\frac{2e}{m}} \cdot \frac{r_T \sigma \cos\theta_T}{\sqrt{U_0}} \cdot \left(\frac{U}{U_0} - 1\right)\right] \times \left[\frac{4\rho\sqrt{U_0 e}}{4\rho\sqrt{U_0 e} + 3\pi r_T^2 Z\sqrt{2m}}\right] \tag{2.2}$$

For FEEP needles, when the indium fluid thickness on the shaft is greater than 1 μm, the correction factor in the brackets can be neglected [236]. These high impedance needles were characterized by having a smooth, non-grooved surface. Mair *et al.* [156, 151] also provided Eq. 2.3, a relation for the geometrical flow impedance of a well-wetted low- and high- Z paraboloidal needle.

$$\begin{aligned} \text{low } Z[\Omega] &= \frac{64\mu}{a_{groove}^3 \pi^2}\sqrt{\frac{2L_n}{r_c}} \\ \text{high } Z[\Omega] &= \frac{12\mu}{\pi^2 F_T^3}\sqrt{\frac{L_n}{2r_c}} \end{aligned} \tag{2.3}$$

Here, μ is the fluid viscosity, a_{groove} the groove radius, F_T the fluid thickness, L_n is the needle length, and r_c the needle tip radius of curvature. When the propellant becomes thinner, overall flow resistance increases greatly. To a good approximation,

the I-V trace can be treated as a linear function of impedance.

$$U = U_0 + Z \cdot I \tag{2.4}$$

Longer and smaller-tipped needles and more viscous and thinner fluid also increase this flow resistance. Figure (2.1) shows how the flow resistance varies with these factors.

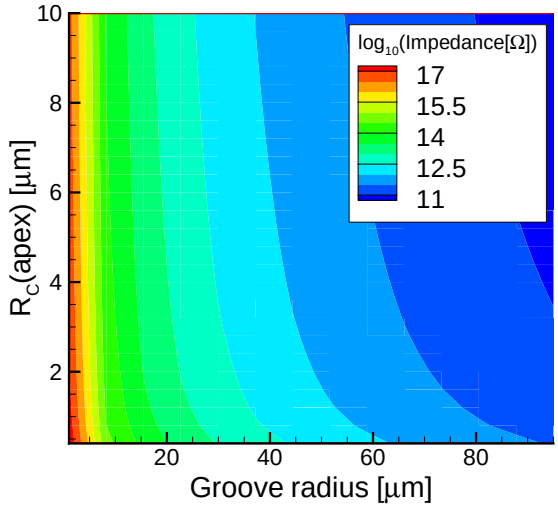

Figure 2.1: Flow impedance as a function of needle radius and groove thickness

Efficiency/impedance relationship

FEEP propellant moves at different speeds as it travels from reservoir to needle tip. However, the largest amount of time is spent moving along the constant radius cylindrical surface of the needle body. In contrast to capillary tubes where the propellant is internal, indium on the external needle surface can vary in fluid thickness and creeping velocity, thereby causing variations of the measured mass efficiency. This efficiency is the ratio between the mass emitted as singly charged ions and the

total mass loss of the liquid metal reservoir, Δm. In Eq. (2.5), m_{ion} is the mass of the emitted ion.

$$\eta_m = \frac{m_{ion}}{e} \frac{\int I\, dt}{\Delta m} \tag{2.5}$$

The strong correlation of impedance with overall mass efficiency makes it very instructive to examine methods of varying the magnitude of the Z term. Figure (2.2) presents ARCS data [237] that relates an increasing impedance with a higher η_m. Each data point is a differentially manufactured emitter producing 100 μA of current, with the necessary voltage varying from 2.5-8.2 kV. The high efficiency obtained at high impedance relationship is examined further in the next few sections.

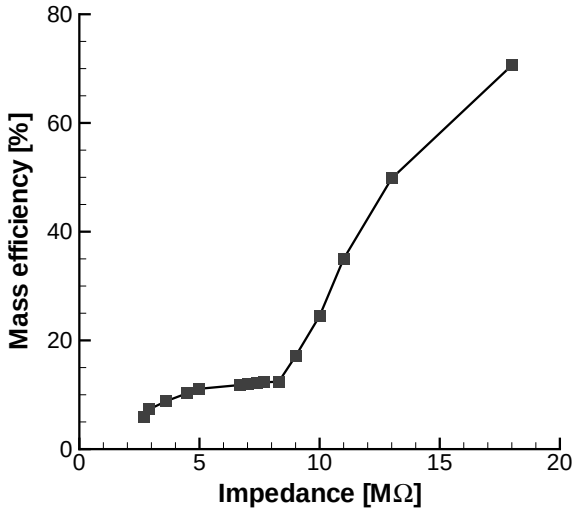

Figure 2.2: Experimental mass efficiency and impedance for multiple ARCS indium needle FEEPs at 100 μA [237]

The height of the mini jet formed atop the Taylor cone due to space charge limits and the velocity of that fluid were given as Eq. (1.15). The ratio of the two is the time for the propellant to transit across the jet. Equation (2.6) describes how mass

efficiency is related to this local time fraction.

$$\frac{h}{\nu_{jet}} = \frac{8m}{e}\frac{d_{te}I}{V^2} \propto \frac{1}{\eta_m} \tag{2.6}$$

Inserting this relation into Eq. (2.4) and using the definition of an electric field as the potential difference over the distance, $E = U/d_{te}$ gives Eq. (2.7), a relationship between efficiency and impedance [237].

$$\eta_m \propto E\left(\frac{U_0}{I} + Z\right) \tag{2.7}$$

Therefore, the mass efficiency increases as the impedance increases, but more system power is needed due to the higher potential required to initiate emission.

Minimum fluid velocity

For a given η_m, mass conservation allows for the computation of indium velocity up the sides of the needle. Figure (2.3) relates indium's wicking velocity versus film thicknesses for currents of 10, 100 and 250μA. For low flow rates where $I < 15\,\mu A$, experiments have shown that almost all the field emission current is in the form of ions [72]. At these lowest charge levels the data collapse to Eq. (2.8), an empirical relation for fluid velocity ν_{feh} derived by Fehringer [71].

$$\nu_{feh} = \frac{19.7\,I}{F_T r_c} \tag{2.8}$$

His prediction method uses only gross flow properties to predict wicking speed. Here, r_c is the needle radius of curvature [μm] with indium film thickness F_T. As the measured current increases, a greater percentage of droplets is formed in the emitted stream, resulting in a faster fluid flow for a given thickness; more material has to pass over the needle surface to emit a given number of electrons per second. Also it

can be noted that a particular emitter occupies only one point along each curve at the current value of $\nu_{\{x\}\,\mu A}$, and as the current is increased for a given geometry, the indium velocity and film thickness for that emitter also increase.

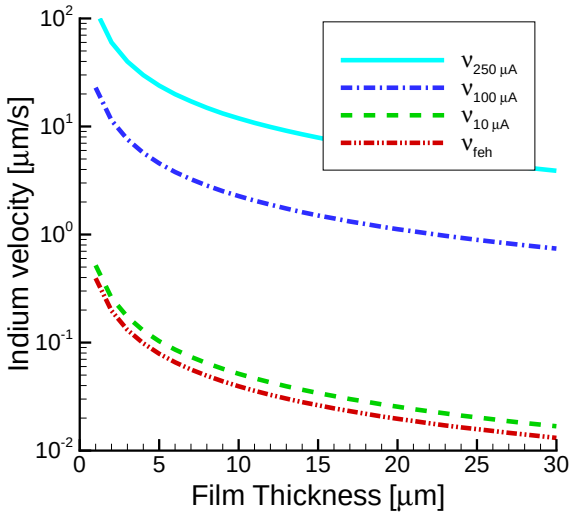

Figure 2.3: Emitted current effects on film thickness and indium velocity

ARCS Experiments

A series of needle life and efficiency tests for a particular needle FEEP technology family was performed in Austria [91, 92, 93, 94, 240]. The following subsection describes their experimental setup.

Experimental setup The endurance test was carried out at ARCS in the Large Indium FEEP Endurance Testing facility (LIFET) # 1, which is a cylindrical, stainless steel vessel 1 m in diameter, 1.5 m long with a volume of 1.2 m^3. An aluminum ion beam collector is mounted inside the chamber. It has a chevron configuration, which results in large angles (typically greater than 50^o) between the expected ion trajectories and the direction normal to the aluminum surface [94]. This

reduces the amount of sputtered material directed back towards the thruster. The chamber is also equipped to measure mass flow in real time using a quartz crystal microbalance (QCM) at the base of the collector facing the cluster. This enables investigation into any variation in the ion/droplet current ratio [94].

Experimental data The proposed relation between needle mass efficiency, voltage, fluid thickness and velocity was made using ARCS data from their 2002 In-FEEP thruster. Figure (2.4) displays current/voltage and current/efficiency traces for this thruster, taken with the equipment setup just outlined. Equation (2.9) empirically relates mass efficiency to extraction voltage for a particular technology family of ARCS's LMIS needle emitters [238].

$$U_0 = \sqrt{\frac{4.1 \times 10^{11} \times I}{1.38 - \eta_m}} \tag{2.9}$$

Note that as the efficiency increases, if the current is constant the voltage increases and if the voltage is constant the current increases. Therefore, $\eta_m \propto \frac{U}{I}$, in agreement with Vladmirov's earlier theoretical analysis in Eqs. (1.15 and 2.6).

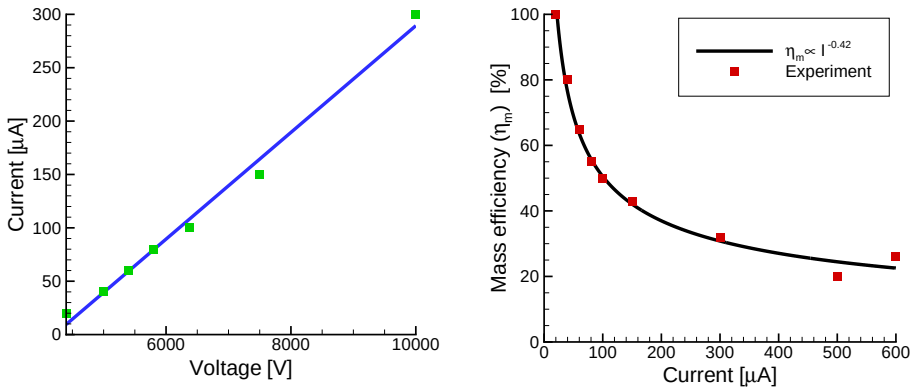

Figure 2.4: Current vs. voltage curve observed experimentally by ARCS [238]

2.1.2 Proposed algorithm

With the above relationships, it is possible to unite discrete elements of experimentally observed mass efficiency and geometrically calculated impedance. A proposed algorithm is developed to predict how a given voltage affects these properties. The method can be used in either direction, either from mass efficiency to velocity (as listed below) or the reverse problem where changing fluid flow velocity affects system mass utilization. The algorithm steps are as follows:

1. Start with a measured mass efficiency η_m and current I
2. Relate η_m to the minimum electrode voltage U_0 through Eq. (2.9)
3. Relate U_0 with the local needle radius of curvature r_c through Eq. (1.22)
4. Relate r_c and impedance Z to local film thickness through Eq. (2.3)
5. Calculate necessary velocity through mass conservation, assuming steady flow rates

Through interrelating mass efficiency, current, voltage, impedance and flow velocity, the value of any one of these properties can be determined from the others. Figure (2.5) shows the predicted dependencies for a current of 150 μA. Several important trends are shown in this graph. As electrode voltage increases, the electrostatic pull and resulting acceleration of the propellant increased, with a corresponding increase in mass efficiency. As a consequence, the fluid becomes thinner and moves more rapidly. The trends of all three variables reinforce the claim that a higher power gives a greater mass efficiency, for a given mass flow. This change is I_{sp} was addressed in Sec. (1.4.3).

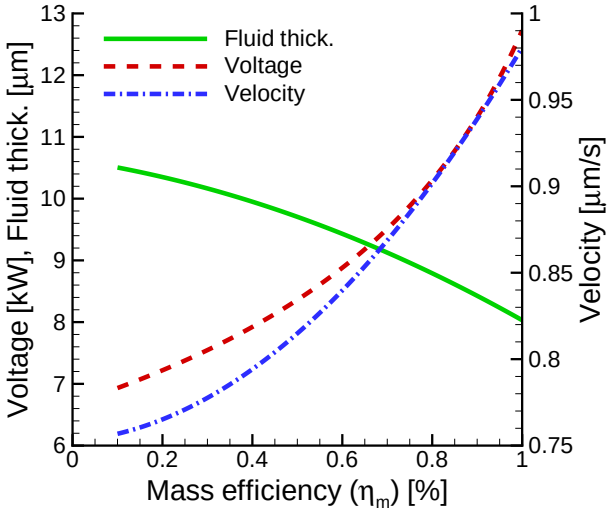

Figure 2.5: Mass efficiency related to extraction voltage, fluid thickness and film velocity on an ARCS FEEP needle emitter at 150 μA

The algorithm allows for increased experimental design flexibility. For example, if we need an emitter with at least 50% mass efficiency up to an emission current of 100 μA, an electrical impedance of at least 13 MΩ is required. In addition, the calculation of hard to measure fluid properties such as film thickness can be determined as well as the effect of a perturbation of one variable on another. Following the algorithm set forth and using the needle length L_n as 1 mm, the tip radius of curvature r_c as 3 μm, the groove depth a_{groove} as 1 μm and the viscosity μ as 1.91×10^{-2} $\left[\frac{N \cdot s}{m^2}\right]$ [204], sample field emission current-voltage properties for two gallium needle LMISs [130] are shown in Fig. (2.6) with film thickness and mass efficiency predicted in Table (2.1).

2.1.3 Conclusions

Detailed needle geometry was combined with an experimentally determined relationship between current and voltage of a field emission electric propulsion needle

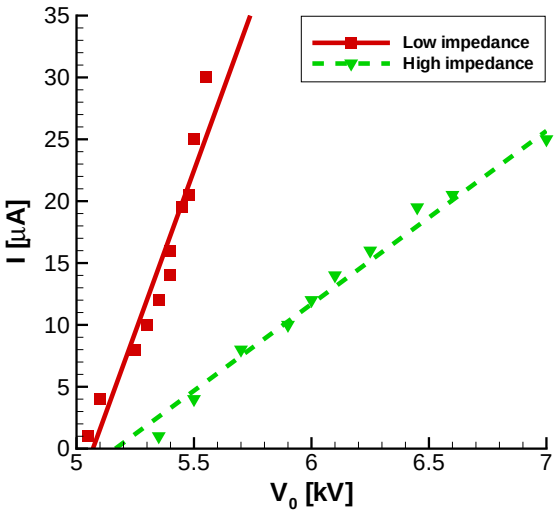

Figure 2.6: Current to voltage trace for a high and low impedance needle [130]

	Impedance	Velocity	F_T	η_m
	$[\Omega]$	$\left[\frac{\mu m}{s}\right]$	$[\mu m]$	[%]
rough(low)	3.2×10^{15}	0.3	10	67
smooth(high)	3.0×10^{17}	0.9	1	98

Table 2.1: Modeled gallium needle LMIS properties at 2 impedances

thruster. This allowed the determination of indium film thickness, local impedance and fluid velocity calculations prior to initial operation. A model algorithm provided a quantitative estimation of mass efficiency increase due to variation of needle smoothness and grooving.

2.2 Propellant composition effect on performance

Similar to altering the needle surface and fluid thickness to induce varying mass efficiencies, modifying the composition of the indium propellant itself holds potential to increase thrust and lower heater power requirements. The formation of binary and tertiary alloys instead of pure indium can provide superior emitter performance. Additional alloy processing can also reduce solid contaminants, thereby reducing sparking losses.

2.2.1 Binary and ternary alloys

An ideal propellant replacement alloy reduces the melting point compared to pure indium, retains a very low vapor pressure and decreases overall flow viscosity, as mentioned in Sec. (1.4.2). It is important to keep the vapor pressure low to minimize sublimation losses from the liquid surface of the emitter. Higher vapor pressures may cause condensation everywhere on the thruster assembly, thus coating the apparatus with a thin solid metal film [168].

A change in viscosity of the propellant through selective alloying holds potential as a method to increase operational mass efficiency while reducing or retaining present heater power requirements. A simple method for estimating the viscosity μ_{alloy} [Pa·s] of molten metallic alloys [40] is

$$\log_{10}(1000 \cdot \mu_{alloy} + 1) = 10^{b_{1,e}} \times T^{b_{2,e}} \tag{2.10}$$

where T [K] is the operating temperature and the power coefficients $b_{1,e}$ and $b_{2,e}$ are experimentally determined for each alloy. Note that alloys can in fact have *lower* melting temperatures than their original constituent elements. Using χ_i as the atomic fraction of each of the n elements, the alloyed coefficients are given by Eq. (2.11).

$$\begin{aligned} b_{1,e} &= \Sigma_{i=1}^{n} \chi_i b_{1i} \\ b_{2,e} &= \Sigma_{i=1}^{n} \chi_i b_{2i} \end{aligned} \tag{2.11}$$

Appendix (A.2) lists $b_{1,e}$ and $b_{2,e}$ for various elements. Of those elements with equal or lower vapor pressure than indium [264], only tin and gallium have similar melting points [253]. The melting points and vapor pressure of various combinations of these alloys are shown below in Figs. (2.7 and 2.8) [269]. Two element fractions are on the x and y axes, while the third element fraction is the remainder. For example, a 20% indium, 20% gallium, 60% tin alloy is found at (0.2, 0.2) and has a melting point of about 390 K. Note the log scale for the vapor pressures in Fig. (2.8).

Using Eq. (2.10), alloy viscosities can be calculated at any temperature above melting. Figure (2.9) displays the dynamic viscosity at a particular combined alloy's melting point, while Fig. (2.10) shows the much simpler picture of all alloys at 510 K. A depiction of temperature bands where a higher viscosity could be achieved compared to pure indium is shown in Fig. (2.11). Figure (2.12) combines Figs. (2.7 and 2.9) by plotting only those exact alloy compositions that result in comparable or lower vapor pressure and higher viscosities of operation.

Previous work [83] examined spot binary and ternary eutectic compositions of indium, gallium and tin as possible replacement propellants. Using this approach, the entire alloy spectrum can be analyzed. This analysis indicates that selective

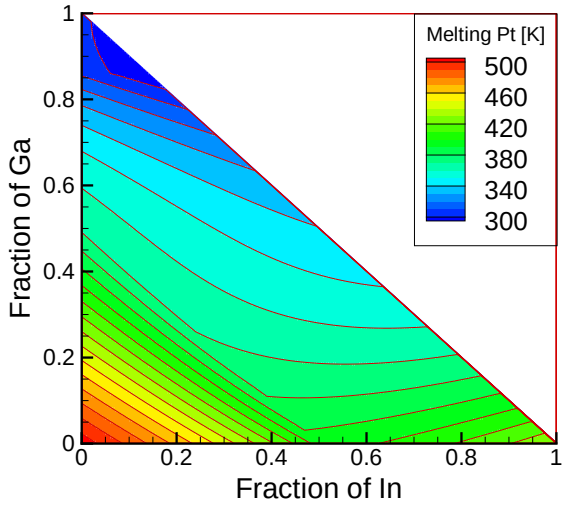

Figure 2.7: Melting points for alloys of indium, gallium, and tin

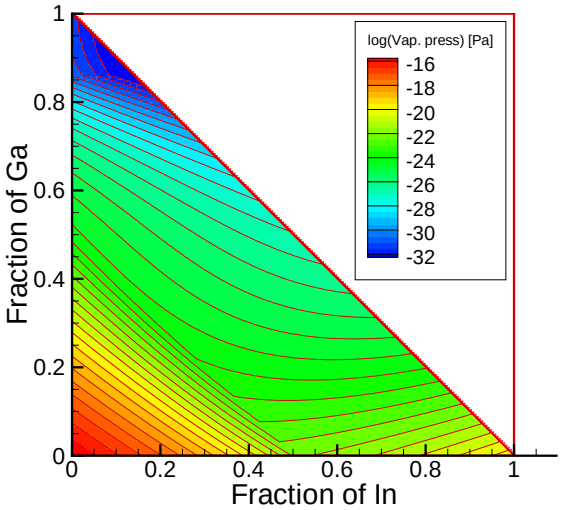

Figure 2.8: Vapor pressure for alloys of indium, gallium and tin

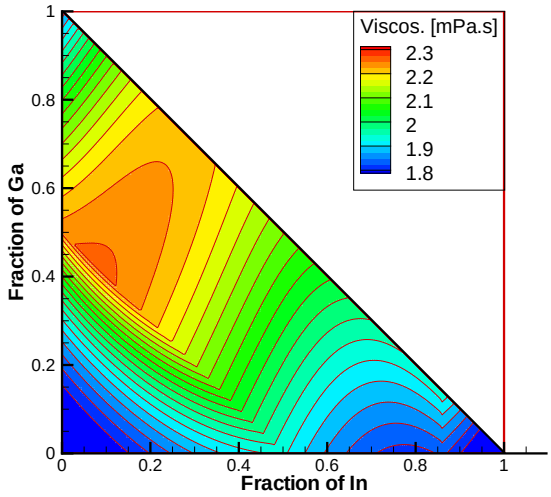

Figure 2.9: Viscosities for alloys of indium, gallium and tin at $T = T_{melt}$

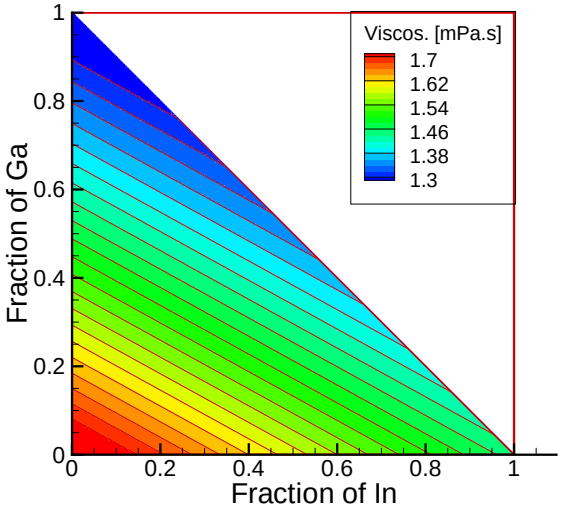

Figure 2.10: Viscosities for alloys of indium, gallium and tin at 510 K

propellant alloying can result in up to a 0.4 mPa·s increase in fluid viscosity, or about 25% greater than pure indium. It appears that tin is very effective in increasing viscosities slightly while reducing the alloyed melting temperature. This combination provides a doubly positive change in resulting efficiency and power budgets. Notably, several composition points in this ternary alloy consist of over 80% indium, retaining the usefulness of a majority of prior experiments. Also, a significant cross-section of materials produce useful (>0.1 mPa·s) viscosity increases with decreased operating temperature.

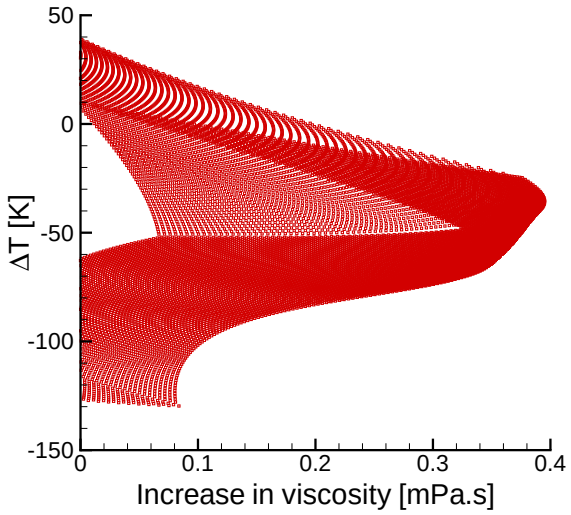

Figure 2.11: Design space of temperatures for mixed alloys that result in a viscosity increase compared to pure indium

Substituting this 0.4 $mPa \cdot s$ higher impedance back into the Z calculations described earlier gives roughly a **9% increase in overall mass efficiency** at a given fluid velocity, as seen in Fig. (2.13). It is expected that operating temperature decreases will have the largest impact, as the same efficiency can be potentially achieved heating the propellant to a final state that is less than 100 K cooler. The

"suggested" alloy is chosen as a good combination of viscosity increase (0.1 $mPa \cdot s$), melting point reduction (80K) and usage of indium ($> 70\%$) with a [0.75, 0.1, 0.15] fraction of indium, gallium and tin. The 'best' alloy has the maximum viscosity increase (0.4 $mPa \cdot s$) and a 30 K reduction in melting point but retains only a small fractional composition of indium; the system has a [0.2, 0.5, 0.3] fraction of indium, gallium and tin, respectively. Note that the vapor pressure is 10 orders of magnitude larger than pure indium; the alloy would be rejected due to overall out gassing levels listed in Sec. (1.4.2).

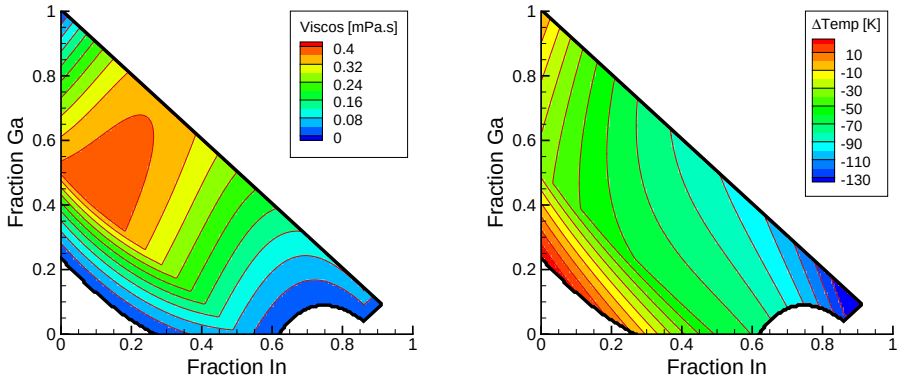

Figure 2.12: Composition of alloys that provide a) higher viscosity and b) the temperature change to a new melting temperature

2.2.2 Surface tension

Besides varying the viscosity and vapor pressure of the propellant, the needle material itself can be altered to increase the necessary critical emission potential and hence mass efficiency.

Background

The surface tension of the propellant varies depending on what material it is in contact with. The angle formed by a drop when resting stably on a surface varies -

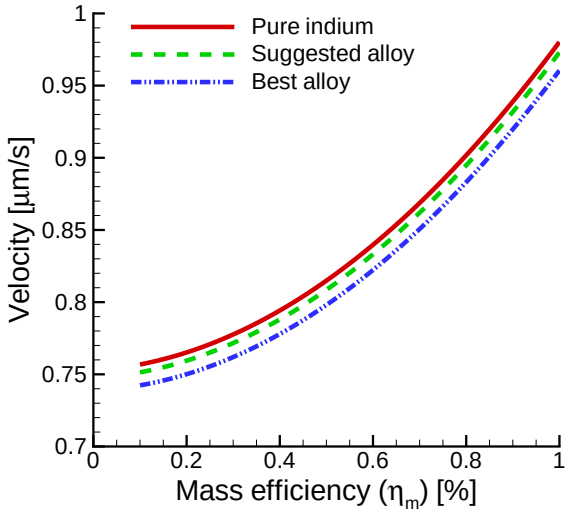

Figure 2.13: Effect of changed viscosity on mass efficiency

the wetting angle θ_{wet} [^{o}] is a quantitative measurement of this tension. This contact angle variation is seen in Fig. (2.14), where water is placed on two different silicon surfaces [269]. The smaller the contact angle, the better a material wets and the more efficient the fluid flow. Contact angle is directly related to the surface energy of the solid surface (σ_{gs}), the surface tension of the liquid surface (σ_{gl}), and the interface energy between liquid and solid (σ_{ls}).

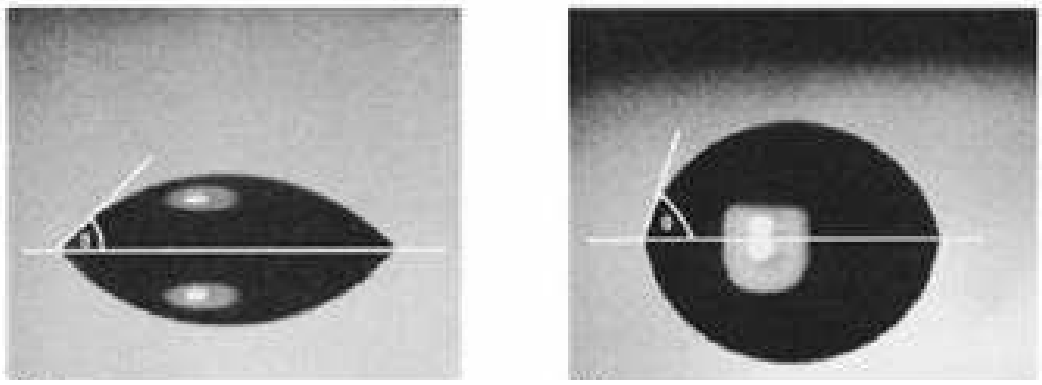

Figure 2.14: Wetting angle for water on different surfaces

The net work of adhesion, W_a $\left[\frac{N}{m}\right]$, is the reversible work necessary to create or separate an interface area of 1 cm^2 between two different materials in their liquid and solid phases. This adhesive work is defined by the Young-Dupre equation, with the force orientation as demonstrated in Fig. (2.15). If the spreading of the liquid on the solid proceeds to some intermediate equilibrium stage, then Eq. (2.12) relates these forces to the work of adhesion. The subscript "g" refers to the gas phase, "l" the liquid, and "s" the solid phase.

$$\begin{aligned} W_a &= \sigma_{gl} + \sigma_{gs} - \sigma_{ls} = (1 + \cos\theta_{wet})\sigma_{gl} \\ \sigma_{ls} &= \sigma_{gs} - \sigma_{gl}(\cos\theta_{wet}) \end{aligned} \tag{2.12}$$

Equation (2.12) indicates that the solid-liquid work of adhesion can be estimated from the surface tension of the liquid and the contact angle of the liquid formed on the solid.

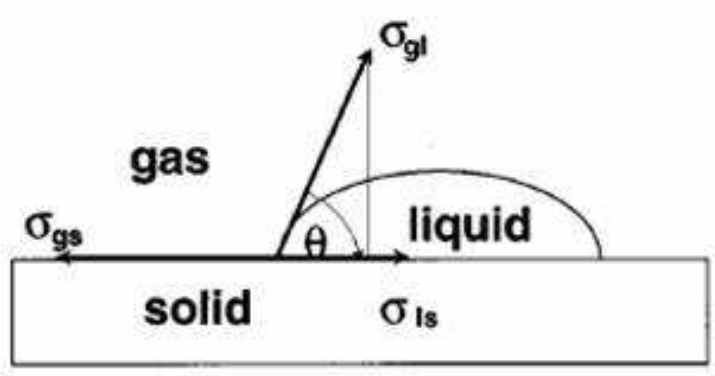

Figure 2.15: Schematic of surface force orientation

It has been proposed that the surface energy (σ) is composed of two components: the polar component (σ^p) and the dispersion (nonpolar) component (σ^d) [79]. These aspects of surface energy are caused by dipole interaction, induced dipole moments and hydrogen bonds and by dispersion energy between molecules respectively.

Applying the drop method, σ^p and σ^d can be measured simultaneously, with total surface energy (σ_{ij}) calculated by summing the force components as in Eq. (2.13).

$$\sigma_{ij} = \sigma_{ij}^p + \sigma_{ij}^d \tag{2.13}$$

This canonical approach is based on Fowkes and Wu [79, 273]. The model of harmonic mean [269] is used to approximate interaction of low energy phases. Combining these models and Eqs. (2.12 and 2.13) gives the adhesive work (W_a) shown in Eq. (2.14).

$$W_a = (1 + \cos\theta_{wet})\sigma_{gl} = 4\left(\frac{\sigma_{gl}^d \sigma_{gs}^d}{\sigma_{gl}^d + \sigma_{gs}^d} + \frac{\sigma_{gl}^p \sigma_{gs}^p}{\sigma_{gl}^p + \sigma_{gs}^p}\right) \tag{2.14}$$

For an insoluble metal (A) on metal (B) interaction, Eq. (2.14) becomes

$$\frac{1}{\cos(90 - \theta_{wet})} = \frac{\sigma_{gl}^A}{\sigma_{gl}^B} - \frac{\lambda}{L_e^B} \tag{2.15}$$

where λ (ΔH_{ij}) $\left[\frac{kJ}{mole}\right]$ is the average of partial enthalpies for a case of solutions of infinite dilution of A in B and an infinite dilution of B in A [68] ; L_e^B $\left[\frac{kJ}{mole}\right]$ is the molar heat of evaporation of metal B. In this formulation, liquid indium is component (B). Sample values of all the terms above are shown in Table (2.2). Values of surface tension of all materials vary with temperature; the ratios quoted are at melting points. The ratios can be adjusted for any temperature by utilizing σ_{gl} data, such as in Eustathopoulos [68]. In metal (B) / metal (A) systems, an increase in temperature is expected to favor desorption of B from the A surface, thus increasing σ_{gs}. Therefore, contact angles should decrease with increasing temperature. Generally, any increase in σ_{gs} leads to stronger adhesive work and decreasing contact angles.

Contact angles can also be treated dynamically instead of statically [82]. In this approach of Francois and Shyy, if the instantaneous contact line velocity is within

5% of the impact velocity, then the contact angle varies linearly from the advancing and receding values. If the contact velocity is greater than 5% of the impact velocity, the contact angle is assigned the fixed impact velocity value. However, in light of the very slow fluid velocity in Fig. (2.3), a static contact angle approximation is sufficiently accurate.

Binary surface tension analysis

Using Eqs. (2.12 and 2.15) with Fig. (2.15), it is possible to calculate an effective wicking tension for an insoluble binary metallic system. This new value incorporates the σ_{ls} deduced for each indium-[x] combination. Note that Eq. (2.15) references the σ_{gl} of the solid needle material. The effective σ_{gs} is calculated by equating adhesive work functions and solving for σ_{ls}. The last column in Table (2.2) is normalized to σ_{ls} (indium/tungsten) = 0.555 for easier experimental comparison; this is the baseline surface tension of pure liquid indium/vapor at the indium melting point on a tungsten needle. Larger values in the last column are more desirable and generally indicate that metal A is an element with a high melting point. Tungsten adheres to indium stronger than any of the other needle material choices.

This method is able to correctly predict wetting angles observed experimentally within 0.1^o [83]. Higher effective surface tension requires a higher onset voltage to ionize the indium (see Eq. (1.22)), therefore feeding back into the model discussed in Sec. (2.1). Figure (2.16) displays how overall mass efficiency at 150 μA current and 453 K changes with various theoretical needle material surface tensions.

This analysis suggests that if the needle material is changed from a material similar to tin to one closer to tungsten, the same fluid velocity of 0.85 m/s can result in an increase of up to 30% in mass efficiency. The causal chain of effects is:

Metal(A) Needle	$\frac{\sigma_{gl}^{A}}{\sigma_{gl}^{In}}$ [68]	$\frac{\lambda}{L_e^B}$	Predicted angle [^{o}] at T=melting point	Effective σ_{gs} $\left[\frac{N}{m}\right]$
Al	1.57	0.25	49	0.472
Cr	2.93	0.69	27	0.539
Fe	3.35	0.66	22	0.550
Mn	2.08	0.08	30	0.532
Pb	0.82	-0.03	> 90	-
Sn	1.01	-0.01	79	0.340
W	4.45	1.41	19	0.555

Table 2.2: Relative surface tensions and predicted wetting angles of indium on various needle materials

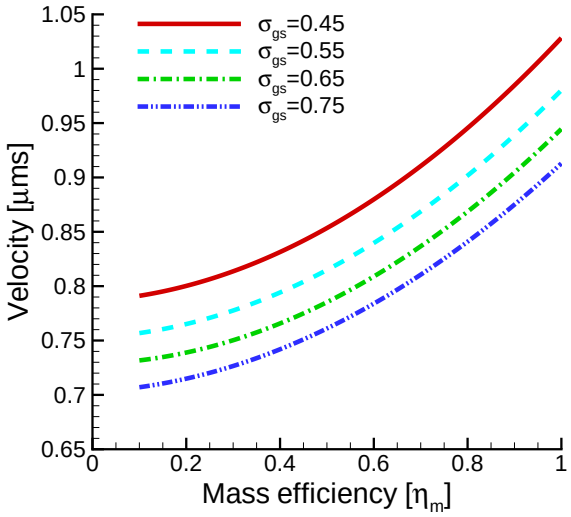

Figure 2.16: Effect of needle material on fluid velocity

higher surface tension leads to a higher electrode potential to pull off. This higher potential requires more power, but results in faster ion and droplet acceleration. The faster the droplets move, the greater their mass efficiency, as shown early on, in Eq. (1.2). While none of the materials examined are expected to perform better than the currently used tungsten needles, the strong trend toward greater efficiency with increasing surface tension implies that needle tip material composition represents a pathway towards very substantial increase in overall mass efficiency.

2.2.3 Solid contaminants in propellant

The effect of propellant contamination has been a continuing concern in the experimental field emission electric propulsion thruster community, especially for ARCS in Austria [236]. Particulate matter from the reservoir accumulates as thermal diffusion transfers atoms from the container walls to the indium propellant. The wall material is then wicked to the needle surface where it partially blocks field emission and drastically reduces performance. Diffusion models predict up to $1 \times 10^{-3} \frac{\%}{\text{hr}}$ relative molar occultation rates. This prediction of contaminant accumulation frequency is made possible by utilizing a method from other disciplines that provides qualitative and quantitative impacts of unwanted elements along the needle.

Section (2.1.1) described prior theoretical and experimental work to change the film thickness of indium along a FEEP needle thruster that demonstrably affected geometrical impedance [156, 261] and overall mass efficiency [238]. Previous analysis assumed a completely pure substance transported over the FEEP needle surface. In reality, particulate matter from the thruster's reservoir contaminates the indium propellant and eventually accumulates on the needle tip [71, 234]. The solid particles float above the liquid indium [71], forming a slowly moving skin under which

the propellant wicks to the surface. The tip accumulation reduces the flow cross-sectional area and mass efficiency and drastically increases the chance of sparking from the accelerating electrode to the solidified needle impurities. These sparks from an acceleration plate at 10 kV potential relative to the needle cause local heating that vaporizes the contaminants, reducing thruster operational lifetime and useful thrust [218]. The tip erosion problem is severe enough that reducing spark energy results in a substantial increase in predicted lifetime [236]. Needle impurity accretion rates are nonlinear, with no clogging observed for low mass flow ion regimes up to catastrophically large deposition rates at currents greater than 100 μA. Iron and chromium have been particularly troublesome contaminants; their high melting points need large sparks to eliminate them from the needle tip [90]. Figure (2.17) displays two field emitters from ARCS that have failed due to contamination after hundreds of hours of operation [240].

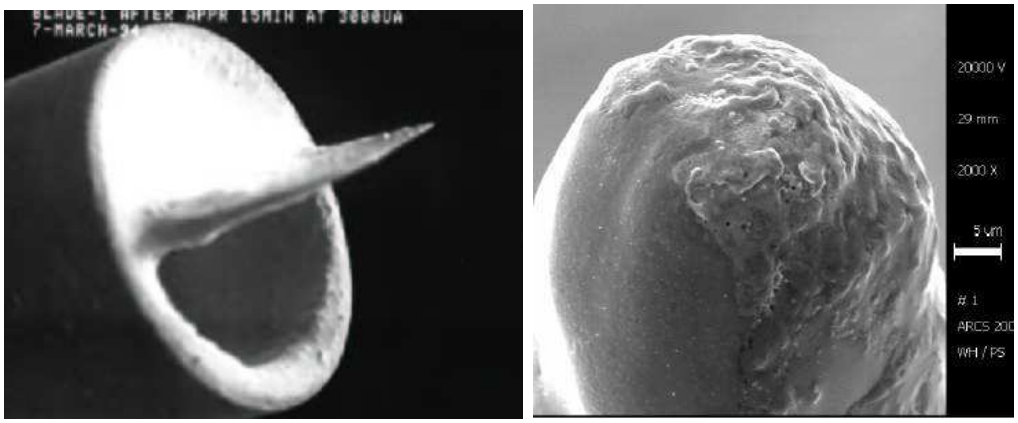

(a) Blade emitter (b) Needle emitter

Figure 2.17: Magnified ARCS tip contamination

Thermal diffusion

The migration of contaminant atoms can be successfully modeled by treating them as heat fluxes in a semi-conductive material [166]. The theory of thermal

diffusion in liquids has been developed so far only within the limits of the thermodynamics of the irreversible processes, with no external forces or chemical reactions and mechanical equilibrium [109]. Concentration and temperature gradients induce an atomic diffusion rate j_i $\left[\frac{\#\text{atoms}}{m \cdot s}\right]$ [216]. This can be written as Eq. (2.16),

$$j_i = -\nu D(\Delta\nu_{10} + a_{Sor}\nu_{10}\nu_{20}\Delta T) \tag{2.16}$$

where ν is the total number of moles per unit volume, $\nu_{10} = \frac{\nu_1}{\nu}$, $\nu_{20} = \frac{\nu_2}{\nu}$, D is the diffusion rate, and a_{Sor} is an empirically determined value called the *Soret* coefficient. Assuming that the above reaction follows Fick's First Law of steady state diffusion, a constant number of atoms migrate into the liquid indium per unit time, giving Eq. (2.17).

$$\begin{aligned} J_{dif} &= -D\frac{\partial c}{\partial x} \\ D &= D_o \exp\left(\frac{-E_a}{RT}\right) \end{aligned} \tag{2.17}$$

Here, J_{dif} $\left[\frac{mol}{cm^2 \cdot s}\right]$ is the total diffusion rate, c $\left[\frac{mol}{cm^3}\right]$ is the molar concentration, x [cm] is the depth into the material, D_o $\left[\frac{cm^2}{s}\right]$ is the diffusion rate constant and E_a $\left[\frac{J}{mole}\right]$ is the activation energy of the material. Table (2.3) gives the diffusion parameters for chromium, indium and iron in a variety of conductor matrices.

Metal/matrix	$D_o\left[\frac{cm^2}{s}\right]$	$E_a\left[\frac{J}{mole}\right]$	$D^*\left[\frac{m^2}{s}\right]$	$D_{T=473K}\left[\frac{m^2}{s}\right]$
Cr/C	9×10^{-3}	26,500	$0.47\exp\left(\frac{-3{,}187}{T}\right)$	7.9×10^{-10}
In/Ag			$2 \times 10^{-20}\exp(0.0153T)$	2.047×10^{-17}
Fe/Au			$1 \times 10^{-18}\exp(0.0105T)$	1.16×10^{-16}

Table 2.3: Diffusion rates [208]

Equation (2.17) is true only with a steady stream of particles flowing into the

indium propellant at all depths. However, the concentration rate changes as more contaminants move into the liquid indium from the reservoir walls. This is a result of unsteady diffusion, a process captured by Fick's Second Law. With zero original contamination, the concentration c at depth x is

$$\begin{gathered} \frac{\partial c}{\partial t} = D\frac{\partial^2 c}{\partial x^2} \\ c = c_o \operatorname{erfc}\left(\frac{x}{2\sqrt{Dt}}\right) \end{gathered} \tag{2.18}$$

using the complementary error function *erfc*. With the indium propellant flow moving at 1 $\frac{\mu m}{s}$, the liquid is exposed to the 2-cm high reservoir walls for up to 20,000 seconds. The reservoir walls are made of stainless steel grade *A4(18/8)* that contains 18% chromium. The surface forms a layer of Cr_2O_3 when exposed to the air; this layer is impervious to water while remaining transparent to the metal beneath. Assuming the same steel manufacturing process, the diffusion coefficient, thermal diffusion depth and total amount of material leeched after 20,000 seconds are shown in Table (2.4).

Contam.	$c_o\left[\frac{mol}{cm^3}\right]$	0.1%	1%	10%	rel. contam $\left[\frac{mol_{contam}}{mol_{In}}\right]$	total diffused [kg]
Cr	0.0247	1.9 cm	1.5 cm	0.9 cm	1.06×10^{-5}	5.52×10^{-6}
Fe	0.0847	7.1 μm	5.6 μm	3.6 μm	5.32×10^{-12}	2.98×10^{-12}

Table 2.4: Contamination magnitude in indium from reservoir walls

Modeling solid contaminant flow

Modeling solid impurities in indium flows is critical. Current experimental efforts are discovering a wide range of solid concentration rates at the FEEP needle tip. An increase in these nonlinear accumulation rates make a theoretical understanding

to leaching a prerequisite to simulating how foreign elements change the system impedance. This system impedance, *Z,* has been previously related to overall mass efficiency in Sec. (2.1.1).

GUEST erosion model Borrowing from hydrological research, the *GUEST* model gives a simultaneous erosion and deposition steady-state calculation of solid particles in a fluid when the flow is assumed to move independent of the amount of contamination present [166, 197]. This model predicts

$$\frac{d(c_i q_{flow})}{dx} = r_i + r_{ri} - \Psi_i \tag{2.19}$$

where c_i is mean impurity concentration $\left[\frac{kg}{m^3}\right]$, q_{flow} is the flow rate per unit width $\left[\frac{m^2}{s}\right]$, r_i is the rate of flow entrainment $\left[\frac{kg}{m^2 \cdot s}\right]$, r_{ri} is the rate of flow re-entrainment and Ψ_i is the rate of deposition. Each term on the right hand side involves a series of competing processes and must be modeled separately. As a first cut lifetime estimate, many simplifying assumptions can be made in the context of solid impurities in the indium stream on a FEEP needle. They include:

- the entire needle is evenly coated with impurities, so $r_i = 0$.
- uniform impurity size with constant settling velocity, eliminating all i subscripts
- all coefficients are constant and do not change with distance x along the needle
- constant vertical impurity concentrations

Equation (2.19) for net deposition then becomes [277]

$$\frac{d(c_i q_{flow})}{dx} = \Psi\left(1 - \frac{c_i}{c_t}\right) + \Theta \tag{2.20}$$

where c_t is the maximum carrying capacity of fluid $\left[\frac{kg}{m^3}\right]$, v is the settling velocity for the particle $\left[\frac{m}{s}\right]$, $\Psi = \mathrm{v}c_t$, and Θ the source term representing lateral fluid input. Then the general solution of Eq. (2.20) is Eq. (2.21).

$$c_i = c_0 \exp\left[\frac{x_0 - x}{\lambda_d}\right] + c_t\left(1 + \frac{\Theta}{\Psi}\right)\left\{1 - \exp\left[\frac{x_0 - x}{\lambda_d}\right]\right\} \tag{2.21}$$

Using $\lambda_d = \frac{q_{flow}}{v}$ as the characteristic length of deposition, the downward drift is the distance a particle travels downstream when the particle settles a vertical distance equal to the indium depth F_T.

Modeled contaminant transfer results Using total measured experimental mass loss, the maximum level of impurities the indium flow could carry indefinitely is 0.5% Fe by mass, with a droplet size roughly 1 micron in diameter. The analysis sets a fluid thickness of $5\,\mu m$ and particle velocity of $1\,\frac{\mu m}{s}$. No iron or other element re-entrains once it deposits on the surface. Combining these approximations with an overloaded 5% initial iron concentration gives $c_0 = 394\,\frac{kg}{m^3}$, $c_t = 39.4\,\frac{kg}{m^3}$, $q_{flow} = 5 \times 10^{-12}\,\frac{m^2}{s}$, $\mathrm{v} = 2 \times 10^{-7}\,\frac{m}{s}$ [39], $\mathrm{x_0}$= 0 m, $\lambda_d = 2.5 \times 10^{-5}$ m and $\Theta = 0$. Equation (2.21) then becomes

$$c_i = 393.5\,\exp\left[\frac{-x}{1.8 \times 10^{-4}}\right] + 39.4\left\{1 - \exp\left[\frac{-x}{1.8 \times 10^{-4}}\right]\right\} \tag{2.22}$$

Figure (2.18) shows how the concentration of iron in the liquid indium changes if the starting impurity concentration is higher than the carrying capacity of the propellant. Figure (2.19) shows the more physically realistic scenario of an initially low contaminant density stream piling up at the needle tip, where it cannot evaporate

due to higher melting temperatures of the stainless steel components. As impurities concentrate at the tip, the requisite voltage necessary for ion emission increases. This higher voltage leads to a higher probability of sparking from the electrode to the closest point. The sparks vaporize the solid impurities and flow then resumes with an unimpeded path.

Figure (2.20) demonstrates the settling out of impurities. It depicts the total and fractional deposition of contaminants in Fig. (2.19). The change in contamination levels from initial concentration to needle tip is not the same for all pollution fractions, as larger leaching rates cause a substantially more rapid accumulation around the edge of the thruster. As higher rates of impurity deposition incur a significantly higher rate of thruster failure, the tip level concentration c_t is raised to an order of magnitude above the beginning contaminant density c_0 as in Eq. (2.23).

$$\begin{aligned} c_0 &= \xi\rho \\ c_t &= c_0 \times 10^{(\xi\zeta_{conc})} \end{aligned} \tag{2.23}$$

Here, ξ is the fractional mass percentage of impurities in the stream, ρ is the density $\left[\frac{kg}{m^3}\right]$ of the impurity and ζ_{conc} is an experimentally determined nonlinear coefficient raising the tip level rate (1,300 and 56 for 0.1% and 1% initial impurities ξ, respectively).

Needed experimental information for contaminant modeling

If the following components can be determined on both a failed and successful needle, the model coefficients can be benchmarked:

- Tip volume fraction blocked by contaminants

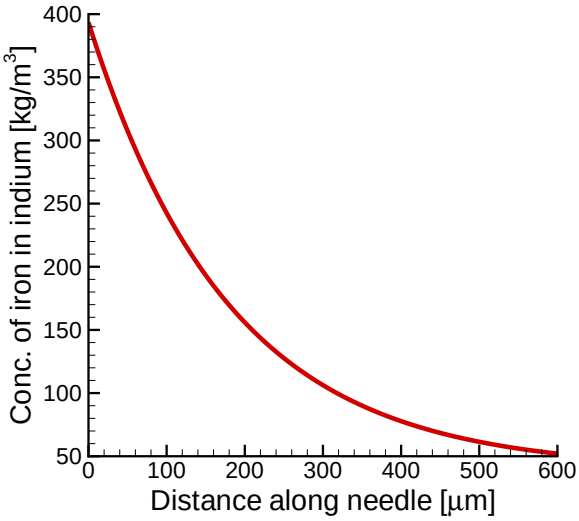

Figure 2.18: Change in iron concentration along the needle from a higher initial level of solid impurity

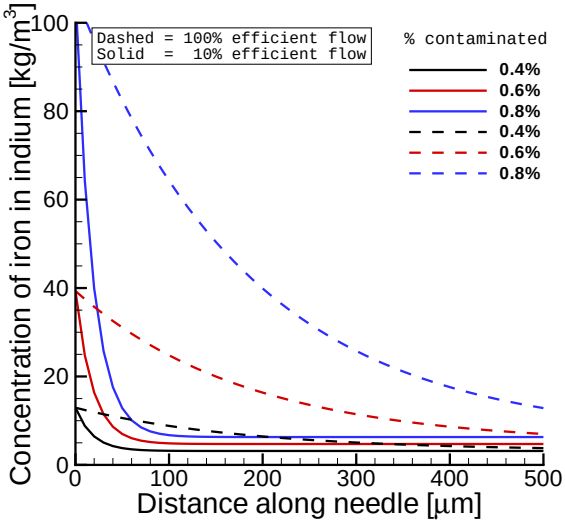

Figure 2.19: Change in iron concentration from a lower initial level of impurity

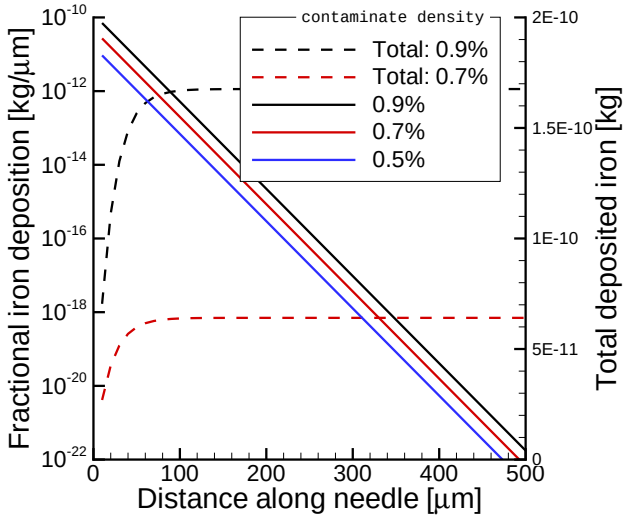

Figure 2.20: Fractional and total deposition of iron impurities on a FEEP needle

- Mass percentage contamination of propellants in feed stream during normal operation
- Operational mass efficiency
- Thruster run time

The analysis would then quantitatively predict how contamination percentages of other elements will impact impedances and thus overall mass efficiency. Modeled time for the emitter to become 25% blocked with iron and chromium is shown in Fig. (2.21). The behavior of uncontaminated indium is covered in previous analysis. These models demonstrate that a small level of impurities can cause a very substantial change in overall mass efficiency.

Conclusions

Solid particulate matter gradually contaminates liquid indium stored in a FEEP reservoir, and can be modeled as diffusion of a solid into a liquid. The theoretical

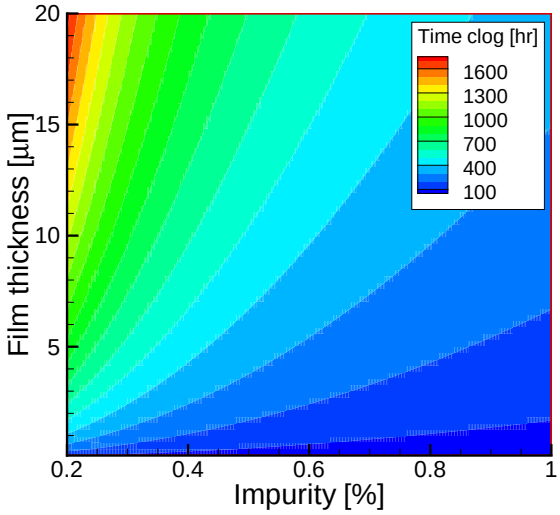

Figure 2.21: Simulated time for needle to clog based on impurity level

leaching rate of impurities is $2.71 \times 10^{-10}\ \frac{kg}{s}$ with an expected range of leaching for various components in stainless steel of 1.0×10^{-16} to $2.7 \times 10^{-10}\ \frac{kg}{s}$. Relatively large amounts of iron and chromium have been found experimentally on FEEP needle tips after hundreds of hours of operation. New modeling algorithms predict the nonlinear accumulation rates occurring for currents spanning orders of magnitude. This model also predicts that reducing the reservoir diffusion rate by 10% will lead to an increase of lifetime of up to 25%.

2.3 Parametric analysis summary

The parametric FEEP ARCS needle emitter model predicts many trends. In particular, better thruster performance will occur when:

- needle radius of curvature is smaller
- extractor voltage is higher
- impedances are higher

- percentage of tip wetted is increased
- contamination rates from the reservoir are lower

These trends are already known. The improvement achieved in the present study is that the model qualitatively and quantitatively predicts the interaction of these changes and the corresponding change in thruster lifetime. Therefore, the model can be used to address experimental design questions such as:

- Is it worth the effort to develop a needle that has a 2-μm smaller radius of curvature?
- What increase in mass efficiency should be expected for another 1 kV of extractor voltage?
- Should pure indium propellant be alloyed?
- Should pure tungsten needle compositions be altered?
- What range of fluid thickness should be attempted?
- Will sealing the propellant container walls make a measurable change in overall mass efficiency?

The interrelationship model can also attempt to answer some theoretical questions. A short list includes:

- How sensitive is mass efficiency to new designs that have different current - voltage - mass efficiency characteristics?
- What is the trade-off between operating temperatures and mass efficiency?

- What component of time-varying mass efficiency is due to changed wetting angles?
- If the power of the system must be reduced, what reduction in mass efficiency will occur?
- Does back-sputtering play a significant role in the de-wetting process?

The model is a very useful tool, although it should be noted that model coefficients need to be recomputed for each technology family, similar to the constraint on the impedance modeling.

CHAPTER III

Slender Jet Asymptotic Analysis

FEEP operation can be better understood through a systematic study of competing physical forces on the needle and fluid. However, a brute force, full 3-D, free surface simulation is highly impractical in terms of computational time. Mathematical perturbation schemes allow for the derivation of rapid 1-D models for slender jets and fibers. This chapter details the theoretical basis for the rapid 1D models and produces a perturbation scheme that is consistent to all levels of approximation. The underlying approach to identifying force influence was originally discussed in Bechtel [21]. Here, the governing equations are derived for a generic fluid regime through the use of nondimensional numbers. Then, specific experimental FEEP parameters are used to quantify the largest force and the order of the perturbation forces.

Subsequently, simulations of the time evolution of a slender needle jet driven by these forces are presented. A careful choice of the boundary conditions is important, since the modeling tensors are prone to catastrophic oscillations. A left and right hand side fixed asymptotic stress setup is needed for smoother results. Simulation of the shape evolution is performed using up to fifth-order forward, backward and central differencing schemes. An additional analysis of the system sensitivity to boundary condition perturbations determined that certain initial conditions, al-

though physically reasonable, lead to numerical instability.

In FEEP operation, an indium jet is elongated by electrostatic forces with the jet shape and size governed by surface tension, viscosity and inertial forces, among others. In this chapter, we present a practical application of a comprehensive perturbation theory for slender viscoelastic jets with a computational example for an operating indium-fed needle FEEP thruster mimicking the ARCS experimental set up [240].

3.1 Perturbation expansion and nondimensional variables

A useful prerequisite to the slender jet governing equations is the concept of nondimensional terms. The goal of non-dimensionalization is to identify the dominant forces and evaluate the relative magnitude of perturbation contributed by each force. This determination is partially made by expressing all the forces as a sum of Taylor-expanded and normalized components. This section will define some nondimensionalized terms and describe how variables can be expressed through recursive power series.

3.1.1 Power series expansion

A power series expansion is a mathematical tool used here to determine the relative importance of various forces. Formally, it is an infinite series of the form

$$f(x) = \sum_{n=0}^{\infty} a_n \epsilon^n = a_0 \epsilon^0 + a_1 \epsilon^1 + a_2 \epsilon^2 + ... \tag{3.1}$$

where a_n represents the coefficients of the n^{th} term and ϵ is the perturbation level. For a converging series, as n increases, the terms are defined to contribute a smaller and smaller part of the total sum. The leading order ϵ^0 terms are defined as those

values that are not subject to boundary condition fluctuations. In addition, only the leading-order physical effects are present in the corrections. If the values are uniformly small, first order ϵ^1 corrections will include boundary fluctuations, but not any weak effects. As the correction order ϵ^i increases, all prior perturbation corrections ϵ^{i-1} are considered fixed. Therefore, for the ϵ^2 correction $\frac{d\epsilon^1}{dt} = 0$. The power of the perturbation expansion, also known as the slenderness ratio ϵ, is given by Eq. (3.2). This ratio utilizes the two primary length scales for the free surface boundary value problem: r_0 and z_0, which correspond to the transverse and axial scale, respectively. In needle FEEP terms, these are the width and length of the needle. Another scale used in the nondimensional approach is the time scale $t_0 = \frac{z_0}{v_0}$, where v_0 is the velocity of the fluid along the needle length.

$$\epsilon = \frac{r_0}{z_0} \ll 1 \tag{3.2}$$

The radial (v_r) and axial (v_z) velocity components and the free surface (ϕ) are expanded in a double power series about both ϵ and ϵr in Eq. (3.3). The tilde ($\tilde{}$) notations for these terms $\left(\text{e.g. } \tilde{r} = \frac{r}{r_0}\right)$ denote the nondimensionalized version of the original parameter. The superscripts above the terms are derivatives of time $\left(\frac{\partial}{\partial t}\right)$ and axial distance $\left(\frac{\partial}{\partial z}\right)$. Thus, $v_r^{0,m}(r,z,t) = \frac{dv_r^m\left(\tilde{r},\tilde{z},\tilde{t}\right)}{dz^m}$ and $\tilde{r}^2 v_z^{n,m}(r,z,t) = \tilde{r}^2 \cdot \left[\frac{\partial^n}{\partial t^n}\frac{\partial^m}{\partial z^m} v_z\left(\tilde{r},\tilde{z},\tilde{t}\right)\right]$.

$$
\begin{aligned}
v_z(r,z,t) &= \tfrac{z_0}{t_0}\left\{v_z^{0,0}\left(\tilde{z},\tilde{t}\right)+\epsilon\left[v_z^{0,1}\left(\tilde{z},\tilde{t}\right)\right]+\epsilon^2\left[v_z^{0,2}\left(\tilde{z},\tilde{t}\right)+\tilde{r}^2 v_z^{1,0}\left(\tilde{z},\tilde{t}\right)\right]+...\right\} \\
&= \tfrac{z_0}{t_0}\Sigma_{n,m\geq 0}\epsilon^{2n+m}\tilde{r}^{2n}v_z^{n,m}\left(\tilde{z},\tilde{t}\right) \\
v_r(r,z,t) &= \tfrac{z_0}{t_0}\left\{\epsilon\tilde{r}v_r^{0,0}\left(\tilde{z},\tilde{t}\right)+\epsilon^2\tilde{r}v_r^{0,1}\left(\tilde{z},\tilde{t}\right)+\epsilon^3\left[\tilde{r}v_r^{0,2}\left(\tilde{z},\tilde{t}\right)+\tilde{r}^3 v_r^{1,0}\left(\tilde{z},\tilde{t}\right)\right]+...\right\} \\
&= \tfrac{z_0}{t_0}\Sigma_{n,m\geq 0}\epsilon^{2n+m+1}\tilde{r}^{2n+1}v_r^{n,m}\left(\tilde{z},\tilde{t}\right) \\
\phi(z,t) &= r_0\left\{\phi^0\left(\tilde{z},\tilde{t}\right)+\epsilon\phi^1\left(\tilde{z},\tilde{t}\right)+\epsilon^2\phi^2\left(\tilde{z},\tilde{t}\right)+...\right\} \\
&= r_0\Sigma_{m\geq 0}\epsilon^m\phi^m\left(\tilde{z},\tilde{t}\right)
\end{aligned}
\tag{3.3}
$$

The axisymmetry condition implies that v_z is an even function of r and v_r is an odd function of r. However, ϕ depends on all powers of r and ϵ. ϕ is not a function of r because it is the surface location at axial point z and time t whereas v_r and v_z are present at multiple radii.

3.1.2 Dimensionless forces

The various nondimensional forces are defined in Eq. (3.4) as $f_{[x]}$s representing the inertial, viscous, capillary and gravitational forces. These forces are compared to each other, with the largest of the four $f_{[x]}$ becoming the f_0 in subsequent dimensionless variables. The $p_{[x]}$ terms describe the electrostatic and ambient pressures.

$$
\begin{aligned}
f_{inertial} &\triangleq \frac{\rho r_0^2 z_0^2}{t_0^2}, & f_{viscous} &\triangleq \frac{\mu r_0^2}{t_0}, & f_{capillary} &\triangleq \sigma r_0 \\
f_{gravitational} &\triangleq \rho r_0^2 z_0 g, & p_{es} &\triangleq \frac{r_0^2\tilde{p}_{es}}{f_0}, & p_a &\triangleq \frac{r_0^2\tilde{p}_a}{f_0}
\end{aligned}
\tag{3.4}
$$

Using the physical descriptors f, the nondimensionalized governing free surface boundary problem and field equations involve combinations of the characteristic length, time and force scales and the material, interfacial and ambient properties

in Eq. (3.5). The forces in the parenthesis imply that the dimensionless variable is the ratio of those two effects. The λ's listed in the Λ_1 and Λ_2 definitions are the characteristic elastic and relaxation times for the fluid, respectively.

$$\begin{aligned}
B &\triangleq \frac{f_0 t_0^2}{\rho r_0^2 z_0^2} = \left(\frac{1}{\text{Inertia}}\right) \\
F_r &\triangleq \frac{z_0}{g t_0^2} = \text{Froude number } \left(\frac{\text{Inertia}}{\text{Gravity}}\right) \\
W &\triangleq \frac{\rho r_0 z_0^2}{\sigma t_0^2} = \text{Weber number } \left(\frac{\text{Inertia}}{\text{Surface tension}}\right) \\
Z_\nu &\triangleq \frac{\mu r_0^2}{t_0 f_0} = \text{Zero strain viscosity} \\
\Lambda_1 &\triangleq \frac{\lambda_1}{t_0} = \text{Weissenberg number (elasticity)} \\
\Lambda_2 &\triangleq \frac{\lambda_2}{t_0} = \text{Retardation} \\
\frac{1}{B \cdot Z_\nu} &\triangleq \frac{\rho z_0^2}{\mu t_0} = \text{Reynolds number} \\
\frac{1}{B \cdot W} &\triangleq \frac{r_0 \sigma}{f_0} = \left(\frac{\text{Capillary}}{\text{Characteristic}}\right)
\end{aligned} \tag{3.5}$$

3.1.3 Stress tensor expansion

As the velocity components of Sec. (3.1.1) were rewritten as a power series expansion, the stress tensor and pressure are also expanded in a similar manner around ϵ and r. The stress tensor subscripts denote which face of the volume and in which direction the stress acts, as shown in Fig. (3.1). Note that the (x, y, z) of the figure map to (r, θ, z) in cylindrical coordinates.

For example, T_{rr} denotes the stress on the radial face applied radially, while T_{rz} denotes the stress on the same face in the axial direction. Equation (3.6) outlines the power series expansions of the stress tensor and pressure. These stress and pressure terms are preceeded by the nondimensionalized stress, $\frac{f_0}{r_0^2}$.

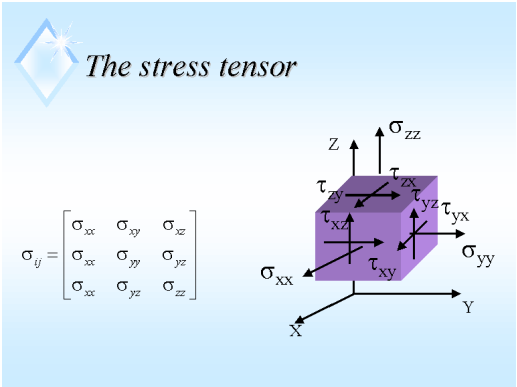

Figure 3.1: Cauchy stress tensor

$$
\begin{aligned}
T_{rr}(r,z,t) &= \tfrac{f_0}{r_0^2}\left\{T_{rr}^{0,0} + \epsilon T_{rr}^{0,1} + \epsilon^2\left[T_{rr}^{0,2} + r^2 T_{rr}^{1,0}\right] + ...\right\} \\
T_{\theta\theta}(r,z,t) &= \tfrac{f_0}{r_0^2}\left\{T_{\theta\theta}^{0,0} + \epsilon T_{\theta\theta}^{0,1} + \epsilon^2\left[T_{\theta\theta}^{0,2} + r^2 T_{\theta\theta}^{1,0}\right] + ...\right\} \\
T_{zz}(r,z,t) &= \tfrac{f_0}{r_0^2}\left\{T_{zz}^{0,0} + \epsilon T_{zz}^{0,1} + \epsilon^2\left[T_{zz}^{0,2} + r^2 T_{zz}^{1,0}\right] + ...\right\} \\
T_{rz}(r,z,t) &= \tfrac{f_0}{r_0^2}\left\{\epsilon r T_{rz}^{0,0} + \epsilon^2 r T_{rz}^{0,1} + ...\right\} \\
p(r,z,t) &= p_a + p_{es} + \tfrac{f_0}{r_0^2}\left\{p^{0,0} + \epsilon p^{0,1} + \epsilon^2\left[p^{0,2} + r^2 p^{1,0}\right] + ...\right\}
\end{aligned}
\tag{3.6}
$$

The stress and pressure coefficients are dimensionless functions of the scaled axial coordinate. Axisymmetrical modeling requires that T_{rr}, $T_{\theta\theta}$, T_{zz} and p are even functions of r while T_{rz} is an odd perturbation of the power series expansion.

3.2 Model equations

The surface of a FEEP thruster is simulated using a 1-D axisymmetric slender jet model. The free evolving surface F of the model is defined by Eq. (3.7). It adopts a cylindrical polar coordinate system and assumes that the free jet is torsionless and axisymmetric along the centerline.

$$F(r,z,t) = \phi(z,t)\hat{r} - r\hat{r} = 0 \tag{3.7}$$

Here, ϕ is the free surface radius, r the radial coordinate and $\hat{r}$ the radial unit vector.

The surface evolution is restricted by the kinematic boundary condition, where "$|_\partial$" denotes that the constraint is evaluated at the interface boundary.

$$\left(\frac{\partial}{\partial t} + v \cdot \nabla\right) F|_\partial = 0 \tag{3.8}$$

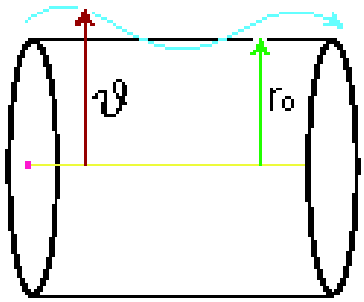

Figure 3.2: Illustration of a free surface

The standard assumptions for such a model include the idea that the jet radius decreases slowly in the axial direction $\left(\frac{dr(z)}{dz} \ll 1\right)$, and the axial velocity v_z is uniform throughout the jet cross section at a given radius $\left(\frac{dv_z}{dr} = 0\right)$. Therefore, knowledge of the velocity v_z captures a large portion of the evolution behavior of the surface deformation. The governing equations for a 3D free surface boundary value problem within a free jet surface are:

$$\begin{aligned} \nabla \cdot v &= 0 \\ \rho\left[\tfrac{\partial v}{\partial t} + (v \cdot \nabla)v\right] &= \nabla \underline{\mathbf{T}} - \nabla p + \rho g \\ \underline{\mathbf{T}} + \lambda_1 \tfrac{D\underline{\mathbf{T}}}{Dt} &= 2\mu\left[\underline{\mathbf{D}} + \lambda_2 \tfrac{D\underline{\mathbf{D}}}{Dt}\right] \end{aligned} \tag{3.9}$$

corresponding to, respectively, incompressible continuity, conservation of linear momentum and a stress constitutive model. In Eq. (3.9), v is the fluid velocity, ρ is the density, $\underline{\mathbf{T}}$ is the Cauchy stress tensor, p is the pressure, $\underline{\mathbf{D}}$ is the symmetric part of the velocity gradient, λ_1 is the characteristic relaxation time, λ_2 is the characteristic retardation time, and μ is the fluid viscosity.

3.2.1 Surface curvature and pressure differential

To balance the pressure differential inside the fluid with that of the ambient atmosphere, there is a discontinuity in pressure at the surface that is equal to the surface tension multiplied by the surface curvature $\kappa\left[\frac{1}{m}\right] = \frac{1}{s}\int r(s)\,ds$. Assume that shearing is continuous across the interface and the normal force is discontinuous by an amount proportional to that curvature. Then, the stress is given by ($\underline{\mathbf{T}}$-p$\mathbf{I}$), where $\mathbf{I}$ is the identity matrix. Equating this pressure differential to the curvature stress gives Eq. (3.10), where T_a is the stress from the ambient atmosphere (0 in a vacuum), $\overrightarrow{n}$ is the outward surface normal and σ the surface tension. While not included in this analysis, addition of electrostatic forces to the expansion would be in the form of an additional term on the right hand side.

$$(T_a - \underline{\mathbf{T}} + p\mathbf{I})|_{\partial} \cdot \overrightarrow{n} = \sigma\kappa \cdot \overrightarrow{n} \tag{3.10}$$

Using small angle approximations [21], the surface curvature is approximated as a power series expansion in Eq. (3.11).

$$\kappa = \frac{1}{r_0}\left[\frac{1}{\phi^0} + \epsilon\left\{\frac{-\phi^1}{(\phi^0)^2}\right\} + \epsilon^2\left\{\frac{(\phi^1)^2}{(\phi^0)^3} - \frac{\phi^2}{(\phi^0)^2} - \frac{1}{2}\frac{\frac{\partial\phi^0}{\partial z}}{\phi^0} - \frac{\partial^2\phi^0}{\partial z^2}\right\}\right] \tag{3.11}$$

Equation (3.12) outlines the radial component ϵ stress tensor perturbation, whereas Eq. (3.13) displays the axial version. A crucial note is that when the nondimensional inertial and surface tension forces B and W from Sec. (3.1.2) are multiplied, their magnitude determines which order ϵ terms are equated.

$$\hat{e}_r : p - p_a - p_{es} + \frac{\partial \phi}{\partial z} T_{rz} - T_{rr} = \sigma\kappa$$

$$\epsilon^0 \left\{p^{0,0} - T_{rr}^{0,0}\right\} + \epsilon^1 \left\{p^{0,1} - T_{rr}^{0,1}\right\} + \epsilon^2 \left\{p^{0,2} - T_{rr}^{0,2} + \left(p^{1,0} - T_{rr}^{1,0}\right)\left[\phi^0\right]^2 + \phi^0 T_{rz}^{0,0} \frac{\partial \phi^0}{\partial z}\right\} =$$

$$\frac{1}{B \cdot W}\left[\frac{p_a r_0}{\sigma} + \frac{p_{es} r_0}{\sigma} + \kappa_0 + \epsilon^1 \kappa^1 + \epsilon^2 \kappa^2\right] \tag{3.12}$$

$$\hat{e}_z : \left(T_{zz} - p + p_a + p_{es}\right) \frac{\partial \phi}{\partial z} - T_{rz} = -\sigma\kappa \frac{\partial \phi}{\partial z}$$

$$\epsilon^0 \left\{\left(T_{zz}^{0,0} - p^{0,0}\right) \frac{\partial \phi^0}{\partial z} - \phi^0 T_{rz}^{0,0}\right\} + \epsilon^1 \left\{\left(T_{zz}^{0,1} - p^{0,1}\right) \frac{\partial \phi^0}{\partial z} + \left(T_{zz}^{0,0} - p^{0,0}\right) \frac{\partial \phi^1}{\partial z}\right.$$

$$\left. - \phi^0 T_{rz}^{0,1} - \phi^1 T_{rz}^{0,0} - \phi^1 T_{rz}^{0,0}\right\} - \frac{1}{B \cdot W}\left[\epsilon^0 \left\{\frac{p_a}{\sigma} \frac{\partial \phi^0}{\partial z}\right.\right. \tag{3.13}$$

$$\left. + \frac{p_{es}}{\sigma} \frac{\partial \phi^0}{\partial z} + \kappa^0 \frac{\partial \phi^0}{\partial z}\right\} + \epsilon^1 \left\{\frac{p_a}{\sigma} \frac{\partial \phi^1}{\partial z} + \frac{p_{es}}{\sigma} \frac{\partial \phi^1}{\partial z} + \kappa^1 \frac{\partial \phi^0}{\partial z}\right.$$

$$\left.\left. + \kappa^0 \frac{\partial \phi^1}{\partial z}\right\} + \epsilon^2 \{...\}\right]$$

3.2.2 Continuity

The assumption of an incompressible fluid combined with mass conservation yields Eq. (3.14).

$$\nabla \cdot v = \frac{1}{r} \frac{\partial}{\partial r} \left(r \cdot v_r\right) + \frac{1}{r} \frac{\partial}{\partial \theta} \left(v_\theta\right) + \frac{\partial}{\partial z} \left(v_z\right) = 0 \tag{3.14}$$

Substituting the expression for velocity expansions of Eq. (3.3) produces a power series expansion to describe the material continuity.

$$\sum_m \epsilon^m \left\{\frac{\partial \phi^{(m)}}{\partial t} + \sum_n \sum_p \epsilon^{2n+p} \left(\sum_q \phi^{(q)} \epsilon^q\right)^{2n} \left[v_z^{n,m} \frac{\partial \phi^{(p)}}{\partial z} - v_r^{n,m}\right]\right\} = 0 \tag{3.15}$$

Equating the terms corresponding to the powers of ϵ in Eq. (3.15) results in a perturbation balance.

$$\begin{aligned}
\epsilon^0 :&\quad \tfrac{\partial \phi^0}{\partial t} + v_z^{0,0}\tfrac{\partial \phi^0}{\partial z} - v_r^{0,0}\phi^{(0)} = 0 \\
\epsilon^1 :&\quad \tfrac{\partial \phi^1}{\partial t} + v_z^{0,0}\tfrac{\partial \phi^1}{\partial z} + v_z^{0,1}\tfrac{\partial \phi^0}{\partial z} - v_r^{0,0}\phi^1 - v_r^{0,1}\phi^0 = 0 \\
\epsilon^2 :&\quad \tfrac{\partial \phi^2}{\partial t} + \textstyle\sum_{L=0}^{2}\left[v_z^{0,L}\tfrac{\partial \phi^{2-L}}{\partial z} - v_r^{0,L}\phi^{2-L}\right] + \phi^{0^2}\left[v_z^{1,0}\tfrac{\partial \phi^0}{\partial z} - v_r^{1,0}\phi^0\right] = 0
\end{aligned} \tag{3.16}$$

This expansion continues infinitely for $\phi^n > 2$. Inserting the power series expansion into the incompressibility condition of Eq. (3.9) results in a component summation of the directional velocities. The inner bracketed term is restated as Eq. (3.18), where it becomes a boundary condition for incompressible flow.

$$\sum_{n,m} \tilde{r}^{2n}\epsilon^{2n+m}\left[(2n+2)v_r^{n,m} + \frac{\partial v_z^{n,m}}{\partial z}\right] = 0 \tag{3.17}$$

$$-(2n+2)v_r^{n,m} = \frac{\partial v_z^{n,m}}{\partial z} \tag{3.18}$$

3.2.3 Linear momentum

The second entry from the governing equations conserves linear momentum, with individual stress tensor terms being designated by $T_{[xx]}$. It is restated below, with the radial and axial components of momentum conservation given by Eqs. (3.19-3.20).

$$\rho\left[\frac{\partial v}{\partial t} + (v\cdot\nabla)v\right] = \nabla\underline{\mathbf{T}} - \nabla p + \rho g$$

$$\text{radial} : \rho\left[\tfrac{\partial v_r}{\partial t} + v_r\tfrac{\partial v_r}{\partial r} + v_z\tfrac{\partial v_r}{\partial z}\right] = \tfrac{\partial T_{rr}}{\partial r} + \tfrac{\partial T_{rz}}{\partial z} + \tfrac{1}{r}\left(T_{rr} - T_{\theta\theta}\right) - \tfrac{\partial p}{\partial r} \tag{3.19}$$

$$\text{axial} : \rho\left[\frac{\partial v_z}{\partial t} + v_r\frac{\partial v_z}{\partial r} + v_z\frac{\partial v_z}{\partial z}\right] = \frac{\partial T_{rz}}{\partial z} + \frac{\partial T_{zz}}{\partial z} + \frac{T_{rz}}{r} - \frac{\partial p}{\partial z} + \rho g \tag{3.20}$$

Substituting the power series expansion and differentiating with respect to time and space, nondimensionalizing and then matching powers of perturbation gives the radial (3.21) and axial (3.22) ϵ momentum balance equations.

$$\begin{aligned}&\text{radial}: \epsilon^2\left\{r\tfrac{\partial v_r^{0,0}}{\partial t}+rv_z^{0,0}\tfrac{\partial v_r^{0,0}}{\partial z}+r^2\left(v_r^{0,0}\right)^2\right\}+\epsilon^3\left\{r\tfrac{\partial v_r^{0,1}}{\partial t}+rv_z^{0,0}\tfrac{\partial v_r^{0,1}}{\partial z}\right.\\&\left.+rv_z^{0,1}\tfrac{\partial v_r^{0,0}}{\partial z}+2rv_r^{0,0}v_r^{0,1}\right\}=\tfrac{B}{r}\left[\epsilon^0\left(T_{rr}^{0,0}-T_{\theta\theta}^{0,0}\right)+\epsilon^1\left(T_{rr}^{0,1}-T_{\theta\theta}^{0,1}\right)\right.\\&\left.+\epsilon^2\left\{T_{rr}^{0,2}-T_{\theta\theta}^{0,2}+r^2\left(2T_{rr}^{1,0}+T_{rr}^{1,0}-T_{\theta\theta}^{1,0}+\tfrac{\partial T_{rz}^{0,0}}{\partial z}-2p^{1,0}\right)\right\}\right]\end{aligned}\tag{3.21}$$

$$\begin{aligned}&\text{axial}: \epsilon^0\left\{1+v_z^{0,0}\tfrac{\partial v_z^{0,0}}{\partial z}\right\}+\epsilon^1\left\{\tfrac{\partial v_z^{0,1}}{\partial t}+v_z^{0,0}\tfrac{\partial v_z^{0,1}}{\partial z}+v_z^{0,1}\tfrac{\partial v_z^{0,0}}{\partial z}\right\}=\\&B\left[\epsilon^0\left\{2T_{rz}^{0,0}+\tfrac{\partial T_{zz}^{0,0}}{\partial z}-\tfrac{\partial p^{0,0}}{\partial z}\right\}+\epsilon^1\left\{2T_{rz}^{0,1}+\tfrac{\partial T_{zz}^{0,1}}{\partial z}-\tfrac{\partial p^{0,1}}{\partial z}\right\}\right]\end{aligned}\tag{3.22}$$

3.2.4 Stress tensor

The evolution of the stress components in a fluid depend on velocity gradients, fluid characteristic relaxation times, viscosity and retardation stresses. This process can be modeled via the Johnson-Segalman constitutive approach. The third governing constraint from Eq. (3.9) is reproduced below.

$$\underline{\mathbf{T}}+\lambda_1\frac{D\underline{\mathbf{T}}}{Dt}=2\mu\left[\underline{\mathbf{D}}+\lambda_2\frac{D\underline{\mathbf{D}}}{Dt}\right]$$

The total derivative $\frac{D}{Dt}(\cdot)$ captures the complete time and space evolution of a parameter. Including the velocity gradients, its form becomes Eq. (3.23), where $\underline{\mathbf{D}}$ is the symmetric part and $\underline{\mathbf{W}}$ is the skew symmetric part of the velocity gradient.

$$\frac{D}{Dt}(\cdot)=\left\{\frac{\partial}{\partial t}+(v\cdot\nabla)\right\}(\cdot)+(\cdot)\underline{\mathbf{W}}-\underline{\mathbf{W}}(\cdot)-a[(\cdot)\underline{\mathbf{D}}+\underline{\mathbf{D}}(\cdot)]\tag{3.23}$$

The total derivative captures the complete time and space evolution of a parameter. Let a be the slip parameter and the upper convected rate corresponds to the case

when a=1. Nondimensionalizing the time by $\Lambda = \frac{\lambda}{t_0} = \tilde{\Lambda}\epsilon^{q_t}$ allows the time perturbation importance to be determined. The time sensitivity exponent q_t is determined similarly by normalizing the variables as described earlier. Equation (3.24) displays the renormalized time perturbation terms.

$$\begin{aligned} \epsilon = \epsilon^{q_t}: &\quad \tilde{\Lambda}\left(\tfrac{\partial T_{rr}^{0,0}}{\partial t} + v_z^{0,0}\tfrac{\partial T_{rr}^{0,0}}{\partial z} - 2a v_r^{0,0} T_{rr}^{0,0}\right) \\ \epsilon = \epsilon^{q_t+1}: &\quad \tilde{\Lambda}\left(\tfrac{\partial T_{rr}^{0,1}}{\partial t} + v_z^{0,0}\tfrac{\partial T_{rr}^{0,1}}{\partial z} + v_z^{0,1}\tfrac{\partial T_{rr}^{0,0}}{\partial z} - 2a\left\{v_r^{0,1}T_{rr}^{0,0} + v_r^{0,0}T_{rr}^{0,1}\right\}\right) \end{aligned} \tag{3.24}$$

The rr (3.25), zz (3.26), $\theta\theta$ (3.27), and rz (3.28) terms of the stress tensor follow, organized by the degree of expansion ϵ. Depending on the degree of ϵ^q in Eq. (3.24), an additional term of Λ for nondimensional time might need to be added to each expansion power. Similarly, the Z_ν term, representing nondimensionalized viscous forces from Sec. (3.1.2), is expanded and normalized by letting $Z_\nu = \tilde{Z}\epsilon^z$. Since the Λ and Z_ν terms could be included at any particular level ϵ of the power series expansion, the placeholder is designated with an over brace ($\overbrace{\ }$). Later sections on experimental parameters evaluate the relative importance of these terms for an indium-fed needle FEEP.

$$\begin{aligned} \text{rr tensor perturbation expansion} — \epsilon^0 r^0: &\quad T_{rr}^{0,0} + \overbrace{\Lambda} &&= 2\overbrace{Z_\nu} v_r^{0,0} \\ \epsilon^1 r^0: &\quad T_{rr}^{0,1} + \overbrace{\Lambda} &&= 2\overbrace{Z_\nu} v_r^{0,1} \\ \epsilon^2 r^0: &\quad T_{rr}^{0,2} + \overbrace{\Lambda} &&= 2\overbrace{Z_\nu} v_r^{0,2} \\ \epsilon^2 r^2: &\quad T_{rr}^{1,0} &&= 6\overbrace{Z_\nu} v_r^{1,0} \end{aligned} \tag{3.25}$$

$$\begin{aligned}
\text{zz tensor perturbation expansion} — \epsilon^0 r^0 : \quad & T_{zz}^{0,0} + \widehat{\Lambda} && = 2\widehat{Z_\nu}\,\tfrac{\partial v_z^{0,0}}{\partial z} \\
\epsilon^1 r^0 : \quad & T_{zz}^{0,0} + \widehat{\Lambda} && = 2\widehat{Z_\nu}\,\tfrac{\partial v_z^{0,1}}{\partial z} \\
\epsilon^2 r^0 : \quad & T_{zz}^{0,0} + \widehat{\Lambda} && = 2\widehat{Z_\nu}\,\tfrac{\partial v_z^{0,2}}{\partial z} \\
\epsilon^2 r^2 : \quad & T_{zz}^{0,0} && = 2\widehat{Z_\nu}\,\tfrac{\partial v_z^{1,0}}{\partial z}
\end{aligned} \tag{3.26}$$

$$\begin{aligned}
\theta\theta \text{ tensor perturbation expansion} — \epsilon^0 r^0 : \quad & T_{\theta\theta}^{0,0} + \widehat{\Lambda} && = 2\widehat{Z_\nu}\, v_r^{0,0} \\
\epsilon^1 r^0 : \quad & T_{\theta\theta}^{0,1} + \widehat{\Lambda} && = 2\widehat{Z_\nu}\, v_r^{0,1} \\
\epsilon^2 r^0 : \quad & T_{\theta\theta}^{0,2} + \widehat{\Lambda} && = 2\widehat{Z_\nu}\, v_r^{0,2} \\
\epsilon^2 r^2 : \quad & T_{\theta\theta}^{1,0} && = 2\widehat{Z_\nu}\, v_r^{1,0}
\end{aligned} \tag{3.27}$$

$$\text{rz tensor perturbation expansion} — \epsilon^1 r^1 : \quad T_{rz}^{0,0} + \widehat{\Lambda_{rz}} = \widehat{Z_\nu}\left\{\tfrac{\partial v_r^{0,0}}{\partial z} + 2v_z^{1,0}\right\} \tag{3.28}$$

While the possible time expansion for the first three equations is designated $\widehat{\Lambda}$, the rz stress tensor component of the additional potential term is labeled $\widehat{\Lambda_{rz}}$ and described by Eq. (3.29).

$$\begin{aligned}
\widehat{\Lambda_{rz}} \;=\; & \frac{\partial T_{rz}^{0,0}}{\partial z} + v_z^{0,0}\frac{\partial T_{rz}^{0,0}}{\partial z} + (1-a)v_r^{0,0}T_{rz}^{0,0} - aT_{rz}^{0,0}\frac{\partial v_z^{0,0}}{\partial z} + \frac{1}{2}(1-a)T_{rr}^{0,0}\frac{\partial v_r^{0,0}}{\partial z} \\
& -\frac{1}{2}(1+a)T_{zz}^{0,0}\frac{\partial v_r^{0,0}}{\partial z} - (1+a)v_z^{1,0}T_{rr}^{0,0} + (1-a)v_z^{1,0}T_{zz}^{0,0}
\end{aligned} \tag{3.29}$$

3.2.5 Kinematic boundary expansion

Substituting in the earlier Taylor velocity and surface expansions of Sec. (3.1.1) into Eq. (3.8) and matching powers of the perturbation ϵ results in Eq. (3.30).

$$\Sigma_m \epsilon^m \left\{ \frac{\partial \phi^m}{\partial t} + \Sigma_n \Sigma_p \epsilon^{2n+p} \left(\Sigma_q \epsilon^q \phi^q\right)^{2n} \left[v_z^{n,m} \frac{\partial \phi^p}{\partial z} - \phi^m v_r^{n,m} \right] \right\} = 0 \tag{3.30}$$

When expanding the free surface restraint into the leading order and the first correction terms, the stipulation on the surface motion is given by Eq. (3.31). This restricts the ϕ location and the corresponding radial and axial surface velocities in a 2D axisymmetric framework and prevents separation of the surface sheet.

$$\begin{aligned} \epsilon^0 : \quad & \frac{\partial \phi^0}{\partial t} + v_z^{0,0}\frac{\partial \phi^0}{\partial z} - v_r^{0,0}\phi^0 && = 0 \\ \epsilon^1 : \quad & \frac{\partial \phi^1}{\partial t} + v_z^{0,0}\frac{\partial \phi^1}{\partial z} - v_r^{0,0}\phi^1 + v_z^{0,1}\frac{\partial \phi^0}{\partial z} - v_r^{0,1}\phi^0 && = 0 \end{aligned} \tag{3.31}$$

3.3 FEEP expressions

Having listed the full set of possible governing equations, the perturbation equations for a slender jet in a specific configuration can be determined. Table (3.1) shows experimental values for a representative indium-fed needle FEEP set up at ARCS. Using the actual values from the first column, nondimensional force ratio terms can be calculated and the final order ϵ perturbation of those variables displayed. The last column is significant because it determines which order ϵ terms are matched up at each power series expansion level. Larger values indicate a less important component while negative order ϵ values imply that a force has a greater effect than the perturbation level would otherwise indicate.

The governing equations with this unique set up will be shown to be sparse. This is because Λ_1, Λ_2, P_a and Z_ν are not of small enough order ϵ to have their corresponding expansion terms remain in the leading order or in the first correction for free jet evolution. Therefore, the possible time and viscous corrections laid out in Sec. (3.2.4) will not be used, since they are too small of an effective perturbation. To correctly model only the driving forces for this jet, the terms multiplied by a large order ϵ nondimensionalized force need to be removed. After this step, rewriting all

Experimental parameters		Nondimensional terms		Order ϵ
ρ $\left[\frac{kg}{m^3}\right]$	6994	W	7.5×10^{-4}	4
σ $\left[\frac{N}{m}\right]$	0.546	B	1330	-3
$\tilde{p_{es}}$ [Pa]	8.85×10^6	F_r	0.060	2
v_0 $\left[\frac{m}{s}\right]$	0.02	Z_ν	7.2×10^{-6}	6
r_0 [m]	1×10^{-4}	Λ_1	2.4×10^{-4}	4
z_0 [m]	1×10^{-3}	Λ_2	0.01	2
$\tilde{p_a}$ [Pa]	0.13	$\frac{p_a r_0}{\sigma}$	4.4×10^{-9}	9
μ $\left[\frac{N \cdot s}{m^2}\right]$	1.9×10^{-3}	$\frac{p_{es} r_0}{\sigma}$	2.95×10^{-1}	1
f_{capil} [N]	6.0×10^{-5}	$\frac{1}{B \cdot W}$	1	0

Table 3.1: FEEP experimental parameters and resulting nondimensional terms

the incompressibility, momentum, stress, free surface, surface tension and surface curvature restraints of Sec. (3.2) gives a new power series approximation of an axisymmetric jet.

The $\epsilon = 0$ leading order set of equations is listed as Eq. array (3.32). Recall that B, F and W are nondimensionalized numbers from various combinations of forces, as originally defined in Sec. (3.1.2). These equations are drawn one apiece from the analysis of Sec. (3.2). Specifically, these terms come from Eqs. (3.12, 3.13, 3.18, 3.21, 3.22, 3.25, 3.26 and 3.31).

$$
\begin{aligned}
p^{0,0} - T_{rr}^{0,0} &= \tfrac{1}{B\cdot W}\left\{\tfrac{1}{\phi^0}\right\} \\
(T_{zz}^{0,0} - p^{0,0})\,\tfrac{\partial \phi^0}{\partial z} - \phi^0 T_{rz}^{0,0} &= -\tfrac{1}{B\cdot W}\left\{\tfrac{1}{\phi^0}\tfrac{\partial \phi^0}{\partial z}\right\} \\
2v_r^{0,0} + \tfrac{\partial v_z^{0,0}}{\partial z} &= 0 \\
\tfrac{B}{r}\left\{T_{rr}^{0,0} - T_{\theta\theta}^{0,0}\right\} &= 0 \\
B\left\{2T_{rz}^{0,0} + \tfrac{\partial T_{zz}^{0,0}}{\partial z} - \tfrac{\partial p^{0,0}}{\partial z}\right\} &= -\tfrac{1}{F}r \\
T_{rr}^{0,0} &= 0 \\
T_{zz}^{0,0} &= 0 \\
\tfrac{\partial \phi^0}{\partial t} + v_z^{0,0}\tfrac{\partial \phi^0}{\partial z} - v_r^{0,0}\phi^0 &= 0
\end{aligned}
\tag{3.32}
$$

Following similar reasoning and again using the order ϵ weighting from Table (3.1), the $\epsilon = 1$ first order corrections are given by Eq. array (3.33).

$$
\begin{aligned}
p^{0,1} - T_{rr}^{0,1} &= \tfrac{1}{B\cdot W}\left\{-\tfrac{\phi^1}{(\phi^0)^2}\right\} \\
(T_{zz}^{0,1} - p^{0,1})\,\tfrac{\partial \phi^0}{\partial z} + (T_{zz}^{0,0} - p^{0,0})\,\tfrac{\partial \phi^1}{\partial z} - \phi^0 T_{rz}^{0,1} - \phi^1 T_{rz}^{0,0} &= \tfrac{1}{B\cdot W}\left\{-\tfrac{1}{\phi^0}\tfrac{\partial \phi^1}{\partial z} + \tfrac{\phi^1}{(\phi^0)^2}\tfrac{\partial \phi^0}{\partial z}\right\} \\
2v_r^{0,1} + \tfrac{\partial v_z^{0,1}}{\partial z} &= 0 \\
\tfrac{B}{r}\left\{T_{rr}^{0,1} - T_{\theta\theta}^{0,1}\right\} &= 0 \\
B\left\{2T_{rz}^{0,1} + \tfrac{\partial T_{zz}^{0,1}}{\partial z} - \tfrac{\partial p^{0,1}}{\partial z}\right\} &= 0 \\
T_{rr}^{0,1} &= 0 \\
T_{zz}^{0,1} &= 0 \\
\tfrac{\partial \phi^1}{\partial t} + v_z^{0,0}\tfrac{\partial \phi^1}{\partial z} - v_r^{0,0}\phi^1 + v_z^{0,1}\tfrac{\partial \phi^0}{\partial z} - v_r^{0,1}\phi^0 &= 0
\end{aligned}
\tag{3.33}
$$

3.3.1 Matrix formulation

The leading order and first ϵ correction arrays in Eqns. (3.32-3.33) each contain eight equations with eight unknowns. However, they can be reduced to a coupled system of four quasi-linear PDE's referencing ϕ, v_z, T_{rr} and T_{zz} in the form

$$\frac{\partial \overline{u}}{\partial t} + M(\overline{u})\frac{\partial \overline{u}}{\partial z} = P(\overline{u})\overline{u} + f \tag{3.34}$$

where $\overline{u} = [\phi,\, v_z,\, T_{rr},\, T_{zz}]^{'}$ and $M(\overline{u})$ is a 4x4 array of coefficients on the spatial derivatives of $\overline{u}$. $P(\overline{u})$ is a similar array but acts on $\overline{u}$ directly. Finally, f is a vector of constants. This matrix reformulation can be accomplished because the system of Eqs. (3.32-3.33) are over defined. For example, the last equation of the first correction, $p^{0,1} - T_{rr}^{0,1} = \frac{1}{B \cdot W}\left\{\frac{-\phi^1}{(\phi^0)^2}\right\}$, allows the pressure term to be determined if T_{rr} and ϕ are known. Therefore, a solution to Eq. (3.34) at each level of perturbation $\epsilon \in [0...N)$ allows for the computation of all eight variables. In matrix form, the leading order problem of array Eq. (3.32) becomes Eq. (3.35).

$$\begin{bmatrix} \frac{\partial \phi^0}{\partial t} \\ \frac{\partial v_z^{0,0}}{\partial t} \\ \frac{\partial T_{rr}^{0,0}}{\partial t} \\ \frac{\partial T_{zz}^{0,0}}{\partial t} \end{bmatrix} + \begin{bmatrix} v_z^{0,0} & \frac{1}{2}\phi & 0 & 0 \\ \frac{2B}{\phi^0}\left\{T_{zz}^{0,0} - T_{rr}^{0,0} + \frac{1}{BW}\left(\frac{1}{\phi^0}\right)^2\right\} & 0 & -B & B \\ 0 & 0 & 0 & 0 \\ 0 & 0 & 0 & 0 \end{bmatrix} \times$$

$$\begin{bmatrix} \frac{\partial \phi^0}{\partial z} \\ \frac{\partial v_z^{0,0}}{\partial z} \\ \frac{\partial T_{rr}^{0,0}}{\partial z} \\ \frac{\partial T_{zz}^{0,0}}{\partial z} \end{bmatrix} = \begin{bmatrix} 0 \\ -\frac{1}{F_r} \\ 0 \\ 0 \end{bmatrix} \tag{3.35}$$

Using the form and reasoning behind Eq. (3.34) again, the first order perturbation $\epsilon = 1$ correction matrix of Eq. (3.33) transforms into Eq. (3.36). The potentially 20-equation, 24-variable system's evolution can be successfully described using just one 4-row matrix per expansion level.

$$\begin{bmatrix} \frac{\partial \phi^1}{\partial t} \\ \frac{\partial v_z^{0,1}}{\partial t} \\ \frac{\partial T_{rr}^{0,1}}{\partial t} \\ \frac{\partial T_{zz}^{0,1}}{\partial t} \end{bmatrix} + \begin{bmatrix} v_z^{0,0} & \frac{1}{2}\phi & 0 & 0 \\ \frac{2B}{\phi^0}\left\{T_{zz}^{0,0} - T_{rr}^{0,0} + \frac{1}{BW}\left(\frac{1}{\phi^0}\right)\right\} & 0 & -B & B \\ 0 & 0 & 0 & 0 \\ 0 & 0 & 0 & 0 \end{bmatrix} \times$$

$$\begin{bmatrix} \frac{\partial \phi^1}{\partial z} \\ \frac{\partial v_z^{0,1}}{\partial z} \\ \frac{\partial T_{rr}^{0,1}}{\partial z} \\ \frac{\partial T_{zz}^{0,1}}{\partial z} \end{bmatrix} = \begin{bmatrix} -\frac{1}{2}\frac{\partial v_z^{0,0}}{\partial z} & -\frac{\partial \phi^0}{\partial z} & 0 & 0 \\ \frac{2BT_{rz}^{0,0}}{\phi^0} + \frac{2}{W(\phi^0)^3}\frac{\partial \phi^0}{\partial z} & 0 & \frac{2B}{\phi^0}\frac{\partial \phi^0}{\partial z} & -\frac{2B}{\phi^0}\frac{\partial \phi^0}{\partial z} \\ 0 & 0 & 0 & 0 \\ 0 & 0 & 0 & 0 \end{bmatrix} \begin{bmatrix} \phi^1 \\ v_z^{0,1} \\ T_{rr}^{0,1} \\ T_{zz}^{0,1} \end{bmatrix} \tag{3.36}$$

3.3.2 Matrix simplification

Examining the last two rows of Eq. (3.35) shows that $\frac{\partial T_{rr}^{0,0}}{\partial t} = \frac{\partial T_{zz}^{0,0}}{\partial t} = 0$. This implies that $T_{rr}^{0,0} = f(r,z)$ and $T_{zz}^{0,0} = g(r,z)$ do not depend on time and are therefore fixed in space to their initial profiles. Setting non-zero values for these stress components yields a constant stress in the fluid - which is physically meaningless. Therefore, we choose $T_{rr}^{0,0} = T_{zz}^{0,0} = 0$ and reduce the matrix in Eq. (3.35) to a 2x2 system shown in Eq. (3.37) with six dependent variables.

$$\begin{bmatrix} \frac{\partial \phi^0}{\partial t} \\ \frac{\partial v_z^{0,0}}{\partial t} \end{bmatrix} + \begin{bmatrix} v_z^{0,0} & \frac{1}{2}\phi^0 \\ \frac{2}{W}\frac{1}{(\phi^0)^3} & 0 \end{bmatrix} \begin{bmatrix} \frac{\partial \phi^0}{\partial z} \\ \frac{\partial v_z^{0,0}}{\partial z} \end{bmatrix} = \begin{bmatrix} 0 \\ \frac{-1}{Fr} \end{bmatrix} \tag{3.37}$$

Setting $\eta_v = \frac{\partial v_z^{0,0}}{\partial z}$ and operating the first equation by $\frac{\partial}{\partial t}$ and the second by $\frac{\partial}{\partial z}$, the term $\frac{\partial^2 v_z^{0,0}}{\partial t \partial z}$ can be removed and the entire system can then be modeled at $\epsilon = 0$ leading order with Eq. (3.38).

$$\frac{\partial^2 \phi^0}{\partial t^2} + v_z^{0,0}\frac{\partial^2 \phi^0}{\partial t \partial z} - \frac{1}{W}\frac{1}{(\phi^0)^2}\frac{\partial^2 \phi^0}{\partial z^2} + \frac{3}{2}\eta_v \frac{\partial \phi^0}{\partial t} + \frac{3}{W}\frac{1}{(\phi^0)^3}\left(\frac{\partial \phi^0}{\partial z}\right)^2 = 0 \tag{3.38}$$

Similarly, the last two rows of Eq. (3.36) show that $T_{rr}^{0,1} = \frac{\partial T_{rr}^{0,1}}{\partial z} = T_{zz}^{0,1} = \frac{\partial T_{zz}^{0,1}}{\partial z} = 0$, and therefore the matrix can be again reduced to a 2x2 system, as shown in Eq. (3.39) with six dependent variables.

$$\begin{bmatrix} \frac{\partial \phi^1}{\partial t} \\ \frac{\partial v_z^{0,1}}{\partial t} \end{bmatrix} + \begin{bmatrix} v_z^{0,0} & \frac{1}{2}\phi^0 \\ \frac{2}{W}\frac{1}{(\phi^0)^2} & 0 \end{bmatrix} \begin{bmatrix} \frac{\partial \phi^1}{\partial z} \\ \frac{\partial v_z^{0,1}}{\partial z} \end{bmatrix} = \begin{bmatrix} -\frac{1}{2}\frac{\partial v_z^{0,0}}{\partial z} & \frac{\partial \phi^0}{\partial z} \\ \frac{2}{W(\phi^0)^3}\frac{\partial \phi^0}{\partial z} & 0 \end{bmatrix} \begin{bmatrix} \phi^1 \\ v_z^{0,1} \end{bmatrix} \tag{3.39}$$

Setting $\eta_t = \frac{\partial \phi^1}{\partial t}$, $\eta_z = \frac{\partial \phi^1}{\partial z}$ and operating the first equation by $\frac{\partial}{\partial t}$ and the second by $\frac{\partial}{\partial z}$, the term $\frac{\partial^2 v_z^{0,1}}{\partial t \partial z}$ can be canceled from both sides. Since leading order terms are considered constants for all orders ϵ greater perturbation, setting all $\frac{\partial}{\partial z}(\cdot)^{0,0} = \frac{\partial}{\partial t}(\cdot)^{0,0} = 0$ allows the modeling of the entire system to the first correction $\epsilon = 1$ using Eq. (3.40).

$$\frac{\partial \eta_t}{\partial t} + v_z^{0,0}\eta_t \eta_z - \frac{1}{W}\frac{\partial \eta_z}{\partial z} = 0 \tag{3.40}$$

3.4 Stability analysis

It is important to use the perturbation equations of the previous section so as to obtain physically meaningful results. A well-posed, steady problem must have boundary conditions consistent with the PDE problem [21]. Successful simulations resulted from using an initial pressure and final tangential stress. Positive characteristics of a matrix system propagate information in the positive axial direction, i.e. to the right, by our convention. It follows that each positive characteristic has one condition specified at the left boundary. Similarly, each negative characteristic requires boundary data at the right in order to define the solution in the interior at future points. Boundary conditions chosen from viewing the equations in isolation run the risk of unknowingly predicting highly unstable, and thus physically impossible, steady states. The two characteristic equations for Eq. (3.37) are given in Eq. (3.41).

$$\begin{aligned} s_1 &= \frac{1}{2W\phi}\left[W\phi v_z + \sqrt{W^2\phi^2 v_z^2 + 4W}\right] \\ s_2 &= \frac{1}{2W\phi}\left[W\phi v_z - \sqrt{W^2\phi^2 v_z^2 + 4W}\right] \end{aligned} \tag{3.41}$$

Performing an eigenvalue analysis, the solution is hyperbolic when both characteristics are real and the system is not degenerate. If imaginary values are chosen for $s_{1,2}$, a mixed hyperbolic/elliptic solution set results. The presence of this mixed solution type means that surface evolution predictions will be catastrophically unstable, regardless of how reasonable the physical constraints. While s_1 in Eq. (3.41) is guaranteed to be positive definite, s_2 is positive if $(W\phi v_z)^2 \geq W^2\phi^2 v_z^2 + 4W$. The second characteristic turns out to be positive if and only if:

$$0 > 4W \tag{3.42}$$

Since the Weber number is normalized to lie between $\epsilon < W < \frac{1}{\epsilon}$, it should be in the range [0.1:10]. Therefore, the system will provide a second characteristic that is **always** negative and requires one left hand and one right hand boundary condition to remain stable. Figure (3.3) shows an example plot of ϕ versus z where the expected surface behavior is a flat line. However, using an inappropriate initialization of two beginning boundary conditions, unpreventable chaotic behavior ensues regardless of the computational differencing scheme or stencil used. This surface shape is shown after 8,000 time steps simulating 0.01 seconds of evolution.

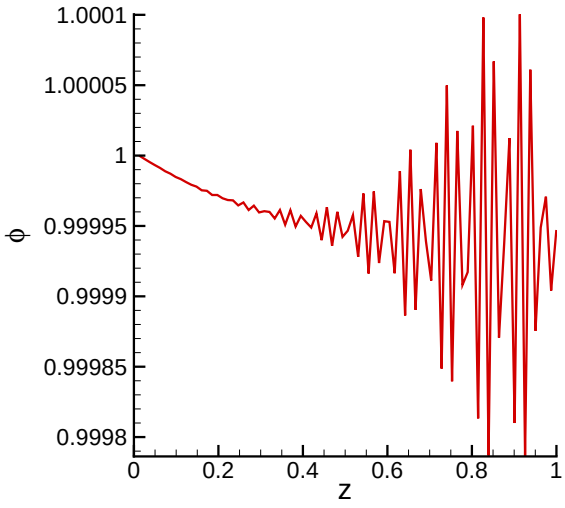

Figure 3.3: Unstable solution to droplet evolution from using two initial boundary conditions

3.5 Simulation results

An example of the shape, velocity, axial force and stress for a steady-state slender jet with all forces equally contributing is given in Figs. (3.4-3.5). The solid line is the ϵ^0 main term while the dotted line is the ϵ^1 first correction. The correction is shown to cause only a small variation in the jet values, with the variable plus the correction

always being within 0.5% of the variable itself. This supports the initial claim that increasing correction levels make ever-smaller changes to their main variable, or $\lim_{i\to\infty} \epsilon^i = 0$. To avoid the instability mentioned previously, these forces require boundary conditions for a constant pressure on both ends of the jet.

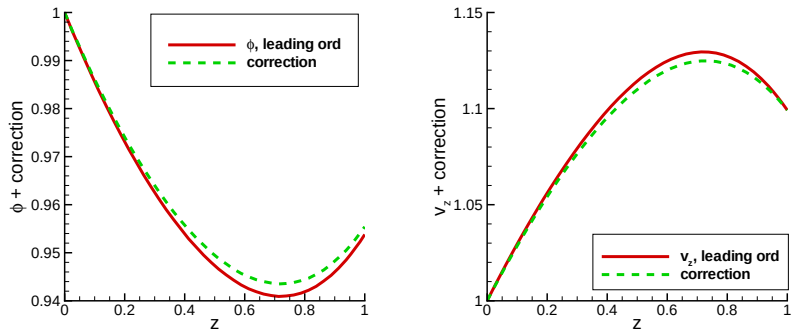

Figure 3.4: a) Slender jet free surface and b) axial velocity with ϵ^1 correction

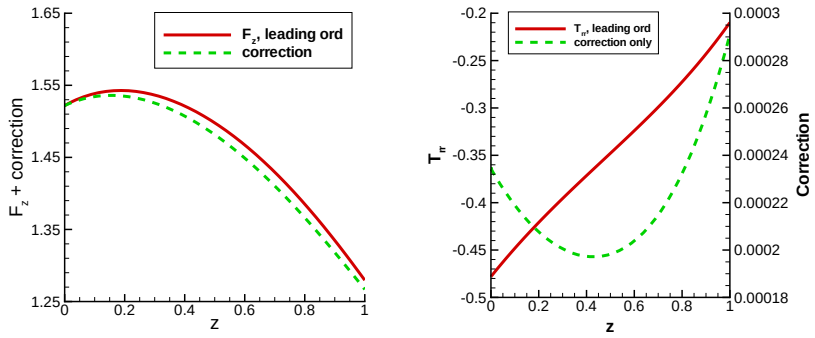

Figure 3.5: a) Slender jet axial force and b) radial stress with ϵ^1 correction

The surface ϕ begins at 1 and reduces approximately 6% in width to 0.94 at the minimum, resembling a hanging string, so as to match exit pressure zero gradient conditions. To preserve mass conservation, the jet velocity v_z increases and the nondimensional axial force $F_z = \int (T_{zz} - p)\, da$ declines at the far right end, towards z=1. The force is strongest in the region where the surface gradient is changing most

rapidly with the max $\left(\frac{d^2\phi}{dz^2}\right)$ around z=$\{0.1,0.3\}$.

The "equal force" case assumes the physical effects of inertia, gravity, surface tension, viscosity, and elastic relaxation are all vital in the modeling of jet behavior. The behavior of the free surface, axial velocity and axial force all drastically diverge when the governing equations are changed from the original assumption of equal importance for all forces to using the equations of Sec. (3.3). This divergence occurs when inputting the experimental characteristics of a FEEP needle covered in liquid indium as shown in Table (3.1).

Figures (3.6-3.8) show that with the imposition of non-equal forces expected in the indium FEEP, a power series expansion simulation predicts several notable trends. The free surface ϕ decreases rapidly ("bottle necks") in the absence of retarding radial stress. With $T_{rr} = 0$ because of no Λ or Z_ν terms counteracting the $\frac{d\phi}{dz}$ slope, the far edge z=1 decreased. There is also no linear radial momentum $rv_z^{0,0}\frac{\partial v_r^{0,0}}{\partial z}$ term to act as a brake on the free surface and allows the axial velocity to increase. Note that the area reduction occurs as the square of the radius, so the velocity will increase much faster than ϕ shrinks. Finally, the axial force decreases in magnitude to nearly zero as the right hand of the streaming jet is not tugging on prior points. The result is an asymptotic breakup of a FEEP droplet-jet whereby the stream accelerates, tapers and ceases to pull other droplets along. All of these trends have been observed in experimental studies of field emission thrusters as well, as initially described in Chapter I.

3.6 Conclusion

The asymptotic analysis presented considers the forces on a slender jet through the use of nondimensional numbers and power series expansions of those forces.

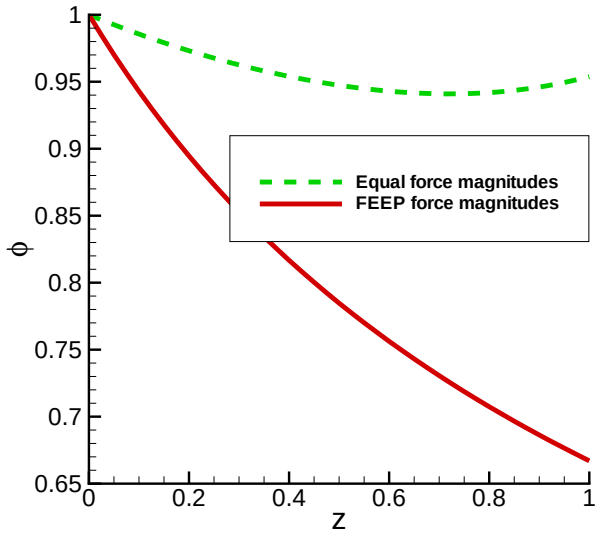

Figure 3.6: Free surface evolution difference between equal force assumption and FEEP experimental parameters

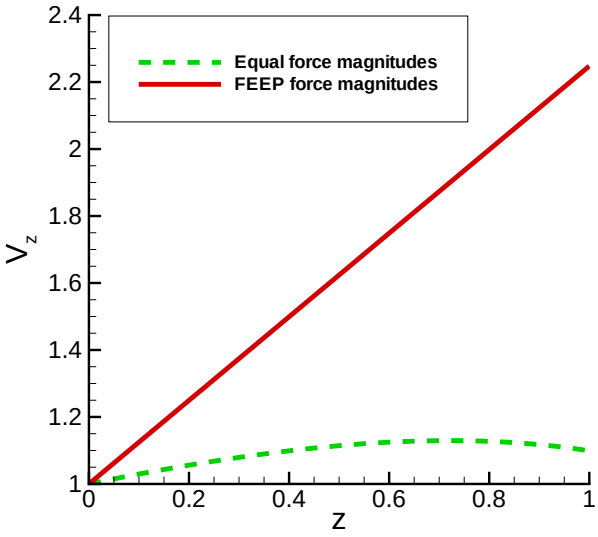

Figure 3.7: Axial velocity difference between equal and FEEP parameter force assumptions

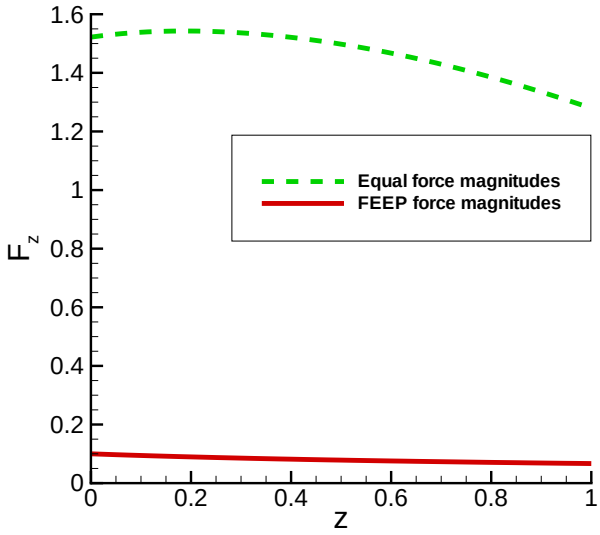

Figure 3.8: End stress difference between equal and FEEP parameter force assumptions

Among the assumptions used in the formulation of this model are that there is always a thin fluid of nonzero radius stretched along the axis and that the jet angle $\theta_{jet} \in (0, \frac{\pi}{2}]$. The consequence of these assumptions was a rapid 1D model, with run times from 0.01 to 20 seconds. A related stability analysis examined the importance of the correct boundary conditions. Unless both beginning and ending jet parameters are fixed, the system is unconditionally unstable. This instability was shown mathematically and the surface evolution chaotic behavior was also observed even when using up to 5^{th} order accurate stencils.

For the FEEP experimental set up, the order ϵ of the nondimensional numbers portend that a complete approximation to fluid behavior requires surface tension and electrostatic forces as model components. The ordering and magnitudes of the forces from least to greatest is viscosity (-10), elasticity (-8), atmospheric pressure (-5), inertia (-3), gravity (-2), surface tension and electrostatics (0). That is, the effect

of 101 kPa pressure on the surface has 1×10^{-5} the influence of surface tension on the jet development. As well as identifying the magnitude of the force contribution, several figures demonstrated that if all forces were equally important, the overall evolution of the jet would be substantially different in terms of position, velocity and internal stress.

CHAPTER IV

Droplet Snap Off Algorithms

Having established a numerical framework for the formation of a FEEP droplet, we can now examine the results of snap off. In this chapter, we simulate the emission of charged indium droplets from an indium-fed needle FEEP in 2D and 2D-axisymmetric coordinate systems. The boundary element method is used to rapidly and directly calculate the electric field on the fluid surface, with the surface then being advected forward in time using level sets. This unique combination will allow us to successfully address difficult issues with surface tracking. Finally, algorithms to increase speed and accuracy of the simulation are described.

For computational tracking of solid-liquid or liquid-vacuum interface surfaces, the determination of the normal electric field $\overrightarrow{E_n}$ commonly is quite lengthy and error-prone. This chapter will discuss the physical model used to simulate droplet detachment and the level set and boundary element methods. This combination of approaches enables accurate and rapid spatial resolution for charged surfaces, handles a changing irregular shape and includes the effects of electrostatic forces on the behavior of droplets after pinch off. In addition, the changes required to run axisymmetric cases and a discussion of additional approaches used to provide ever faster run times within the level set and boundary element methods are outlined.

4.1 Model description

In 2D, the simulation model considers an incompressible, isothermal, viscous liquid. The propellant, indium, is treated as a perfect conductor and its atoms are accelerated by rectangular electrodes. The governing equations for the system are listed as Eqs. (4.1-4.3). The electric field $\overrightarrow{E}$ is a surface normal force, since $\overrightarrow{E}$=0 inside a conductor. Continuity and conservation of momentum are enforced, where

$$\begin{aligned} \tfrac{\partial u}{\partial x} + \tfrac{\partial v}{\partial y} &= 0 \\ \mathbf{A}_t + \mathbf{B}_x + \mathbf{C}_y &= -\nabla p \end{aligned} \tag{4.1}$$

the main variables in the second vector equation are below.

$$\mathbf{A} = \begin{bmatrix} u \\ \\ v \end{bmatrix}, \mathbf{B} = \begin{bmatrix} u^2 \\ \\ uv \end{bmatrix}, \mathbf{C} = \begin{bmatrix} uv \\ \\ v^2 \end{bmatrix} \tag{4.2}$$

The free surface is subject to a combined boundary pressure condition.

$$p = \sigma\kappa + q\overrightarrow{E_n} + 2\mu_{liquid}\left(D_{defm} \cdot \overrightarrow{n}\right) \cdot \overrightarrow{n} \tag{4.3}$$

The subfunction variables u and v are local velocity vectors along the x and y axes respectively; σ is the surface tension; κ is the surface curvature; and D_{defm} is the rate of deformation tensor. The electric field is computed by $E = -\nabla U\left(\overrightarrow{x}\right)$, where $U\left(\overrightarrow{x}\right)$ is the electrostatic potential at position $\overrightarrow{x}$.

4.1.1 Parameter submodels

The surface tension (σ_{In}) of liquid indium does not vary rapidly with temperature [56], as indicated by Eq. (4.4). During normal FEEP thruster operation, the temperature remains within the narrow operational range of 440-450 K when indium

is far enough above its melting point to be fully liquid [93]. Figure (4.1) displays the percentage change in surface tension, viscosity and density over the expected temperatures.

$$\sigma_{In} = \frac{555 - 0.12(T[K] - 430)}{1,000} \left[\frac{N}{m}\right] \tag{4.4}$$

The ability of indium to flow over a solid surface is determined largely by its viscosity (μ), which varies with temperature through the weak exponential relationship shown in Eq. (4.5). Over the expected temperature range, the fluid viscosity changes only 4% [56].

$$\mu_{In} = 3 \times 10^{-4} e^{800/T[K]} \left[\frac{kg}{m \cdot s}\right] \tag{4.5}$$

The density of indium (ρ) is given by Eq. (4.6) and changes about 0.01% per degree Celsius [68].

$$\rho_{In} = 1,000 \times (7.1295 - 6.7987 \times 10^{-4}(T - 273.15)) \left[\frac{kg}{m^3}\right] \tag{4.6}$$

Among the model assumptions, the treating of the propellant as a perfect conductor is very reasonable. Since indium is a metal, the conductivity is so high that an electron can travel through the liquid surface along the needle body at $8 \times 10^7 \frac{m}{s}$, as described in Appendix (C). The fluid flows at a maximum speed 11 orders of magnitude slower, only $1 \times 10^{-4} \frac{m}{s}$. The isothermal assumption for droplets is accurate because only radiation is available to cool them after snap off. For example, detachment occurs in 0.1 μs, but a 100 μm diameter droplet at 450 K treated as a blackbody cools less than 0.1 mK in that time [175]. Therefore, σ, μ and ρ can accurately be treated as constant.

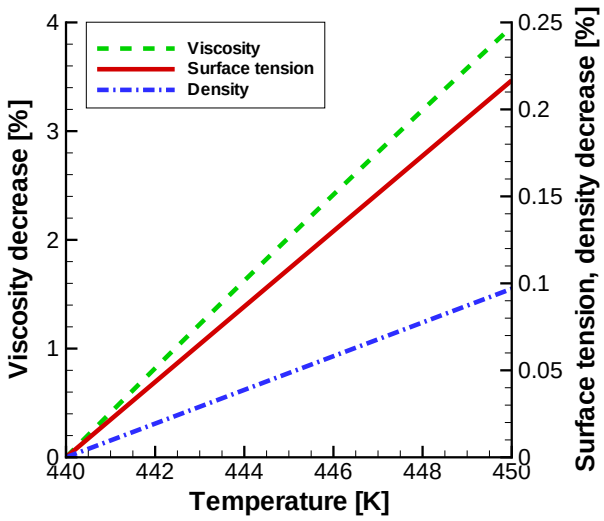

Figure 4.1: Change in surface tension, viscosity and density over operational temperature range

4.1.2 Possible surface modeling approaches

Several different methods exist that can theoretically model the movement of a surface. One of the most difficult aspects in tracking an interface is dealing with the detachment and merging of that surface. The other main issue is that in addition to the shape and movement of the interface to be computed, the large property jumps associated with phase changes add significant computational burden. Simulations with a sharp interface tend to be more accurate and numerically stable [211, 276]. For example, a large density ratio across an interface makes the computation stiff and often leads to numerical instabilities. Tables (4.1-4.2) list several approaches to simulate droplet surfaces and some advantages and disadvantages of each.

Front-tracking Numerical techniques in smoothing, regularization and surface surgery are collectively referred to as *front tracking* methods. Unverdi [254] and

Method	Advantages	Disadvantages
Boundary integral [14, 147]	• Entire solution from only boundary nodes • Rapid and possible infinite precision	• Requires surface derivatives • Complex shapes need significant mathematics. • Points need to be in order • Trouble with detachment and viscosity
Front tracking (MAC [107], SLIC [180])	• Interface tracked explicitly • Allows for surface tension and sharp density fields • One set of governing equations • No numerical diffusion	• Effort needed to normalize panel lengths, compute curvature • Very complex method • Grid regeneration needed • Loses mass
Ghost fluid [54, 70]	• Allows multidimensional advection • Avoids interface splitting • Simple to program	• Requires more points tracked • Shape of cells around interface nontrivial • Low accuracy, from surface orientation assumption

Table 4.1: Overview of droplet simulation approaches I

Method	Advantages	Disadvantages
Immersed boundary [69, 100]	• Can use regular, unchanging mesh • Combines best parts of Eularian and Lagranian approaches	• Spurious oscillations at nodes • Requires complex force spreading • Uses small timesteps for stiff matrices
Level set [186, 226]	• Allows topology changes • Can merge and break up without extra coding	• Grid based • Needs to reinitialize ϕ at every time step • Loses mass
Volume of fluid [111, 194]	• Can provide 2nd order accuracy for interface velocity • Easy to implement • Mass conserved	• Hard to determine curvature • Small volumes detach and drift

Table 4.2: Overview of droplet simulation approaches II

Tryggvason [248] describe various algorithms for three dimensional front tracking. They are based on multiple sets of governing equations over the entire computational domain, with a separate solution for each fluid. A separate front marks the interface, but a fixed grid is used for the fluid within each phase. The interface conditions are explicitly enforced at the interface.

The Navier-Stokes equations are solved on a fixed, regular, staggered grid, and the sharp interface separating the fluids is explicitly tracked by an additional moving grid called the *front*. The flow is taken as incompressible and the interfacial source terms such as surface tension are computed on the front and transferred to the fixed grid.

Immersed boundary Using boundary body forces, this algorithm allows the imposition of the boundary conditions on a given surface not coinciding with the computational grid. The governing equations, therefore, can be discretized and solved on a regular mesh.

Front capturing The basic approach is to use a finite volume discretization of the entire domain, while modifying the numerical approximation to minimize numerical difficulties. This generally involves using a second order scheme and adding artificial viscosity around the front to avoid oscillations.

Boundary integral method (BIM) The basic formulation of the BIM is due to Baker [14], and modified by Lundgren to account for toroidal geometry [147]. Only the surfaces are discretized, with forces and curvature computed from edge interpolation. While this method is computationally efficient, it assumes that the solution is governed by potential flow in each fluid, thereby being limited in how they

model viscosity.

This method has a noteworthy history in bubble simulation. It has been used to model the collapse of vapor bubbles [26, 27, 28], the topology change of an inviscid air bubble [281], drop oscillations [146] and raindrops on a pool [182]. Three dimensional applications can be found in [128, 158].

Level set method Level sets allow for computational tracking of a surface between discrete interfaces. A grid is used, with a continuously differentiable variable ϕ across the domain. They were introduced by Osher and Sethian in 1988 [187], and have been heavily analyzed over the following decades [12, 66, 185, 222, 228]. Many physical phenomena have been simulated using level sets, including ink jets [278], electrical tomography [46], turbulent channel flow [279], hypothalamus structural mapping [139] and radar image processing [24, 116].

4.2 Level set method

Using the model framework of Eqs. (4.1-4.3), numerical methodologies and algorithms must be chosen to simulate the characteristics of FEEP droplets. In the following section, a level set method is used to model material interfaces.

The method most similar to this investigation is by Gibou [96]. He proposed an Eulerian approach that discretized the problem using a symmetric, second-order accurate method with variable coefficient Poisson equations on evenly spaced mesh points in an irregular domain. However, while Gibou's approach did deal with irregular interfaces, it did not have the ability to handle gradients that change in space and time that occur when droplets detach.

Interface tracking using level set computation relies on the determination and

movement of the boundary. In FEEP operation, liquid propellant exists between a solid tungsten needle and a vacuum. As outlined in the prior chapter, the dominating forces are surface tension and electrostatic potential. Here, we present results that demonstrate the adaptability of the model on irregular shapes and domains. In the simulations, the position of the vacuum-liquid interface is updated via the level set equation:

$$\phi_t + \overrightarrow{v} \cdot \nabla\phi = 0 \tag{4.7}$$

where ϕ is the level set function; positive in the liquid and negative in the vacuum. The interface velocity $\overrightarrow{v}$ is the indium fluid velocity. In the vacuum, lines of constant $\overrightarrow{v}$ are projected normal to the indium surface. The interface is advected by only the normal velocity component of $\overrightarrow{v}$. This component is the normalized gradient of the level set surface, as given by Eq. (4.8). The extension was first suggested in [38], analyzed carefully in [283], and further discussed in [70] and [190]. In the special case where $\overrightarrow{v_n}$=1, then Eq. (4.7) becomes a Hamilton-Jacobi equation whose solution generally develop kinks, or jumps in derivatives. The unique viscous solution is then chosen [186]. See [15, 51] for more details.

$$\overrightarrow{v_n} = \frac{\overrightarrow{v} \cdot \nabla\phi}{|\nabla\phi|} \tag{4.8}$$

Integrating Eq. (4.7) results in the movement of ϕ contours along the directions normal to the interface. Equation (4.7) also implies that ϕ remains constant on droplet paths. If a point starts on the surface $\partial\Omega$ where $\phi = 0$, that particle moves through time, but remains on the surface. Figure (4.2a) shows the $\phi \geq 0$ cross-section of a double-humped shape intersected at 3 different heights while Fig. (4.2b) demonstrates how the ϕ level set values around the rightmost hump reproduce the

surface contour at a point [6].

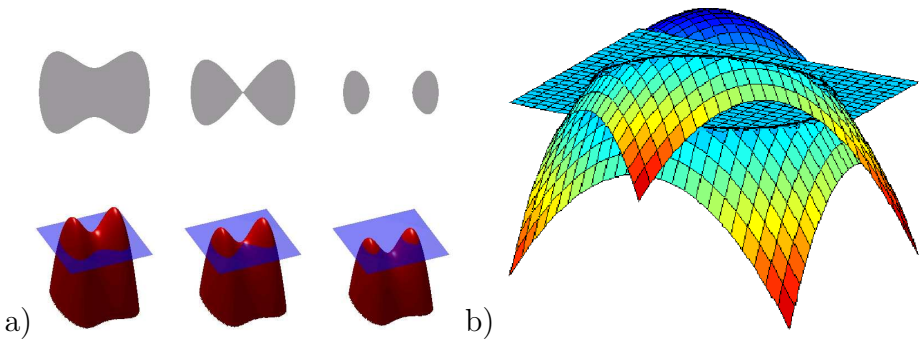

Figure 4.2: Level set a) surface determination at various heights and b) ϕ values around the upper right hump at the highest point.

4.2.1 Fundamental integrals and constraints

To more fully analyze level sets, several new functions need to be introduced. The unit normal $\overrightarrow{n}$ to Γ is given by Eq. (4.9).

$$\overrightarrow{n} = \frac{\nabla\phi}{|\nabla\phi|} \tag{4.9}$$

Given an arbitrary function $f(\overrightarrow{x})$, several fundamental integrals can be obtained. If we define the volume $V \in \Re^3$ as the closed set of points such that

$$V = \{\overrightarrow{x} | \phi(\overrightarrow{x}) \geq 0\} \tag{4.10}$$

with a boundary surface Ω defined by

$$\Omega = \{\overrightarrow{x} | \phi(\overrightarrow{x}) = 0\} \tag{4.11}$$

then the surface and volume integrals are represented by Eq. (4.12).

$$\begin{array}{c} \oint_{\Omega} f\left(\overrightarrow{x}\right)\, d\Omega \\ \int_{V} f\left(\overrightarrow{x}\right)\, dV \end{array} \tag{4.12}$$

To normalize ϕ, it is important to define the distance function $d\left(\overrightarrow{x_I}\right)$ as the length between any point $\overrightarrow{x_I}$ in $\Re^3$ to the nearest point $\overrightarrow{x}$ on the surface Ω. The negative gradient $(-\nabla d)$ at any point on the line segment from $\overrightarrow{x}$ to that $\overrightarrow{x_I}$ location gives the vector that points between them. Since d is a Euclidian distance, it is constrained by Eq. (4.13).

$$|\nabla d| = 1 \tag{4.13}$$

A signed distance function is an implicit function ι with $|\iota\left(\overrightarrow{x}\right)| = d\left(\overrightarrow{x}\right)$ for all $\overrightarrow{x}$. Thus, $\iota\left(\overrightarrow{x}\right) = d\left(\overrightarrow{x}\right) = 0$ for all surface $\overrightarrow{x} \in \Omega$, $\iota\left(\overrightarrow{x}\right) = -d\left(\overrightarrow{x}\right)$ for all points outside the volume, and $\iota\left(\overrightarrow{x}\right) = d\left(\overrightarrow{x}\right)$ for all interior locations $\overrightarrow{x} \in V$. Due to this relationship, the same distance constraint applies in Eq. (4.14).

$$|\nabla \iota| = 1 \tag{4.14}$$

So, given $\overrightarrow{x_I}$ and using the fact that $\iota\left(\overrightarrow{x_I}\right)$ is the signed distance to the closest point on the interface, Eq. (4.15) provides the closest boundary point.

$$\overrightarrow{x} = \overrightarrow{x_I} - \iota\left(\overrightarrow{x_I}\right) \cdot \overrightarrow{n} \tag{4.15}$$

The normalized constraints of the distance function cause other equations to simplify. For example, if the level set variable is restricted via ι, then the mean surface curvature can be expressed as Eq. (4.16).

$$\kappa = -\nabla \cdot \overrightarrow{n} = -\nabla \cdot \left(\frac{\nabla \phi}{|\nabla \phi|}\right) = -\frac{\phi_{xx}\phi_y^2 - 2\phi_x\phi_y\phi_{xy} + \phi_{yy}\phi_x^2}{\left(\phi_x^2 + \phi_y^2\right)^{3/2}} \tag{4.16}$$

Note that in our implementation, the curvature is *not* expressed using level set variables. The reinitialization step is only second order accurate; the curvature computed from ϕ alone will not give the second order accuracy that a volume of fluid set up provides. While other alternative interface representations provide higher order location descriptions [42], the accuracy of the simulation is limited instead by the order of the boundary conditions implementation [222].

4.2.2 Numerical implementation

To numerically compute the surface evolution, a hybrid approach is used to determine the location of the surface while increasing the simulation accuracy. A combined level set (CLS) and volume of fluid (VOF) approach is used (CLSVOF) [227]. The surface normals are computed from the level set function with Eq. (4.8) which are used in the volume of fluid piecewise linear reconstruction step. The level set reinitialization process then replaces the existing ϕ with the revised level set function. This produces the signed normal distance from the surface, where $\phi(\overrightarrow{x}) = \iota(\overrightarrow{x})$.

Numerical algorithms

A variety of numerical algorithm schemes are needed in the CLSVOF approach [183]. The method is briefly outlined below [224].

1. Advance the location of the interface using the coupled level set and volume of fluid method. Velocity and pressure fields are computed based on variable density projection methods [226].

2. Calculate nonlinear advective force terms in each fluid separately using high order, upwind, slope limited discretization. The liquid indium is discretized using a Godunov second-order upwind predictor-corrector step [99]. See Appendix

(B.3) for a fuller description.

3. Compute the viscous forces. Use the Crank-Nicholson [223] and Runge-Kutta methods. The new velocity field is continuous across the $\phi = 0$ surface. Surface tension is included as a body force, as in [227]. Curvature is calculated directly from volume fractions.

4. Cell centered forces are interpolated to face centered forces

5. Pressure and velocity fields are updated and implicitly projected via Eq. (4.17).

$$\begin{aligned} \nabla \cdot \frac{\nabla p}{\rho} &= \nabla \cdot v \\ u &= v - \frac{\nabla p}{\rho} \end{aligned} \tag{4.17}$$

   The new velocity field satisfies the continuity condition and the new pressure satisfies the appropriate jump conditions [p]=g and $\left[\frac{1}{\rho}\nabla p \cdot \overrightarrow{n}\right]$=h. The Cartesian-grid approach is used to approximate the divergence operator.

6. The liquid velocity is extrapolated in a narrow band around the $\phi = 0$ interface.

7. The face centered velocity is interpolated back to cell centered velocities.

8. Finally, the cell centered pressure gradient term is updated.

Reinitialization of level set distance

To evolve a surface requires the continual adjustment of the level set field on all grid points, not solely those on the surface. The convection implied by Eq. (4.7) allows the nonzero ϕ values to move with differing velocities than the $\phi = 0$ interface [173]. If unequal ϕ propagation occurs, the distance field will become distorted. Consequently, to prevent the level set gradient from becoming too flat or too step

near the surface, at each time step the ϕ values near the surface need to be changed. Therefore, it is necessary to reinitialize ϕ via Eq. (4.18) in order for it to be a signed distance function analogous to ι. To minimize computational load, ϕ was only solved in a bandwidth of ε around the interface and for a time τ_{LS} that is limited by the fastest particle traveling a distance ε in Eq. (4.18).

$$\frac{\partial \phi}{\partial \tau_{LS}} + \overleftrightarrow{\text{sgn}(\phi)} \{|\nabla \phi| - 1\} = 0 \tag{4.18}$$

The one dimensional spread signum function $\overleftrightarrow{\text{sgn}(\phi)}$ is approximated numerically as Eq. (4.19). The function replaced the discontinuity in $\text{sgn}(\phi)$ at $\phi = 0$ with a smooth transition from -1 to 1.

$$\overleftrightarrow{\text{sgn}(\phi)} = \frac{\phi}{\sqrt{\phi^2 + (\Delta x)^2}} \tag{4.19}$$

If surface distance renormalization is not performed, then Eq. (4.14) is no longer guaranteed to be an exact representation as the surface evolves. Without a constrained gradient operator, a curved surface could overlap other level set values and the interface identification capabilities of Eq. (4.7) would become invalid.

To solve for the updated level set field, several methods have been proposed in the literature. Distance renormalizations in the narrow band can be formed in O(N log N) iterations [190]. Alternatively, a locally second order but global first order accurate approach with a very low truncation error was proposed in [206]. Finally, a fast sweeping method from [249] appears to have O(N) complexity while also being first order accurate. The method used for the reconstructed interface in cell (i,j) is decided by Eq. (4.20).

$$\phi_{i,j}^{n,R}(r, z) = a_{i,j}(r - r_i) + b_{i,j}(z - z_j) + c_{i,j} \tag{4.20}$$

The coefficients $a_{i,j}$, $b_{i,j}$ and $c_{i,j}$ are chosen so that the interface represents the best fit line for the piece of the zero level set passing through that cell [227]. In other words, a, b and c minimize the error of Eq. (4.21).

$$E_{i,j} = \int_{r_{i-1/2}}^{r_{i+1/2}} \int_{z_{j-1/2}}^{z_{j+1/2}} H'(\phi)(\phi - a_{i,j}(r - r_i) - b_{i,j}(z - z_j) - c_{i,j})^2 \tag{4.21}$$

Timestep

The timestep Δt at time t^n is determined by restrictions due to the CFL condition, surface tension, and gravity [224]. While the simulation is run without gravity, it can be included through the last term in Eq. (4.22).

$$\Delta t < \min_{i,j} \left(\frac{1}{2} \frac{\Delta x}{|U^n|}, \frac{1}{2} \Delta x^{3/2} \sqrt{\frac{\rho^L}{8\pi\sigma}}, \frac{1}{2} \frac{2\Delta x}{|U^n| + \sqrt{(U^n)^2 + 4g\Delta x}} \right) \tag{4.22}$$

The stability condition regarding gravity was determined through the inequality:

$$(U + \Delta t g)\Delta t < \Delta x \tag{4.23}$$

The relation for surface tension is taken from [32, 81], with other stability references at [7, 164].

4.2.3 Numerical errors

The numerical approaches presented simulate interface advection and convection. However, the detailed numerics associated with modeling the motion of the surface often cause errors in calculating the $\phi = 0$ location. In this subsection, modeling errors are identified and then solutions are presented. Errors can arise for many reasons in a level set code. Truncation, extrapolation, uneven surfaces and incorrect reference locations are among sources of error.

Surface definition not restricted to grid nodes If the velocity field is only defined on the interface, movement of the surface using Eq. (4.7) is difficult since the grid nodes do not necessarily intersect the surface. Frequently, the surface will not pass through any edges of the computational domain. Therefore, the velocity field $\overrightarrow{v}$ needs to be defined away from the interface. This involves extending the field normal to the surface. If the bandwidth of the velocity definition is increased to $\approx 5 \cdot \min(\Delta x, \Delta y)$, then the computational effort is minimized while at the same time preserving the resolution of the interface.

Irregular surface elements form over time A surface possesses an infinite number of points. These must be discretized into a finite span of nodes upon which the velocity field will act. Even simple velocity fields can cause large distortions of boundary elements via uneven acceleration on individual surface segments. The resulting surface element deformations rapidly reduce the accuracy of the method. The discretization of the surface will become less accurate and the resulting solution would require extensive surface patching and smoothing to correct. Figure (4.3) illustrates both these types of potential errors. The blue circles do not pass through the 'x' grid nodes, nor are they evenly spaced apart.

Degradation of signed distance function As pointed out in Sec. (4.2.2), if the signed distance function is not modified and reinitialized, it no longer measures the distance from the surface. The curvature and gradient of the surface would then grow increasingly skewed over time. After each time step, ϕ must be re-constrained via Eq. (4.14) or the calculated velocity normal will be increasingly in error.

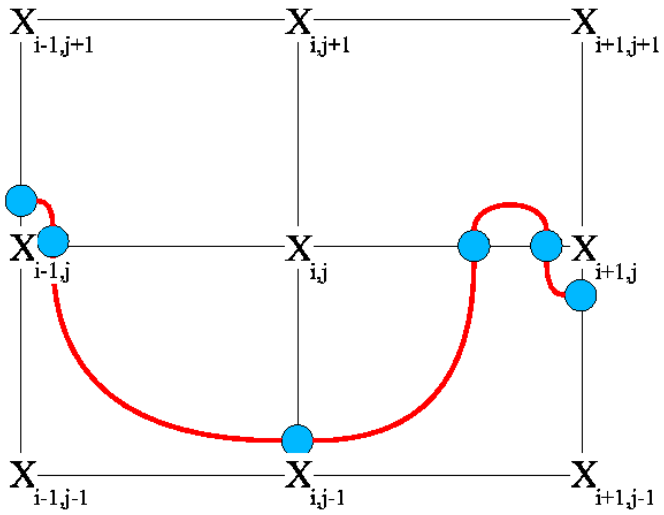

Figure 4.3: Level set node potential errors from intersection away from the nodes and uneven spacing

Detachment of surface If a particular node is defined solely as being on the surface of element A, its detachment should redefine it as a member of a newly formed element B. In a similar manner, intersections of discrete elements should form a single new border. However, it is frequently seen that computations do not reassign node membership in the $\Gamma(t) \in \partial\Omega_i$ list. Therefore, the listing of points belonging to a particular shape must be updated each time step.

To reduce the impact of the above sources of error, a volume of fluid and interpolation scheme are introduced. These additions provide second order spatial accuracy by locating and adjusting the surface with greater resolution.

Volume of fluid

As introduced in Sec. (4.2.2), to reduce the surface location drift over time the interface is represented with second order spatial accuracy through the CLSVOF method. In addition to solving the level set equation, the volume-of-fluid function V_F is computed [222, 138],

$$\frac{\partial V_F}{\partial t} + \overrightarrow{v} \cdot \nabla V_F = 0 \tag{4.24}$$

where the net volume of fluid is conserved both locally and globally. Interfaces are tracked in this volume-of-fluid method by locally calculating the flux of volume in or out of a given computational cell. If a cell has no fluid, $V_F = 0$; totally filled grid points have $V_F = 1$. Interface ('mixed') cells have $V_F \in (0, 1)$ [194]. The cell (i,j) fluid volume fractions are determined by averaging the interior spot fluid presence via Eq. (4.25).

$$V_F(x, y) = \begin{cases} 1 & \text{if fluid at } (x, y) \\ 0 & \text{if no fluid at } (x, y) \end{cases} \tag{4.25}$$

These local fluid values are combined with H, the Heaviside function evaluated in Eq. (4.26). A graphical representation of fractionally filled cells is given in Fig. (4.4).

$$V_{F_{ij}} = \frac{1}{\Delta x \Delta y} \int_i \int_j V_F(x, y)\, dx\, dy \tag{4.26}$$

Using the earlier descriptions of level sets, VOF builds on prior two- and three-dimensional efforts of interface migration by Sussman [228]. The level set and VOF are coupled as follows:

1. The normals are determined from calculating Eq. (4.7) over time.

2. The level set truncates the volume fractions, correcting truncation error located more than one grid cell away from the interface.

3. On a cell to cell basis, mass is conserved by combining the volume fraction values with the slopes of the level set surface. Figure (4.5) displays this linkage,

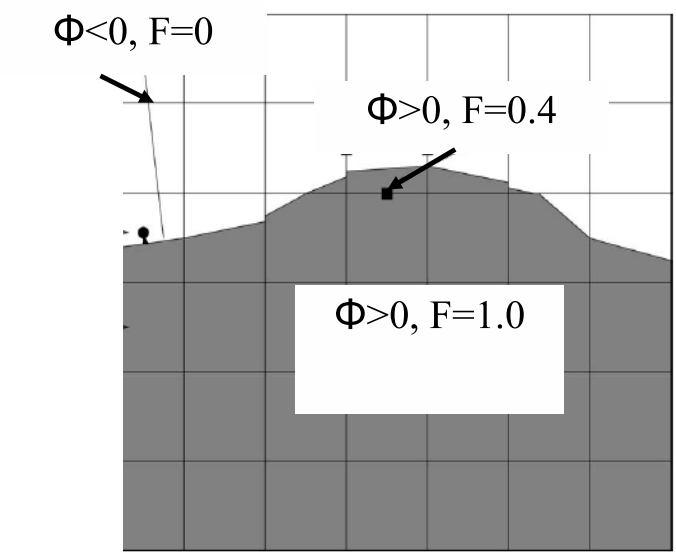

Figure 4.4: Volume of fluid and level set cell values

where the linear reconstructed interface combines the area $V_{F_{ij}}$ and the slope $n = \frac{\nabla\phi}{|\nabla\phi|}$.

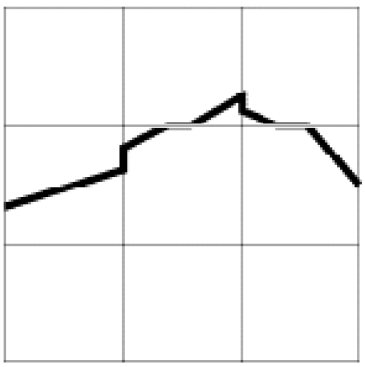

Figure 4.5: CLSVOF grid combination [224]

4. Volume fractions then express interfacial curvature to second order accuracy. $V_{F_{i+1,j}} - V_{F_{i-1,j}}/2\Delta x$ is a second-order approximation to the slope h' and $V_{F_{i+1,j}} - 2V_{F_{i,j}} + V_{F_{i-1,j}}/\Delta x^2$ is second order for h".

Hamilton-Jacobi essentially non-oscillatory (HJ-ENO) schemes

In addition to VOF corrections, higher-order approximations of surface convection can also reduce location error. A more accurate calculation of the surface can be achieved through implementation of Hamilton-Jacobi essentially non-oscillatory (HJ-ENO) polynomials.

Once ϕ and $\overrightarrow{v}$ are defined at every point in the smoothing region near the interface, the surface can be marched forward in time from $\phi\left(t^n\right) = \phi^n$ to $\phi\left(t^{n+1}\right)$ where $t^{n+1} = t^n + \Delta t$. Using the explicit first-order forward Euler method, Eq. (4.7) can be numerically computed as Eq. (4.27).

$$\phi^{n+1} = \phi^n - \Delta t \left[\overrightarrow{v^n} \cdot \nabla \phi^n\right] \tag{4.27}$$

Considering Eq. (4.27) in one dimension at x_i gives Eq. (4.28). If $u_i > 0$, then the method of characteristics points towards the left-hand element to determine ϕ_x at the end of the time step. Conversely, if $u_i < 0$ the situation is reversed and the right-hand characteristics should be used.

$$\phi_i^{n+1} = \phi_i^n - \Delta t \left[u_i^n \left(\frac{d\phi}{dx}\right)_i^n\right] \tag{4.28}$$

A necessary physical condition for stability of Eq. (4.27) is achieved by restricting the time step in a manner such that a particle cannot travel through more than one grid cell in a single time interval. This is referred to as the CFL condition, given by Eq. (4.29).

$$\Delta t < \frac{\Delta x}{\max|u|} \tag{4.29}$$

Higher order accurate methods are achievable using ENO, giving a better approx-

imation for the left or right characteristics [187]. Under this second-order scheme, the distance between the characteristics and ϕ_x is computed using the smoothest possible polynomial interpolants $P_{[x]}$ for ϕ_x where $\phi\,(\overrightarrow{x}) = P_0\,(\overrightarrow{x}) + P_1\,(\overrightarrow{x}) + P_2\,(\overrightarrow{x}) + P_3\,(\overrightarrow{x})$. Moving to third order accuracy requires a shift from a three- to a five-point stencil. A weighted version of ENO, WENO, uses convex combinations of the approximations, by reducing the input of any points that interpolate across a discontinuity. This weighting change improves the surface approximation of the characteristic to fifth-order accurate [67].

Convergence studies and grid refinement

Multiple refinement studies were performed, with the problem of surface tension-driven drop oscillations being presented. According to the linearized results of [136], Section 275, the position of a drop interface can be described via Eq. (4.30),

$$R(\theta, t) = a + \epsilon P_n(\cos\theta)(\sin(\omega_n t + \pi/2)) \tag{4.30}$$

where P_n is the Legendre polynomial of order n=2, the offset is a=1, the scaling $\epsilon = 0.05$ and the driving frequency ω_n is described by Eq. (4.31).

$$\omega_n^2 = \sigma \frac{n(n-1)(n+1)(n+2)}{a^3(\rho_L(n+1) + \rho_G n)} \tag{4.31}$$

Figure (4.6) shows the perturbed surface R($\frac{\pi}{2}$,t) when ρ_L=1, ρ_G=0, σ=0.5. Grid sizes vary from 32x32 to 256x256, with a time step of 7×10^{-4} and symmetry boundary conditions imposed at r=0 and z=0 [224]. Grid convergence occurs above 128x128 density.

The volume loss over time for the level sets versus grid density is shown in Fig. (4.7). Convergence is demonstrated above the 256x384 node level, at a cell length of

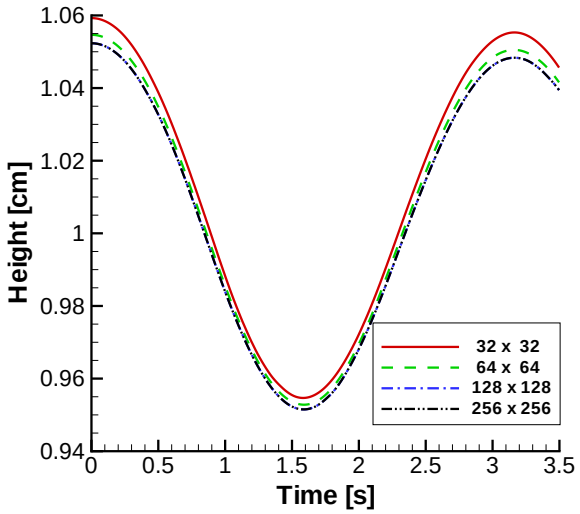

Figure 4.6: Surface tension driven droplet oscillations

12 μm. The instantaneous calculation of the shape area with varying grid densities in Fig. (4.8) demonstrates the method's second-order accuracy as the error drops two decades for each order of magnitude increase in the number of nodes.

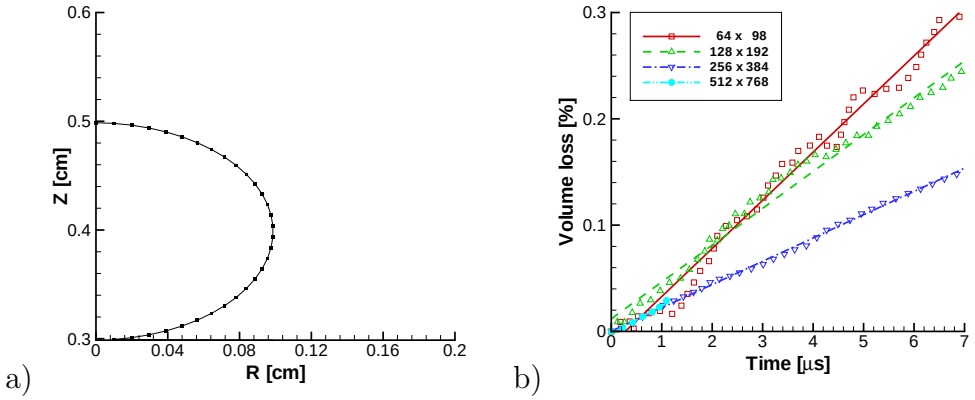

a) b)

Figure 4.7: Volume loss over time of a) a semicircle versus b) level set grid density

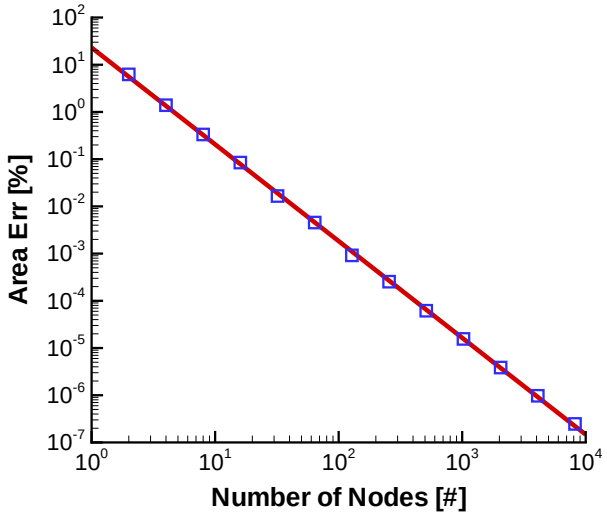

Figure 4.8: Area calculation error versus number of grid nodes. With a log/log slope of two, it demonstrates a second order method.

4.2.4 Summary of level set method

The operation of level sets was outlined with its governing equations, numerical calculation issues were raised that could potentially introduce great error into the algorithm and then several potential solutions to those issues were presented. Level set theory combined with a volume of fluid approach provided a mass-conserving method to model the formation and evolution of an interface between two elements. This work built on prior two- and three- dimensional efforts of interface migration by Sussman [228]. The accurate location of the interface is vital to calculate the surface curvature force component ($\sigma\kappa$) presented in Sec. (4.1).

However, while the CLSVOF method is able to simulate detaching and re-attaching droplets on a surface, it can not provide a calculation of the magnitude of the normal electric field E_n in Eq. (4.3). A proposed algorithm for determining this electrostatic force is the boundary element method (BEM).

4.3 Boundary element methods

A complementary technique to level sets for surface simulation is the boundary element method (BEM). It allows analysis of the behaviors of mechanical systems and engineering structures that are subjected to external loading through heat, mass or inhomogeneous boundary conditions [125, 104]. This approach mimics the more common finite element method, except that boundary elements span only the boundaries of the problem instead of the entire volume. Figure (4.9) displays examples of how the BEM places nodes around a notched plate and a sphere.

The BEM's nodal placement only on the edges results in faster computation due to fewer total nodes, avoidance of adaptive meshing, easier design changes, and accurate calculation of gradients and infinite domains. Multiple commercial software packages use the boundary element method and can include charged particles, thereby allowing for electrostatic potential and electric field solutions in otherwise untenable complex geometries [120, 209, 131]. However, a major potential limitation of the approach is that the points have to be listed in order. Each location has to be identified as well as its left and right neighbors.

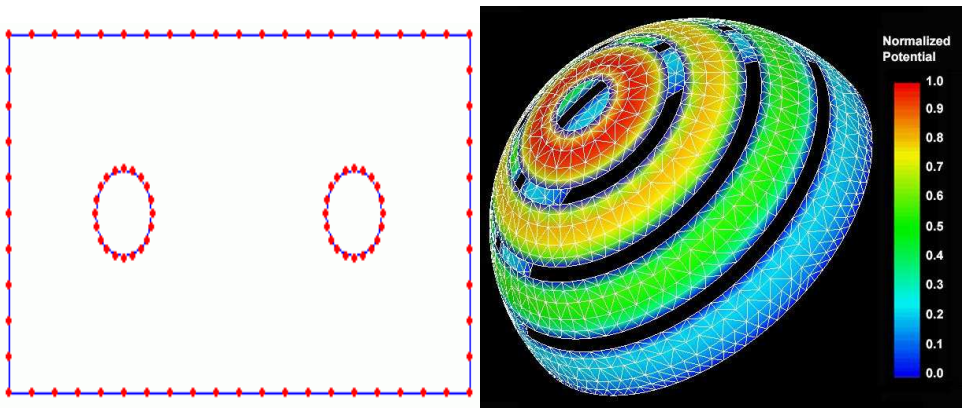

(a) Notched plate (b) Sphere

Figure 4.9: Boundary elements on various surfaces [95]

For example, consider Poisson's equation:

$$\nabla^2 U(\overline{x}) = -\frac{\breve{\rho}}{\epsilon_0} \tag{4.32}$$

where $\breve{\rho}$ is the charge density and U is the potential. If electrostatic problems always involve discrete distributions of charge with infinite volumes, the general solution of the potential given by Eq. (4.33) is the most straightforward solution. It describes the scalar potential at interior location x using a volumetric charge density integral.

$$U(x) = \frac{1}{4\pi\epsilon_0} \int \frac{\breve{\rho}(x')}{|x - x'|} \mathrm{d}^3 x' \tag{4.33}$$

However, solving for the electrical potential in $\Re^3$ means there are finite volumes with distributed charge. In practice, to handle these conditions requires a different perspective, such as solving Poisson's equation on arbitrary surfaces using Green's functions. The following subsections discuss how to numerically calculate U(x) with varying surfaces and boundary types.

4.3.1 Potential calculation from Green's functions

To expand Eq. (4.33) and allow a potential calculation at any point using just the boundary nodes requires Green's functions. These mathematical constructs belong to the class of functions identified as Fredholm or Volterra integrals of the first kind. Here, K is an integral kernel [270] and f is the unknown function to be solved for [11]. The integrals are of the form

$$g(\alpha) = \int_a^b f(t) K(\alpha, t)\, \mathrm{d}t \tag{4.34}$$

and provide a method of solving inhomogeneous differential equations. The term $g(\alpha)$ serves an analogous role in partial differential equations that Fourier analysis does

in the solution of ordinary differential equations [11, 266]. The exact form depends on the differential equation, the body shape, and the type of boundary conditions.

The most useful form of the Green's functions for this model defines $\mathrm{G}(\overline{x}\,|\,\overline{x}_0)$ as the delta gradient for the Laplace operator. Therefore, this is the solution to

$$\Delta G = \delta(\overline{x} - \overline{x}_0) \tag{4.35}$$

where $\overline{x} = (x,\, y)$ is a boundary point and $\overline{x}_0$ is a point on the interior of the domain. In 2D, the Green's function becomes Eq. (4.36).

$$G = -\tfrac{1}{4\pi} \ln\left\{(x_0 - x)^2 + (y_0 - y)^2\right\} \tag{4.36}$$

Green's identities

Green's functions are used as a component in determining the potential. The first steps to form these solutions of Eq. (4.34) invokes a vector calculus identity called the divergence theorem. Given by Eq. (4.37), this theorem applies to any continuous vector field R defined in volume V and bounded by the closed surface S.

$$\int_V \nabla \cdot R \,\mathrm{d}^3x = \oint_S R \cdot \overrightarrow{n} \,\mathrm{d}a \tag{4.37}$$

Let $R = \Gamma\nabla\psi$, where Γ and ψ are arbitrary scalar fields. Now,

$$\nabla \cdot (\Gamma\nabla\psi) = \Gamma\nabla^2\psi + \nabla\Gamma \cdot \nabla\psi \tag{4.38}$$

and $\Gamma\nabla\psi \cdot \overrightarrow{n} \triangleq \Gamma\partial_{\overrightarrow{n}}\psi$, where $\overrightarrow{n}$ is the outward surface derivative acting on surface S from volume V. Substituting these field definitions into Eq. (4.37), leads to Green's 1st identity.

$$\int_V \left(\Gamma\nabla^2\psi + \nabla\Gamma \cdot \nabla\psi\right) \,\mathrm{d}^3x = \oint_S \Gamma \frac{\partial\psi}{\partial n} \,\mathrm{d}a \tag{4.39}$$

Upon reversal of the Γ and ψ terms, subtraction of it from Eq. (4.39) leads to the cancellation of $\nabla\Gamma \cdot \nabla\psi$. This results in Green's 2nd identity, or Green's theorem [121].

$$\int_V \left(\Gamma\nabla^2\psi - \psi\nabla^2\Gamma\right) \mathrm{d}^3x = \oint_S \left[\Gamma\frac{\partial\psi}{\partial n} - \psi\frac{\partial\Gamma}{\partial n}\right] \mathrm{d}a \tag{4.40}$$

Green's theorem for electrostatics

Using the result of Green's theorem, Eq. (4.40), and replacing Γ by the Green's function G and ψ by the potential U gives Eq. (4.41).

$$U(x) = \frac{1}{4\pi\epsilon_0}\int_V \frac{\breve{\rho}(x')}{|x - x'|}\,\mathrm{d}^3x' + \frac{1}{4\pi}\oint_S \left[G(x,x')\frac{\partial U}{\partial n'} - U(x')\frac{\partial G(x,x')}{\partial n'}\right] \mathrm{d}a' \tag{4.41}$$

Since a perfect conductor has no internal charge, the charge density $\breve{\rho}(\overline{x}_0) = 0$ and the potential at any point can be calculated from the boundary flux and potential conditions alone. For Dirichlet boundary conditions the surface S_D is constrained by

$$U_D(x,x') = 0;\ x \in S_D \tag{4.42}$$

and the solution of the potential field in an arbitrary shape [121] becomes Eq. (4.43).

$$U(x) = \frac{1}{4\pi\epsilon_0}\int_V \rho(x')G_D(x,x')\,\mathrm{d}^3x' + \frac{1}{4\pi}\oint_S G_D(x,x')\frac{\partial U_D}{\partial n'}\,\mathrm{d}a' \tag{4.43}$$

Laplacian description

There is some additional difficulty for the Neumann boundary conditions. Unless some of the defined surfaces are relatively distant from the droplet, there is an extra term in the expansion of Eq. (4.41). The difficulties are caused by the nonzero potential flux at singularities and are established as follows.

Consider the Laplacian of the distance relationship $G = \frac{1}{r}$ where $r = |\overline{x} - \overline{x}'|$. Then for $r \neq 0$, it is a well-behaved continuous function and $\nabla^2(1/r) = 0$. This is seen by:

$$\nabla^2 G = \nabla^2 \left(\frac{1}{r}\right) = \frac{1}{r^2}\frac{\partial}{\partial r}\left(r^2 \frac{\partial \left[\frac{1}{r}\right]}{\partial r}\right) = \frac{1}{r^2}\frac{\partial}{\partial r}(-1) = 0 \tag{4.44}$$

Using the divergence theorem again, consider the Laplacian of the integral over $\Re^3$ [112].

$$\nabla^2 \int_V \frac{1}{|x - x'|}\,\mathrm{d}^3x' = \nabla \cdot \int \nabla \frac{1}{|x - x'|}\,\mathrm{d}^3x' \tag{4.45}$$

Then, Gauss' Law finds the volume flux relationship for the integral.

$$\int \nabla \cdot G(x, x')\,\mathrm{d}^3x' = \oint_S G(x, x') \cdot dS = -4\pi \int_V \mathrm{d}^3x' \tag{4.46}$$

Therefore, the formal closure for the distance Laplacian with a desired volume including the $r = 0$ limit is given by Eq. (4.47).

$$\nabla \cdot \int \nabla \cdot G(x, x')\,\mathrm{d}^3x' = \nabla \cdot (-4\pi \int_V \mathrm{d}^3x') = -4\pi\delta(x - x') \tag{4.47}$$

Implication for Neumann boundary conditions

The simplest boundary choice for a Neumann fixed flux surface length S_N is given by Eq. (4.48).

$$\frac{\partial U(x, x')}{\partial n'} = 0;\ x \in S_N \tag{4.48}$$

This option makes the second term vanish in Eq. (4.41). But, applying Gauss' theory as in Eq. (4.46) gives

$$\frac{1}{4\pi\epsilon_0}\left[\int_V \rho(x')G_D(x, x')\,\mathrm{d}^3x' - \oint_S U(x')\frac{\partial G(x, x')}{\partial n'}\,\mathrm{d}a'\right] = -4\pi \tag{4.49}$$

Consequently, the least complex allowable boundary condition is given by Eq. (4.50),

$$\frac{\partial U(x,x')}{\partial n'} = -\frac{4\pi}{S_N};\ x \in S_N \tag{4.50}$$

and leads to the resulting potential solution for fixed flux.

$$U_{S_N}(x) = < \frac{\partial U(x,x')}{\partial n'} >_{S_N} + \frac{1}{4\pi\epsilon_0}\left[\int_V \rho(x')G_N(x,x')\,\mathrm{d}^3x' - \oint_S U(x')\frac{\partial G(x,x')}{\partial n'}\,\mathrm{d}a'\right]' \tag{4.51}$$

$< \frac{\partial U(x,x')}{\partial n'} >_{S_N}$ is the average value of the potential flux over the entire Neumann surface. If the boundaries are placed distantly, that is $\lim_{r\to\infty} G(r) = 0$, then the boundary length S_N increases without bound and the restriction of Eq. (4.50) reduces to 0. This changes the problem back into a homogeneous solution. Assuming a finite boundary where $S_N \gg S_{D,droplet}$ yields $\frac{\partial U(x,x')}{\partial n'} \to 0$ and the problem reduces to the intended homogeneous differential equation with a less than 0.1% approximation error. The error magnitude upper limit is determined from a test case examination of the non-normal flux induced on an uncharged wall from a droplet 20 radii away.

Definition of potential

The result of taking the limits of the single and double layered potential [74] gives the boundary integral formulation for Laplace's equation from the inside of the domain, Eq. (4.52).

$$\frac{1}{2}U(\overline{x}_0) = \oint_{\partial\Omega} U(\overline{x})\partial_{\overrightarrow{n}}G(\overline{x}|\overline{x}_0)\,\mathrm{d}s - \oint_{\partial\Omega} \partial_{\overrightarrow{n}}U(\overline{x})G(\overline{x}|\overline{x}_0)\,\mathrm{d}s \tag{4.52}$$

The normal derivative of Eq. (4.52) is

$$\frac{\partial U(\overline{x}_0)}{\partial n} = \oint_{\Omega}\left(U(\overline{x})\frac{\partial^2 G(\overline{x}|\overline{x}_0)}{\partial_{\overrightarrow{n},x}\partial_{\overrightarrow{n},x_0}} - \frac{\partial U(\overline{x})}{\partial_{\overrightarrow{n},x}}\frac{\partial G(\overline{x}|\overline{x}_0)}{\partial_{\overrightarrow{n},x}}\right)\,\mathrm{d}s$$

where the surface $\partial\Omega$ consists of an arbitrary combination of $U(\overline{x})$ along Dirichlet ($\partial\Omega_D$) or $\partial_{\overrightarrow{n}}V(\overline{x})$ along Neumann ($\partial\Omega_N$) boundary conditions, with $\partial\Omega = \partial\Omega_D \bigcup \partial\Omega_N$.

4.3.2 Numerical discretization of the problem

Defining all the surface boundaries with a given Dirichlet potential 'f' or Neumann flux 'g'

$$U|_{\partial\Omega} = f \text{ or } \nabla U|_{\partial\Omega} \cdot \overrightarrow{n} = g,\ \overline{x} \in \Omega \tag{4.53}$$

and treating the potential and flux of each panel as being a C^0 constant over the N_k panels along surface ds gives the following approximation.

$$\begin{aligned} \oint_{\partial\Omega_k} U(\overline{x})\partial_n G(\overline{x}|\overline{x}_0)\,\mathrm{d}s &\doteq \textstyle\sum_{i=1}^{N_k} U(\overline{x}_i) \oint_{\partial\Omega_i} \partial_n G(\overline{x}|\overline{x}_0)\,\mathrm{d}s \\ \oint_{\partial\Omega_k} \partial_{\overrightarrow{n}} U(\overline{x})G(\overline{x}|\overline{x}_0)\,\mathrm{d}s &\doteq \textstyle\sum_{i=1}^{N_k} \partial_{\overrightarrow{n}} U(\overline{x}_i) \oint_{\partial\Omega_i} G(\overline{x}|\overline{x}_0)\,\mathrm{d}s \end{aligned} \tag{4.54}$$

Inserting Eq. (4.54) into Eq. (4.52) gives the full descriptive integrals for both boundary types. A sample series of two panels is presented in Eqs. (4.55). The first term represents a Dirichlet boundary condition and the second a Neumann one. The terms $\frac{1}{2}U(\overline{x}_0)$ and $\frac{\partial U(\overline{x}_1)}{\partial n_1}$ in the expansion arise from the effect of a panel on itself.

$$\begin{aligned} U(\overline{x}_0) = &\oint_{\partial\Omega_D} U(\overline{x})\partial_{n,0} G(\overline{x}|\overline{x}_0)\,\mathrm{d}s + \oint_{\partial\Omega_N} \partial_{\overrightarrow{n},0} U(\overline{x})G(\overline{x}|\overline{x}_0)\,\mathrm{d}s + \tfrac{1}{2}U(\overline{x}_0) \\ \tfrac{\partial U(\overline{x}_1)}{\partial n_1} = &\oint_{\partial\Omega_D} U(\overline{x})\partial^2_{\overrightarrow{n},1} G(\overline{x}|\overline{x}_1)\,\mathrm{d}s + \oint_{\partial\Omega_N} \partial_{\overrightarrow{n},1} U(\overline{x})\partial_{\overrightarrow{n},1} G(\overline{x}|\overline{x}_1)\,\mathrm{d}s + \tfrac{1}{2}\tfrac{\partial U(\overline{x}_1)}{\partial n_1} \end{aligned} \tag{4.55}$$

If $\overline{x}$ is on the boundary, then using Eq. (4.52) calculates the potential at interior point $\overline{x}_0$ as Eq. (4.56). Note that the flux on Dirichlet and the potential on Neumann boundaries is unknown and needs to be solved, that is the $\partial_{\overrightarrow{n}}U(\overline{x})|_{\partial\Omega_D}$ and $U(\overline{x})|_{\partial\Omega_N}$ terms.

$$\begin{aligned}\tfrac{1}{2}U(\overline{x}_0) = \quad & \textstyle\sum_{i=1}^{N_D} U(\overline{x}_i) \oint_{\partial\Omega_{D,i}} \partial_{n,0} G(\overline{x}_i|\overline{x}_0)\,\mathrm{d}s + \sum_{j=1}^{N_N} U(\overline{x}_j) \oint_{\partial\Omega_{N,j}} \partial_{\overrightarrow{n},j} G(\overline{x}_j|\overline{x}_0)\,\mathrm{d}s \\ & + \textstyle\sum_{i=1}^{N_D} \partial_{\overrightarrow{n},i} U(\overline{x}_i) \oint_{\partial\Omega_{D,i}} G(\overline{x}_i|\overline{x}_0)\,\mathrm{d}s + \sum_{j=1}^{N_N} \partial_{\overrightarrow{n},j} U(\overline{x}_j) \oint_{\partial\Omega_{N,j}} G(\overline{x}_j|\overline{x}_0)\,\mathrm{d}s\end{aligned} \tag{4.56}$$

Using the prior discretization and by collecting terms, the matrix can be described as in Eq. (4.57) and mathematically as Eq. (4.58).

$$\begin{bmatrix} \text{distance from one} \\ \text{panel to another} \end{bmatrix} \begin{bmatrix} \text{unknown Dirichlet and} \\ \text{Neumann BC} \end{bmatrix} = \begin{bmatrix} \text{known Neumann and} \\ \text{Dirichlet BC} \end{bmatrix} \tag{4.57}$$

$$\left[\begin{array}{cc} a_{1,1}..a_{1,N_D} & b_{1,1}..b_{1,N_N} \\ \hline a_{N_D,1}..a_{N_D,N_D} & b_{N_D,1}..b_{N_D,N_N} \\ \hline c_{1,1}..c_{1,N_D} & d_{1,1}..d_{1,N_N} \\ c_{N_N,1}..c_{N_N,N_D} & d_{N_N,1}..d_{N_N,N_N} \end{array}\right] \begin{bmatrix} \partial_{\overrightarrow{n},1} U(\overline{x}_{1,1}) \\ .. \\ \partial_{\overrightarrow{n},1} U(\overline{x}_{1,N_D}) \\ U(\overline{x}_{2,1}) \\ .. \\ U(\overline{x}_{2,N_N}) \end{bmatrix} = \begin{bmatrix} \breve{\gamma}(\overline{x}_{1,1}) \\ .. \\ \breve{\gamma}(\overline{x}_{1,N_D}) \\ \alpha_N(\overline{x}_{2,1}) \\ .. \\ \alpha_N(\overline{x}_{2,N_N}) \end{bmatrix} \tag{4.58}$$

The matrix values are defined by Eq. (4.59). Here, the $a_{i,j}$ represent the inter-panel distances between Dirichlet-Dirichlet types of boundaries, $b_{i,j}$ are the Dirichlet-Neumann distances, $c_{i,j}$ are the Neumann-Dirichlet distances and $d_{i,j}$ describe the Neumann-Neumann distances. The known right hand side potentials $\breve{\gamma}$ and fluxes α_N are also shown.

$$
\begin{aligned}
a_{i,j} = &\quad \int_{\partial\Omega_{D,j}} G(\overline{x}_{1,i}|\overline{x}_j)\,\mathrm{d}s \\
b_{i,j} = &\quad \int_{\partial\Omega_{N,j}} \partial_{\overrightarrow{n_j}} G(\overline{x}_{1,i}|\overline{x}_j)\,\mathrm{d}s \\
c_{i,j} = &\quad \int_{\partial\Omega_{D,j}} \partial_{\overrightarrow{n_j}} G(\overline{x}_{2,i}|\overline{x}_j)\,\mathrm{d}s \\
d_{i,j} = &\quad \int_{\partial\Omega_{N,j}} \partial^2_{\overrightarrow{n_j}} G(\overline{x}_{2,i}|\overline{x}_j)\,\mathrm{d}s \\
\breve{\gamma}(\overline{x}_{1,i}) = &\quad U(\overline{x}_1)\left[\tfrac{1}{2} - \int_{\partial\Omega_{D,j}} \partial_{\overrightarrow{n_j}} G(\overline{x}_{1,i}|\overline{x}_j)\,\mathrm{d}s\right] \\
\alpha_N(\overline{x}_{2,i}) = &\quad \tfrac{\partial U(\overline{x}_2)}{\partial n_1}\left[\tfrac{1}{2} - \int_{\partial\Omega_{N,j}} \partial_{\overrightarrow{n_j}} G(\overline{x}_{2,i}|\overline{x}_j)\,\mathrm{d}s\right]
\end{aligned}
\tag{4.59}
$$

The actual boundaries do not have to be all Dirichlet and then all Neumann types as described above; the boundary conditions can alternate back and forth arbitrarily. The potential at any point in the domain is thus given by summing the contributions from fixed, diverse boundaries types, as in Eq. (4.56).

4.3.3 Calculating the electrostatic force

One of the main advantages of the BEM formulation of Eq. (4.58) is the direct computation of the interface force. However, a critical limitation for electrostatics using the boundary element approach is that the normal electric field has to be much larger than the tangential one, or $E_n \gg E_t$. This is due to the assumption that the product of the normal electric field and area equals the entire flux. As noted in Appendix (C), unless the conductivity of the material is large (on the order of 10,000 S/m), the drift velocity will not be much smaller than the conduction velocity.

Solving for the $\partial_{\overrightarrow{n}} V(\overline{x}_1)|_{\partial\Omega_D}$ term of the normalized test shape in Fig. (4.10a) provides the normal component of the electric field (E_n) for points in the interval $(x, y) \in [-0.05, 0.05] \times [0.7, 0.75]$, as seen in Fig. (4.10b). To calculate the electrostatic force term qE in the model, consider the droplets' position. Gauss' Law states that the total flux of the electric field through an element dA is given by the sum

of the electric field's surface normals; this is shown in Eq. (4.60) where the flux is $\beta = 1$ unit into the page, along panel length L.

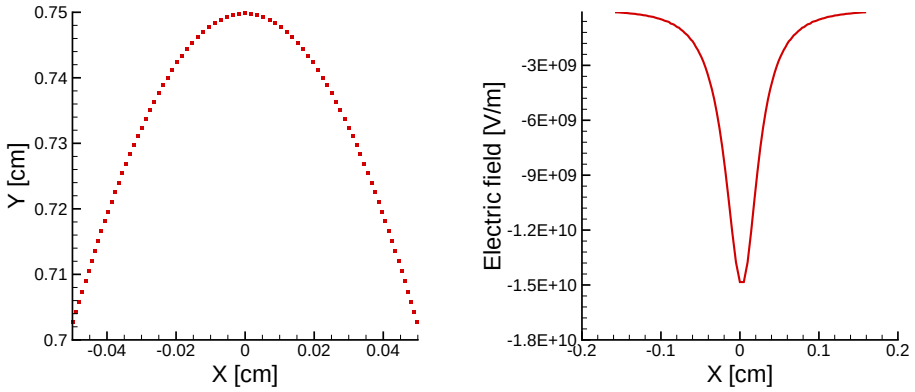

(a) Fluid surface boundary nodes (b) Normal electric field at the surface

Figure 4.10: Boundary nodes and normal electric field along a curved surface

$$UL\left[\frac{N \cdot m^2}{C}\right] = \int E\, dA = \oint \vec{E} \cdot \vec{n}\, dS = \frac{q}{\epsilon_0} \tag{4.60}$$

By drawing a box around each computational panel, the earlier assumption of a perfect conductor now implies that all electric flux is normal to the surface so $\vec{E} \equiv \vec{E}_n$ and there is no tangential electric field. The panel charge is given by Eq. (4.61).

$$q = \epsilon_0 L E_n \beta \tag{4.61}$$

As a result, the total electrostatic force experienced by the panel is given by Eq. (4.62).

$$F_E\,[N] = qE_n = \epsilon_0 L E_n^2 \tag{4.62}$$

As stated in Sec. (4.1), the primary goal for the BEM is to solve for qE_n. The

electrostatic solution is computed independent of a surrounding volume grid. The calculation method for the electrical force holds for all non-crossing complex geometries, including the nesting of multiple shapes at different potentials. The model is capable of determining electrostatic surface forces on a needle FEEP.

4.3.4 Determining droplet potential

After detaching, the droplets need to have the appropriate boundary conditions. Since they are treated as perfect conductors, there is no internal electric field and thus no change in potential. Therefore, the entire droplet **must** have the same electrostatic potential, regardless of shape. While a constant electric field (Euler) limiter could act as a *de facto* potential stabilizer for circular drops, it does **not** provide a constant potential for arbitrarily shaped surfaces. Instead, an incorrect force is computed on the panels, and if simulated this way, any pretense of physicality is abandoned.

As a result, the correct mathematical description of droplets has to be a fixed Dirichlet condition ($U(\overline{x}) = c_1$). One way to do so is to compute the charge distribution self-consistently through the use of variational capacitances. However, due to the fact that a full capacitance analysis needs to be rerun each timestep, there is a substantial degradation in numerical efficiency. Instead, system-consistent droplet potentials can be determined iteratively. The BEM electrostatic algorithm can be summarized as follows:

1. Obtain level set ϕ gridded data

2. Using that data, find the linearly interpolated zero surface crossing points

3. Separate the $\phi = 0$ surface into discrete droplets.

4. To enforce charge preservation, either match each droplet with a previous timestep's droplet or as a newly formed shape. This allows fissioning of droplets even after detachment.

5. For each droplet, order the points as non-crossing and consecutive.

6. Create new surface coordinates where each panel is approximately the same length.

7. Determine correct boundary conditions, appropriate droplet charges

8. Create distance-based, Green's function A matrix

9. Solve the $Ax{=}b$ matrix iteratively with GMRes

10. Calculate the force on the panels using the normal electric field as in the previous section.

11. Pass evenly spaced surface points of each droplet, with their normals, panel locations and force back to the level set module.

Step 7 is performed by initially assigning the droplets the background potential. At that point, steps 7-10 are iteratively repeated, with the potential of each detached droplet influencing the potentials on all other detached droplets. The needle and electrode potentials are fixed. This continues until the change in droplet potential is less than 1%, commonly about 3 iterations. The routine then writes the intermediate data files and passes the forces on each panel to the level set module.

4.4 2D axisymmetric case

When adapting the previously introduced methods to a 2D axisymmetric setup, multiple changes in the formulation occur. All such modifications that are needed

to transition from a Cartesian setup are described in this section. The simulation governing equations, panel effect relations and the formation of the Green's function are directly altered when modeling in cylindrical coordinates.

4.4.1 Model assumptions and governing equations

While the simulation model still considers an incompressible, isothermal and viscous liquid, the indium propellant is now accelerated by a ring electrode instead of two rectangles. The two dimensional axisymmetric governing equations for the system are listed as Eqs. (4.63-4.64). Continuity and conservation of momentum are enforced.

$$\begin{aligned} \tfrac{1}{r}\tfrac{\partial}{\partial r}\left(r v_r\right) + \tfrac{\partial v_z}{\partial z} &= 0 \\ \tfrac{\partial \mathbf{A}}{\partial t} + \left(v_r \tfrac{\partial}{\partial r} + v_z \tfrac{\partial}{\partial z}\right)\mathbf{A} &= \mathbf{B} + \sigma\kappa + q\overrightarrow{E_n} \end{aligned} \tag{4.63}$$

The main momentum equation variables are listed in Eq. (4.2).

$$\mathbf{A} = \begin{bmatrix} v_r \\ \\ v_z \end{bmatrix}, \mathbf{B} = \begin{bmatrix} -\frac{1}{\rho}\frac{\partial p}{\partial r} + \nu\left(\nabla^2 v_r - \frac{v_r}{r^2}\right) \\ \\ -\frac{1}{\rho}\frac{\partial p}{\partial z} + \nu\nabla^2 v_z \end{bmatrix} \tag{4.64}$$

Since the surface curvature is represented as $\kappa = \frac{\nabla\cdot(\nabla\phi)}{|\nabla\phi|}$, the new axisymmetric surface curvature is expressed in terms of the level set as shown in Eq. (4.65).

$$\kappa = \frac{\frac{1}{r}\frac{\partial}{\partial r}(r\frac{\partial\phi}{\partial r}) + \frac{\partial^2\phi}{\partial z^2}}{\left|\left(\frac{d\phi}{dr}, \frac{d\phi}{dz}\right)\right|} \tag{4.65}$$

4.4.2 Axisymmetric Green's function

The 2D axisymmetric Green's function is more convoluted than either the Cartesian two or full three dimensional case. This additional complication is due to the

rotation about the z-axis. There are integrals that cannot be evaluated analytically and no full recursion relationship for Taylor expansion terms is known.

Green's function derivation

The function can be derived by integrating the 3D Green's function in the θ-direction [65]. This is analogous to Eq. (4.36), in $\Re^3$ with $\overline{x}$ being the point at which the potential is computed and $\overline{x}_1$ being the source point.

$$G(\overline{x},\overline{x}_1) = \frac{1}{4\pi}\frac{1}{\overline{r}} = \frac{1}{4\pi}\frac{1}{\sqrt{(x-x_1)^2+(y-y_1)^2+(z-z_1)^2}} \tag{4.66}$$

Conversion of the system to radial coordinates occurs from a substitution of $x = r\,\cos\theta$ and $y = r\,\sin\theta$ into Eq. (4.66).

$$G(\overline{x},\overline{x}_1) = \frac{1}{4\pi}\frac{1}{\sqrt{(r\,\cos\theta - r_1\,\cos\theta_1)^2+(r\,\sin\theta - r_1\,\sin\theta_1)^2+(z-z_1)^2}} \tag{4.67}$$

This can be simplified via the relations $\sin^2\theta + \cos^2\theta = 1$, $\cos\theta\,\cos\theta_1 + \sin\theta\,\sin\theta_1 = \cos(\theta-\theta_1)$ and $1+\cos(2\theta) = 2\cos^2\theta$. The Green's function now becomes

$$G(\overline{x},\overline{x}_1) = \frac{1}{4\pi}\frac{1}{\sqrt{r^2+r_1^2-2rr_1\cos(\theta-\theta_1)+(z-z_1)^2}} \tag{4.68}$$

Because the domain is axisymmetric, the absolute values of θ and θ_1 are unimportant; only the difference ζ_θ between them. In addition, this coordinate system transformation of the Green's function requires some new variables.

$$\begin{aligned} \zeta_\theta &= \theta - \theta_1 \\ L &= (r+r_1)^2+(z-z_1)^2 \\ m &= \tfrac{4rr_1}{L} \end{aligned} \tag{4.69}$$

After changing the limits of integration and substituting Eq. (4.69) into Eq. (4.68), the ring charge can be calculated by performing a rotational integration.

$$G(\overline{x},\overline{x}_1) = \frac{1}{2\pi\sqrt{L}}\int_0^{\pi}\frac{d\zeta_\theta}{\sqrt{1-m\,\cos^2\zeta_\theta}} \tag{4.70}$$

Since the integration is from $0 \hookrightarrow \pi$, $\int \sin^2\zeta_\theta\, d\theta = \int \cos^2\zeta_\theta\, d\theta$ and these terms are interchangeable. With $\sin\zeta_\theta$ being symmetric about $\frac{\pi}{2}$, the integration is equivalent to $2\int_0^{\frac{\pi}{2}}[\ ]\, d\zeta_\theta$. Therefore, Eq. (4.71) is the axisymmetric Green's function.

$$G(\overline{x},\overline{x}_1) = \frac{1}{\pi\sqrt{L}}\int_0^{\frac{\pi}{2}}\frac{d\zeta_\theta}{\sqrt{1-m\,\sin^2\zeta_\theta}} = \frac{K(m)}{\pi\sqrt{L}} \tag{4.71}$$

The K(m) function is a complete elliptic integral of the first kind [4] and can be approximately determined using a method of arithmetic-geometric means [210, 65].

Derivative recursion relations

The formulation of Eqs. (4.56 and 4.71) requires the first and second derivatives of the Green's function. In contrast to the two and three dimensional cases, no full recursion relationship for Green's function derivatives is known to exist in 2D axisymmetry. A partial solution provides the next greater term of the Taylor expansion, but still requires extensive calculations at each step [220]. These derivatives can be calculated via the axisymmetric Laplace equation, Eq. (4.72). The fundamental solution is [252] Eq. (4.73), where r_1 is the source point, r_2 is the reference point and E(p) is an elliptic integral of the second kind.

$$\frac{1}{\overline{r}}\Psi^* = -\delta(r_1-r_2)\delta(z_1-z_2) \tag{4.72}$$

$$\Psi^* = \frac{\sqrt{r_1 r_2}}{\pi p}\left\{K(p)(1-\frac{p^2}{2}) - E(p)\right\},\ p^2 = \frac{4r_1r_2}{(r+r_1)^2+(z-z_1)^2} \tag{4.73}$$

Taking the derivative of Ψ^* with respect to r_1 and r_2 gives two equations [65]:

$$\begin{aligned}\frac{\partial^{a+b+c}G}{\partial z^a \partial r_1^b \partial r_2^c} &= \frac{-\partial^{a+b+c}G}{\partial z^{a+2} \partial r_1^{b-2} \partial r_2^c} - \sum_{i=0}^{b-2} \frac{(-1)^i}{r_1^{i+1}} \frac{(b-2)!}{(b-2-i)!} \frac{\partial^{a+b+c-i-1}G}{\partial z^a \partial r_1^{b-i-1} \partial r_2^c} \\ \frac{\partial^{a+b+c}G}{\partial z^a \partial r_1^b \partial r_2^c} &= \frac{-\partial^{a+b+c}G}{\partial z^{a+2} \partial r_1^b \partial r_2^{c-2}} - \sum_{j=0}^{c-2} \frac{(-1)^j}{r_2^{j+1}} \frac{(c-2)!}{(c-2-j)!} \frac{\partial^{a+b+c-j-1}G}{\partial z^a \partial r_1^b \partial r_2^{c-j-1}}\end{aligned} \tag{4.74}$$

Redefining $z = z_1 - z_2$ requires that the derivative with respect to z_2 be multiplied by (-1). The first equation in Eq. (4.74) is only valid when b is greater than one while the second equation similarly requires c to be greater than one. A full listing of 2D axisymmetric Green's functions up to the a+b+c=3 derivative is provided in Sec. (D.4).

4.4.3 Panel charge and radius normalization

For a 2D axisymmetric model, the boundary panel description needs to be modified. Consider a distribution of particles in a cylindrical system randomly scattered along r and θ. To produce a constant overall potential, the charge density must remain constant. However, with an increasing area as the radius increases, the relative charge must increase. Thus, the charge on each panel integration point is multiplied by the normed radius $r_{point}/r_{midpoint}$. This increases the charge further from the center, leaves it unchanged at the midpoint and reduces it as the integration proceeds towards the axis.

4.4.4 *A* matrix form variation

While Eqs. (4.58-4.59) demonstrate how to set up the A matrix, moving to a 2D axisymmetric realm creates several new concerns. The primary issue is the lack of strong diagonal dominance in A. As a result, the matrix is stiff and the solution to the linear system is unstable. The matrix is of full rank but poorly conditioned, so practical solution techniques are inaccurate. With a high condition number on the order of 1×10^5 for 1000 panels, computed strengths vary greatly due to small

system perturbations.

Computational load also becomes a concern. Previously, the matrix formulation automatically solved for both the potential and electric field at every panel center. In this model, both of these quantities are not necessary for every position, so changing the A matrix interpretation can save time by reducing the number of computed integrals from the original $2N_p^2$ panels to N_p^2 [65].

An alternative method replaces the $\partial_{\overrightarrow{n}} U(\overline{x}_{1,1})$ and $U(\overline{x}_{2,1})$ terms in Eq. (4.56) with constants φ_i and ϖ_i. For fixed potential panels φ_i is set to zero while ϖ_i is zero for fixed potential flux panels. Equation (4.58) is then rewritten as Eq. (4.75) [65]:

$$\left[\begin{array}{cc} \grave{a}_{1,1}..\grave{a}_{1,N_D} & \grave{b}_{1,1}..\grave{b}_{1,N_N} \\ \hline \grave{a}_{N_D,1}..\grave{a}_{N_D,N_D} & \grave{b}_{N_D,1}..\grave{b}_{N_D,N_N} \\ \hline \grave{c}_{1,1}..\grave{c}_{1,N_D} & \grave{d}_{1,1}..\grave{d}_{1,N_N} \\ \grave{c}_{N_N,1}..\grave{c}_{N_N,N_D} & \grave{d}_{N_N,1}..\grave{d}_{N_N,N_N} \end{array}\right] \left[\begin{array}{c} \varpi_1 \\ .. \\ \varpi_{N_D} \\ \varphi_1 \\ .. \\ \varphi_{N_N} \end{array}\right] = \left[\begin{array}{c} U(\overline{x}_{1,1}) \\ .. \\ U(\overline{x}_{1,N_D}) \\ \partial_{\overrightarrow{n_N}} U(\overline{x}_{2,1}) \\ .. \\ \partial_{\overrightarrow{n_N}} U(\overline{x}_{2,N_N}) \end{array}\right] \tag{4.75}$$

where the values in the matrix are given by Eq. (4.76).

$$\begin{aligned} \grave{a}_{i,j} &= \int_{\partial\Omega_D} \partial_{\overrightarrow{n_D}} G(\overline{x}|\overline{x}_{1,j})\,\mathrm{d}s + \left\{\tfrac{1}{2} \in \mathrm{i{=}j}\right\} \\ \grave{b}_{i,j} &= \int_{\partial\Omega_N} G(\overline{x}|\overline{x}_{1,j})\,\mathrm{d}s \\ \grave{c}_{i,j} &= \int_{\partial\Omega_D} \partial_{\overrightarrow{n_D}} \partial_{\overrightarrow{n_N}} G(\overline{x}|\overline{x}_{2,j})\,\mathrm{d}s \\ \grave{d}_{i,j} &= -\int_{\partial\Omega_N} \partial_{\overrightarrow{n_N}} G(\overline{x}|\overline{x}_{2,j})\,\mathrm{d}s + \left\{\tfrac{1}{2} \in \mathrm{i{=}j}\right\} \end{aligned} \tag{4.76}$$

Once the values of $\{\varpi_1..\varpi_{N_D}\}$ and $\{\varphi_1..\varphi_{N_N}\}$ have been calculated, they can be used to calculate the potential throughout the domain by using Eq. (4.77).

$$U(\overline{x}) = \sum_{j=1}^{N_D} \varpi_j \int_{\partial\Omega_{D_j}} \frac{\partial G(\overline{x}|\overline{x}_j)}{\partial n_j} dS + \sum_{k=1}^{N_N} \varphi_k \int_{\partial\Omega_{N_k}} G(\overline{x}|\overline{x}_k) dS \tag{4.77}$$

4.4.5 Electrostatic force calculation

When calculating the potential flux from Sec. (4.3.3), recall that

$$UL\left[\frac{N \cdot m^2}{C}\right] = \int E\, dA = \oint \overrightarrow{E} \cdot \overrightarrow{n}\, dS = \frac{q}{\epsilon_0}$$

and therefore $q = E_n \epsilon_0 A$. While the cross sectional area in 2D is the panel length one unit deep ($L \times 1$), the surface area A_{torus} of the torus in Fig. (4.11) is

$$A_{torus} = 4\pi^2 Rr \tag{4.78}$$

and with the relative radius r equal to the panel length L, the charge is given by Eq. (4.79).

$$q = 4\pi^2 E_n \epsilon_0 RL \tag{4.79}$$

The total electrostatic force experienced by the panel in 2d axisymmetric coordinates is given by Eq. (4.80).

$$F_E\,[N] = qE_n = 4\pi^2 E_n^2 \epsilon_0 RL \tag{4.80}$$

4.5 Improvement of accuracy and speed algorithms

The definition of two dimensional surface tracking was described in Secs. (4.2-4.3). However, important issues remain concerning accurate and rapid implementation of these methods. This section details approaches to obtain improved simulation performance.

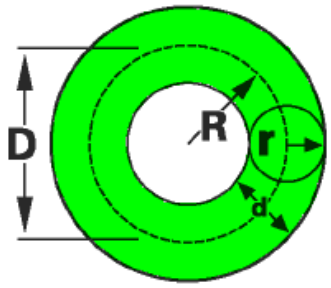

Figure 4.11: Torus geometry framework used to convert simulation area to axisymmetric droplet volume

4.5.1 Generalized Minimal Residual (GMRes)

Many methods are suitable for quickly obtaining solutions for the unknowns in Eq. (4.58). An excellent candidate used here is Generalized Minimal Residual (GMRes). GMRes is an iterative matrix solver for large, unsymmetric, semi-positive, definite, $Ax=b$ linear systems. Substantial time savings can be achieved using this method to calculate the electrostatic force on a set of points within a Poisson problem.

Background

Determining the force on N particles from all of the other charged particles usually requires the formation of an $Ax=b$ matrix. Here, A denotes a real, unsymmetric $N \times N$ matrix with eigenvalues λ_1, λ_2, ..., λ_n [199]. Solving this system through full Gaussian inversion takes $O(N^3)$ operations, whereas GMRes can solve the same system to tolerance x_{tol} in approximately $O(N^2 \ln(N))$ time. For large matrices, this can result in significant time savings. An improvement on standard GMRes occurs if the matrix-vector product is computed with a tree code; x can then be computed in $O(N \ln(N))$ time. For matrices of various sizes, the approximate computational effort is given in Table (4.3).

GMRes solves systems of non-linear partial differential equations by approximat-

ing the solution with the Arnoldi method on a projected Krylov subspace. The mathematics and algorithm of the above methods are described in the following sections. Note that if the matrix operator A_k is a constant linear operator, then GMRes is identical to another matrix solving method labeled gradient conjugate residual (GCR). In general, GMRes remains more stable for an arbitrary A matrix than GCR [260].

Matrix solution method	size= 100^2	1000^2	$10,000^2$	$100,000^2$
Gaussian inversion	1×10^6	1×10^9	1×10^{12}	1×10^{15}
GMRes	5×10^4	7×10^6	9×10^8	1×10^{11}
GMRes tree code	5×10^2	7×10^3	9×10^4	1×10^6

Table 4.3: Order of magnitude computational effort for various A matrix dimensions using 3 different solution methods

Krylov subspaces

A projection method approximates a solution of the linear system Ax=b by extracting or "projecting" onto a spanning subspace [198]. GMRes projects the solution onto the m^{th} Krylov subspace formed by Eq. (4.81)

$$\kappa_m(\mathcal{A}, \upsilon) = span\left\{\upsilon, \mathcal{A}\upsilon, \mathcal{A}^2\upsilon, ... \mathcal{A}^{m-1}\upsilon\right\} \tag{4.81}$$

where υ is the initial normalized residual. Subspaces are useful due in large part to their embedded characteristic polynomial. In Eq. (4.82), that polynomial provides a more accurate and better fitting approximation to the system solution as the size of m increases.

$$\det(\lambda I - \mathcal{A}) = h_0 + h_1\lambda + h_2\lambda^2 + ... h_N\lambda^N = 0 \tag{4.82}$$

Here, h_i are coefficients and λ are the eigenvalues of the A matrix. Using the Cayley-Hamilton theorem, the eigenvalues can be replaced by A while the sum remains zero [10].

$$h_0 I + h_1 \mathcal{A} + h_2 \mathcal{A}^2 + ... h_{N-1} \mathcal{A}^{N-1} + \mathcal{A}^N = 0 \tag{4.83}$$

By rearranging Eq. (4.83), renaming the h_i coefficients with the residual υ_i and substituting into $Ax{=}b$, a linear combination that approximates x can be calculated.

$$x = \mathcal{A}^{-1} b = \upsilon_1 b + \upsilon_2 \mathcal{A} b + \upsilon_3 \mathcal{A}^2 b + ... \upsilon_N \mathcal{A}^{N-1} b \tag{4.84}$$

Equation (4.84) is a polynomial describing a Krylov combination of order N. The N^{th} Krylov subspace can form a basis vector in $\Re^N$. That is, any N-dimensional vector can be written as a linear combination of its basis vectors. The projection onto the Krylov subspace yields an approximate solution of the linear system [110].

Arnoldi method

Arnoldi's method was first introduced in 1951 as a way to reduce a dense matrix into upper Hessenberg form. This occurred by making a set of linearly independent vectors orthogonal. It was thought that this process would approximate the eigenvalues of the original dense matrix with the eigenvalues given by the Hessenberg matrix [198]. While that did not happen, it was determined eventually that this strategy can efficiently approximate eigenvalues of larger matrices.

Therefore, the Arnoldi method finds the exact solution at the N^{th} step, since at that point the Krylov subspace completely spans A, and $\kappa \in \Re^N$. This method starts with a given vector υ_1 with unit norm and then at each step m (m¿1) constructs an orthonormal basis υ_m by computing $\overbrace{w} = \mathcal{A}\upsilon_{m-1}$. Afterwards, it ortho-normalizes

$\overbrace{w}$ with respect to $v_1 \rightarrow v_{m-1}$ to obtain v_m. The original vector guess x_1 is commonly $\{0\}$. The upper Hessenberg matrix can be formed through $H = v^T A v$; see Sec. (D.3) for more details. The newly formed Hessenberg matrix and its eigenvalues populate the Krylov subspace and help to provide approximations of the m eigenvalues of the A matrix [205].

GMRes algorithm

The algorithm for the generalized minimal residual iterative solver sets up the component matrices in steps 1 and 2, applies the Arnoldi method in steps 3-11 and determines the residual and improved guess for x_m at the end. The algorithm then repeats until the approximated solution results in a system residual less than a specified threshold. One reason the method is so rapid is that the Hessenberg begins as a [1x1] matrix and then grows iteratively. So instead of solving an [NxN] matrix directly, it solves a [2x2], a [3x3], [4x4]... only up until convergence when the residual is less than the chosen tolerance [110]. In these simulations, the matrix solution is commonly arrived at using N/10 iterations.

1. Compute $r_1 = b - Ax_1$; $\beta = \| r_1 \|_2$; $v_1 = \frac{r_1}{\beta}$
2. Define the $(m+1) \times m$ upper Hessenberg matrix $\overline{H}_m = \{h_{ij}\}_{1 \leq i \leq m+1, 1 \leq j \leq m}$. Set $\overline{H}_m = 0$.
3. For j=1,2...m Do:
4. Compute $\overbrace{w}_{j} = Av_j$
5. For i=1,2...j Do:
6. $h_{ij} = \overbrace{w}^{T}_{j} v_i$

7. $\overbrace{w}^{}_{j} = \overbrace{w}^{}_{j} - h_{ij} v_i$

8. End Do i

9. $h_{j+1,j} = \| \overbrace{w}^{}_{j} \|_2$. If $h_{j+1,j} = 0$ set m=j and goto 12

10. $v_{j+1} = \frac{\overbrace{w}^{}_{j}}{h_{j+1,j}}$

11. End Do j

12. Compute x_m, the minimizer of $\left\| \beta e_1 - \overline{H}_m x \right\|_2$ and $v_m = v_1 + v_m x_m$

Speedups to the GMRes algorithm

Through the steps in Sec. (4.5.1), the GMRes algorithm approaches O(N^2 ln(N)) computational cost. To reduce the total runtime to O(N ln(N)) time requires substantial reworking and recasting of variables. The most significant change involves the panel-panel Green's function calculation. Here, a tree code method is introduced that removes the need to form the A matrix at all.

Tree code utilization The most computationally expensive parts of the standard GMRes algorithm come in the calculation of the matrix-vector product, an O(N^2) operation. Implementation of a point-cluster reduction scheme is most effective in calculating the b, A or Av_j terms identified in the previous numbered list. An approach that avoids forming most of A can be derived by recalling that for a representative charge distribution, Av_j is the potential arising from that set up. For 2D coordinates on a Dirichlet boundary, if the distance is large between the centers of panel i and panel j compared with the panel sizes, then $A_{ij} \simeq \frac{\ln(\|x_i - x_j\|)}{4\pi}$. That is, for widely separated panels, the distributed j^{th} panel charge has the same effect on the potential at x_i as would a point charge located at panel j's center [172]. A

variety of concepts for tree codes with their branches and clusters [59, 195, 105, 263] have been published.

Clusters There are two main steps in using a tree code: constructing the tree for a given set of panels and then computing the electric field using that structure. The $\overrightarrow{E}_n$ field calculation is determined from the formation of Green's function and then uses the boundary element method of Sec. (4.3). The tree is constructed by subdividing the panels into a nested set of clusters. Once the tree is computed, each particle's potential U is then expressed as a sum of panel-cluster interactions of strength Υ.

$$\begin{aligned} U\left(\overline{x},\, C_j\right) = &\ \tfrac{1}{\epsilon_0} \textstyle\sum_{i=1}^{N_{P,j}} \Upsilon_i \int_{\partial\Omega_j} G\left(\overline{x},\, \overline{x}_i\right)\, ds \\ U\left(\overline{x}\right) = &\ \textstyle\sum_{j=1}^{N_c} U\left(\overline{x},\, C_j\right) \end{aligned} \tag{4.85}$$

where $C_j = \{\overline{x}_i,\, i = 1, ...N_{P,j}\}$ denotes a cluster of N_P panels in cluster j [141] and N_c is the number of non-overlapping clusters. The panels are grouped into this set of clusters using a divide-and-conquer strategy [16]. The first level is one cluster containing all the panels, with successive levels containing geographically grouped sections split into 4 subclusters. Figure (4.12) shows an example quad tree after construction. Figure (4.12b) was formed by beginning from the top-left square of Fig. (4.12a) and rotating clockwise through the hierarchy. The dotted lines correspond to empty squares that were subsequently removed to save storage space.

Tree codes can be used to approximate the panel integrals. The approximate Green's function in two dimensions can be written in terms of the Taylor expansion around point $\overline{x}$ with respect to $\overline{x}_i$ about particle cluster $\overline{x}_C$ [44]:

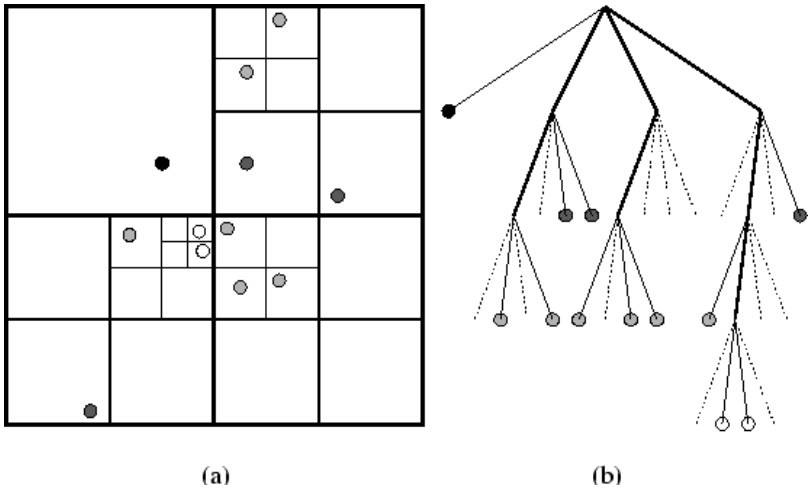

Figure 4.12: Representation of quad tree a) spatially and b) tree-linked [188]

$$\begin{aligned} G\left(\overline{x},\, \overline{x}_i\right) = &\quad G\left(\overline{x},\, \left(\overline{x}_i - \overline{x}_c\right) + \overline{x}_c\right) \\ &\simeq \sum_{k=0}^{p} \sum_{L=0}^{k} \tfrac{1}{L!(k-L)!} \partial_{x_i}^{L} \partial_{y_i}^{k-L} G\left(\overline{x},\, \overline{x}_c\right) \left(x_i - x_c\right)^{L} \left(y_i - y_c\right)^{k-L} \end{aligned} \tag{4.86}$$

where p is the order of approximation. The derivative of the Green's function for Neumann conditions is one power higher, and hence the moments have a greater exponent on their respective distances from cluster center.

$$\begin{aligned} \partial_n G\left(\overline{x},\, \overline{x}_i\right) = &\quad \partial_n G\left(\overline{x},\, \left(\overline{x}_i - \overline{x}_c\right) + \overline{x}_c\right) \\ = &\quad \partial_x G\left(\overline{x},\, \left(\overline{x}_i - \overline{x}_c\right) + \overline{x}_c\right) + \partial_y G\left(\overline{x},\, \left(\overline{x}_i - \overline{x}_c\right) + \overline{x}_c\right) \\ \simeq &\quad \sum_{k=0}^{p} \sum_{L=0}^{k} \tfrac{1}{L!(k-L)!} \partial_{x_i}^{L} \partial_{y_i}^{k-L} G\left(\overline{x},\, \overline{x}_c\right) \left(x_i - x_c\right)^{L+1} \left(y_i - y_c\right)^{k-L} \\ &+ \sum_{k=0}^{p} \sum_{L=0}^{k} \tfrac{1}{L!(k-L)!} \partial_{x_i}^{L} \partial_{y_i}^{k-L} G\left(\overline{x},\, \overline{x}_c\right) \left(x_i - x_c\right)^{L} \left(y_i - y_c\right)^{k-L+1} \end{aligned} \tag{4.87}$$

Using Eqs. (4.85-4.86), the panel-cluster interaction is given by Eq. (4.88).

$$
\begin{aligned}
U\left(\overline{x},\, C\right) \simeq & \;\; \tfrac{1}{\epsilon_0} \int \textstyle\sum_{i\in C} \sum_{k=0}^{p} \sum_{L=0}^{k} \tfrac{1}{L!(k-L)!} \partial_{x_i}^{L} \partial_{y_i}^{k-L} G\left(\overline{x},\, \overline{x}_c\right) (x_i - x_c)^L (y_i - y_c)^{k-L} \Upsilon_i \, ds \\
= & \;\; \tfrac{1}{\epsilon_0} \int \textstyle\sum_{k=0}^{p} \sum_{L=0}^{k} \tfrac{1}{L!(k-L)!} \partial_{x_i}^{L} \partial_{y_i}^{k-L} G\left(\overline{x},\, \overline{x}_c\right) \sum_{i\in C} (x_i - x_c)^L (y_i - y_c)^{k-L} \Upsilon_i \, ds \\
= & \;\; \tfrac{1}{\epsilon_0} \textstyle\sum_{k=0}^{p} \sum_{L=0}^{k} \tfrac{1}{L!(k-L)!} \partial_{x_i}^{L} \partial_{y_i}^{k-L} G\left(\overline{x},\, \overline{x}_c\right) \times \\
& \textstyle\sum_{i=1}^{N_p} \tfrac{P_{L,i}}{2} \Upsilon_i \sum_{m=1}^{M} w_m (x_{im} - x_c)^L (y_{im} - y_c)^{k-L} \\
= & \;\; \tfrac{1}{\epsilon_0} \textstyle\sum_{k=0}^{p} \sum_{L=0}^{k} T_{L,k}\left(\overline{x},\, \overline{x}_c\right) \; M_{L,k}(C)
\end{aligned}
\tag{4.88}
$$

where w_m is the m^{th} Gaussian quadrature weight (see Sec. (4.5.2)), P_L is the length of the i^{th} panel in that cluster, $T_{L,k}\left(\overline{x},\, \overline{x}_c\right)$ is the (L,k) Taylor coefficient of the Green's function and $M_{L,k}(C)$ is the corresponding moment of the cluster. Following similar steps, the panel-cluster Neumann interaction is given by Eq. (4.89).

$$
\begin{aligned}
\partial_n U\left(\overline{x},\, C\right) \simeq & \;\; \textstyle\sum_{k=0}^{p} \sum_{L=0}^{k} \tfrac{1}{L!(k-L)!} \partial_{x_i}^{L} \partial_{y_i}^{k-L} G\left(\overline{x},\, \overline{x}_c\right) \times \\
& \Big\{ \textstyle\sum_{i=1}^{N_p} \tfrac{P_{L,i}}{2} \Upsilon_i \sum_{m=1}^{M} w_m (x_{im} - x_c)^{L+1} \times \\
& (y_{im} - y_c)^{k-L} + \textstyle\sum_{i=1}^{N_p} \tfrac{P_{L,i}}{2} \Upsilon_i \sum_{m=1}^{M} w_m (x_{im} - x_c)^L (y_{im} - y_c)^{k-L+1} \Big\} \\
= & \;\; \textstyle\sum_{k=0}^{p} \sum_{L=0}^{k} T_{L,k}\left(\overline{x},\, \overline{x}_c\right) \; M_{L,k}^{N}(C)
\end{aligned}
\tag{4.89}
$$

Note that Taylor coefficients are not affected by the points i in cluster C, nor do the cluster moments change due to the location of $\overline{x}$ [45]. To calculate step 4 in Sec. (4.5.1) with a tree code requires the determination of the correct cluster interaction A_{tree} for each iterate v_j. Instead of N cluster calls, approximately ln N clouds are evaluated.

Fast potential evaluation As indicated in Eq. (4.85), the potential at a point is expressed as the sum of particle-cluster interactions for suitably chosen clusters C. The tree code has two options for evaluating each interaction: either direct sum with all particles or applying the Taylor approximation in Eq. (4.88). Replacing the panel strengths with the iterative matrix-vector product in step 4 of Sec. (4.5.1) gives Eq. (4.90), where $\overbrace{w}$ is the next iterated x guess.

$$\begin{aligned}\overbrace{w}\,(\overline{x},\,C) = \;& \sum_{k=0}^{p}\sum_{L=0}^{k}\int\left\{\tfrac{1}{L!(k-L)!}\partial_{x_i}^{L}\partial_{y_i}^{k-L}G\,(\overline{x},\,\overline{x}_c)\;ds\right\}\times \\ & \sum_{i\in C}\sum_{m=1}^{M}(x_{im}-x_c)^{L}(y_{im}-y_c)^{k-L}v_i\omega_m\end{aligned} \tag{4.90}$$

Using the Barnes-Hut criteria [16], it is possible to determine when the Taylor cluster approach is sufficiently accurate [44]. If $\overline{x}_C$ is the cluster center, let r_C be the cluster radius and $R = |\overline{x} - \overline{x}_C|$ the particle-cluster distance. A user-specific error parameter $\theta < 1$ is also defined. In practice, $\theta = 0.2$ is commonly used [45]. If $r_C < \theta R$, the bodies are said to be *well-separated* and the approximation is appropriate. Otherwise, the code recursively considers interactions between the particle and the children of the cluster C_j. If the cluster has no children then it is a leaf on the node and direct summation is used.

Preconditioning the matrix

Besides tree codes, another approach to decreasing solution time is to cluster the eigenvalues through preprocessing the matrix. The simplest preprocessor is called a block Jacobi; it utilizes the inverse of the main diagonal, as shown in a sample 3x3 matrix by $\overbrace{A}$ in Eq. (4.91).

$$A = \begin{bmatrix} A_{1,1} & A_{1,2} & A_{1,3} \\ A_{2,1} & A_{2,2} & A_{2,3} \\ A_{3,1} & A_{3,2} & A_{3,3} \end{bmatrix}, \widehat{A} = \begin{bmatrix} \frac{1}{A_{1,1}} & 0 & 0 \\ 0 & \frac{1}{A_{2,2}} & 0 \\ 0 & 0 & \frac{1}{A_{3,3}} \end{bmatrix} \tag{4.91}$$

The preconditioned matrix is then formed through Eq. (4.92). The span-reduction results of such an operation are shown in Fig. (4.13). The range of matrix entries are reduced from over $(-1 \times 10^6 : 1 \times 10^7)$ down to $[-10 : 10]$.

$$\begin{aligned} Ax &= b \\ \widehat{A}\,Ax &= \widehat{A}\,b \end{aligned} \tag{4.92}$$

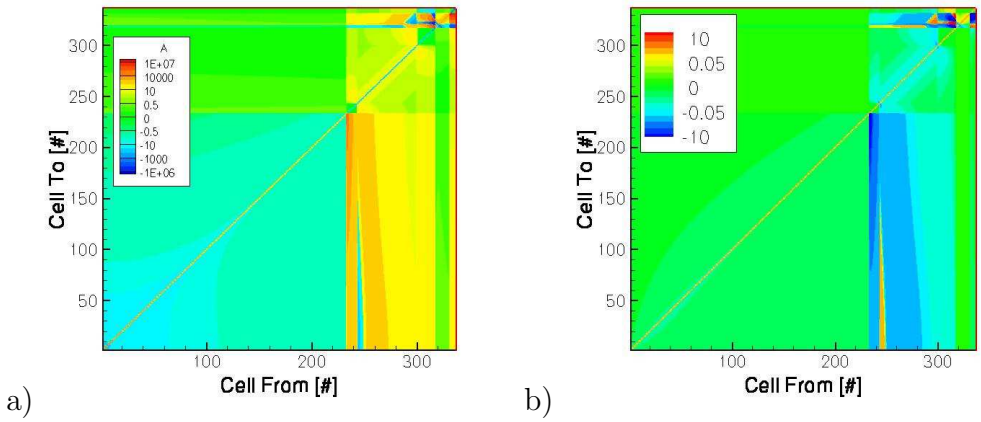

a) b)

Figure 4.13: Matrix values a) before and b) after application of a block Jacobi preconditioner

While an extra multiplication is needed on both sides of the equation, Fig. (4.14) displays the reduced total computation time when solving for the A matrix. Figure (4.15) demonstrates the lower time occurs due to drastically fewer iterates needed for a given residual. Convergence is achieved in about one fourth the number of iterations.

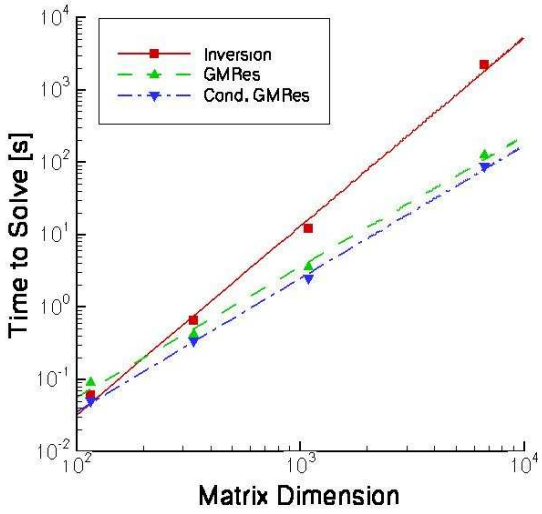

Figure 4.14: Matrix solution time reduction to a specified level of accuracy

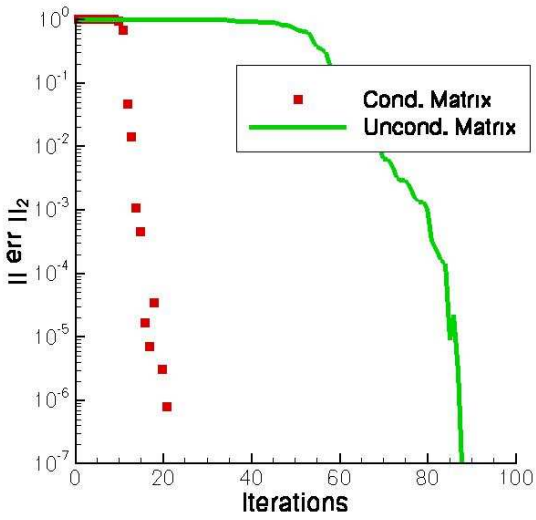

Figure 4.15: Matrix residual versus iteration number for a preconditioned and unconditioned matrix

GMRes summary

GMRes is an iterative rapid solver for semi-positive nonsymmetric matrices. Combined with the boundary element method, it solves Poisson's equation with arbitrary combinations of Dirichlet and Neumann boundary conditions to determine electrostatic forces on the surface in O(N ln N) time for arbitrary and complex 2D geometries in a grid-free setup. The method is amenable to problems having 3-D geometries after changing the Green's function to $\frac{1}{|R|}$. As discussed earlier, full inversion is the slowest approach to solve for the unknowns in an Ax=b system, followed by GMRes, and finally the most rapid technique of preconditioned GMRes. In this section, the mathematical basis, algorithm and numerical implementation were outlined and described.

4.5.2 Integration point placement and type

Three other concerns arise as to how to improve simulation accuracy. Since they are well known, details of these approaches are referenced and discussed briefly. References to more complete descriptions are provided. The within panel integration point location and type and the overall panel relative lengths are examined.

Gaussian quadrature

In numerical analysis, a quadrature rule is an approximation of the definite integral of a function, usually stated as a weighted sum of function values at specified points within the domain of integration. Careful choice of the location of these points can provide a specified level of accuracy using fewer function evaluations [61]. A specific type of numerical approximation called Gaussian quadrature uses half the computing effort of the more common linear interpolation while retaining the same accuracy.

The fundamental theorem of Gaussian quadrature is that the abscissas of the formula are precisely the roots of the orthogonal polynomial for the same interval and weighting function [265]. The simplest form is based on the use of an optimally chosen polynomial to approximate f(x) over [-1,1]. Then, using n points provides a *2n-1* degree Legendre polynomial fit for

$$\int_{-1}^{1} f(x)\,dx \approx \sum_{i=1}^{n} w_i f(x_i) \tag{4.93}$$

where w is the point's weight [4]. To evaluate it over a more general range [σ,ϵ], linearly map to [-1,1] via the transformations of Eq. (4.94).

$$\begin{aligned} x &= c + mt \\ c &= \tfrac{1}{2}(\epsilon + \sigma) \\ m &= \tfrac{1}{2}(\epsilon - \sigma) \end{aligned} \tag{4.94}$$

Combined with Eq. (4.93), a general integral evaluation Q [61] can be determined via Eq. (4.95).

$$Q = \int_{\sigma}^{\epsilon} f(x)\,dx \approx m \sum_{i=1}^{n} w_i f(c + mt_i) \tag{4.95}$$

For a full derivation of the Legendre polynomials for arbitrary shapes, see Rohklin or Sidi [148, 212]. Sample weights and locations for n= 2 or 4 integration points are in Appendix (B.2). Figure (4.16) demonstrates how the error in calculating the area of the shape changes with the number of integration points. Gaussian quadrature produces the same amount of error with a significantly fewer number of locations. The error decreases as O(N^2); due to fewer integrations, the model then takes less time to complete.

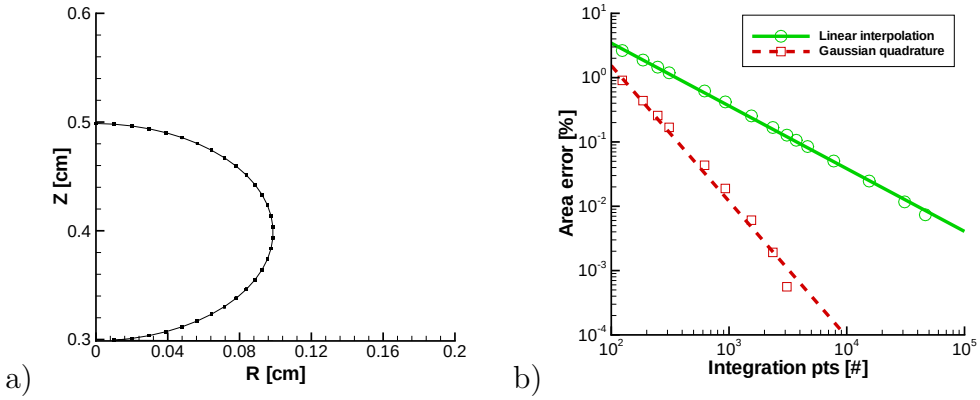

a) b)

Figure 4.16: Area calculation error for a) half-sphere b) based on the number of integration points

Panel potential approximations

Another way of increasing the accuracy of panel integration is connected to the level of approximation used for each panel. The overall simulation accuracy does not change if our current implementation of constant potential C^0 panels are replaced with linear C^1 representations.

Constant boundary conditions The potentials and fluxes that are on the right hand (i.e. $=b$), known side of Eq. (4.58) are defined as known and constant. The assumption of a perfect conductor means that the electrode and needle have a fixed potential throughout. Therefore, changing the panels from C^0 to C^1 potential representations for constants does not increase accuracy. The Green's functions $(a_{i,j}...d_{i,j})$ and $\left(\grave{a}_{i,j}...\grave{d}_{i,j}\right)$ in Eqs. (4.59 and 4.76) are not affected by the potential representation scheme, and therefore remain unchanged regardless of the implementation chosen.

Varying boundary conditions Even if the assumption of a perfect conductor is not true, the 2D axisymmetric implementation is acceptable. The known variables $\breve{\gamma}$ and α_N in Sec. (4.3.2) have $U(\overline{x_i})\partial_{\overline{n}}G(\overline{x}|\overline{x}_1)$ and $\{\partial_{\overline{n}}U(\overline{x_i})\}G(\overline{x}|\overline{x}_2)$ terms, respectively. However, due to the differing formulation outlined in Sec. (4.75), these values do not contain any panel integrals, but terms containing only $U(\overline{x})$ and $\partial_{\overline{n}}U(\overline{x})$. Since the panels are integrated, the current choice of $U(\overline{x}_{center}) = \frac{1}{s}\int U(\overline{x})\,ds$ is identical whether or not one integrates the length of the panel along its height or utilizes the rectangle + triangle sum approach of a linearly interpolated C^1 panel.

Conclusion Due to the assumption of all surfaces being perfect conductors and hence at constant potential and the specific implementation of the algorithm, the utilization of a C^0 constant potential assumption does not degrade the claimed 2^{nd} order accuracy of the approach.

Panel integration point spacing

Implicit in all the previous analysis is the assumption that panel integrals over the surface can be performed accurately. If the panels are formed using the uneven coordinate spacing shown in Fig. (4.3), then drastically different panel lengths result. Figure (4.17) demonstrates how this unequal distance between points can cause errors. Compared to the correct constant potential, the test case in Fig. (4.17a) shows contours of error due to the widely spaced vertical grid points. Figure (4.17b) graphs how this maximum error varies with relative panel length variation.

To counteract this numerical integration error, the shape must have evenly spaced points along the surface. When any panel gets to be more than 30% longer than other panels, integral sums become increasingly incorrect.

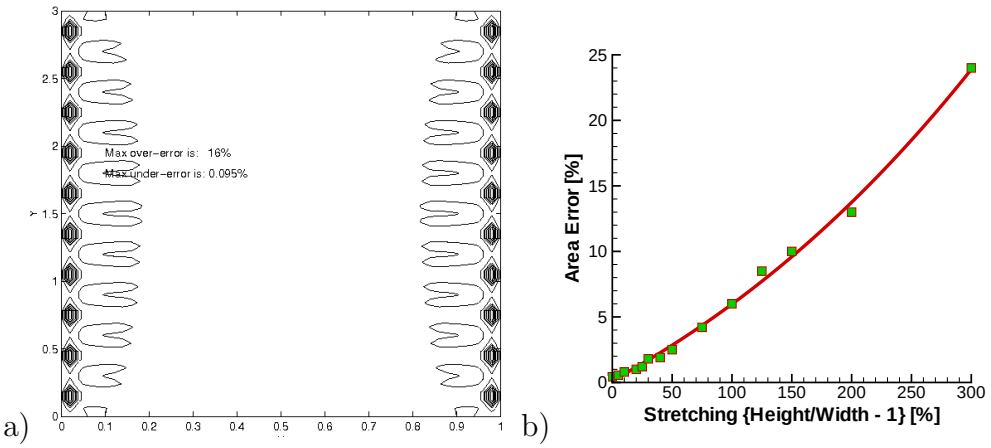

a) b)

Figure 4.17: Maximum potential error resulting from differential panel spacing a) in space and b) as a function of integration inter-point distance variation

4.5.3 Computational issues at detachment

When a droplet detaches from a needle FEEP, several complex computational issues arise. The electrostatic potential around the detachment location changes quickly, causing very large $U(\overrightarrow{x})$ gradients. In addition, the surface shape rapidly varies in space and time, is non-symmetric and evolves with increasingly complex geometries. There are several methods for dealing with these concerns.

Curvature computation

Near pinch off, determination of the surface curvature (κ) is more prone to errors as a greater change in $\kappa = \frac{\nabla \cdot \nabla \phi}{|\nabla \phi|}$ occurs within a smaller area. Three nonexclusive methods to deal with this potentially greater curvature error are distance gradients, volume of fluid and adaptive mesh refinement.

Lowengrub and Macklin suggested improving the κ determination through the inclusion of an intermediary step [149]. They solve a system of Poisson-like problems in a moving domain with a velocity that depends on the gradients of the solutions. A faster solution that does not depend on a directional gradient reconstruction is

the earlier VOF approach. Sussman calculates the curvature at the $\phi = 0$ surface based on the reconstruction of the height function directly from the volume of fluid. Mass is conserved by tracking the fraction of each cell filled [227]. A method that can be used to supplement either of the above approaches is that of adaptive mesh refinement. It is used to locally generate more cells in a given area, so that the curvature/cell is kept below a global maximum [150, 225]. Figure (4.18) shows how an area can be subdivided into four blocks (a quad tree) to allow greater resolution with fewer total cells.

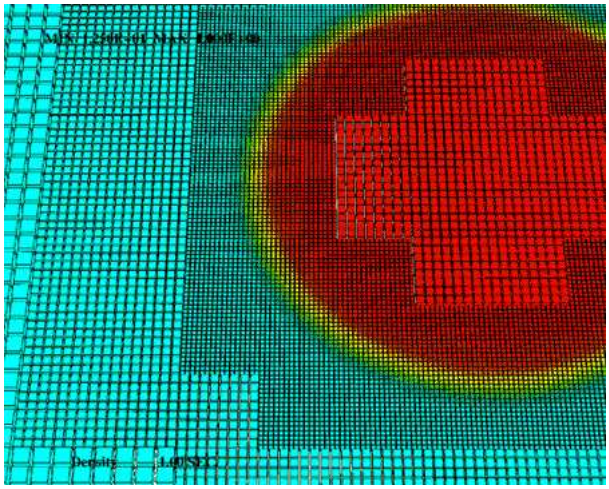

Figure 4.18: Adaptive mesh refinement example [150]

Surface node generation

Recall that the BEM is a directional method, so not only do all the interface locations have to be determined, but they also have to be examined sequentially. This computational task of ordered surface node generation from level set grid data is an issue that has consistently arisen over the last few years. Shape determination strongly impacts model behavior; problems in calculating the physical connectivity between panels arise from the existence of: areas of high curvature, variational spac-

ing between located surface points, multiple surfaces, and variation in both time and space. Figure (4.19) displays a situation commonly encountered that concerns surface recognition and separation of five unique droplets. In Fig. (4.19a), the level set variable is graphed for values $[-0.001 \leq \phi \leq 0.001]$, while the second picture displays the $\phi = 0$ locations. Figure (4.20) displays the droplets along with the possible separation points. The top three drawn circles are discrete droplets; any surface tracking program has to recognize this and that droplet #5 extends over an area whose middle is necking, but not detached.

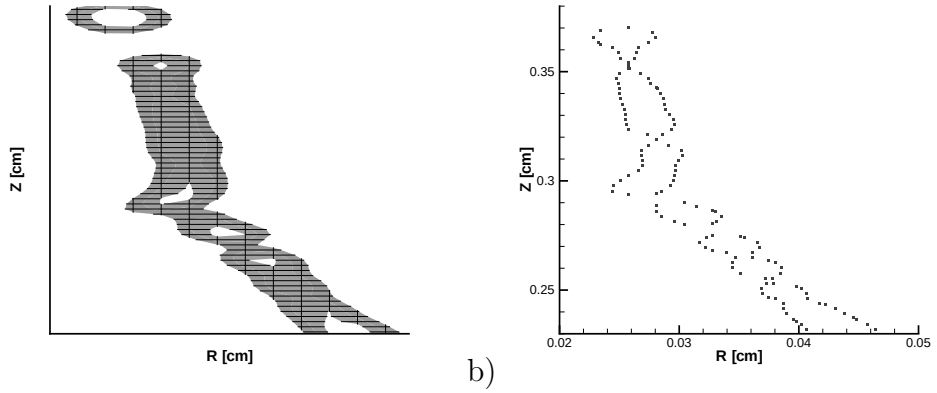

a) b)

Figure 4.19: Surface as represented by the a) level set variable ϕ from $[-0.001 \leq \phi \leq 0.001]$ and b) surface reconstruction points

Numerous approaches for discrete shape identification were attempted before settling on a hybrid anti-crossing, tracking normal-weighting (ACTNOW) scheme. This method was created using parts of many discrete schemes in the literature. It can generate connected droplets using only ϕ values, including parallel lines and necking. Other alternative schemes investigated for the shape connectivity include nearest neighbor, limited distance, normal minimization, angle gradient minimization and pseudo-entropy reduction [8, 30, 67, 144, 185].

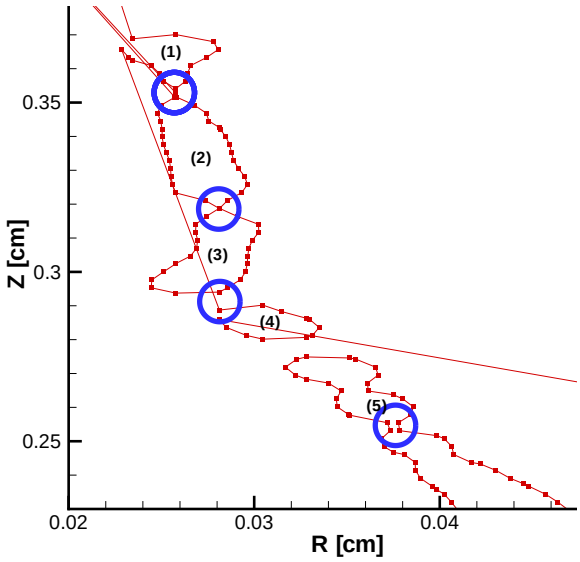

Figure 4.20: Individual droplets with circled potential detachment locations

Starting from the top point on the midline, the ACTNOW approach traverses the level set grid vertically until the first positive ϕ value is encountered. The direction moving is then recorded, with the first instance being south. The algorithm then looks at the level set values 135 degrees counter-clockwise, or northeast in Fig. (4.21). From there, the level set values are examined every 45 degrees to see if ϕ changes sign. When that sign change is identified, the new surface point is marked and the 8-point circle check is continued from the new location. In this way, a listing of the intersection points for each shape is determined. Using the list of individual droplet nodes, the order of points is determined using a combination of all the prior methods. If two lines cross when linking nodes, a connection between two nodes was mistakenly drawn, and the process for that particular shape is begun again, with that connection no longer possible. The most successful sub-techniques used in ACTNOW include limiting the length of the proposed connection near the average of the other connections and restricting the interior angle change from one point to

the next.

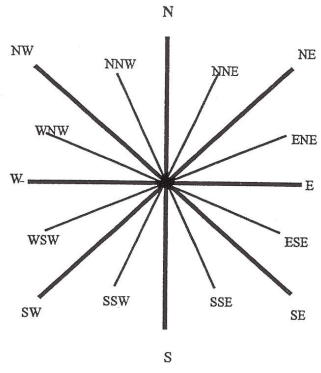

Figure 4.21: Compass directions used in the -135^0 back step ACTNOW algorithm

4.6 Algorithms to allow experimental confirmation

One way to potentially compare modeled with measured droplet behavior is to simulate an experiment. Three approaches that allow possible comparison are mass to charge ratio (MTCR), time of flight (TOF) and initial droplet formation current.

4.6.1 Bigaussian data fitting

A variety of techniques are useful in computing the detached droplet characteristics. One of these approaches is to fit histogram data with a bigaussian distribution.

To create a droplet histogram requires binning ranges of droplet properties such as relative mass to charge ratio (MTCR). For instance, while no point has an MTCR of exactly 4,234.1, a finite number fall in the range $4,200 \leq \text{MTCR} \leq 4,250$. In the case of a relatively small number of droplets (anything less than a few thousand), the overall shape of the PDF can vary significantly depending on the bin number and location. Figure (4.22) displays the percentage of droplets η expected for a specified MTCR range. The graphic shows how changing the total number of MTCR bins by even one bin can substantially change the raw histogram shape. The high shape

variation between 24 and 25 histogram bins is due only to a user choice of the number of divisions and does not represent an underlying physical mechanism.

Note that as the number of droplets per bin increases, the need to fit the overall distribution is less important. The central difference theorem requires the histogram shape to approach the true size or charge distribution as more samples are included. However for all the cases currently examined, the number of points has been small, and thus curve fitting the distribution is of substantial aid in smoothing variations caused by relative charge distributions.

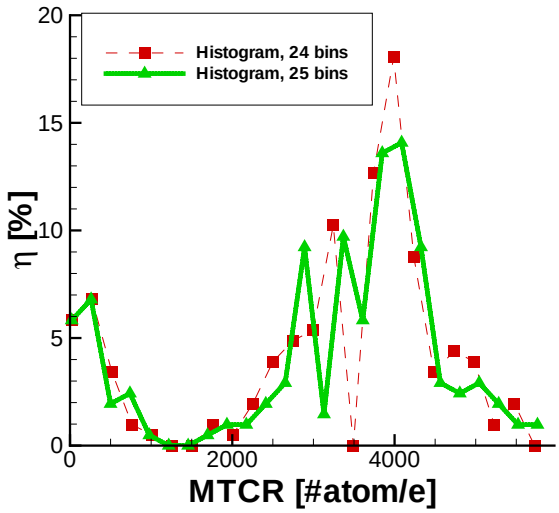

Figure 4.22: Histogram bin effect on PDF distribution

To change discrete simulated data points into a smoother continuous distribution, a mathematical data fit is required. This allows knowledge of individual points to provide high-fidelity predictions of unknown locations. That is, it is desirable to transform $y_i = f(x_i)$ into the more general $y = f(x)$. The best fit allows for the calculation of slope, rate constants, etc. even if numerical noise or experimental error is present. When curve-fitting the previous binned datasets, the new fitted

probability density functions are very similar despite the difference in number of bins. Hence, by imposing a least-squares bigaussian fit on the underlying simulation result, the error arising from bin number variability is reduced.

Linear regression

The most basic method of determining a fit to data is *linear regression*, where $y = mx + b$. Given a set of data (x_i, y_i) with n data points, the slope, y-intercept and correlation coefficient r can be determined through Eq. (4.96) [280].

$$\begin{aligned} m &= \frac{n\sum(xy)-\sum x\sum y}{n\sum(x^2)-(\sum x)^2} \\ b &= \frac{1}{n}\left(\sum y - m\sum x\right) \\ r &= \frac{n\sum(xy)-\sum x\sum y}{\sqrt{\left[n\sum(x^2)-(\sum x)^2\right]\left[n\sum(y^2)-(\sum y)^2\right]}} \end{aligned} \tag{4.96}$$

However, standard linear regression may not be the appropriate technique for many types of data analysis. The regression procedure assumes that all the x values are known perfectly and that all the uncertainty is in the assessment of the y points. This is why it minimizes the sum of the squares of the *vertical* distances of the points on the line. While it is possible to assume non-equal dual systemic errors (e.g. Deming regression [49]), the fit line must then go through zero.

The more important concern is that linear regression performs poorly in predicting many real-world data patterns. It does not capture curvature, peaks or sinks shown in modeling. In Fig. (4.23), a characteristic double hump can be seen. However, linear regression does not capture this, nor can it predict future MTCR:η values. To accurately predict droplet mass to charge ratio probabilities requires an alternative type of regression scheme, namely nonlinear.

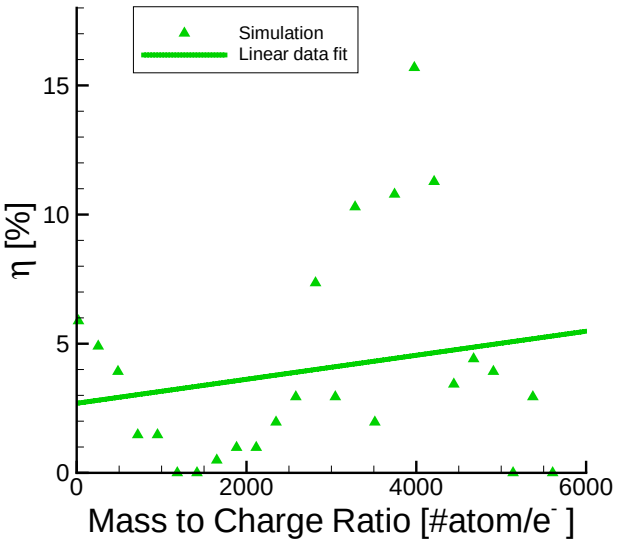

Figure 4.23: Sample data, linear fit

Nonlinear regression

Before nonlinear regression tools were readily available, the best way to analyze complex data was to transform it to create a linear graph and then examine the transformed data with linear regression (e.g. Lineweaver-Burke [142] and Scatchard [202] plots). However, the variable transformations can distort the experimental error, often over-weighting the contribution of the least important data points, where the concentration is minimal. They also plot $\frac{y}{x} = f(x)$, thereby violating the assumption of variable independence [192].

To fit the data to a double Gaussian probability density function of Eq. (4.97), the relationship $\eta = f(MTCR)$ is approximated via two independent normal distributions with their own mean (μ), standard deviation (σ) and weight $A_{[x]}$. Results of the data fitting are shown in Fig. (4.24). This bigaussian curve represents a much better relationship between the simulation points and the underlying shape. It displays the double peaks and local minima.

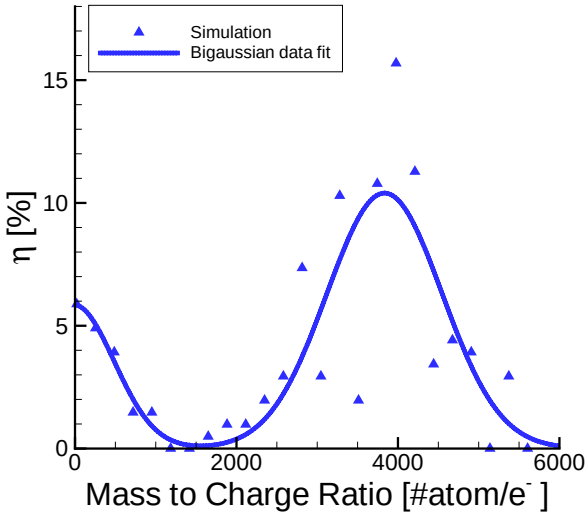

Figure 4.24: Sample data, bigaussian fit

$$\eta = A_1 \exp\left[-\frac{1}{2}\left(\frac{MTCR-\mu_1}{\sigma_1}\right)^2\right] + A_2 \exp\left[-\frac{1}{2}\left(\frac{MTCR-\mu_2}{\sigma_2}\right)^2\right] \tag{4.97}$$

Generating a smooth line to a multiple exponential approximation is difficult due to the extreme sensitivity of the terms to perturbation, the non-integer character of the variables, the constraints against negative standard deviations and non-sequential additive nature of the functions. Most commercial software programs utilize a two-step method to solve for the distribution coefficients. Initially, the method of steepest descent is used. Starting from an initial guess, compute the sum-of-squares (SoS), $\sum(\bar{x}^2)$. Then the points are varied slightly to find out the direction which reduces the SoS. Using a χ^2_m merit function to assess how good a value is produced, the determination of the coefficients must then proceed iteratively. Assuming a good initial guess $a_{current}$, the next a_{next} values of the fit parameters are given by Eq. (4.98).

$$a_{next} = a_{current} - \text{const} \cdot \nabla \chi_m^2(a_{current}) \tag{4.98}$$

After getting closer to the vector global minima a_{min} and away from any local minima, rapid convergence is achieved with the Gauss-Newton method. In Eq. (4.99), D is the second derivative matrix (Hessian matrix) of the merit function [181], as shown in Appendix (B.1). Since the equations are nonlinear, the SoS curve is irregularly shaped and hence the Gauss-Newton method can not determine the global minima through direct calculation alone. Note that iterative methods are needed not only to evaluate nonlinear terms but also to construct the Hessian matrix.

$$a_{min} = a_{current} + D^{-1} \cdot \left[-\nabla \chi_m^2(a_{current}) \right] \tag{4.99}$$

The method of differential corrections is used in tandem with Gauss-Newton. Figure (4.25) presents a graphical visualization of this dual proposal. In this hybrid approach, an initial guess for the fitting parameters is used to expand the fitting function into a Taylor series about the current estimate. First order terms are retained and the resulting linear system is solved for incremental changes. Finite difference methods are used to compute the partial derivatives in D and the resulting matrix is inverted and solved. Central limit distribution estimates are obtained from the inverse matrix diagonal [170]. No special goal-seeking, precision-preserving (e.g. pivoting), convergence-acceleration or iteration-stabilizing techniques are used.

An alternative tactic for finding the global minimum of a nonlinear function is the Nelder-Mead (NM) method [176]. It is a direct search method of stochastic optimization that is based on evaluating a function at the vertices of a simplex, then iteratively shrinking the simplex as better points are found until some desired tolerance is obtained [268]. The restrictions on the initial guess a_{init} are looser than

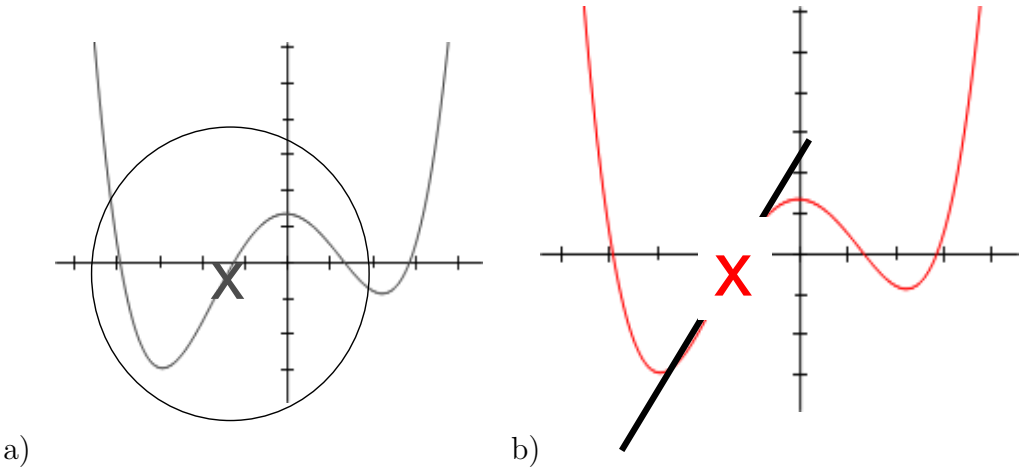

Figure 4.25: Hybrid nonlinear global minima finding algorithm using a) sum of squares and b) Gauss-Newton methods

for a steepest descent approach, but NM is less effective in dealing with the multiple local minima needed for a bigaussian data fit.

4.6.2 Time of flight

Literature searches show many time of flight (TOF) thruster tests, especially for colloid emitters. These experiments utilize a needle, electrode, and current collector. After flow cessation, the current arriving at the collector is measured as a function of time. In the following pages, the details of this approach are outlined, numerical implementation issues are described and then conclusions about similarities to published data are drawn.

An example experimental setup used by Gamero-Castañ̃o is shown in Fig. (4.26) [85]. The emitter on the left is operated in a steady-state mode for awhile and then is abruptly turned off. The stream of droplets moves past the electrode and towards the collector C_{TOF}, being accelerated at different rates depending on their individual mass to charge ratio, where relatively lower-charged droplets take longer to arrive.

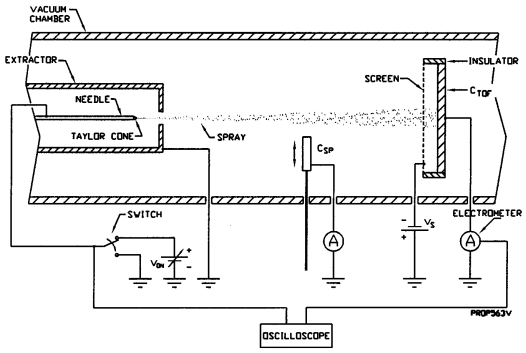

Figure 4.26: Experimental Busek TOF setup [85]

Background on time of flight

Droplet time of flight is a way to calculate accurate values for many operational characteristics of charged beams [118]. A TOF measurement is a time-dependent spectrum of a current signal associated with the beam *I(t)* following its instantaneous interruption. The spectrometers utilize the principle that particles of different masses with the same energy E travel with different velocities inversely proportional to the square root of the mass [256].

$$v = \sqrt{\frac{2E}{m}} \tag{4.100}$$

The time-of-flight time t_{TOF} of the particle over a prescribed distance d_{TOF} is therefore directly proportional to the square root of the mass. If this particle is a droplet with charge q which has traveled through a potential V, the flight time and mass per charge are given via Eq. (4.101).

$$\begin{aligned} t_{TOF} &= d_{TOF}\sqrt{\tfrac{m}{2E}} \\ \tfrac{m}{q} &= 2U_A\left(\tfrac{t_{TOF}}{d_{TOF}}\right)^2 \end{aligned} \tag{4.101}$$

For a known acceleration voltage, analysis of *I(t)* yields the specific charge distribution function of the droplets. Through current integration, Eq. (4.102) describes the

thrust, mass flux, specific impulse and propulsive efficiency of the thruster.

$$\begin{aligned} F &= \int_0^\infty \frac{2U_A(t)}{d_{TOF}} tI\, dt \\ \dot{m} &= \int_0^\infty \frac{2U_A(t)}{d_{TOF}^2} t^2 I\, dt \\ I_{SP} &= \frac{F}{\dot{m}g} \\ \eta &= \frac{F^2}{2\dot{m}V_N I} \end{aligned} \tag{4.102}$$

With U_A as the accelerating voltage, a simulated time of flight curve can be generated from a specific starting state. However, several computational issues have been addressed to correctly compute these unknowns.

Numerical issues in modeling TOF

Multiple significant obstacles arise when attempting to numerically evolve a probability density function into a modeled time of flight curve.

Acceleration voltage Unfortunately, the acceleration voltage on the beam drops is not simply the voltage difference between the needle and the electrode. In fact, droplets with different voltages are generated at breakup. Voltage losses of over 500 V have been previously measured [87]. The difference is associated with both electric conduction losses in the cone jet and changes in the sum of kinetic and potential energies of the fluid occurring during the acceleration of the jet and its breakup [85]. The actual force felt on the droplets can be determined using the so-called stopping potential technique [117]. Experiments have shown that most acceleration voltages are approximately 85% of the needle-electrode voltage difference [196].

Converting droplet frequency PDF to location PDF A processing technique to allow a TOF computation to be performed rapidly is to introduce a velocity-

shifting function to the droplets at their detachment. This function predicts I(t) at the distant collector without tracking the droplets through the entire pathway. Instead of having a numerical domain of meters, a length of millimeters is sufficient. Without the need for droplets to travel through the system, the domain can be smaller, run for fewer time steps and use a rougher grid at the extremities. The cumulative result from all these changes is a substantial speedup for a droplet emission prediction.

It is important to realize that velocity-shifting a droplet PDF impacts multiple components of the final prediction. Both the shifted velocity and the resulting time of flight (TOF) are noticeably changed depending on the form of the shifting algorithm. The final mass to charge information desired is a frequency distribution, or how many droplets are produced with $MTCR_i \leq \frac{m}{q} \leq MTCR_{i+1}$.

However, the experimental TOF data is taken not by how many droplets are in a volume of space, but instead how quickly these drops travel. It records a *spatial* not a *temporal* distribution. Faster moving particles remain in any location [x, x+dx) for a shorter period of time than slower moving droplets. Therefore, the charged droplet PDF needs to be re-normed so that looking at any volume at any time snapshot results in the likelihood of seeing each speed of droplet in that volume. The methodology is described in the following section.

Define the vector b such that b_i denotes the number of droplets produced at the needle in time τ with an acceleration α in the interval $[a_{i-1}, a_i)$ for $1 \leq i \leq N$ acceleration intervals. That is, looking at Fig. (4.24), the b_i are the frequency η values for the bin i. The acceleration is a function of the charge and electric field, with $a_i = \text{const} \times \frac{1}{MTCR_i} \times E$. Let a_0 be the minimum and a_N be the maximum acceleration. Since all droplets are charged, $a_0 > 0$. Next define the flux distri-

bution function $\Xi(\alpha)$ to represent the number of particles produced per unit time with an acceleration in the infinitesimal interval $[\alpha, d\alpha)$. Converting from indium [particles/electron] to [kg/C] expresses the acceleration term as a function of relative charge, or $\alpha = \frac{8.453\times10^{14}}{MTCR}$. Larger blobs with less charge move slower, so the minimum acceleration α_{min} occurs at $MTCR_{max}$. The density of droplets with a given acceleration is then given by Eq. (4.103),

$$\Xi(\alpha)d\alpha = \frac{1}{t_{TOF}} \sum_{i=1}^{N} H\left(\alpha - a_{i-1}\right) H\left(a_i - \alpha\right) \frac{b_i}{a_i - a_{i-1}} d\alpha \tag{4.103}$$

where H(x) is the Heaviside step function of Eq. (4.104).

$$H(x-c)H(d-x) = \begin{cases} 1 \text{ if x} \in [c,d) \\ \\ 0 \text{ otherwise} \end{cases} \tag{4.104}$$

Since the thruster is operated in a steady state before emission cutoff, $\Xi(\alpha, t) = \Xi(\alpha)$ and from Fig. (2.3), the initial velocity of the droplets leaving the needle is effectively zero. Define the spatial distribution function $f(x, \alpha)$ to represent the number of drops at any given time. In order to derive $f(x, \alpha)$, first consider the range of possible flux populations $\Xi(\alpha)$ possible when a drop leaves the needle. In the infinitesimal interval [x+dx), the time when the droplet has traveled x is $t_{in} = \sqrt{2x/\alpha}$ while the time it leaves $x+dx$ is $t_{out} = \sqrt{2(x+dx)/\alpha}$. Therefore,

$$t(x,\alpha) = t_{out} - t_{in} = \sqrt{\frac{2(x+dx)}{\alpha}} - \sqrt{\frac{2x}{\alpha}} \tag{4.105}$$

Recalling the definition of a derivative simplifies the above to Eq. (4.106).

$$t(x,\alpha) = \sqrt{\frac{2x}{\alpha}} \left(\frac{\partial}{\partial x}\sqrt{x}\right) dx = \frac{dx}{\sqrt{2x\alpha}} \tag{4.106}$$

The number of droplets $f(x,\alpha)$ in the spatial location [x, x+dx) with acceleration $\alpha \in [\alpha, \alpha + d\alpha)$ is then given by Eq. (4.107), which multiplies the number of particles produced per time by their changing speed.

$$\begin{aligned} f(x,\alpha) &= \int\int \Xi(\alpha) d\alpha \, t(x,\alpha) dx \\ &= \int_{\alpha_{min}}^{\alpha_{max}} \int_0^{x_{needle}} \frac{1}{t_{TOF}} \sum_{i=1}^{N} H\left(\alpha - a_{i-1}\right) H\left(a_i - \alpha\right) \frac{b_i}{a_i - a_{i-1}} \frac{1}{\sqrt{2x\alpha}} d\alpha dx \end{aligned} \tag{4.107}$$

The double integral allows for the calculation of the spatial and temporal distribution of droplets as a function of their relative charge. The varying accelerations of the many charged points produces a varying current collection profile. The effects of this profile alteration are discussed in more depth in Chapter V.

TOF data conversion process

The overall process for the time of flight conversion is given by Fig. (4.27). The steps listed in the figure correspond to:

1. Record all detached droplets, each with a unique mass to charge ratio.
2. Decide to evolve the MTCR to compare to time of flight instead of differentiating experimental data to produce the underlying relative charges.
3. Form a frequency histogram by binning the droplet MTCR.
4. Nonlinear bigaussian fit the data to remove the underlying bin number dependence.
5. Change the fitted frequency distribution to a velocity-based one. As discussed in the previous section, for various methods, there is a nonzero median of the

boundary velocity distribution function. Particle and droplet statistics need to be adjusted to account for physical fluxes. Equation (4.108) lists the integration domains for stationary and fluxing PDFs. Figure (4.28) displays how the mean and standard deviation are different for log-normal versus Gaussian distributions. C_{1-3} are the distributions for each axis. Since the only droplets recorded are those with a positive x-acceleration towards the collector, the fluxing PDF integrates from $\int_0^\infty$.

$$\begin{aligned} \text{stationary:} \quad & \int_{-\infty}^{\infty} C_1 \int_{-\infty}^{\infty} C_2 \int_{-\infty}^{\infty} C_3 \\ \text{fluxing:} \quad & \int_{\underbrace{0}}^{\infty} C_1 \int_{-\infty}^{\infty} C_2 \int_{-\infty}^{\infty} C_3 \end{aligned} \tag{4.108}$$

6. Change the velocity PDFs into probabilities of how many particles are in a location (x+dx) with acceleration ($\alpha + d\alpha$).

7. Produce a time of flight curve that incorporates limited spatial data to predict current fall off over time.

8. Compare original and shifted current degradation time lines.

4.6.3 Initial current for droplet formation

In addition to TOF, other approaches to potentially compare simulated and experimental results exist. Recently, a dependence between the Taylor cone radius $r_T\,[\mu m]$ and the critical current I_c was hypothesized [237]. Equation (4.109) provides a curve fit for the point at which droplets begin being emitted from a needle FEEP.

$$I_C[\mu A] = 0.0005 r_T^2 - 0.1085 r_T + 10.121 \tag{4.109}$$

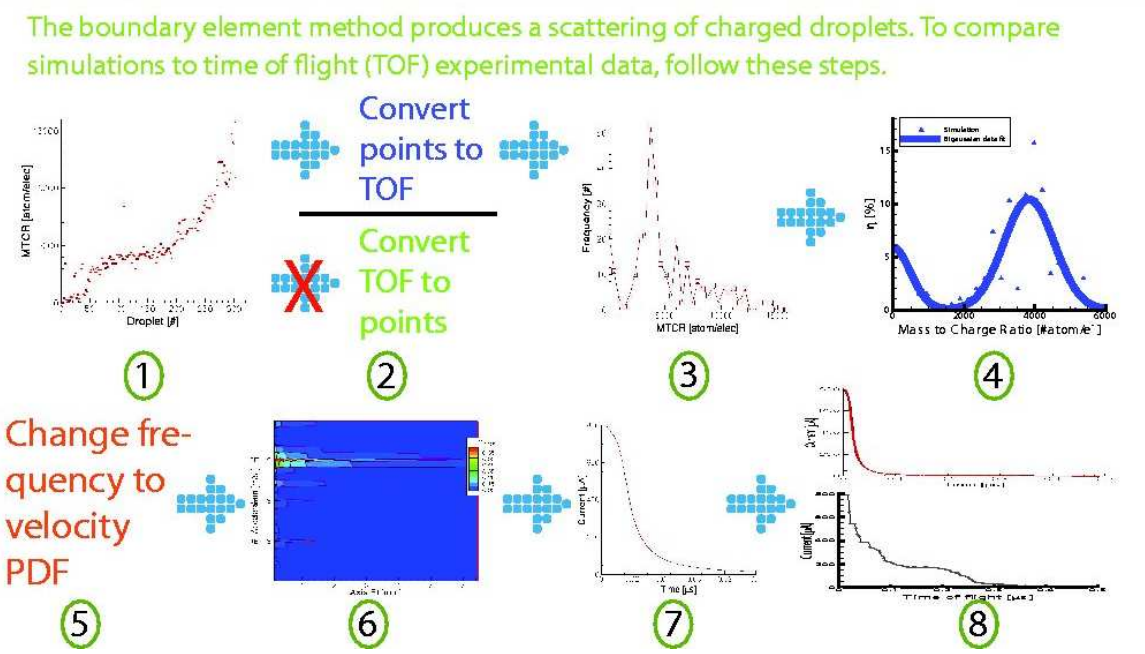

Figure 4.27: Time of flight data conversion process.

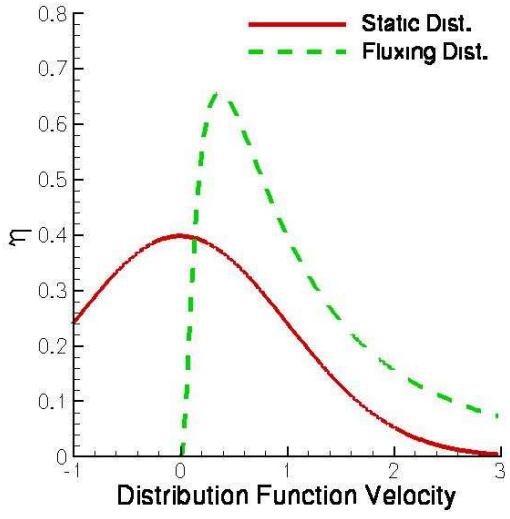

Figure 4.28: Fluxing versus static distribution functions

The mass efficiency of a single indium-fed needle FEEP normalized to 100 μA of current can then be represented by Eq. (4.110) [239].

$$\begin{aligned} I < I_C \quad & \eta = 100\% \\ I \geq I_C \quad & \begin{cases} \eta = \left(\frac{I}{I_C}\right)^{2.01-0.16(r_T)} \\ \eta = \left(\frac{I}{I_C}\right)^{1.13-0.01(r_T)} \end{cases} \end{aligned} \tag{4.110}$$

Figure (4.29) relates the Taylor cone radius, the overall mass efficiency and critical current. Droplets begin forming sooner (at a lower current) from a wider Taylor cone base. With the larger base, and a fixed Taylor cone angle, emission tip height is greater. The corresponding longer sides increase the number of surface instability frequencies possible during Faraday source detachment. (Refer back to Sec. (1.3.3) for a discussion of droplet types.) More droplets lower the mass efficiency because droplets produce much less thrust per kg expelled than do ions. Figure (4.30) displays the percentage of the thrust and number and mass of particles that are ions at three different current levels. Note that while the mass efficiency η decreases precipitously by the time the current reaches $250\,\mu A$, over 99% of the thrust and the number of independent particles are ions. This ion primacy concurs with the analysis presented in Sec. (1.4.3) concerning the relative impact of each type of exhaust.

4.7 Conclusion

The rapid and accurate simulation of a droplet detaching from an indium-fed needle FEEP presented many challenges. A physical model was created that includes surface tension, viscosity and electrostatic potential. The level set and boundary elements algorithms were described in detail. Used in tandem, these approaches can find the surface, compute its curvature and the surface electric field and advect the

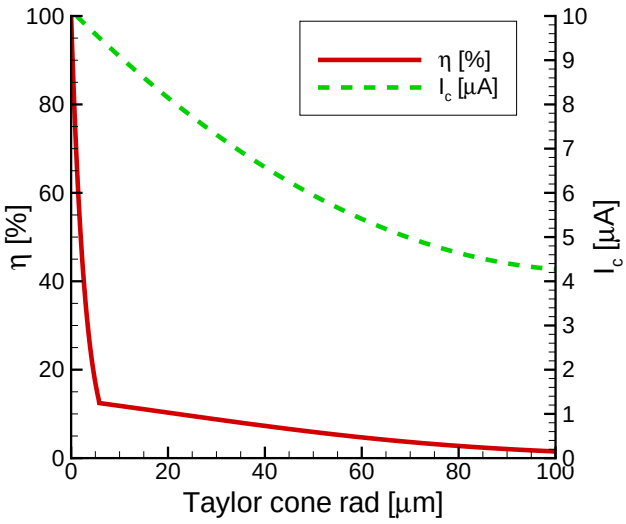

Figure 4.29: Critical current, mass efficiency and Taylor cone radius

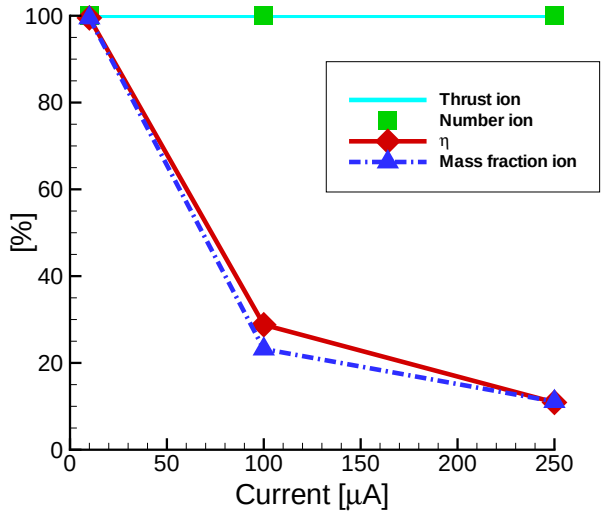

Figure 4.30: ARCS experimental data for ion vs. droplet plume composition at various currents

shape forward in time while retaining conservation of mass and momentum. The sequential linking of approaches provided the capability for simulating an arbitrary, complex and time-variant geometry and the formation of new shapes while dealing with singularities at snap off.

In addition, the model was extended to a 2D axisymmetric framework where the physical model, Green's function and A matrix were extensively adapted. In addition, multiple sub-methods were detailed that reduced the overall computational time, increased the accuracy, reduced computational aberrations and yielded stable linear solutions. Finally, a time of flight simulation capability was introduced along with its corresponding data algorithms. These allowed FEEP current and mass efficiency to be predicted.

CHAPTER V

Parametric Studies of the System

The mass efficiency of the system and relative charge of the exhaust can be significantly influenced by the values assigned to various droplet and needle properties. Drawing on all prior analysis, this chapter presents simulation results of the formation and propagation of droplets from the tip of a needle FEEP. It includes varying the needle shape and propellant properties identified in Chapter II; the asymptotic force order of magnitude from Chapter III; and the level set and boundary element methods of Chapter IV. The surface evolution of the baseline is presented, followed by alterations due to various solid and liquid modifications. Next, droplet stream characteristics are presented via a probability distribution and time of flight data filtering. Finally, comparison with independent simulations are presented that reproduce the surface evolution until snap off and the subsequent droplet angular spread.

From Eq. (4.62) of the boundary element method, the force on a droplet can be calculated and the surface advected forward in time using the level set Eqs. (4.1 and 4.7). The baseline parameters for a 2D axisymmetric simulation of a needle field emitter similar to the ARCS design and with indium propellant is given in Table (5.1).

Phys. var	Units	Value	Comp. var	Units	Value
Electrode gap	mm	1	Fluid accel.	$\frac{m}{s^2}$	1.4×10^9
Electrode height	mm	6.5	Max. velocity	km/s	6.5
Electric field	V/nm	10	BEM panels	#	˜800
Surface tension	N/m	0.552	LS grid	#	100x200
Temperature	K	453	Δt_{comp}	ns	10
Viscosity	$\frac{mN \cdot s}{m^2}$	1.7	Δt_{run}	hr	12

Table 5.1: Baseline parameters for 2D axisymmetric simulation

The 2D axisymmetric computational domain is given in Fig. (5.1). The rectangle at the top of the figure represents the position of the ring electrode while the red triangle in the bottom center is the underlying solid tungsten needle. A picture of the corresponding experimental systems was presented in the introductory chapter as Fig. (1.10b). An example of an intermediate step is shown in Fig. (5.2) as a snapshot of the liquid surface evolution, showing both adaptive mesh refinement boxes and instantaneous velocity vectors. The run time using the converged grid spacing of Fig. (4.7b), is 15 hours to obtain 100 detached droplets. As the original curvature increases, the initial surface electric field is smaller and more time is spent forming the Taylor cone, prior to snap off.

5.1 Variation of the simulation parameters

All the design variables of the simulation can be varied. This section examines how needle FEEP performance is affected in 2D axisymmetric simulations by varying electrode geometry, liquid properties and the field emitter operating condition.

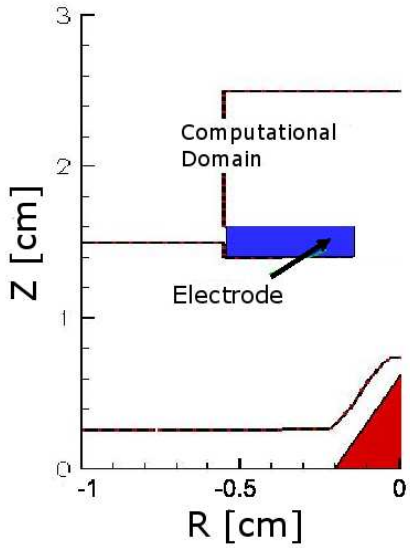

Figure 5.1: Computational domain, 2D axisymmetric case

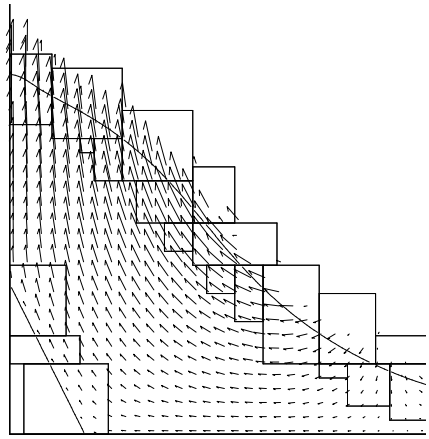

Figure 5.2: Indium surface evolution with adaptive mesh refinement boxes and overlaid velocity vectors

5.1.1 Effects of electrode axial gap size

The horizontal width of the gap between the axis centerline and the edge of the electrode has a negligible impact on the shape of the droplet pulled off the tip. As the gap approaches zero and the electrode resembles a flat plate, the corresponding electric field becomes perpendicular to the accelerating surface and a three-pronged emission surface forms. As the electrode widens, the droplet is preferentially pulled towards the edges, both at the surface itself and after droplet separation. When the electrode spacing is changed, the corresponding position and velocity of the resulting droplets evolves as well. Figure (5.3) displays how the surface shape formation process differs as the radius of the ring electrode increases. Wider rings result in an effective lower surface electric field and therefore a longer rise time for the droplet tip. Figure (5.3b) shows that as the gap width increases past δ >0.1 mm, the surface is pulled laterally. At each subsequent height, the droplet is shifted a greater amount from the centerline (a greater radius at Z) than for smaller gaps. As δ increases, the surface offset distance widens even further.

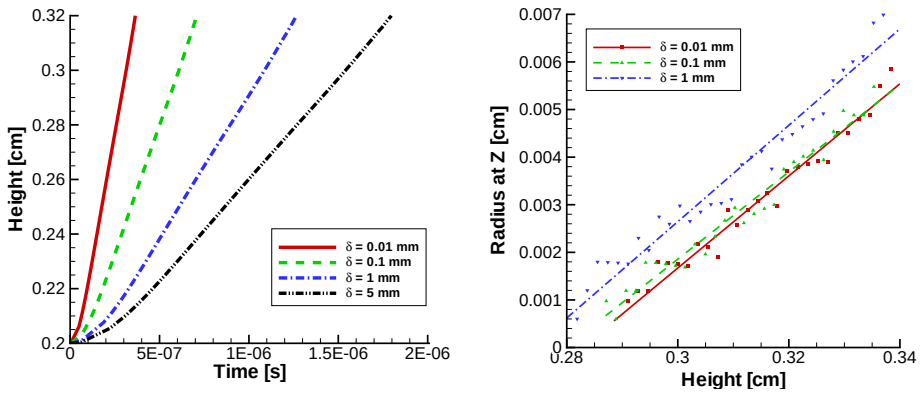

(a) Maximum droplet height versus time (b) Radial position versus maximum height

Figure 5.3: Effect of electrode gap variation on droplet spread

5.1.2 Effects of electric field

As predicted in previous analysis, the strength of the electric field at the surface strongly influences the speed of formation, behavior and shape of indium droplets. There is a strong two-stream pull towards the edge of the two electrodes in this simulation. Note that with a stronger field, significantly smaller drops occur since the shorter formation time pulls off the droplets before local surface equilibrium restabilizes the shape.

The effect of varying the electric field can be demonstrated in multiple ways. By plotting the uppermost point on the axis, Fig. (5.4) shows its height and velocity versus time as a function of electric field. The pattern is similar for all cases, with a trend of later separation and lower velocity for smaller electrode potentials. Under the smallest electric field of 0.1 V/nm, the surface height eventually reaches the same vertical position as under the other larger fields, but with a significant time delay. The claim of droplet evolution similarity is supported by the fact that the surface height is shifted, but otherwise identical in Fig. (5.4a).

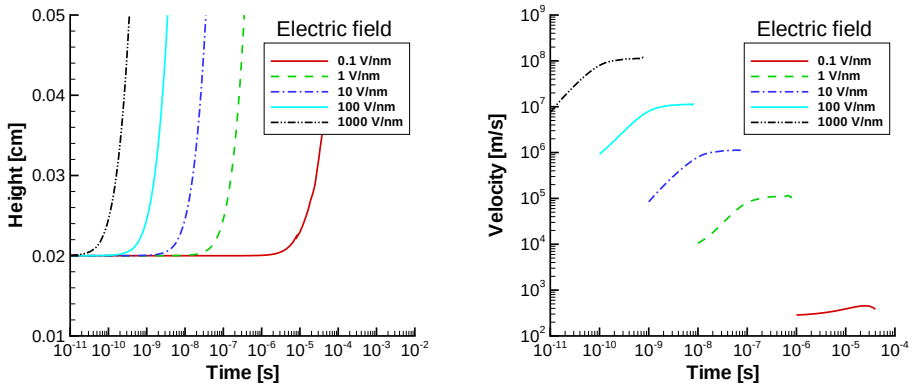

Figure 5.4: Effect of electric field variation on droplet vertical position and velocity

5.1.3 Effects of viscosity

The viscosity of the simulations is varied over several orders of magnitude; The viscosity of 0.1 μ_{In} occurs around 2,000 K while the more viscous 10 μ_{In} occurs near 200 K. As the fluid becomes thinner at higher temperatures, it forms into droplets sooner, the droplets form closer to the original surface, and disturbances in the fluid move down the needle much more rapidly. This increase in surface instability is associated with the formation of Faraday droplets, as discussed previously in Sec. (1.3.3).

In Chapter III, it was shown that viscosity does not have an important role in shaping the surface evolution. Figure (5.5) confirms this, with the shape barely changing despite varying the viscosity μ from zero to one thousand times indium's operational viscosity at 453 K.

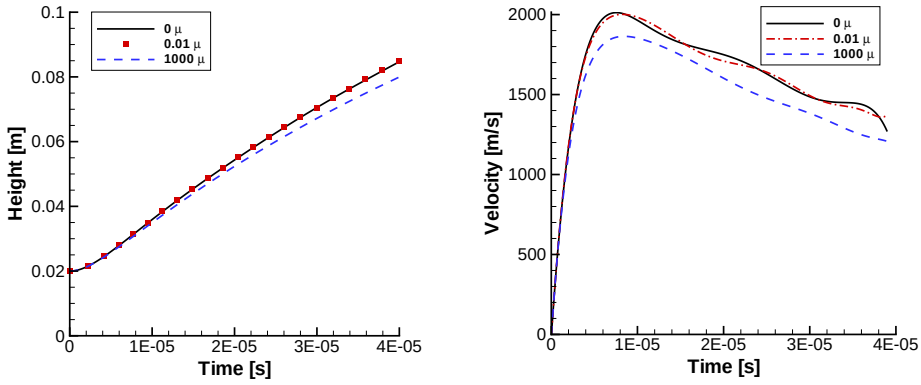

Figure 5.5: Effect of viscosity variation on droplet vertical position and velocity

Treating the needle as a 1.0 x 0.3 cm cone, and assuming that the liquid is one thousand times as viscous (i.e. like glycerin), 3.2×10^{-3} N of resistive force exists along the length of the needle. For a 100 μA current and corresponding mass flux of 0.3 $\frac{\mu g}{s}$ [72], this equates to a 1.07×10^{7} $\frac{m}{s^2}$ deceleration force of the fluid. In the first

8 μs of the propellant being on the needle in Fig. (5.5b), this resistive force slows the detachment velocity by 85 m/s, mirroring the small decrease in speed shown in the simulation.

5.1.4 Effects of surface tension

Simulations were also performed in which the surface tension was varied by a couple orders of magnitude higher and lower. At higher values of surface tension σ_{In}, the droplets snap off more slowly since the high cohesion and tension of the surface interface resists droplet formation. As mentioned in Sec. (4.1), surface tension resists the electrostatic pull from the ring electrode. Hence, increased surface cohesion reduces the pre-snap off droplet formation velocity. This illustration furthers the dissertation's claim of surface tension as a driving force of surface shape and time evolution.

Liquid indium has a tremendous surface tension, about ten times greater than water and larger than mercury. None of the reference books listed any material that had more than three times indium's pull, and only liquid platinum came close [78]. As σ is increased from zero to one thousand times indium's operational surface tension in Fig. (5.6), the liquid velocity is reduced from 2,500 m/s to zero. At these extreme values, a droplet cannot form from a surface electric field of 10 V/nm. As the initial surface begins narrowing around t=8×10^{-6} seconds, the shape curvature increases and the impact of the higher $-\sigma \nabla \cdot \overrightarrow{n}$ term from Sec. (4.1) causes surface necking and droplet formation to precipitate.

5.1.5 Importance of parameters at needle tip

Previous sections addressed the gross impact of various forces, such as surface tension and viscosity. However, in a microscopic volume around the needle tip,

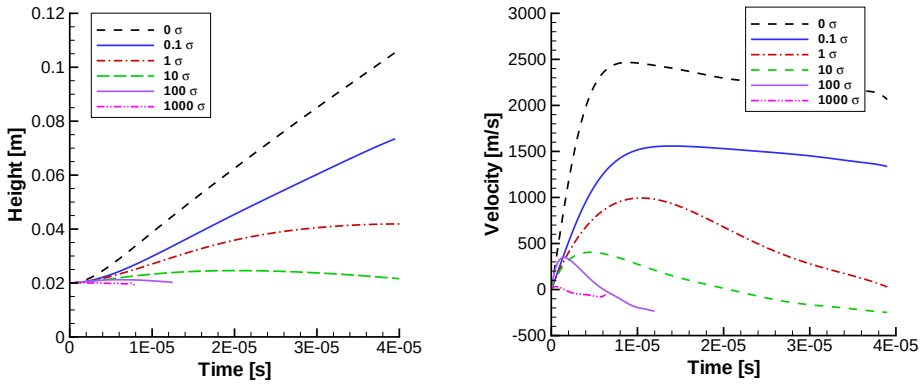

Figure 5.6: Effect of surface tension variation on droplet vertical position and velocity

the relative magnitudes of these forces could be dramatically different. Equation (5.1) presents the nondimensional Navier-Stokes equation [57]. Using the local tip parameters allows an investigation of forces in the droplet snapoff regime.

$$c_t^* + (c^* \cdot \nabla)c^* = -\nabla P^* + \frac{1}{Re}\nabla^2 c^* \tag{5.1}$$

Here, c=(u,v) is the fluid velocity in the (r,z) direction and P is the hydrodynamic pressure. Arrive at the nondimensionalized pressure term $P^* = P/P_0$ through dividing P by $P_0 = \frac{1}{2}\epsilon_0 E^2 = 4.4 \times 10^8$ Pa. The other starred terms can be calculated by using the needle radius of curvature $r_0 = 5 \times 10^{-6}$ m, time $t_0 = \frac{r_0}{E}\sqrt{\frac{2\rho}{\epsilon_0}} = 2.1 \times 10^{-8}$ s, fluid velocity $c_0 = r_0/t_0 = E\sqrt{\frac{\epsilon_0}{2\rho}} = 241$ m/s and viscosity $\nu = 2.4 \times 10^{-7}\,\frac{m^2}{s}$. In terms of these quantities, nondimensional Ohnesorge, Reynolds and Weber numbers are given in Table (5.2). The E*ötvös* (Eo), Morton (Mo), Froude (Fr) and drag (Cd) numbers are not listed since they incorporate gravity, a force neglected in our simulations.

If the droplet tip has a low Ohnesorge (Oh) number, viscous effects are small and the breakup is relatively independent of viscosity. At a large Weber (We) number,

Abbr.	Measures	Represents	Value
Oh	$\frac{\mu}{\sqrt{\rho\sigma r}}$	$\frac{\text{viscosity}}{\text{surface tension}}$	0.012
Re	$\frac{cr}{\nu}$	$\frac{\text{inertia}}{\text{viscosity}}$	4,950
We	$\frac{\rho c^2 r}{\sigma}$	$\frac{\text{inertia}}{\text{surface tension}}$	3,840

Table 5.2: Dimensionless numbers

the jet is unstable to shorter waves, resulting in smaller droplets [248]. As the tip radius of curvature decreases, viscosity become more important [64, 231] as the $\frac{1}{Re}$ term shrinks. However, there is a physical minimum to the curvature, as the needle tip is a physical object. With the rapid velocity c, even reducing the tip curvature κ over two orders of magnitude to 20 nm still has the viscous term having a minimal impact with $\frac{1}{Re} \ll 1$.

Repeating the dimensional analysis from Chapter (3), Table (5.3) plots the nondimensional numbers using the dimensions of the needle tip. Table (5.4) uses those values to plot the relative important of inertia, surface tension, viscosity and gravity within this small volume. Smaller perturbation order values relate to stronger impact on surface evolution, so inertia is many times more important than gravitational forces.

The conclusion from both examinations of nondimensional numbers is that due to the extreme electric field in a needle FEEP, viscosity at the microscopic and macroscopic levels is not an important force in determining surface evolution. The rapid fluid movement at the tip, however, causes inertia to become the driving force component. While the level set/ boundary element hybrid approach can simulate all these forces, this analysis supports the overall claim of viscosity being of secondary importance.

Experimental parameters		Nondimensional terms		Order ϵ
ρ $\left[\frac{kg}{m^3}\right]$	7310	W	3.9×10^3	-3
σ $\left[\frac{N}{m}\right]$	0.546	B	1	0
$\tilde{p_{es}}$ [Pa]	1×10^{10}	F_r	1.2×10^8	-8
v_0 $\left[\frac{m}{s}\right]$	241	Z_ν	2.2×10^{-5}	5
r_0 [m]	5×10^{-6}	Λ_1	2.4×10^{-4}	4
z_0 [m]	5×10^{-5}	Λ_2	0.01	2
$\tilde{p_a}$ [Pa]	0.13	$\frac{p_a r_0}{\sigma}$	3.0×10^{-12}	12
μ $\left[\frac{N \cdot s}{m^2}\right]$	1.76×10^{-3}	$\frac{p_{es} r_0}{\sigma}$	2.96×10^{-4}	4
$f_{inertia}$ [N]	1.06×10^{-2}	$\frac{1}{B \cdot W}$	2.57×10^{-4}	4

Table 5.3: FEEP experimental parameters and resulting nondimensional terms around tip

Force	O(ϵ)
inertia	0
surface tension	3
viscosity	5
gravity	8

Table 5.4: Relative force importance at needle tip

5.1.6 Summary of parameter adjustment

Variation of the electrode's horizontal spacing and potential affects the size and velocity of droplets detaching from the surface. Since the droplet velocity is used for mass efficiency calculations, wider rings, lower potentials and larger needle tips result in lower η_m, as a greater percentage of emission is in the form of large droplets. Increased numbers of droplets produce less thrust per milligram of propellant, as discussed in Sec. (1.4.3). Finally, large surface electric fields give rise to large power requirements, sharper surface curvature and higher efficiency, with there being a minimum critical electric field below which droplets will not form. As that point is approached, fewer and larger droplets are produced over a longer time.

Altering the viscosity of the propellant had a very small effect on the velocity of detached droplets. Increasing from an inviscid flow to one of a thousand times indium's true viscosity resulted in a less than 5% reduction in vertical surface velocity.

However, surface tension provided a very significant retarding force on the evolution of a droplet. The velocity of the droplet surface is substantially reduced and the characteristic evolution time increased as σ grows. Multiple approaches such as asymptotic analysis and the surface curvature feedback of Eqs. (1.20 and 4.3) confirm that same conclusion.

5.2 Stream predictions

Many predictions about the characteristics of detached droplets can be made. Two of the analyses that are most amenable to future experimental validation are the generation of probability density functions and time of flight current decay.

5.2.1 Probability density functions

As discussed in Sec. (4.6.1), relative droplet charges can be more accurately viewed when fitting the data to a bigaussian distribution. After detachment, Eq. (4.62) demonstrates that droplets have calculable charge and area. During operation, a steady stream of droplets detach from around the needle tip. Those droplets are then tracked as they travel upwards towards the electrodes. As described in Sec (1.3.3), overcharged droplets lose charge over time. In Fig. (5.7), an example droplet with too many electrons for its mass is shown breaking up into smaller droplets at y=0.762 cm and y=0.768 cm. The change in relative charge for the first droplet is shown in an increasing mass-to-charge ratio from 9,000 to 11,000 to 14,000 atoms per electron.

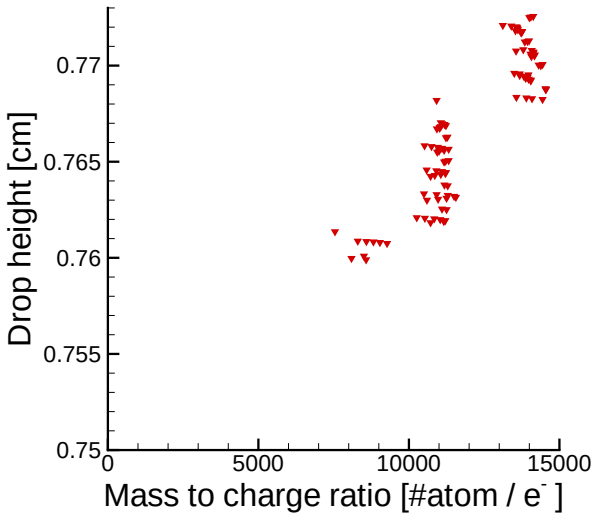

(a)

Figure 5.7: Overcharged droplets undergoing Coulomb fission

Mass to charge ratio

Recording the properties of 7,600 droplets at snap off gives a mass to charge ratio distribution of Fig. (5.8). The first figure is the entire distribution, from an MTCR range of [0:20,000], with most of the droplets having a charge from 1,000-9,000 atoms/electron, while the finer resolution "zoomed" picture of Fig. (5.8b) yields a double humped bigaussian within this range. They are from the same simulation, with the increased histogram details due to the smaller bin size. The bigaussian shows two sub-peaks at 500-1500 and 3,500-4,500 atoms/electron. There is a large high-mass tail to this distribution, predicting a larger population of massive, slow moving droplets.

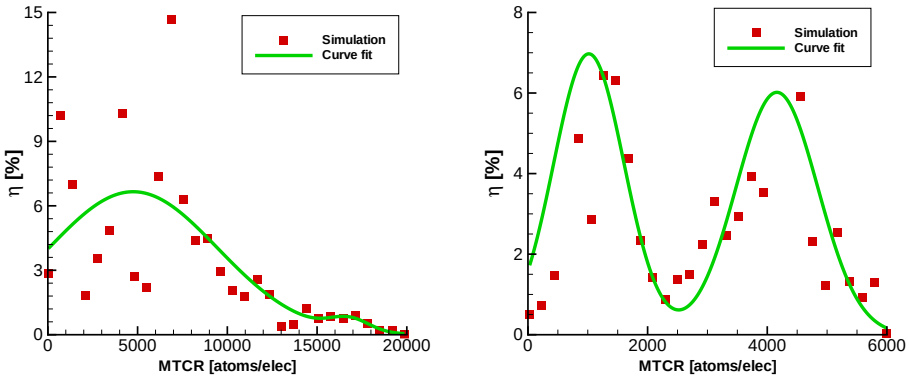

Figure 5.8: Mass to charge probability density distributions for 7,600 droplets

The simulated MTCR relative charge of 4,000 in Fig. (5.8) is in remarkable agreement with experimental measurements. Fehringer found that the most common sized droplet had a radius of 0.04 μm [72]. Charged to the Rayleigh limit, those droplets have $q = \frac{\sqrt{64\pi^2\epsilon_0\sigma r^3}}{e} = 2,774$ charges, where the number of indium atoms is determined by Eq. (5.2).

$$\begin{aligned} \#\text{in. atoms} = &\quad \rho A_b (MW)_{in} \\ = &\quad (7300)\left\langle \tfrac{4}{3}\pi(4\times10^{-8})^3 \right\rangle \left(\tfrac{1\,\text{amu}}{1.6606\times10^{-27}kg}\right)\left(\tfrac{1\,\text{molecule}}{114.818\,\text{amu}}\right) = 1.026\times10^{7} \end{aligned} \tag{5.2}$$

Dividing the number of atoms by the number of charges results in an experimental needle FEEP MTCR of $3,699\ \left[\frac{\text{mol}}{\text{charge}}\right]$.

Satellite droplets When droplets form from the tip of a FEEP, smaller satellite droplets also commonly form. The electric field directly impacts the formation and fate of these secondary droplets. The field influences the volume of these satellite droplets by modulating snap off speed and the distribution of surface charge on the satellite droplets, the primary drop and the liquid remaining on the needle. In line with the discussion of Sec. (1.3.3), these satellite droplets have larger relative charges [106] and form the smaller and lower MTCR hump shown in Fig. (5.8). An example detachment location is shown in Fig. (5.9a), where four droplets had detached from the surface. The variation in area of the new droplets is analogous to a faucet, where a large droplet is frequently followed by a small one. Whether electrostatically charged or not, this trend of oscillating the size of detached areas is common in droplet formation [282]. Figure (5.9b) displays the cross sectional area of sequentially created droplets from one location. The substantial changes in droplet area occur from a large volume to a small volume and vice versa, in agreement with MTCR predictions.

The claim of the satellite droplets largely being part of the low MTCR population and therefore having greater relative charge is supported via Fig. (5.10). The greatest number of charges per cubic meter is for the smallest diameter droplets.

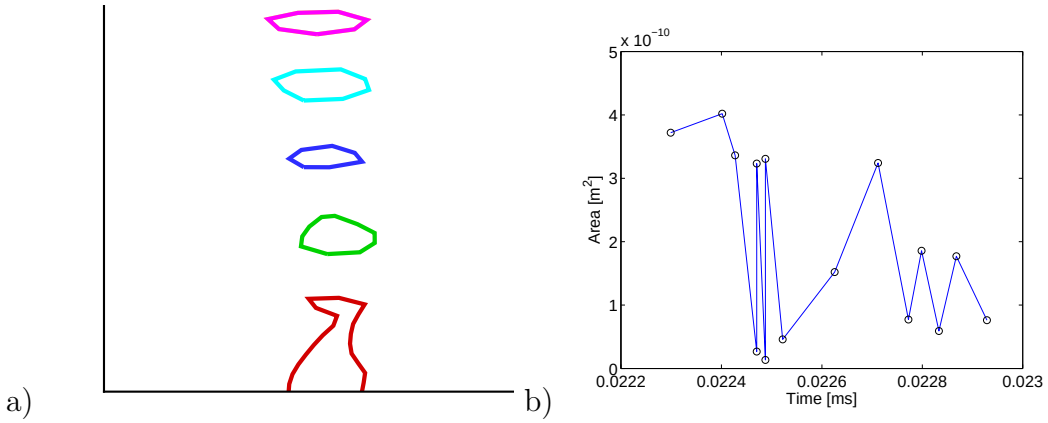

Figure 5.9: Droplets a) detaching from a jet and b) area at initial detachment. The abrupt spiking from large to small droplets is consistent with experiments

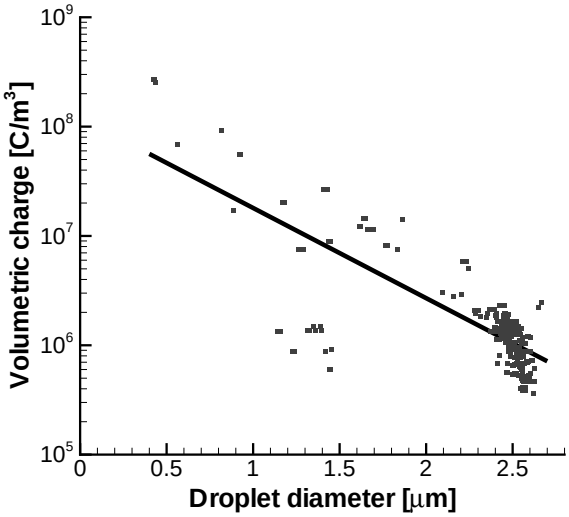

Figure 5.10: Droplet volumetric charge density versus diameter. The smallest satellite droplets are much more highly charged.

As the droplet diameter increases, the Rayleigh limit caps the number of electrons on the surface, with greater diameters having a lower maximum volumetric charge density before Coulombic fission occurs. The large number of droplets with a diameter around 2.5 μm and a tight volumetric charge of that population represent the common MTCR of 4,000 presented earlier.

Charge distributions The cumulative distribution function (CDF) of 7,600 droplet charges is shown in Fig. (5.11). While the largest group of charges is around $2-3\times10^{-8}$ C, there are multiple other fairly evenly distributed populations scattered throughout the range.

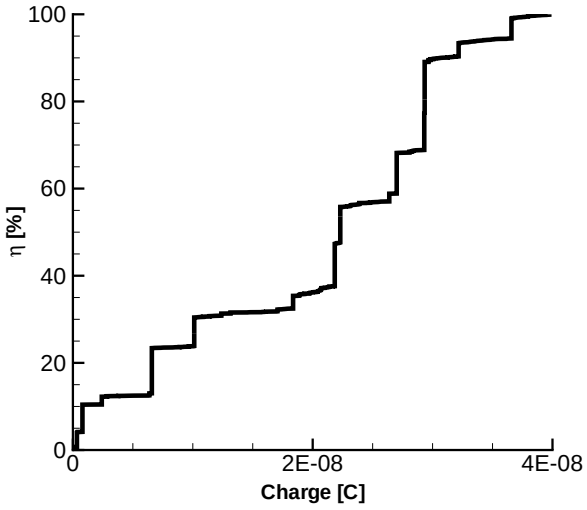

Figure 5.11: Charge CDF. Multiple droplet charges are visible, with the bulk conduction occurring around 3×10^{-8} C.

Droplet diameter

The effective diameter is determined in axisymmetric coordinates by using the position of the droplet center R and radius r_{drop}. Since the boundaries of detached liquid

are not spherical, the radius is based on the equivalent area of the corresponding circle. That circle is then rotated around the axis, forming the torus of Fig. (4.11). Equation (5.3) relates the torus volume V_{torus} and droplet radius to the effective diameter d_{eff}.

$$\begin{aligned} V_{torus} = 2\pi^2 R r_{drop}^2 &= \tfrac{1}{6}\pi d_{eff}^3 \\ d_{eff} &= \sqrt[3]{12\pi R r_{drop}^2} \end{aligned} \tag{5.3}$$

The calculated diameter distribution for 7,600 droplets is provided in Fig. (5.12). Many of these shapes have an effective diameter d_{eff} of 1 μm - 3 μm. The smaller satellite droplets described in Fig. (5.10) of radius 0.5-1.5 μm are clearly shown here. The simulated diameters are larger than the 0.04 μm diameter experimentally reported by ARCS, but only a qualitative comparison is possible since their exact system dimensions (needle radius of curvature, fluid thickness, distance from the electrode, etc.) are unknown. The simulation as run could resolve droplets only down to 0.1 μm, though there is no theoretical smallest bound as the grid size decreases.

An example of how droplet diameter varies due to a changing system setup is shown in Fig. (5.13). In a related simulation, the needle width is doubled while the length is kept constant. The resulting main diameter probability peak separates, with a larger and narrower band centered around 3 μm. Based on the droplet PDF changes, it seems reasonable to conclude that the orders of magnitude uncertainity in the experimental dimensions could explain the factor of fifty difference between the ARCS data and the simulations.

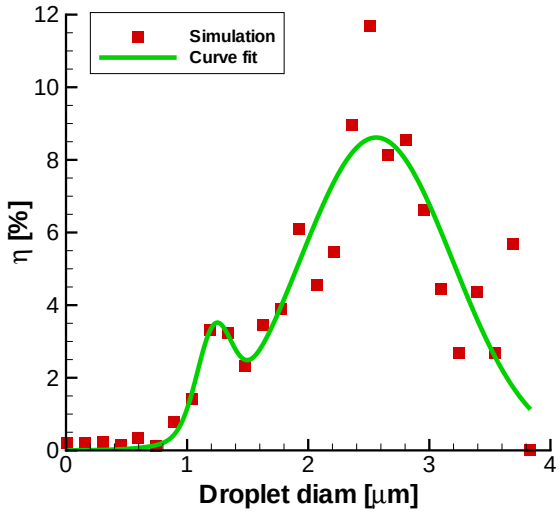

Figure 5.12: Droplet effective diameter d_{eff} PDF

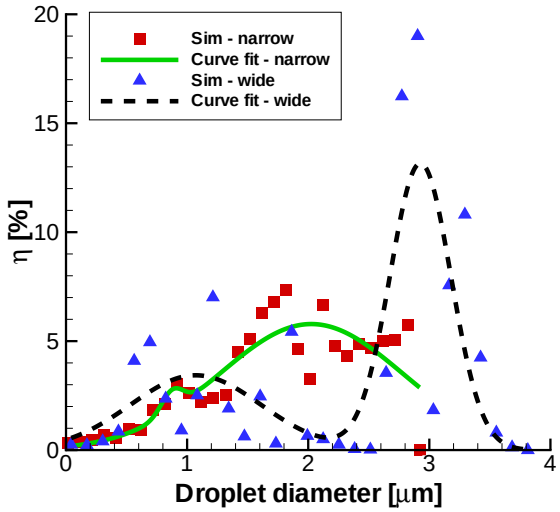

Figure 5.13: Relative charge variation from two different needle widths

5.2.2 Time of flight probability distributions

Using the bigaussian and time of flight algorithms described in Sec. (4.6.2), the MTCR of Fig. (5.8) can be used to create an expected TOF current collection profile. With the spatial distribution of the acceleration function $f(x, \alpha)$ in Eq. (4.107), the relative droplet acceleration density is shown versus the distance above the needle in Fig. (5.14). The contours of $fVol_{PDF}$ in the figure display relatively how many droplets are in a particular region of space. The two pictures display how the density of droplets varies depending on whether or not the histogram uses a fitted bigaussian to smooth the underlying distribution. Further away from the needle (and thus closer to the collecting electrode), the droplets move faster and hence spend less time in any [x+dx) area, yielding a smaller relative flux probability. The result is that when counting droplets in a set volume dx for a finite amount of time dt, the greater their relative charge and velocity the fewer droplets are tallied.

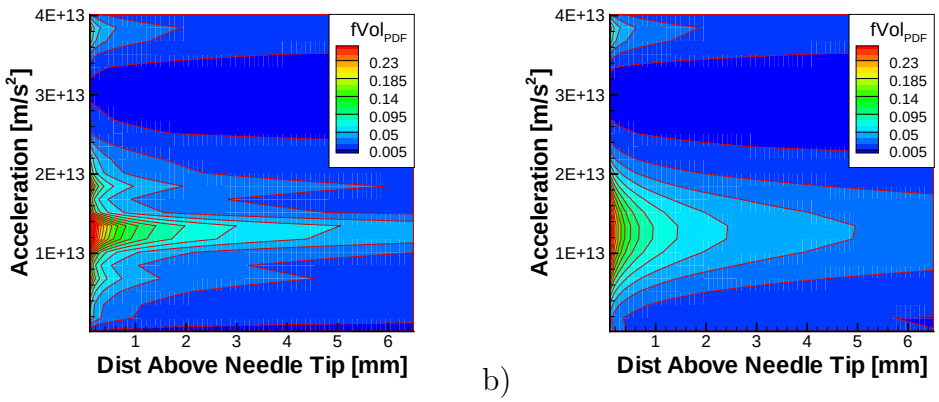

a) b)

Figure 5.14: Variational velocity shifting function from a) unfitted and b) fitted MTCR distributions

However, if the data are not shifted and a zero median velocity vector from Sec. (4.6.2) is assumed, Fig. (5.15) shows how the density of variously accelerated droplets

does not vary downstream. This treatment results in an unrealistic approximation where all droplets move at the same speed, regardless of relative charge.

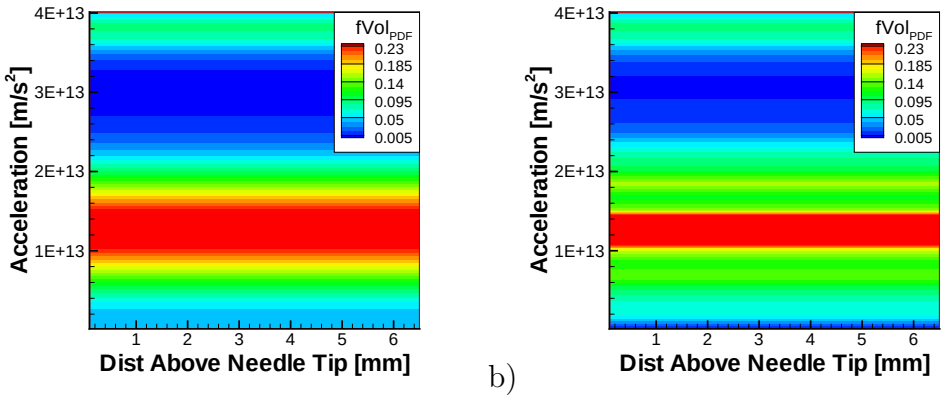

Figure 5.15: Unshifted velocity function using a) unfitted and b) fitted MTCR distributions

The experimental setup used by Gamero-Castaño in Fig. (4.26) was reproduced numerically for a needle FEEP, with indium as a propellant [85]. Figure (5.16) displays predicted TOF current collection profiles for that configuration. The magnitude of the current gradients varies by over 20% depending on whether the data are fitted and shifted to a bigaussian format. In particular, the predicted current at intermediate times from 20 to 40 ns is significantly higher when using the fitted and shifted results from the double humped distribution. Studying the four cases, it follows that data shifting yields the largest contribution towards shape change.

5.2.3 Summary for stream characteristics

In this subsection, droplet breakup, probability density functions for relative and absolute droplet charge and droplet diameter, and time of flight analysis for current collection profiles were presented. When simulating the current as a function of time, it was recognized that droplet velocity varies as they accelerate toward the electrode;

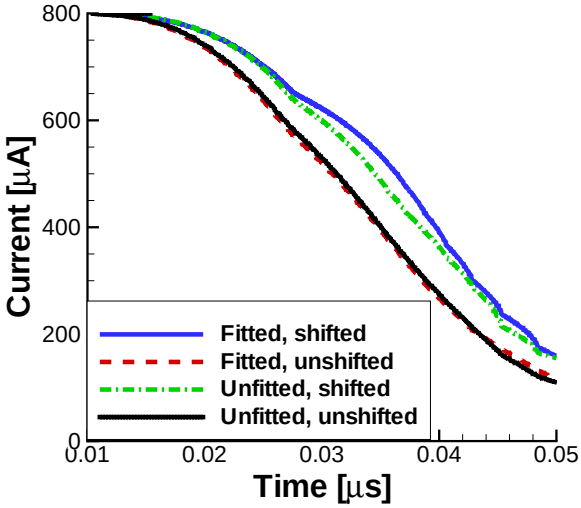

Figure 5.16: Simulated time of flight current collection profiles

this fact needs to be included when modeling time of flight.

5.3 Comparison with independent work

The BEM/LS model matched the shape and characteristics predicted by unrelated approaches. The pre-snap off surface evolution is matched to an independent electrohydrodynamic (EHD) simulation while the predicted MTCR mirrors that required for an experimentally observed droplet angular spread.

5.3.1 Pre-snap off shape

Suvorov presented a self-similar numerical simulation of a perfectly conducting fluid [230]. He modeled the equations of motion using electrohydrodynamics, simulating a field emitter surface evolving up to the full Taylor cone angle. Figure (5.17) displays that work and the level set/boundary element works side by side; note that the EHD method can only track the surface until the Taylor cone angle is reached. Electrode position, surface tension and viscosity were matched, producing models

that are similar in space and time. The surface locations were recorded at 81, 104, 116 and 123 ns. The evolution times for this case are shorter than the previously presented cases in Sec. (5.1) due to a different geometry and surface electric field used.

Figure (5.18) presents the angle of the surface $\chi(r)$, measured from vertical to the surface tangent. A fluid peak on the order of $50\,\mu m$ wide forms and becomes more pronounced over time. As time increases, $\chi(r)$ continues to decrease as the surface becomes vertical and droplet necking begins. This is the initiation point for the first droplet detachment.

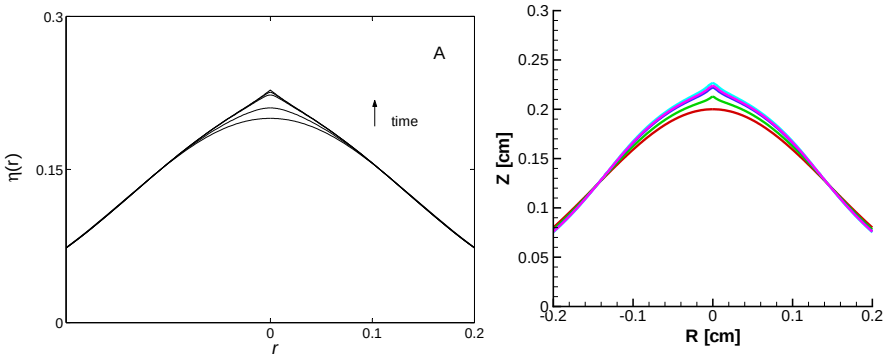

(a) Suvorov EHD simulation (b) BEM/LS replication

Figure 5.17: Centerline tip formation

The radial position of the minimum $\chi(r)$ is plotted in Fig. (5.19) when varying the electric field through five orders of magnitude. Similar behavior is seen for all the runs except for the lowest field of 0.1 V/nm. Here, the relatively weak pull of the electric field allows sufficient time for the surface tension forces to cause the shape to re-establish. This noticeably elongates the duration, shape and extent of the droplet surface evolution. Similar behavior was shown for exceptionally large surface tension when the surface tension and electrostatic forces were in equilibrium.

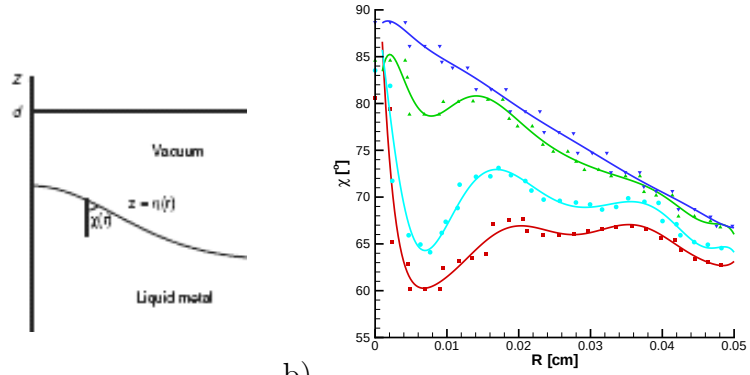

a) b)

Figure 5.18: Angle $\chi(r)$ a) defined from vertical to tangent to the surface and b) plotted versus radial distance at increasing times

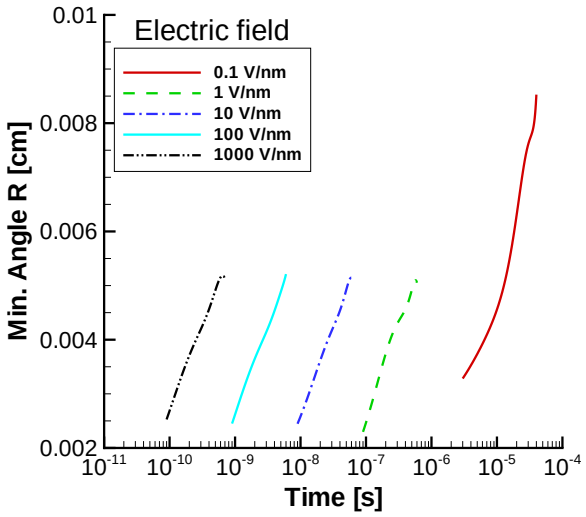

Figure 5.19: Radial location of steepest surface for several electric fields

Suvorov's approach

In this section, the computational methods Suvorov used to electrohydrodynamically simulate the fluid behavior of a field emitter under electrostatic forces [230, 231] are described. This approach produces self-similar, asymptotic conic solutions as $t \rightarrow t_c$, a point where the equations of motion reach a singularity and the tip radius of curvature goes to zero. The evolution equations assume that the apex electric field is much greater than the electrode, $|\nabla U|_{apex} \gg E$. The surface interface η evolution is described via Eq. (5.4).

$$\frac{\partial \eta}{\partial t} = v - u\frac{\partial \eta}{\partial r} \tag{5.4}$$

Time advancement comes from an explicit forward Euler discretization, where the time increment $\delta t < 0.25(Re)\delta r^2$ [191]. At the free surface, the normal stress components are the electrostatic P_{es} and surface tension P_{st} terms. The hydrodynamic pressure is then given by Eq. (5.5).

$$\begin{aligned} P|_{z=\eta(r,t)} &= -P_{es} + P_{st} \\ &= \tfrac{1}{2}\epsilon_0 E^2 + \sigma\kappa \end{aligned} \tag{5.5}$$

The total surface curvature κ is described by Eq. (5.6),

$$\kappa = \frac{1}{\sqrt{1+\eta_r^2}}\left\{\frac{\eta_{rr}}{1+\eta_r^2} + \frac{\eta_r}{r}\right\} \tag{5.6}$$

where subscripts are used to denote partial differentiation with respect to position, e.g. $\eta_r = \frac{\partial \eta}{\partial r}$. These partial derivatives are approximated from 2nd order central difference expressions on a fixed staggered Eulerian grid, where the pressure is located in the cell center and the velocities are at the middle of the cell edges. There is no

approximation of the surface shape by polynomials, nor is there repeated manual interventions to smooth the shape. The boundary conditions for the surface are given in Eq. (5.7).

$$\begin{array}{lll} u, v|_{z=0} = 0 & u, v|_{r=edge} = 0 & u|_{r=0} = 0 \\ U|_{z=electrode} = U_0 & U|_{z=\eta(r,t)} = 0 & \frac{\partial U}{\partial r}|_{r=0,edge} = 0 \end{array} \tag{5.7}$$

Cusp formation discussion

Both the electrohydrodynamic approach of Suvorov and the combined level set and boundary element (LSBEM) approach treat surface tension as applying a pressure on the surface. Both of them calculated that force as the surface tension multiplied by the curvature, $\sigma\kappa$. While [231] determined κ through 2nd order central differencing of the geometrically compressed cells around the tip, the LSBEM applies a volume of fluid (VOF) or level set (LS) method for the cell volume.

One possibility for the difference in surface evolution is that the shape determination in LSBEM could be made using either VOF or LS. Figure (5.20) shows the LSBEM simulations at various times when the volume was computed with both approaches. The level set location of the cell surface tends to slightly overstate the overall volume, with an increasing error in time. However, this error is very small, as both the surface and its derivative in Fig. (5.20a-b) are very similar at each timestep. Therefore, the choice of surface location method does not explain the evolved shape variation.

Another possibility to explain the differences is that the limits of the governing equations are fundamentally different. The formation of a tip cusp is to be *expected* for a dynamic evolution simulation [162, 165]. This is because Taylor's analysis was

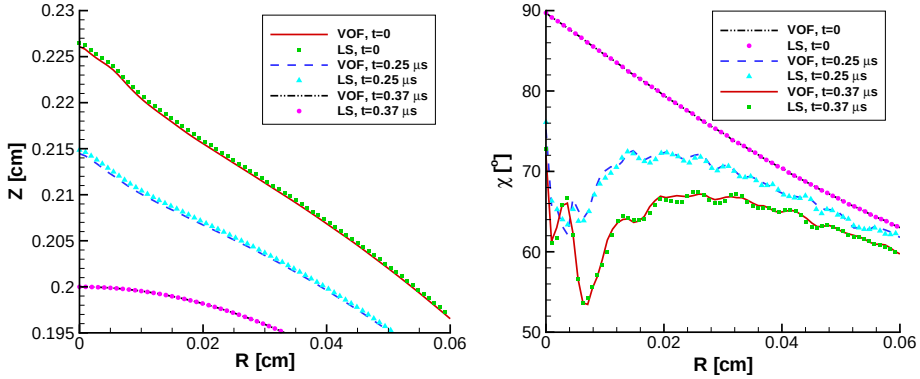

(a) Surface location change over time (b) Surface angle change over time

Figure 5.20: Surface variation using the volume of fluid (VOF) or level set (LS) methods to calculate interface curvature.

for a hydrostatic balance [271], but with a moving liquid there are associated pressure differences and it is not in static equilibrium. In addition, a perfect 49^0 Taylor cone can come about only when the tip space-charge effects are ignored [75, 130]. As the liquid comes to a finer and finer point, the EHD equations ignore viscous stress and predict infinite point stress as simulated time $t \rightarrow t_c$ [230, 231]. This incorrect underlying asymptotic force prediction is shown in Fig. (5.21). The electrohydrodynamic equations do not produce simulations that match those observed in experiments. Since the tip elongation is not seen, the protrusion physically present cannot be explained by pure hydrodynamic effects alone, and a breakdown in the EHD equations occur when the feature size becomes very small [76].

After a further review of the literature, an examination of surface oscillations, a consideration of space charge and noting the incorrect EHD-predicted infinite surface stress, the prediction of a perfect Taylor cone angle from a dynamically evolving liquid metal ion source does not accurately account for the physical effect of surface tension on the evolution of the surface. The formation of a cusp as shown in the LSBEM

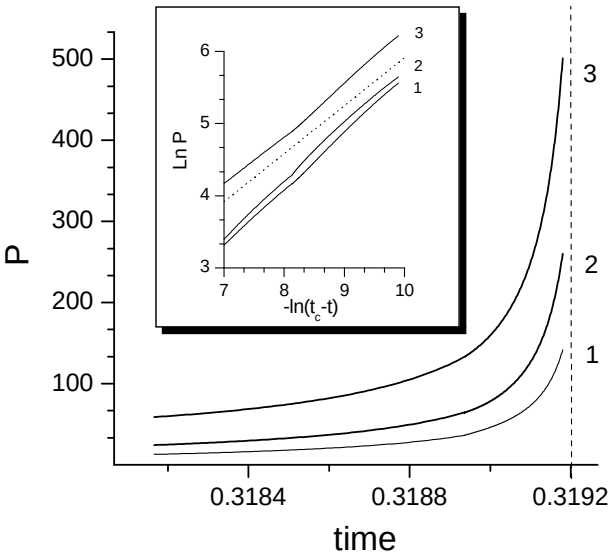

Figure 5.21: Asymptotic (1) kinetic energy density; (2) surface tension stress; and (3) electrostatic stress as $t \rightarrow 0.03192$ [231]

simulations more closely matches with experimental and theoretical behavior at the small scale around an emitter tip.

Surface oscillations

The numerical problem of liquid conductors in a strong electric field is very prone to produce oscillations [258, 257]. This is simply because the driving forces (electrostatics and surface tension) are acting in opposite directions. Both forces are very sensitive to surface curvature, which depends on the surface location's second derivative. Normally, it is easy to distinguish between a real physical effect (electrocapillary waves) and numerical errors (oscillations). The simple criterion is that any physical effect has to be resolved by a reasonable number of numerical points. The dispersion relation z for physical surface waves in the presence of an electric field is given by Eq. (5.8), with the resulting disturbance

$$z(r,t) = (a)\exp[i(kr - \omega t)] \tag{5.8}$$

described as *electrocapillary waves* [137]. The dynamic frequency of growth is given by Eq. (5.9),

$$\omega^2 = -\frac{\epsilon_0 E_0^2}{\rho}k^2 + \frac{\sigma}{\rho}k^3 \tag{5.9}$$

where ω is the frequency and k is the wave number. If $k > k_0 = \frac{\epsilon_0 E^2}{\sigma}$, $\omega > 0$ and the surface is stable. However, if $k < k_0$, ω is imaginary and surface instabilities develop. The maximum growth rate $k = \frac{2}{3}k_0$ leads to a temporal scale T_0 of Eq. (5.10) [231]. For a needle FEEP, $T_0 = 9.5\,\mu s$.

$$T_0 = \frac{\pi\sigma}{E^3}\sqrt{\frac{27\rho}{\epsilon_0^3}} \tag{5.10}$$

Due to these inherent physical instabilities, oscillations will form in the fluid on the side of the needle over time. Figure (5.22) supports the claim that the simulated waves are a natural physical response to an electric field and are not a numerical artifact of grid size. At six different grid densities and levels of adaptive mesh refinement, Fig. (5.22a) displays the same surface location without oscillations at T=2.3 $\mu s < T_0$, while Fig. (5.22b) shows a magnified section indicating that as $T \to T_0$, increasing oscillations occur.

5.3.2 Post-snap off radial spread

The PDF simulation results in Fig. (5.8) have shown a MTCR large frequency in the droplets around 4,000 indium atoms per electron. The following subsection attempts to support this finding by presenting a simple model that relates an observed droplet angular spread to the relative charge necessary to cause this distribution. The

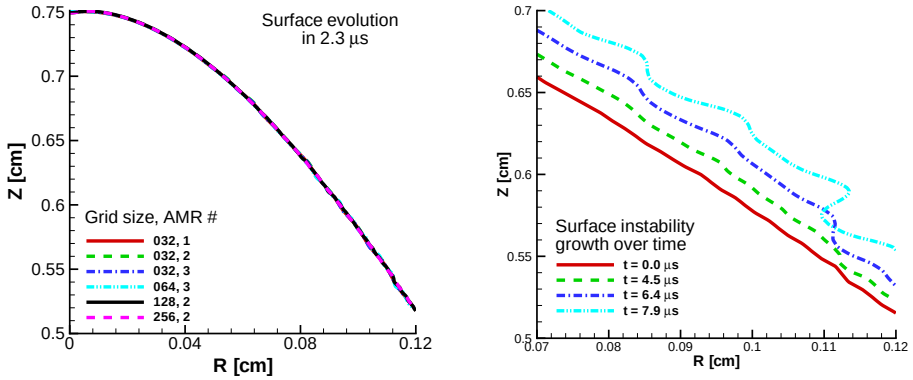

(a) Grid size surface variation with no oscillations

(b) Physical electrostatic oscillations over time

Figure 5.22: Surface instability growth

MTCR of this order-of-magnitude analysis was found to approximate the simulation maximum probability value.

Droplet average accelerations

For a droplet to be deflected in flight, it has to experience a repulsive force. Figure (5.23) shows an experimental set up that records the angular density and volume of droplets from a FEEP [72]. The axial vertical velocity u of the droplet after passing the shutter is constant and is a function only of its relative charge. The off-axis horizontal velocity v is a function of average acceleration $\overline{a}$ and time, or $v = \overline{a}t$. The time of flight is determined by how long it takes the droplet to travel on its angled trajectory before impacting the surface of the catcher studs. Due to the collection surface being a constant radius from the emitter, the larger the offset angle Ψ and therefore the greater the horizontal distance traveled, the less vertical distance needs to be traversed. Using dimensions of the ARCS experiment, the droplet vertical velocity and time of flight are given by Eq. (5.11).

$$\begin{aligned} u\left[\tfrac{m}{s}\right] &= \sqrt{2E\Delta x\left(\tfrac{q}{m}\right)} = 109.1\sqrt{\tfrac{q}{m}} \\ t[s] &= 3.667\times 10^{-5}\cos\Psi\sqrt{\tfrac{m}{q}} \end{aligned} \tag{5.11}$$

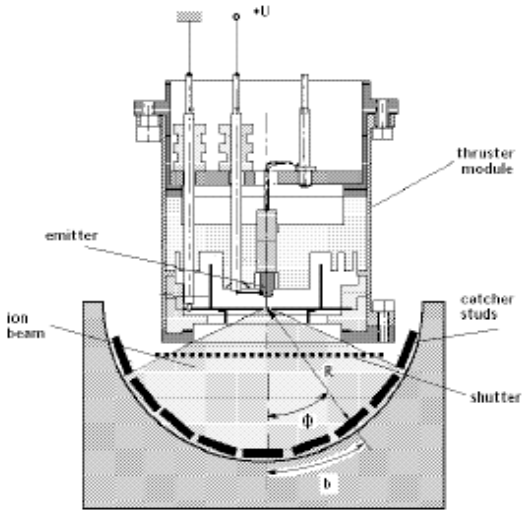

Figure 5.23: ARCS droplet angular measurement apparatus

Inserting the horizontal distance $0.04(\sin\Psi)$ into $r = v_0 + \frac{1}{2}\int_{t_i}^{t_f} at\,dt$, the necessary acceleration and horizontal velocity for a charged droplet to reach the collection ring at an angle of Ψ are described by Eq. (5.12). Using these equations, the accelerations needed to force variously charged droplets off-axis is shown in Fig. (5.24). For example, a droplet with an MTCR of 4,000 needs to experience an acceleration of $10^{10}\,\frac{m}{s^2}$ to be deflected 30^o by the time it travels 4 cm. Note that drops with a larger MTCR are relatively *less* charged, and so have a lower velocity and therefore a longer transit time before impact. Because of this longer flight time, a lower acceleration is needed to reach a given offset angle Ψ.

$$\begin{aligned} \overline{a}\left[\tfrac{m}{s^2}\right] &= 5.948\times 10^7\left(\tan\Psi\sec\Psi\right)\left(\tfrac{q}{m}\right) \\ v\left[\tfrac{m}{s}\right] &= 2181(\tan\Psi)\sqrt{\tfrac{q}{m}} \end{aligned} \tag{5.12}$$

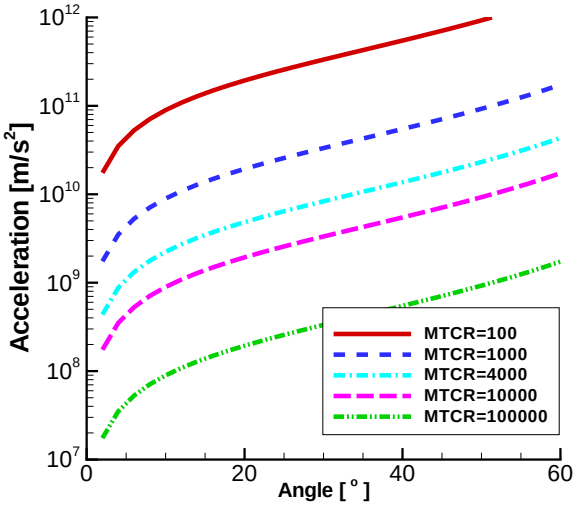

Figure 5.24: Average acceleration needed to cause a droplet with a chosen MTCR to arrive at various angles on the collection plates

Droplet number and volume fluxes

The droplet angular number and volume dependence for two different mass flow rates of 2.67 and 0.28 $\frac{\mu g}{s}$ are shown in Fig. (5.25). The corresponding field emitter currents are 250 and 100 μA respectively [72] . The data fittings are given by Table (5.5), where Ψ is the angle in degrees off axis measured from the electrode center to the collecting plate. The last column of mass-weighted mean angle is the point where half the total droplet volume is closer to the axis and half is further away. Since the droplets have already passed the accelerating electrode before entering the spreading area, the angular distention at higher mass flow rates is caused only by the increased number of particles electrostatically repelling one another.

The claim is that these density spreads can be caused by droplets that are relatively charged to the O(4000) indium atoms per electron predicted by the full BEM/LS hybrid approach. The approach uses the equality qE=F=$\dot{m}\overline{a}$, the repul-

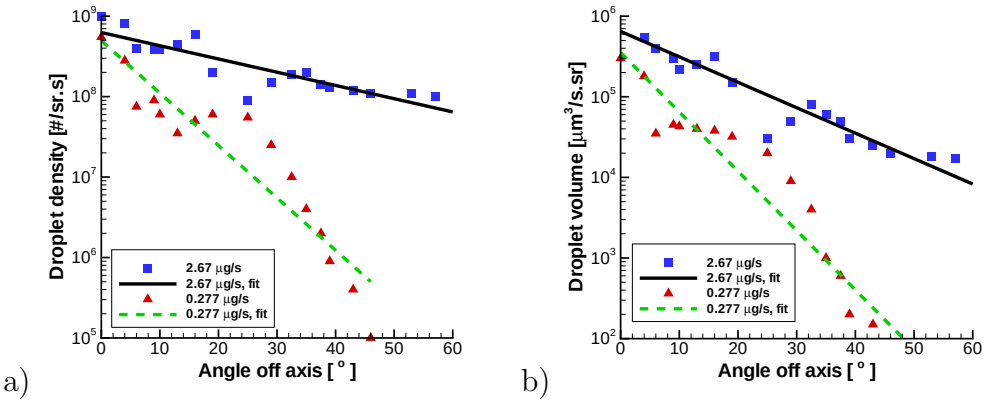

a) b)

Figure 5.25: Droplet a) number and b) volume density per steradian per second versus angle Ψ off axis

Type of flux	Mass flow rate	Fit	Weighted Angle
$\left[\frac{1}{s \cdot sr}\right]$	$\dot{m}$ $\left[\frac{\mu g}{s}\right]$		$[^o]$
Number	2.67	$6.229 \times 10^8 \exp(-0.0378\Psi)$	
Number	0.28	$4.843 \times 10^8 \exp(-0.1494\Psi)$	
Volume	2.67	$6.400 \times 10^8 \exp(-0.0724\Psi)$	16.5
Volume	0.28	$3.443 \times 10^8 \exp(-0.1689\Psi)$	5.5

Table 5.5: Droplet angular flux and volume spray dependencies

sion as the square of the distance and the fact that the average value of the function $\overline{\int_{r_i}^{r_f} \frac{1}{r^2}\, dr} = \frac{1}{(r_f - r_i)^2}$. The model prediction was based on the mass of the j^{th} droplet being much less than the overall mass flux $\dot{m}_{tot}$, the current is 250 μA and the distance from the collecting ring to the needle r_f is 4 cm. The electric field E_j from the N_d detached drops is then given by Eq. (5.13).

$$\begin{aligned} E_j &= k \sum_{i=1, i\neq j}^{N_d} \frac{q_i}{r_i^2} \\ &= k\dot{m} \frac{8.403\times10^5}{MTCR} \sum_{i=1, i\neq j}^{N_d} \frac{1}{r_i^2} \\ &= \frac{1.230\times10^9}{MTCR} \sum_{i=1, i\neq j}^{N_d} \frac{1}{r_i^2} \\ &= 7.687 \times 10^{11}/MTCR \end{aligned} \tag{5.13}$$

Setting the electric field $E_j = \frac{\dot{m}}{q}\overline{a}$ from Eq. (5.12), the predicted MTCR is determined by solving for the mass to charge ratio at the mass-weighted angle 16.6^o. Converting from steradian solid angles, the rudimentary model predicts a $MTCR_{model}$ as given in Eq. (5.14). This simplistic model is remarkably close to the most likely relative charge predicted with the BEM/LS approach and is derived solely from the average droplet relative charge needed to match a given angular dispersion.

$$MTCR_{model} \left[\frac{\#\, atoms}{e^-} \right] = 8,700 \tag{5.14}$$

5.4 Summary

A combination of the level set and boundary element methods was used to simulate high conductivity liquid metal droplets expelled from a field emission thruster tip. This union avoided many of the obstacles of modeling detaching surfaces by reducing the calculation domain. The boundary element method provided a solution of the potentials and normal electric fields, thereby identifying the driving forces for

the liquid's evolution. Level sets allowed arbitrary surface geometries and the joining and separation of droplets. Through the use of level sets to identify the surface location instead of tracking discrete particles, manual boundary modification at each time step was unnecessary.

The qualitative and quantitative effects of varying the axial gap size, electrode potential, viscosity and surface tension were displayed. Larger droplets formed from smaller potentials or greater electrode gaps, viscosity, or surface tension. The formation of microdrops due to Rayleigh overcharging was shown. In addition, droplet charge and size probability density functions were calculated at detachment, with a large percentage of droplets having less than 5,000 atoms/electron and being around 2.5 μm in diameter. The varying size of molecules detaching from a single point and the corresponding formation of satellite droplets was proposed as an explanation for the dual-humped histogram.

Time of flight current predictions were made and the effect of shifting and fitting to simulation data was demonstrated. Finally, validation against two independent data sources was performed. Surface movement pre-snap off matches an EHD model. In addition, changes in droplet angular spread were examined. The off-axis particle densities agreed qualitatively and quantitatively with those predicted for droplets with a mean and mode MTCR between 1,600-40,000. The full LS/BEM hybrid model's simulated most probable relative charge is solidly within this range. The simulation performed significantly beyond liquid detachment without having to restart, reflecting a robust modeling method.

CHAPTER VI

Summary and Future Work

6.1 Conclusions

This thesis has attempted to identify the existence and magnitude of various factors affecting FEEP operation through multiple analysis pathways. It was focused on droplet behavior for field emitter thrusters. Parametric and asymptotic evaluations identified the main forces driving the surface evolution. The combination of level sets and boundary element methods was used to model the droplets after detachment and to provide their relative mass to charge frequency and detailed individual properties of the surface. The various sections have examined different contributors to needle operating performance. Mass efficiency can be increased by varying the parameters in the direction indicated by Table (6.1). These parameters are listed alphabetically, and not by order of magnitude.

6.1.1 Parametric analysis

In Chapter II, a needle FEEP was examined parametrically. Needle geometry modification and propellant alloying were proposed as methods to increase system mass efficiency η_m. The effect of reservoir contamination on reducing η_m was quantified. Correlations between mass efficiency and impedance Z were derived. As the needle becomes smoother and impedance increases, efficiency increases, but more

Smaller/less	Larger/More
Contamination from reservoir	Critical (starting) current
Droplet diameter	Electric field
Electrode width	Electrode voltage
Fluid thickness	Fraction tip wetted
MTCR	Fluid velocity
Taylor cone radius	Impedance
Tip radius of curvature	Surface tension
	Viscosity

Table 6.1: Variables to alter to increase mass efficiency

power is then needed due to the higher potential required to initiate droplet emission. A model was presented that gives quantitative predictions for how voltage, current, fluid thickness, fluid velocity and impedance are interrelated.

Besides adjusting the characteristics of the needle itself, various alternative propellant binary and ternary alloys were examined. While the baseline propellant was pure indium, the melting points, vapor pressures and viscosity of all combinations of indium, gallium and tin were presented. A model was presented that predicted an increase in the viscosity of the fluid resulting in an increased system mass efficiency. This trend was because the electrostatic potential was increased along with increasing viscosity so that the fluid velocity was unchanged. The suggested alloy possessed a good combination of viscosity increase (0.1 $mPa \cdot s$), melting point reduction (80K) and usage of indium ($> 70\%$) with a [0.75, 0.1, 0.15] fraction of indium, gallium and tin. Similarly, altering the composition of the solid needle was proposed to see how surface tension forces vary between solid and liquid elements. The predicted effect of changing the needle material was quantified. The current tungsten needle was shown to be the best element available as an underlying base. In addition, it was

shown that the effect on mass efficiency per percent increase in surface tension was larger than that of similar viscosity changes.

Finally, ARCS has had past performance problems with contaminants migrating from the reservoir to the needle tip. Iron and chromium were shown as the primary foreign constituents. After a sufficient amount of contaminant buildup, sparking occurred between the electrode and the needle tip. This arcing degraded the needle surface and reduced thruster performance. Modeling the occultation as a diffusion of solids into a liquid, the leaching rate of impurities for various components into stainless steel was found to lie in the range of 1.0×10^{-16} to 2.7×10^{-10} $\frac{kg}{s}$. This model related contaminant deposition rate to a rough estimate of emitter lifetime. It also predicted that reducing the reservoir diffusion rate by 10% will lead to an increase of lifetime of up to 25%.

6.1.2 Asymptotic analysis

To better predict the performance of a FEEP thruster, the motions of the propellant surface need to be understood. However, a brute force full 3-D jet free surface simulation is highly impractical in terms of computational time. Mathematical perturbation schemes allow for the derivation of rapid 1-D models. In Chapter III, the order of magnitude of the forces acting on the liquid surface was ascertained. A perturbation scheme using nondimensional numbers was produced that is consistent to any arbitrary order of approximation.

The inertial, viscous, capillary, gravitational, electrostatic and ambient forces were compared. The surface of a FEEP thruster was then simulated using a 1-D axisymmetric slender jet model. Continuity, momentum and surface curvature stress are conserved. A general balance of all the forces was presented, and then specific

ARCS FEEP values were used as inputs. The resulting matrix produced a power series approximation of an axisymmetric jet at every level of expansion ϵ. The order of magnitudes of the forces from least to greatest were viscosity (-10), elasticity (-8), atmospheric pressure (-5), inertia (-3), gravity (-2), surface tension and electrostatics (0). That is, the effect of the 500 Pa vacuum chamber pressure on the indium surface had a relative influence of 1×10^{-5} times the influence of surface tension on the slender jet's development. In addition to identifying the magnitude of the force contribution, several figures demonstrated that if all forces were (incorrectly) treated as equally important, the overall evolution of the jet would be substantially different in terms of position, velocity and internal stress.

Finally, the numerical stability of the system was examined. From an eigenvalue analysis, it was determined that unless both left and right hand boundary conditions are enforced, a mixed hyperbolic/elliptic solution set results and surface evolution predictions become catastrophically unstable, regardless of how reasonable the initial physical constraints.

6.1.3 BEM/LS analysis

As droplets snap off the needle tip, the width of the fluid connecting the droplet and the needle decreases to zero. This computational singularity occurs in a region of very high electrostatic gradients and surface curvature. The method of level sets allows for computational tracking of a surface between discrete interfaces. The boundary element method (BEM) is a complementary algorithm to level sets that span only the boundaries of the problem instead of the entire volume. Restricting the BEM's nodal placement only to the edges resulted in faster computation due to fewer total nodes, avoidance of adaptive meshing, easier design changes, and accurate

calculation of gradients and infinite domains. The combination of the level set and the boundary element methods enabled accurate and rapid spatial resolution for charged surfaces. They also handled a changing irregular shape and included the effects of electrostatic forces from the electrode and other droplets on the behavior of individual droplets after pinch off.

The behavior of these droplets was described for 2D planar and 2D axisymmetric coordinates. In addition, a variety of techniques was implemented that increased accuracy and/or reduced simulation run time. Employing the iterative matrix solver GMRes and fitting of the data with a bigaussian distribution provided especially notable improvements. The electrode separation, electric potential, the fluid viscosity and surface tension were varied over several orders of magnitude. In agreement with the analysis in previous chapters, the potential and surface tension had the largest impact on droplet velocity, position and formation shape.

Besides varying selected experimental parameters, methods were proposed that allow for future experimental validation. Time of flight measurements and various generated droplet probability density functions such as mass to charge ratio (MTCR) provided quantitative predictions on emitted FEEP propellant. The simulations accurately reproduce independent work up to their termination of the droplet formation and the predicted most probable MTCR can explain observed droplet angular dispersion. In addition, the combined approach can model a range of situations unrivaled by other methods.

6.2 Future work

Several possible areas of improvement exist as areas for future research on these topics. The improvements are grouped according to the primary benefit of inclusion,

whether it increases the accuracy, speed or general applicability of the algorithms or increased understanding of parameter correlations.

6.2.1 For increased accuracy

These modifications will mainly increase the accuracy of the simulation. Depending on the implementation method, the overall computation time may increase.

Integrate the influence matrix rather than numerical approximation The use of a boundary integral method (BIM) instead of a boundary element method (BEM) to calculate the influence matrix A could increase the accuracy of the surface force computation. Integrating along the panel surface avoids singularities in the numerical approximations. However, on tilted or curved panels, the BIM is more sensitive to differences in panel lengths and more computationally expensive. Additional effort would be needed so that the integration end points always avoid droplet singularities inherent in the Green's function.

Adapt Green's function for close points At smaller panel grid spacings, the distance between boundary points decreases. As the Green's function uses the natural logarithm function, at these shortening separations the function approaches a singularity. Hence, the matrix A becomes numerically stiffer as panel resolution increases. This stiffness increases the matrix condition number, spreads the solution eigenvalues and causes an iterative solver such as GMRes to converge significantly slower. If droplets are frequently present near the surface, a possible route is to perform the calculations using a quadrature method (see Sec. (4.5.2)) designed for the system Green's function [213]. Another approach is to regularize the singularity and correct the solution afterwards [20].

Incorporate a sink term for ions Currently, only charge on droplets is tracked. At flow rates under $50\mu A$, Fig. (4.30) demonstrates that the contribution of total charge carried by ions increases dramatically. Creating a sink term in the governing equations to represent this ionic charge would more accurately determine the total charge in the system and its distribution among all the components.

6.2.2 For reduced computational time

These modifications will increase the speed of the simulation, although depending on the algorithm, small errors in accuracy due to approximations could be introduced.

Implement a tree code or fast multipole matrix solver Instead of solving the $Ax=b$ system through GMRes or matrix inversion, one could treat the panel points using point-cluster or cluster-cluster approximations for very rapid calculation of normal electric fields. Emhoff's doctoral thesis has significant details about tree code implementation [65]. An even more rapid computation can be obtained by using the fast multipole method. This approach computes the force between two clusters at a time, rather than the particle-particle set up of the current implementation. Taylor expansions are performed about the center of both the target and source cluster. This requires a large amount of memory storage for these cluster moments; however, it can reduce computational cost to approximately O(N) [105].

Parallelize the routines Since the matrix and potential calculations are performed around the computational and surface boundaries, the formation of the A matrix requires each panel to independently assess the rest of the boundary's effect on it. Therefore, parallelizing the code would offer some potential speed-up in total run time as the formation time of the matrix A is reduced.

Apply fixed matrix values For panel distances that do not vary (e.g. the edge-edge connections) or change very slowly (e.g. needle surface-edge), the influence matrix A does not need to be re-calculated for each iteration. The Green's functions need to be recalculated only when a surface moves more than 1% from its prior position.

Improve matrix preconditioning A better conditioned matrix allows for faster eigenvalue determination when using an iterative solver. The main difficulty in indefinite preconditioning of a matrix can be explained as follows. Krylov subspace methods (see Sec. 4.5.1) converge rapidly when the eigenvalues are clustered around 1. This means that the preconditioner, often viewed as an approximation to the inverse of the given matrix, must transfer the eigenvalues to one. It may happen that eigenvalues are transferred to values closer to zero due to approximation errors that are intentionally made in order to keep the process efficient. In that case, the convergence of Krylov methods such as GMRes will be slow, and it may happen that the unpreconditioned iteration process converges faster than the preconditioned iteration. A more sophisticated method than the current block Jacobi (such as block *SSOR*) could result in consistent, rapid solution times.

6.2.3 For broader applicability

These modifications will allow a wider range of problems to be addressed with the simulation method.

Incorporate source term and flow rates The flow rate and current should vary as a function of potential. Currently, the needle tip is treated as possessing a fixed amount of propellant; adding an inflow term would allow for the modeling of

larger- and longer-flux simulations.

Extend to three dimensional coordinates A full 3-D simulation provides a better characterization of droplet detachment. In case the tree code approach in Sec. (4.5.1) is used, a 3-D approach will also be more efficient, as a full recursion relationship exists for the Green's function. Also, the BEM would be more accurate, as singularities are more easily addressed [65]. However, using a volumetric domain requires the boundary elements to be planar rather than linear. This introduces a large number of additional calculations and increases run times substantially.

The main obstacle in performing a 3D simulation is the requirement to correctly connect the nodes. Not only does it need to be determined which blob a level set crossing is attached to, but in what order the (x, y, z) points should be sorted. If points are linked to one another incorrectly, a BEM approach causes the physical forces to be computed inaccurately. While identification of the crossing location itself is fairly rudimentary, this ordering of multiple irregular blobs has proven to be a very difficult problem. Due to the simplication of the Green's function, if a full multipole solver was used and the nodal connectivities were determined quickly, it is estimated that total run time for a 3D case would be the same order of magnitude as the currently implemented 2D axisymmetric version.

6.2.4 Reformulation of the system to be gridless

Originally, the entire electrostatic calculation was envisioned to be grid-free. This would entail using the boundary integral method as a vortex driver. Because this approach uses only the edges, arbitrary precision can be achieved through point insertion. A quick overview of the system follows. See Krasny [59, 141, 134] and Smerka [226] for a fuller review. Mansour [159] used the boundary integral method

to simulate satellite droplet formation in capillary jet breakup without electrostatics.

If the liquid outside a bubble is irrotational and incompressible, its velocity u is given by Eq. (6.1) and the velocity potential Φ.

$$u = \nabla\Phi, \text{ where } \nabla^2\Phi = 0 \tag{6.1}$$

The potential can be represented by a distribution of dipoles on the surface, where μ is the dipole density and g is the Green's function for the Laplacian in $\Re^3$ as in Eq. (6.2).

$$\begin{gathered}\Phi(r) = \int_\Omega \mu(r')n(r') \cdot \nabla' g(r - r')\, dS \\ g(r - r') = -\tfrac{1}{4\pi|r-r'|}\end{gathered} \tag{6.2}$$

The liquid velocity on the boundary can be determined by taking the limit as $r \rightarrow$surface s and using the principal value integral $\oint$ in Eq. (6.3).

$$\Phi_s = \frac{1}{2}\mu(r) + \oint_\Omega \mu(r')n(r') \cdot \nabla' g(r - r')\, dS \tag{6.3}$$

The velocity tangential components come from derivatives of Φ_s. The normal component of the velocity u comes from the vector potential A on the surface, as described by Eq. (6.4).

$$A = \oint \mu(r')n(r') \times \nabla' g(r - r')\, dS \tag{6.4}$$

Then, the evaluation of the normal velocity only requires surface derivatives. The motion of the interface is given by Eq. (6.5).

$$u \cdot n = (n \times \nabla) \cdot A$$
$$\frac{dr}{dt} = u \tag{6.5}$$

6.2.5 Additional uses of the models

Many additional tests can be run using this simulation. A parametric investigation of many of these variables could increase the understanding of the interplay between components.

Electrostatic mixing One of the areas that the BEM/LS model is most easily applied is in the realm of electrostatic mixing. By using electric fields on small liquids and powders, they can be rapidly and thoroughly combined [37, 133, 244].

Timing comparison with level set electrostatics As of publication, neither Prof. Sussman nor I are aware of anyone who has combined electrostatics with the level set method [255]. As a consequence, there is no data on whether it or the thesis BEM approach is faster. While level sets can use AMR, it has diminishing returns. However, BEM has to invert a dense matrix.

Satellite droplets The formation of satellite droplets is influenced by the size and relative charge of the droplets that detached earlier. Depending on the magnitude of the electric field, tiny droplets have been known to be repulsed from highly charged larger drops and back towards the needle [282]. Their unique influence on the path and velocity of the other drops could be more rigorously quantified.

Taylor cone variation Several experiments have shown a mass efficiency dependence on the liquid cone width [237]. By varying the needle radius of curvature,

the mass flow rate and charge could be examined.

Relative heights of liquid bridges Surface evolution of a liquid has been the subject of multiple basic research projects [13, 282]. They have examined the relative width and height of the liquid bridge between a detaching droplet and the underlying solid surface. This ratio has been used to examine the possibility of forming microdroplets smaller than the surface itself as an aid to dispersion and atomization. Therefore, it is conceivable to design an apparatus that produces predominantly single-sized droplets from sessile liquid motion as a consequence of the underlying physical shape.

APPENDICES

APPENDIX A

Element properties and experimental variables

The physical properties of a needle FEEP are listed for reference. In addition, indium and other previously discussed elements and alloy compositions are included. The values are from a selection of published papers [50, 56, 68, 272].

A.1 Needle FEEP values

The physical values parameterizing an indium-fed needle FEEP are presented. The dimensions were used as an educated approximation to ARCS setup, since exact experimental values were unobtainable.

angular spray intensity $= 3.9 \times 10^6 \times \exp\left(\frac{-12.42\psi}{I_e}\right)$ $\left[\frac{\#}{steradian \cdot s}\right]$

background pressure = 0.133 [Pa]

drop diameter = 0.1 half-bubble on the plate, or 0.079 rounded [μm] [72]

emitter current $= 5 - 300 \times 10^{-6}$ [A]

emitter-extractor distance $= 2 \times 10^{-4}$ [m]

extractor hole diameter = 0.004 [m]

extractor potential difference $= 5 - 10 \times 10^3$ [V]

film thickness $= 1 - 20 \times 10^{-6}$ [m]

groove radius $= 1 - 500 \times 10^{-8}$ [m]

mass efficiency $= 10 - 100\%$

needle length $= 0.001$ [m]

temperature $= 453$ [K]

A.2 Element properties

Indium is used as the propellant in ARCS FEEP thruster designs; gallium has been used in past field emitters and tin was discussed in Sec. (2.2) as a possible alloy component to modify the fluid properties.

A.2.1 Indium

atomic mass $= 114.818$ [amu]

density $= 1000 \times (7.1295 - 6.7987 \times 10^{-4}[T - 273.15])$ $\left[\frac{kg}{m^3}\right]$

dielectric constant $(\epsilon) = 1 \times 10^{-5}$ $\left[\frac{F}{m}\right]$

ionization electric field $= 2 \times 10^{9}$ $\left[\frac{V}{m}\right]$

electrical resistivity $= 8.75 \times 10^{-8}$ $[\Omega \cdot m]$

Fermi energy $(e_F) = 8.63$ [eV]

Fermi velocity $(v_F) = 1.74 \times 10^{6}$ $\left[\frac{m}{s}\right]$

melting point $= 429.75$ [K] (156.6 ^{o}C)

molar volume $= 15.76$ $\left[\frac{cm^3}{mole}\right]$

molecular heat adsorption $\left(L_e^B\right) = 1959$ $\left[\frac{kJ}{kmol}\right]$

specific heat at 300 K $= 233$ $\left[\frac{J}{kg \cdot K}\right]$

surface tension $(\sigma) = 0.555 - 1.2 \times 10^{-4}(T - 429.75)$ $\left[\frac{N}{m}\right]$

thermal conductivity $= 42$ $\left[\frac{W}{m \cdot K}\right]$

viscosity $(\mu) = 3.02 \times 10^{-4}(\exp[800/T])$ $\left[\frac{N \cdot s}{m^2}\right]$

wetting angle $(\sigma_{gs}) = 0.674 \pm 0.074$ $\left[\frac{J}{m^2}\right]$

A.2.2 Viscosity fitting coefficients

Eq. (2.10) coefficients, $\log_{10}(1000 \cdot \mu + 1)\,[Pa \cdot s] = 10^{\mathrm{b1}} \times T^{\mathrm{b2}}$

Element	$b_{1,e}$	$b_{2,e}$
Iron (Fe)	4.406	-1.384
Gallium (Ga)	0.85	-0.500
Indium (In)	3.01	-1.280
Tin (Sn)	1.91	-0.8505

References [29, 200, 247].

A.2.3 Vapor pressure curves

Used for Sec. (1.4.2). Indium and manganese are the two elements shown on the far left of Fig. (A.1) with the lowest vapor pressure.

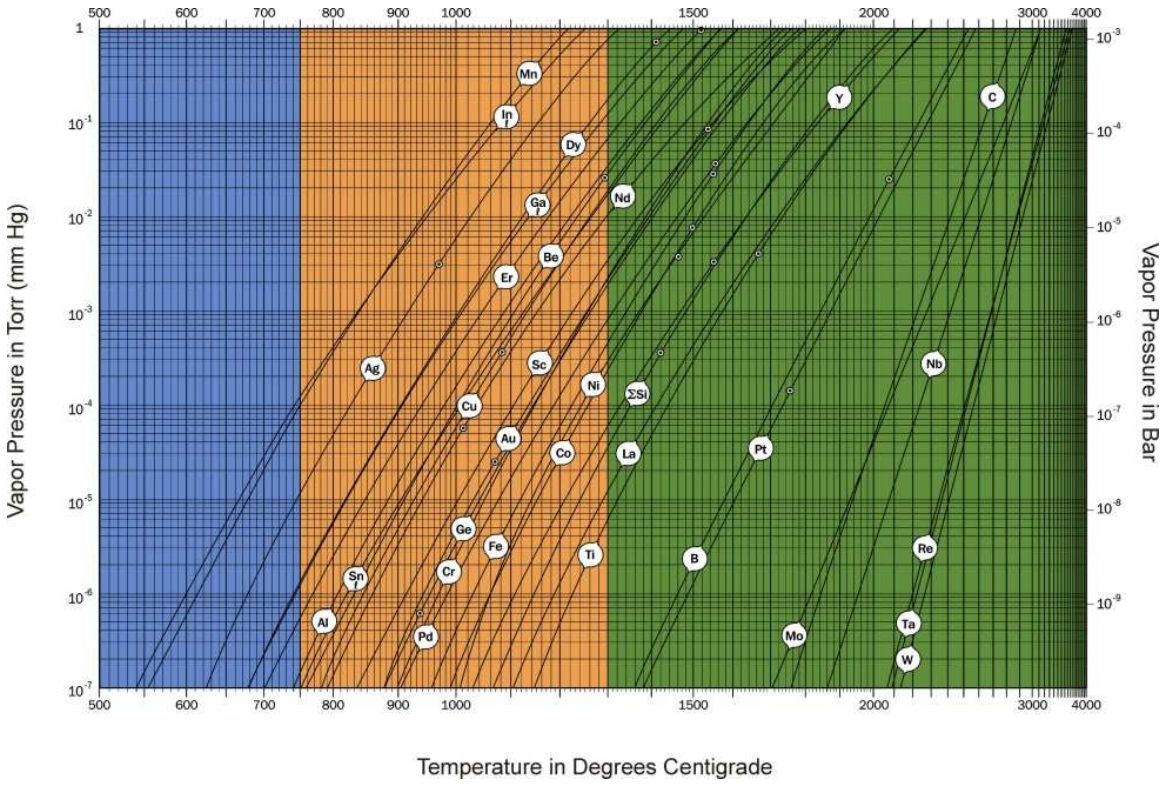

Figure A.1: Vapor pressure curve for various elements versus temperature

A.2.4 Melting point, boiling point and surface tension

Element	Melting Point [^{o}C]	Boiling Point [^{o}C]	Surf. Ten. $\left[\frac{N}{m}\right]$
aluminum	660	2,519	0.871
beryllium	1,287	2,471	
chromium	1,907	2,671	1.627
cobalt	1,495	2,927	
copper	1,085	2,562	1.6
gallium	30	2,204	
germanium	938	2,833	
gold	1,064	2,856	
iron	1,538	2,861	1.86

Element	Melting [^{o}C]	Boiling [^{o}C]	Surf. Ten. $\left[\frac{N}{m}\right]$
lead			0.457
manganese	1,246	2,061	1.152
nickel	1,455	2,913	
palladium	1,555	2,963	
scandium	1,541	2,836	
silver	962	2,162	
tin (gray)	13	2,602	
tin (white)	232	2,602	0.562
titanium	1,668	3,287	
tungsten			2.486

References [140, 275]

A.2.5 Tin and gallium

Property	Unit	Tin	Gallium
kinematic viscosity	$\frac{m^2}{s}$	8.00×10^{-7}	
latent heat of fusion	$\frac{J}{kg}$	6.00×10^4	
liquid density	$\frac{kg}{m^3}$	6,990	6,080
solid density	$\frac{kg}{m^3}$	7.50×10^3	
specific heat	$\frac{J}{kg \cdot K}$	228	371
	$\frac{J}{mol \cdot K}$	27.112	25.86
thermal conductivity	$\frac{W}{m \cdot K}$	60	
thermal expansion	$\frac{1}{K}$	2.67×10^{-4}	

APPENDIX B

Mathematical terms

This section is intended to describe the concepts, rather than give a comprehensive discussion of various mathematical terms used in this research.

B.1 Hessian

The Jacobian matrix of the derivatives $\partial f/\partial x_1$, $\partial f/\partial x_2$, ..., $\partial f/\partial x_n$ of a function $f(x_1, x_2, ..., x_n)$ with respect to x_1, x_2, ..., x_n is called the Hessian H of f [267].

$$H\left\{f(x_1, x_2, ..., x_n)\right\} = \begin{bmatrix} \frac{\partial^2 f}{\partial x_1^2} & \cdots & \frac{\partial^2 f}{\partial x_1 \partial x_n} \\ \vdots & \ddots & \\ \frac{\partial^2 f}{\partial x_n \partial x_1} & & \frac{\partial^2 f}{\partial x_n^2} \end{bmatrix} \tag{B.1}$$

It also is used to refer to the determinant of this matrix [103] via Eq. (B.2).

$$H\left\{f(x, y)\right\} = \begin{vmatrix} \frac{\partial^2 f}{\partial x^2} & \frac{\partial^2 f}{\partial x \partial y} \\ \frac{\partial^2 f}{\partial y \partial x} & \frac{\partial^2 f}{\partial y^2} \end{vmatrix} \tag{B.2}$$

B.2 Gaussian quadrature weights and locations

By properly choosing the location of points along a line during numerical integration, accuracy can be increased while using fewer points. One common method is

labeled *Gaussian quadrature*. See Sec. (4.5.2) for more details about the approach. For two or four quadrature points, representing a 5th or 9th degree polynomial fit, their fractional locations from (-1,1) and weights are listed.

n	*location*	*weight*
2	±0.5773502	1.0000000
4	±0.3399810	0.6521451
	±0.8611363	0.3478548

(B.3)

B.3 Godunov predictor-corrector

Consider the system of conservation laws $U_t + F_x = 0$ where U is a vector of length K and F is a vector-valued function of U. To simulate the spatial and temporal change, a difference scheme of the form

$$U_j^{n+1} = U_j^n - \frac{\Delta t}{\Delta x}\left(F_{j+1/2} - F_{j-1/2}\right) \tag{B.4}$$

can be used, where U_j^n approximates the average value of the solution in cell Δ_j centered at x_j at time t^n and $F_{j+1/2}$ is the numerical flux [23]. For the first-order Godunov method, the numerical flux is $F^G\left(U^L, U^R\right)$, and is defined to be the flux evaluated along the ray x/t=0 [98]. To change to a second-order method, the flux F needs to be second order accurate. This increase in accuracy can occur by constructing a linear approximation to U at time t^n within each grid cell. The quasi-linear form is then used to extrapolate to cell interfaces at $t^{n+1/2}$. This form is represented by Eq. (B.5). For more detail, refer to Colella [48].

$$\begin{aligned} U_{j+1/2}^{n+1/2} &= U_j^n + \tfrac{\Delta x}{2} U_{x,j} + \tfrac{\Delta t}{2} U_{t,j} \\ &= U_j^n + \tfrac{\Delta x}{2} U_{x,j} - \tfrac{\Delta t}{2} F_{x,j} \end{aligned} \tag{B.5}$$

B.4 Discretizing terms

When discretizing the projection step of the CLSVOF,

$$\begin{aligned} \nabla \cdot \tfrac{\nabla p}{\rho} &= \nabla \cdot v \\ \text{Div}\left(\tfrac{\text{Grad}[p]}{\rho}\right) &= \text{Div}(v) \end{aligned} \tag{B.6}$$

where Div is the discrete divergence operator and Grad is the discrete gradient operator given in Eq. (B.7).

$$\begin{aligned} \text{Div}(v_{i,j}) &= \tfrac{u_{i+1/2,j} - u_{i-1/2,j}}{\Delta x} + \tfrac{v_{i,j+1/2} - v_{i,j-1/2}}{\Delta y} \\ \text{Grad}\left[p_{i+1/2,j}\right] &= \tfrac{p_{i+1,j} - p_{i,j}}{\Delta x} \\ \text{Grad}\left[p_{i,j+1/2}\right] &= \tfrac{p_{i,j+1} - p_{i,j}}{\Delta y} \end{aligned} \tag{B.7}$$

Equation (B.6) can then be discretized as Eq. (B.8).

$$\frac{\frac{p_{i+1,j} - p_{i,j}}{\rho_{i+1/2,j}} - \frac{p_{i,j} - p_{i-1,j}}{\rho_{i-1/2,j}}}{\Delta x^2} + \frac{\frac{p_{i,j+1} - p_{i,j}}{\rho_{i,j+1/2}} - \frac{p_{i,j} - p_{i,j-1}}{\rho_{i,j-1/2}}}{\Delta y^2} = Div(v) \tag{B.8}$$

APPENDIX C

Droplet minimum conductivity

This section is intended to list some representative FEEP parameters, calculate sample droplet statistics and determine the lower bound for droplet conductivity where the BEM is appropriate. Reported operating FEEP values of thrust (66 μN), mass flow rate (0.69 $\frac{\mu g}{s}$) and I_{sp} (10,900 s) [179] give a volume flux of $9.44 \times 10^{-14}\ \frac{m^3}{s}$. For needle FEEPs, some versions have cylindrical needle radii of 0.125 mm, needle heights of 3 mm and 10 kV emitter voltages.

Fermi energy and velocity For metals, the Fermi energy (e_F) provides the minimal energy for conducting electrons. However, the maximum amount of energy which can be given to any electron is on O(μeV), so only the electrons very near the Fermi energy can participate in conduction [174]. The Fermi velocity (v_F) of these conduction electrons can be calculated from the Fermi energy. For indium, v_F is:

$$v_F = c\sqrt{\frac{2e_F}{m_e c^2}} = 1.74 \times 10^6 \left[\frac{m}{s}\right] \tag{C.1}$$

Drift velocity and residence time The effective resistance for an electron while traveling through a 2 μm droplet is

$$R = \frac{L}{\sigma A} = \frac{2 \times 10^{-6}}{1.14 \times 10^{7} \times 0.5 \times \pi \times (1 \times 10^{-6})^2} = 0.112\,[\Omega] \tag{C.2}$$

while the current density J is given by Eq. (C.3).

$$J = \frac{U}{RA} = \frac{U\sigma}{L} = \frac{8000}{.112 \times 0.5 \times \pi \times (1 \times 10^{-6})^2} = 4.56 \times 10^{16} \left[\frac{A}{m^2}\right] \tag{C.3}$$

The number of free electrons n is calculated using Avogardo's number and the mass density of indium.

$$n = \frac{N\rho}{M} = \frac{6.022 \times 10^{23} \times 7100}{.1148} = 3.72 \times 10^{28} \tag{C.4}$$

The drift velocity v_d then becomes Eq. (C.5).

$$v_d = \frac{J}{ne} = \frac{4.56 \times 10^{16}}{3.72 \times 10^{28} \times 1.609 \times 10^{-19}} = 7.61 \times 10^{6} \left[\frac{m}{s}\right] \tag{C.5}$$

Finally, an electron traveling a distance of $10\,\mu m$ through the propellant layer at speed v_d takes 1.31×10^{-12} seconds. Since other processes such as snap off occur on a much larger time scale, the droplet behaves as an effective infinite conductor.

Droplet minimum conductivity Since the BEM requires that the tangential electric field be much less than the normal field, or $E_{tangent} \ll E_{normal}$, the relative electron velocity must be high enough to make the assumption of local charge equilibrium reasonable. *Reasonable* is defined as the the conduction time $t_{conduct}$ being less than 1% of drift time t_{drift}. Using the earlier formulas and a 10 μm panel length, a tip to electrode distance $d_{te} = 5 \times 10^{-6}\,m$ and a computational time step of $t_{comp} < 5 \times 10^{-10}$ seconds, the minimum fluid conductivity σ_{min} is calculated via Eq. array (C.6). They make use of the Fermi energy and velocity presented earlier in the Appendix.

$$
\begin{aligned}
v_F &= c\sqrt{\tfrac{2e_F}{mc^2}} = 1.74 \times 10^6 \ \left[\tfrac{m}{s}\right] \\
t_{conduct} &= \tfrac{d_{te}}{v_F} = \tfrac{5\times10^{-6}}{1.7\times10^6} = 2.9 \times 10^{-12}\,[s] \\
J = nev_d &= \sigma E = \tfrac{U}{RA} = 1.6 \times 10^9(\sigma_{min}) \ \left[\tfrac{A}{m^2}\right] \\
v_{drift} &= \tfrac{J}{ne} = 0.218(\sigma_{min}) \ \left[\tfrac{m}{s}\right] \\
t_{drift} &= \tfrac{d_{te}}{v_{drift}} = 2.3 \times 10^{-5} \left(\tfrac{1}{\sigma_{min}}\right) \ [s] \\
\sigma_{min} &\geq 0.01\,(v_F)\,ne\tfrac{d_{te}}{U_0} = 80,000 \ \left[\tfrac{Siemens}{m}\right]
\end{aligned}
\tag{C.6}
$$

APPENDIX D

Derivations

D.1 Surface tension components

If the surface tension of the solids $(\sigma_{s1}, \sigma_{s2})$ is known, the surface tension of the liquids above can be determined by solving Eq. (2.14) using the Newton-Raphson method [18],

$$\sigma_{gl}(start) = \sigma_{s1} F(\theta_1) + \sigma_{s2} F(\theta_2) \tag{D.1}$$

where $F(\theta_i) = \left(1 - \frac{1+cos\theta_i}{4}\right) / \left(\frac{(1+cos\theta_i)}{2}\right)$.

D.2 Electrical relationships

For voltage V and current I, Eq. (D.2) relates the charge to the capacitance.

$$\begin{aligned} V &= \frac{q}{C} = \frac{1}{C}\int_0^t I(t)\,dt \\ I &= \frac{dq}{dt} \end{aligned} \tag{D.2}$$

For a circuit with capacitor C in series with resistor R, Kirchoff's current law gives

$$\frac{1}{C}\int_0^t I(t)\,dt + IR = 0 \tag{D.3}$$

Therefore, the current is described by Eq. (D.4).

$$\begin{aligned} \tfrac{dI}{dt} &= -\tfrac{I}{CR} \\ I(t) &= I_0 \cdot \exp\left(-\tfrac{t}{RC}\right) \end{aligned} \tag{D.4}$$

A Fourier transform with a delta function input current gives $\frac{1}{C\omega}\hat{I}(\omega)$ + R$\hat{I}(\omega)$ =1, or

$$\hat{I}(\omega) = \frac{1}{R + \frac{1}{C\omega}}$$

This is a frequency transformation of a high pass filter; more current is available when ω is large.

D.3 GMRes iterative Hessenberg bounding

The mathematics involved in GMRes require the formation of an upper *Hessenberg* matrix $\overline{H}$. The relationship between the main matrix A, the iterative solution vector v and the Hessenberg is described.

D.3.1 Claim on $\boldsymbol{v}$

$\left[\mathcal{A}\overline{v}_m = \overline{v}_{m+1}\overline{H}_m\right]$

From steps 3 and 10 in Sec. (4.5.1), $w_j = v_{j+1}h_{j+1,j} = \mathcal{A}v_j$. The following equality is then readily derived.

$$\mathcal{A}v_j = \textstyle\sum_{i=1}^{j+1} v_i h_{ij}, \quad j = 1, 2, ...m. \tag{D.5}$$

By defining $\overline{v}_m$ as the $n \times m$ matrix with column vectors v_1, ..., v_m and $\overline{H}_m$ as the $m \times m$ Hessenberg matrix with nonzero entries h_{ij} defined earlier, the following relation holds:

$$A\overline{v}_m = \overline{v}_m\overline{H}_m + \overline{v}_{m+1}h_{m+1,m}e_m \tag{D.6}$$

where e_m is the modified identity matrix with the (m,m) position as the sole non-zero value. However, the last term is equivalent to $\overline{v}_{m+1}$, as seen in Eq. (D.5), so

$$A\{n \times n\}\overline{v}_m\{n \times m\} = \overline{v}_{m+1}\{n,\, m+1\}\overline{H}_m\{m+1,\, m\} \tag{D.7}$$

D.3.2 Claim on iterative Hessenberg identity

$\left[\overline{v}_m^T A\overline{v}_m = \overline{H}_m\right]$

Multiply Eq. (D.6) by $\overline{v}_m^T$ to get

$$\overline{v}_m^T A\overline{v}_m = \overline{v}_m^T\overline{v}_m H_m + \overline{v}_m^T\overline{v}_{m+1}h_{m+1,m}e_m \tag{D.8}$$

The Arnoldi process is premised around the ortho-normality of $\{v_1, ..., v_m\}$, so $\overline{v}_m^T\overline{v}_m = 1$ and $\overline{v}_m^T\overline{v}_{m+1} = 0$. Therefore, Eq. (D.9) relates the Hessenberg and A matrices through the iterative v vector.

$$\overline{v}_m^T\{m \times n\}A\{n \times n\}\overline{v}_m\{n \times m\} = H_m\{m \times m\} \tag{D.9}$$

D.4 Axisymmetric derivatives of the Green's function

Originally described in Sec. (4.3.1), the axisymmetric derivatives of the Green's function are used in a Taylor expansion. The derivatives are given with respect to z and r where $\{\}_1$ is the reference and $\{\}_2$ is the source point. The derivative with respect to z_2 is obtained from the z derivative by multiplying by $(-1)^n$, where n is the order of the derivative. For example, $\frac{\partial^2 G}{\partial z_1 \partial z_2} = (-1)^1\frac{\partial^2 G}{\partial z^2}$. The derivatives for r_1 are the same as for r_2 with the {1,2} interchanged [65].

As a reminder, note that $G = \frac{K}{\pi\sqrt{L}}$ and that K and E are complete elliptic integrals of the first and second kinds, respectively. Equations (D.10-D.17) recapitulate the transformation variables used when changing from a 3D to axisymmetric form of the Green's function while Eqns. (D.18-D.29) are its first three derivatives. Let:

$$r = r_1 + r_2 \tag{D.10}$$

$$z = z_1 - z_2 \tag{D.11}$$

$$L(r, z) = r^2 + z^2 \tag{D.12}$$

$$m(r_1, r_2) = \frac{4r_1 r_2}{L} \tag{D.13}$$

$$w(m) = 1 - m \tag{D.14}$$

$$K(m) = \int_0^{\frac{\pi}{2}} \frac{d\theta}{\sqrt{1 - m\,sin^2\theta}} \tag{D.15}$$

$$E(m) = \int_0^{\frac{\pi}{2}} \sqrt{1 - m\,sin^2\theta}\,d\theta \tag{D.16}$$

$$D(m) = \frac{E(m)}{w(m)} \tag{D.17}$$

The first order derivatives are:

$$\frac{\partial G}{\partial r_1} = -\frac{D(L - 2rr_1) - LK}{2r_1\sqrt{L^3}} \tag{D.18}$$

$$\frac{\partial G}{\partial r_2} = -\frac{D(L - 2rr_2) - LK}{2r_2\sqrt{L^3}} \tag{D.19}$$

$$\frac{\partial G}{\partial z} = -\frac{z\,D}{\sqrt{L^3}} \tag{D.20}$$

The second order derivatives are:

$$\frac{\partial^2 G}{\partial z \partial r_1} = \frac{z}{mw\sqrt{L^5}} \{2D[rm(2-m) - r_2(1+m)] + K(2r_2 - rm)\} \tag{D.21}$$

$$\frac{\partial^2 G}{\partial z \partial r_2} = \frac{z}{mw\sqrt{L^5}} \{2D[rm(2-m) - r_1(1+m)] + K(2r_1 - rm)\} \tag{D.22}$$

$$\frac{\partial^2 G}{\partial z^2} = \frac{1}{w\sqrt{L^5}} \left\{D[2z^2(2-m) - Lw] - z^2 K\right\} \tag{D.23}$$

$$\frac{\partial^2 G}{\partial r_1 \partial r_2} = \frac{1}{mw\sqrt{L^5}} \left\{D[2r^2(mw-1) + Lm(1+m)] + K[r^2(2-m) - mL]\right\} \tag{D.24}$$

The third order derivatives are:

$$\begin{aligned}
\frac{\partial^3 G}{\partial r_2^3} = & \frac{-1}{2w^2 r_2^3 \sqrt{L^7}} \left\{D\left[L^3(2 - m\langle 5 - 4m\rangle) - L^2 r_1 r_2 m(1+m) - L r_2^2 \left(Lm\langle 3 - m\rangle\right.\right.\right. \\
& + r_1^2\langle 1 + 5m + 2m^2\rangle) + 2r_2^3 (r^3\langle 1 + 15m - 8m^2\rangle + 2Lr_1\langle 3 - m\rangle\langle 1 - 3m\rangle) \\
& + L r_2^4(33 - 39m + 14m^2) - 16 r r_2^5(3-m)] \\
& - K[L^3(2-4m) + L^2 r_2 m(10 r_1 - r_2) - 8 r r_2(w r^2 r_2^2 + r_2^4) \\
& - \left.\left.\left. L r_2^2 (w r^2 - 4r_2^2 + 2r\langle 3r_1 - 6r_2 + 4m r_2\rangle)]\right\}\right.
\end{aligned} \tag{D.25}$$

$$\frac{\partial^3 G}{\partial z^3} = \frac{-z}{4w\sqrt{L^7}} \left\{D[6L(2-3m) - 23z^2 w + 2m^2(3L - 4z^2)] + K[4z^2(2-m) - 3Lw]\right\} \tag{D.26}$$

$$\begin{aligned}
\frac{\partial^3 G}{\partial r_2^2 \partial z} = & \frac{-z}{4w^2 r_2^2 \sqrt{L^7}} \{D\langle 2L^2(m^2 + 2m - 1) + 16 L w^2 r_2^2 - 4r_2^2[(12 - 4m)(r^2 - 2r_2^2) \\
& + z^2 w(11 - 8m)]\rangle + K\langle L^2(2-3m) + 8r_2^2[r^2 - 2r_2^2 + z^2(3-2m) - Lw]\rangle\}
\end{aligned} \tag{D.27}$$

$$\begin{aligned}\frac{\partial^3 G}{\partial r_2 \partial z^2} = & \frac{1}{w^2\sqrt{L^7}}\left\{\frac{2r_1}{m}(D-K)(2z^2-r^2)+D[2wr^3(2-m)-z^2r(19-17m+6m^2)\right. \\ + & \left. 2r_1(z^2\langle 7-m\rangle+mr^2)]+K[z^2r(7-3m)-2r_1(r^2+2z^2)-wr^3]\right\}\end{aligned} \tag{D.28}$$

$$\begin{aligned}\frac{\partial^3 G}{\partial r_1 \partial r_2 \partial z} = & \frac{-z}{w^2\sqrt{L^7}}\left\{\frac{6r^2(K-D)}{m}+D[L(3+7m-2m^2)-r^2(9-19m+8m^2)]\right. \\ - & \left. K[L(3+m)+2r^2(3-2m)]\right\}\end{aligned} \tag{D.29}$$

BIBLIOGRAPHY

BIBLIOGRAPHY

[1] Indium metal material safety data sheet. Technical report, Teck Cominco Metals, Ltd., Trall, British Columbia V1R 4L8, Dec. 2003.

[2] Section 380: The Moon rocket challenge. Technical report, Smithsonian Institution, http://www.hrw.com/science/si-science/earth/spacetravel/spacerace/SpaceRace/sec300/sec380.html, 10 Sept. 2006.

[3] M. A. Abbas. *J. Fluid Mechanics*, 30:663, 1967.

[4] M. Abramowitz and I. Stegun. *Handbook of mathematical functions*. Dover Publications, Inc., 1974.

[5] M. Alexander, J. Stark, K. L. Smith, B. Stevens, and B. Kent. Electrospray performance of microfabricated colloid thruster arrays. *J. Propulsion and Power*, 22(3):620–627, May 2006.

[6] O. Alexandrov. Level set – matlab. Technical report, 14 May 2006. http://en.wikipedia.org/wiki/User:Olegalexandrov.

[7] A. Almgren. A conservative adaptive projection method for the variable density incompressible Navier-Stokes equations. *J. Computational Physics*, 142:1–46, 1998.

[8] N. Amenta, S. Choi, T. K. Dey, and N. Leekha. A simple algorithm for homeomorphic surface reconstruction. *J. Computational Geom. Applications*, 12:125–141, 2002.

[9] M. Andrenucci, L. Biagioni, F. Ceccanti, M. Saviozzi, and D. Nicolini. Endurance tests of 150 μN FEEP microthrusters. Number IEPC-2005-183, pages 1–5, Princeton, NJ, Nov. 2005. 29th International Electric Propulsion Conference, AIAA.

[10] T. Antoulas and J. Slavinsky. Cayley-Hamilton theorm. module m2119, The Connexions Project, Rice University, 2002.

[11] G. Arfken. *Mathematical methods for physicists*. Nonhomogeneous Equation – Green's Function. 3rd edition, 1985. pp. 480-491; 897-924.

[12] M. Arienti, P. Hung, E. Morano, and J. Shepherd. A level set approach to Eulerian-Lagrangian coupling. *J. Computational Physics*, 185:213–251, 2003.

[13] A. G. Bailey. *Electrostatic Spraying of Liquids*. Research Studies Press, Ltd., Taunton, England, 1988.

[14] G. R. Baker, D. I. Meiron, and S. A. Orszag. Boundary integral methods for axisymmetric and three dimensional Rayleigh-Taylor instability problems. *Physica*, 12D:19–31, 1984.

[15] G. Barles. *Solutions de Viscosite des Equations de Hamilton-Jacobi*. Springer-Verlag, Berlin, 1966.

[16] J. Barnes and P. Hut. A hierarchical O(N log N) force-calculation algorithm. *Nature*, 324:446, 1986.

[17] R. S. Baty. Space propulsion: let's do it better electronically. *Air University Review*, xxv(1), 14 Oct. 2003. Maj. USAF.

[18] J. Bauer, G. Drescher, and O. Illig. Surface tension, adhesion and wetting of materials for the photolithographic process. *J. Vacuum Science Technology B.*, 14(4):2485–2492, July 1996.

[19] B. Beal. *Clustering of Hall effect thrusters for high-power electric propulsion applications*. PhD thesis, University of Michigan, Dept. Aerospace Engineering, Ann Arbor, Michigan, 2004.

[20] J. T. Beale and M. Lai. A method for computing nearly singular integrals. *SIAM J. on Numerical Analysis*, 38(6):1902–1925, 2001.

[21] S. Bechtel, J. Cao, and M. Forest. Practical application of a higher order perturbation theory for slender viscoelastic jets and fibers. *Journal of Non-Newtonian Fluid Mechanics*, 41:201–273, 1992.

[22] A. E. Bell and L. W. Swanson. Mechanisms of liquid metal ion source operation. *Nucl. Instrum. Methods Phys. Res. B.*, 10/11:783–787, 1985.

[23] J. B. Bell, P. Colella, and J. A. Trangenstein. Higher order Godunov methods for general systems of hyperbolic conservation laws. *J. Computational Physics*, 82:362–397, 1989.

[24] I. Ben Ayed, A. Mitiche, and Z. Belhadj. Multiregion level-set partitioning of synthetic aperture radar images. *IEEE Transactions on Pattern Analysis and Machine Intelligence*, 27(5):793–800, May 2005.

[25] E. Berti, A. Buonanno, and C. M. Will. Estimating spinning binary parameters and testing alternative theories of gravity with LISA. *Physical Review D*, 71(8), Apr. 2005.

[26] J. P. Best and A. Kucera. A numerical investigation of non-spherical rebounding bubbles. *J. Fluid Mechanics*, 245:137–154, 1992.

[27] J. R. Blake and D. C. Gibson. Cavitation bubbles near boundaries. *Ann. Rev. Fluid. Mech.*, 19:99–123, 1987.

[28] J. R. Blake, B. B. Taib, and G. Doherty. Transient cavities near boundaries. Part I: rigid boundary. *J. Fluid Mechanics*, 170:479–497, 1986.

[29] W. Blanke, editor. *Thermophysikalische Stoffgracutea*. Springer-Verlag, New York, 1989.

[30] J. Bloomenthal. Polygonisation of implicit surfaces. *Computer-Aided Geometric Design*, 5(4):341–355, Nov. 1988.

[31] R. J. Bouchard, L. T. Cheng, D. H. Roach, P. J. Moffett, and K. W. Hang. Screen printable dielectric for field emission displays. *J. American Ceramic Society*, 88(6):1465–1467, June 2005.

[32] J. U. Brackbill, D. B. Kothe, and C. Zemach. A continuum method for modeling surface tension. *J. Computational Physics*, 100:335–353, 1992.

[33] H. Busta, Z. Tolt, J. Montgomery, and A. Feinerman. Field emission from teepee-shaped carbon nanotube bundles. *J. Vacuum Science and Technology B*, 23(2):676–679, Mar. 2005.

[34] C. Cai. *Theoretical and numerical studies of plume flows in vacuum chambers*. PhD thesis, Dept. Aerospace Engineering, University of Michigan, 1320 Beal Ave, Ann Arbor, MI, Aug. 2005.

[35] S. Callot. Assessment of chemical propulsion systems for interplanetary missions. Aurora - mars sample return, fstc, Snecma Safran Group, 31 Aug. 2005.

[36] J. Carretero and M. Martinez-Sanchez. Quasi-one-dimensional numerical simulation of a single-emitter colloidal jet. volume AIAA 2002-3812 of *38th Joint Propulsion Conference*, pages 1–7, Indianapolis, Indiana, 7-10 July 2002.

[37] M. Cernak, S. Vodny, D. Bakos, and M. Kosik. Electrostatic mixing of small quantities of viscous-liquids with powders. *Powder Technology*, 47(3):263–264, Aug. 1986.

[38] S. Chen, B. Merriman, S. Osher, and P. Smereka. A simple level set method for solving Stefan problems. *J. Computational Physics*, 135:8–29, 1997.

[39] N.-S. Cheng. Simplified Settling Velocity Formula for Sediment Particles. *Journal of Hydraulic Engineering*, pages 149–152, February 1997.

[40] R. Chhabra. A simple method for estimating the viscosity of molten metallic alloys. *Journal of Alloy and Compounds*, 221:L1–L3, 15 April 1995.

[41] C. D. Child. Discharge from hot CaO. *Phys Rev.*, 32:492, 1911.

[42] D. Chopp. Some improvements of the fast marching method. *SIAM J. Scientific Computing*, 23(1):230–244, 2001.

[43] E. Y. Choueiri. A critical history of electric propulsion: the first 50 years (1906-1956). *J. Propulsion and Power*, 20(2):193–203, Mar. 2004.

[44] A. Christlieb, R. Krasny, and J. Verboncoeur. Efficient Particle Simulation of a Virtual Cathode using a Grid-Free Treecode Poisson Solver. *IEEE Transactions on Plasma Science*, 32(2):384–389, April 2004.

[45] A. Christlieb, R. Krasny, and J. Verboncoeur. A treecode algorithm for simulating electron dynamics in a Penning-Malmberg trap. *Computer Physics Communications*, 164(1-3):306–310, 1 Dec. 2004.

[46] E. T. Chung, T. F. Chan, and X. C. Tai. Electrical impedance tomography using level set representation and total variational regularization. *J. Computational Physics*, 205(1):357–372, 1 May 2005.

[47] M. Chung, N. M. Miskovsky, P. H. Cutler, N. Kumar, and V. Patel. Theoretical analysis of a field emission enhanced semiconductor thermoelectric cooler. *Solid-State Electronics*, 47(10):1745–1751, Oct. 2003.

[48] P. Colella. J. Comput. Phys. in press LBL-17023, Lawrence Berkeley Laboratory, May 1984.

[49] P. J. Combleet and N. Gochman. Incorrect least-squares regression coefficients in method-comparison analysis. *J. Clinical Chemistry*, 25:432–438, 1979.

[50] Cookson Electronics. Technical bulletin:indium...minor metal, major impact. Technical report, www.alphametals.com, Jersey City, NJ, 2003.

[51] M. G. Crandall, H. Ishii, and P. L. Lions. *User's Guide to Viscosity Solutions of Second Order Partial Differential Equations*. Number Bull. 27, 1-67. Amer. Math Society, 1992.

[52] J. M. Crowley. *J. Applied Physics*, 48:145, 1977.

[53] Z. Cui and L. Tong. A new approach to simulating the operation of liquid-metal ion sources. *J. Vacuum Science & Technology B*, 6(6):2104–2107, 1988.

[54] A. Dadone and B. Grossman. Ghost-cell method with far-field coarsening and mesh adaptation for Cartesian grids. *Computers & Fluids*, 35(7):676–687, Aug. 2006.

[55] H. L. Daley, J. F. Mahoney, and J. Perel. Colloid annular array thruster development. Number AIAA-73-1077, Lake Tahoe, New York, Nov. 1973. 10th Electric Propulsion Conference.

[56] J. A. Dean, editor. *Lange's Handbook of Chemistry*. McGraw-Hill, 15th edition, 1999. Table 6.4 - Heats of Fusion, Vaporization. Online at http://www.knovel.com/knovel2/Toc.jsp?BookID=47&VerticalID=0.

[57] J. M. Delhaye. Jump conditions and entropy sources in two-phase systems. Local instant formulation. *Int. J. Multiphase Flow*, 1:395, 1974.

[58] R. B. Doak. Microscopic Rayleigh droplet beams. Number NB.012, 58th Annual Meeting of the Division of Fluid Dynamics, 20 Nov. 2005. American Physical Society.

[59] Z. Duan and R. Krasny. An adaptive treecode for computing nonbonded potential energy in classical molecular systems. *Computational Chemistry*, 22(2):184–195, 30 Jan. 2001.

[60] D. Duft. Rayleigh Jets from Levitated Microdroplets. *Nature*, 421:128, January 2003.

[61] C. Dyer and P. Ip. *An Elementary Introduction to Scientific Computing*. U. of Toronto at Scarborough, Division of Physical Sciences, 2000.

[62] C. J. Edgcombe. Development of Fowler-Nordheim theory for a spherical field emitter. *Phys. Rev. B*, 72:045420, 2005.

[63] C. J. Edgcombe and A. M. Johansen. Current-voltage characteristics of non-planar cold field emitters. *J. Vac. Science Technology B*, 21(4):1519–1522, July 2003.

[64] J. Eggers. Theory of drop formation. *Phys. Fluids*, 7(5):941–953, May 1995.

[65] J. Emhoff. *Simulation of ion optics using particle-in-cell and treecode methods*. PhD thesis, Dept. Aerospace Engineering, University of Michigan, 1320 Beal Avenue, Ann Arbor, MI, May 2005.

[66] D. Enright, F. Losasso, and R. Fedkiw. A fast and accurate semi-Lagrangian particle level set method. *Computers and Structures*, 83:479–490, 2005.

[67] D. Enright, S. Marschner, and R. Fedkiw. Animation and rendering of complex water surfaces. pages 736–744. Proceedings of ACM SIGGRAPH, 2002.

[68] N. Eustathopoulos, M. Nicholas, and B. Drevet. *Wettability at High Temperatures*. Pergamon Materials Series, New York, USA, 1999.

[69] E. A. Fadlun, R. Verzicco, P. Orlandt, and J. Mohd-Yusof. Combined immersed-boundary finite-difference methods for three-dimensional complex flow simulations. *J. Computational Physics*, 161:35–60, 2000.

[70] R. Fedkiw, T. Aslam, B. Merriman, and S. Osher. A non-oscillatory Eularian approach to interfaces in multimaterial flows (the ghost fluid method). *J. Computational Physics*, 152(2):457–492, 1999.

[71] M. Fehringer. The state of the metal film covering the needle of a liquid metal indium ion source. *Vacuum*, 45(9):973–976, 1994.

[72] M. Fehringer, F. Rudenauer, and W. Steiger. Ultra-Precise Indium Thruster, WP 2000: Droplet Emission. Technical Report ESTEC Contract No. 12376/97/NL/PA, Seiborsdorf, Austria, 2000.

[73] J. Fernández de la Mora and I. G. Loscertales. The current emitted by highly conducting Taylor cones. *J. of Fluid Mechanics*, 260:155–184, 1994.

[74] G. Folland. *Introduction to Partial Differential Equations*. Princeton University Press, 1979.

[75] R. Forbes and N. Ljepojevic. Calculation of the shape of the liquid cone in a liquid-metal-ion source. *Surface Science*, 246:113–117, 1991.

[76] R. G. Forbes. *Ultramicroscopy*, 89:1–5, 2001.

[77] R. G. Forbes. Field electron and ion emission from charged surfaces: a strategic historical review of theoretical concepts. *Ultramicroscopy*, 95:1–18, 2003.

[78] W. E. Forsythe. *Smithsonian Physical Tables*. Knovel, 9th revised edition, 2003.

[79] F. Fowkes. *Chemistry and Physics of Interfaces*. American Chemical Society, Washington, D.C. USA, 1971.

[80] R. H. Fowler and L. Nordheim. Electron emission in intense electric fields. *Proc. Royal Society of London*, A119:173–181, 1928.

[81] M. Francois. A balanced-force algorithm for continuous and sharp interfacial surface tension models within a volume tracking framework. *J. Computational Physics*, 213(1):141–173, 2006.

[82] M. Francois and W. Shyy. Computations of drop dynamics with the immersed boundary method, part 2: drop impact and heat transfer. *Numerical Heat Transfer*, 44:119–143, 2003.

[83] Fulmer Research Laboratories. Study on Additional Propellants for Field Emission Thrusters. Technical Report ESTEC Contract No. 3806/78/NL/JS(SC), June 1980.

[84] M. Gamero-Castaño and J. Fernández de la Mora. Direct measurement of ion evaporation kinetics from electrified liquid surfaces. *J. Chemical Physics*, 113(2):815–832, 8 July 2000.

[85] M. Gamero-Castaño and V. Hruby. Electrospray as a source of nanoparticles for efficient colloid thrusters. *J. Propulsion and Power*, 17(5):977–987, Oct. 2001.

[86] M. Gamero-Castaño and J. Ziemer. Characterization of colloid thruster beams. Number IEPC-2005-302, pages 1–6, Princeton, NJ, Nov. 2005. 29th International Electric Propulsion Conference, AIAA.

[87] M. Gamero-Castaño. *The transfer of ions and charged nanoparticles from solution to the gas phase in electrosprays*. Ph.d. dissertation, Dept. of Engineering and Applied Sciences, Yale Univ., New Haven, CT, Dec. 1998.

[88] M. Gamero-Castaño and V. Hruby. Electric Measurements of Charged Sprays Emitted by Cone-jets. *Journal Fluid Mechanics*, 459:245–276, 2002.

[89] P. Garrison. Advanced propulsion activities in the USA. Number 86-170, Innsbruck, Austria, 4 Oct. 1986. 37th Congress Int. Astronaut Fed.

[90] A. Genovese. personal communication, July 2003. ARCS.

[91] A. Genovese and et. al. 2000H Endurance Test of an Indium FEEP Cluster. IEPC 28th International Electric Propulsion Conference, Toulouse, France, July 2003.

[92] A. Genovese, S. Marcuccio, and M. Andrenucci. FEEP thruster performance at high background pressure. Number IEPC-97-186, Cleveland, OH, 1997. 25th Electric Propulsion Conference.

[93] A. Genovese, W. Steiger, and M. Tajmar. Indium FEEP Microthruster: Experimental Characterization in the 1-100 μN Range. volume AIAA 2001-3788 of *37th Joint Propulsion Conference*, pages 1–12, 8-11 July 2001.

[94] A. Genovese, M. Tajmar, and W. Steiger. Indium FEEP endurance test: preliminary results. Number IEPC-01-289 in IEPC 27th International Electric Propulsion Conference, Pasadena, CA, October 2001.

[95] A. Gharakhani. A 3D Galerkin boundary element method for potential flow about thin membranes. Number AIAA-2000-1000, pages 1–8, Reno, NV, Jan. 2000. 38th Aerospace Sciences Meeting and Exhibit.

[96] F. Gibou, R. P. Fedkiw, L. T. Cheng, and M. J. Kang. A second-order-accurate symmetric discretization of the Poisson equation on irregular domains. *J. Computational Physics*, 176(1):205–227, 10 Feb. 2002.

[97] R. H. Goddard. The Green Notebooks. The Dr. Robert H. Goddard Collection, Clark University, Worchester, MA, 1906.

[98] S. K. Godunov. *Math. Sb.*, 47:271, 1959.

[99] S. K. Godunov, A. V. Zabrodin, and G. P. Prokopov. A difference scheme for two-dimensional unsteady aerodynamics and an example of calculations with a separated shock wave. *J. Comput. Math. Math. Phys.*, 2(6):1020, 1961.

[100] D. Goldstein, R. Handler, and L. Strovich. Modeling a no-slip flow boundary with an external force field. *J. Computational Physics*, 109:354, 1993.

[101] M. Gollor and M. Boss. Micro-Newton electric propulsion subsystems for ultra-stable platforms. Number 2006-4825, pages 1–9, Sacramento, CA, July 2006. 42nd Joint Propulsion Conference, AIAA.

[102] C. Goodridge. Properties of droplet ejecting Faraday waves. Number FD.02, Syracuse, NY, 25 Nov. 1996. 49th Annual Meeting of the Division of Fluid Dynamics.

[103] I. S. Gradshteyn and I. M. Ryzhik. *Tables of Integrals, Series, and Products*. Academic Press, San Diego, CA, 6th edition, 2000. p. 1069.

[104] A. Greenbaum, L. Greengard, and G. B. McFadden. Laplace's equation and the Dirichlet-Neumann map in multiply connected domains. *J. Computational Physics*, 105:267–278, 1993.

[105] L. Greengard and V. Rokhlin. A fast algorithm for particle simulations. *Computational Physics*, 73:325–348, 1987.

[106] R. Grimm and J. L. Beauchamp. Dynamics of field-induced droplet ionization: time-resolved studies of distortion, jetting, and progeny formulation from charged and neutral methanol droplets exposed to strong electric fields. *J. Physical Chemistry B*, 109:8244–8250, 2005.

[107] F. H. Harlow and J. F. Welch. *Physics of Fluids*, 8:2182, 1965.

[108] P. Hawkes and E. Kasper. *Principles of Electron Optics II: Applied Geometrical Options*. Academic, London, 1996.

[109] G. Hewitt, G. Shires, and Y. Polezhaev. *International Encyclopedia of Heat and Mass Transfer*. CRC Press LLC, Florida, USA, 1996.

[110] J. Higgins. Introducing GMRes: a simple analysis of the algorithm. Master's thesis, South Dakota School of Mines and Technology, Rapid City, South Dakota 57701, Apr. 2004.

[111] C. W. Hirt and B. D. Nichols. Volume of fluid (VOF) method for the dynamics of free boundaries. *J. Computational Physics*, 39(201-225), 1981.

[112] V. Hnizdo. On the Laplacian of 1/r. *Eur. J. Phys.*, 21:L1–L3, 2000.

[113] R. Hofer. *Development and characterization of high-efficiency, high-specific impulse Xenon Hall thrusters*. PhD thesis, Dept. Aerospace Engineering, University of Michigan, 1320 Beal Avenue, Ann Arbor, MI, 2004.

[114] Y. C. Hong and H. S. Uhm. Production of carbon nanotubes by microwave plasma torch at atmospheric pressure. *Physics of Plasmas*, 12(5), May 2005. Art. No. 053504.

[115] V. Hruby, M. Gamero-Castaño, P. Falkos, and S. Shenoy. Micro-Newton colloid thruster system development. Number 01-281, Cleveland, OH, 2001. 29th International Electric Propulsion Conference, AIAA.

[116] B. Huang, H. Li, and X. Huang. A level set method for oil slick segmentation in SAR images. *International J. of Remote Sensing*, 26(6):1145–1156, Mar. 2005.

[117] M. N. Huberman. Measurement of the energy dissipated in the electrostatic spraying process. *J. Applied Physics*, 41(2):578–584, 1970.

[118] R. E. Hunter and S. H. Wineland. Charged colloid generation research. Los Angeles, CA, 1965. Space Electronics Symposium.

[119] J. V. Iribarne and B. A. Thomson. Evaporation of small ions from charged droplets. *J. Chemical Physics*, 64(6):2287–2294, 1976.

[120] V. Ivanov, A. Krasnykh, G. Scheitrum, and A. Jensen. An improved version of TOPAZ3D. volume 5, pages 3315–3317. Particle Accelerator Conference, 12 May 2003.

[121] J. Jackson. *Classical Electrodynamics*. John Wiley & Sons, Inc., 3rd edition, 1999.

[122] R. Jahn and E. Choueiri. *Encyclopedia of Physical Science and Technology*, volume 5. Academic Press, 3rd edition, 2002.

[123] N. K. Kang and L. W. Swanson. Computer simulation of liquid-metal ion-source optics. *Applied Physics*, A30(2):95–104, 1983.

[124] A. Karlsson. Darwin mission. 2006. http://darwin.esa.int/science-e/www/area/index.cfm?fareaid=28.

[125] J. Katsikadelis. *Boundary Elements: Theory and Applications*. Elsevier Science Ltd, Oxford, UK, 1st edition, 2002.

[126] H. Kaufman. Charge-exchange plasmas generated by an ion thruster. Technical Report NASA CR-134844, 1975.

[127] P. Kebarle. *J. Mass Spectrometry*, 35:804, 2000.

[128] M. R. Kennedy, C. Pozrikids, and R. Skalak. Motion and deformation of liquid drops, and the rheology of dilute emulsions in simple shear flows. *Computers Fluids*, 23:251–278, 1994.

[129] M. Kern. Outlier detection algorithms and their performance in GOCE gravity field processing. *J. Geodesy*, 78(9):509–519, Apr. 2005.

[130] D. Kingham and L. Swanson. *Journal Physics A*, 34:123, 1984.

[131] S. Kirkup. *BEM CD 2005: the Boundary Eement Method*. boundary-element-method.com, 2005.

[132] J. Koo. *Hybrid PIC-MCC computational modeling of Hall thrusters*. PhD thesis, Dept. Aerospace Engineering, University of Michigan, 1320 Beal Avenue, Ann Arbor, MI, Jan. 2005.

[133] W. Kowalski. Liquid extraction with electrostatic mixing and separation of phases. *Inzynieria Chemiczna I Procesowa*, 10(1):141–149, 1989.

[134] R. Krasny and M. Nitsche. The onset of chaos in vortex sheet flow. *J. Fluid Mechanics*, 454:47–69, 2002.

[135] V. Krohn. Research on the generation and acceleration of submicron-size particles. Contract AF 33(616)-6775 8937-6005-CU-000, Aeronautical Research Laboratories, Wright-Patterson AFB, Ohio, 28 Feb. 1962. Prepared by Physical Electronics Laboratory Space Technologies Laboratories, Inc. 8433 Fallbrook Avenue Canoga Park, CA.

[136] H. Lamb. *Hydrodynamics*. Dover Publications, New York, 1932.

[137] L. D. Landau and E. M. Lifshits. *Electrodynamics of Continuous Media*. Nauka, Moscow, 1982. p. 55.

[138] M. Lappa. A CFD level-set method for soft tissue growth: theory and fundamental equations. *Biomechanics*, 38:185–190, 2005.

[139] A. Leow, C. L. Yu, S. C. Huang, H. Protas, R. Nicolson, K. M. Hayashi, A. W. Toga, and P. M. Thompson. Brain structural mapping using a novel hybrid implicit/explicit framework based on the level-set method. *Neuroimage*, 24(3):910–927, 1 Feb. 2005.

[140] D. R. Lide, editor. *CRC Handbook of Chemistry and Physics*. CRC Press LLC, 3rd electronic edition, 2004. "Melting, boiling and critical temperatures of the elements".

[141] K. Lindsay and R. Krasny. A particle method and adaptive treecode for vortex sheet motion in 3D flow. *Computational Physics*, 172(2):879–907, 20 Oct. 2001.

[142] H. Lineweaver, D. Burk, and C. K. Horner. The temperature characteristic of respiration of azotobacter. *J. General Physiology*, 15:497–505, 1932. by the Rockefeller University Press.

[143] J. M. Lopez-Herrera, A. M. Gañán-Calvo, and M. Perez-Saborid. One-dimensional simulation of the breakup of capillary jets of conducting liquids. Application to E.H.D. spraying. *J. Aerosol Sci.*, 30(7):895–912, 1999.

[144] W. E. Lorensen and H. E. Cline. Marching cubes: a high resolution 3D surface construction algorithm. *Computer Graphics (Proceedings of SIGGRAPH 87)*, 21(4):163–169, July 1987.

[145] P. Lozano and M. Martinez-Sánchez. Experimental Measurements of Colloid Thruster Plumes in the Ion-Droplet Mixed Regime. Number 2002–3814 in AIAA 38th Joint Propulsion Conference, pages 1–7, Indianapolis, IN, July 2002.

[146] T. S. Lundgren and N. N. Mansour. Oscillations of drops in zero gravity with weak viscous effects. *J. Fluid Mechanics*, 194:479–510, 1988.

[147] T. S. Lundgren and N. N. Mansour. Vortex ring bubbles. *J. Fluid Mechanics*, 224:177–196, 1991.

[148] J. Ma, V. Rohklin, and S. Wandzura. Generalized Gaussian quadrature rules for systems of arbitrary functions. *SIAM J. Num Ana*, 33(3):971–996, June 1996.

[149] P. Macklin and J. Lowengrub. Evolving interfaces via gradients of geometry-dependent interior Poisson problems: application to tumor growth. *J. Computational Physics*, 203:191–220, 2005.

[150] P. MacNeice, K. M. Olson, C. Mobarry, R. deFainshtein, and C. Packer. PARAMESH: A parallel adaptive mesh refinement community toolkit. *Computer Physics Communications*, 126:330–354, 2000.

[151] G. Mair. On the dynamics of liquid metal ion sources. *Journal Physics D: Applied Physics*, 35:1392–1396, 2002.

[152] G. L. R. Mair. *Nucl. Instrum. Methods*, 172:567, 1980.

[153] G. L. R. Mair. *J. Physics D: Appl. Phys.*, 17:2323, 1984.

[154] G. L. R. Mair. On the onset voltage of liquid metal ion sources. *Nuclear Instruments and Methods in Physics Research*, B43:240–242, 1989.

[155] G. L. R. Mair. Electrohydrodynamic instabilities and the energy spread of ion drawn from liquid metals. *J. Physics D: Applied Physics*, 29:2186–2192, 1996.

[156] G. L. R. Mair. The effects of flow impedance on the current-voltage characteristics of liquid-metal ion sources. *Journal Physics D: Applied Physics*, 30:1945–1950, 1997.

[157] C. Malmary, S. Carbonne, Y. Aurégan, and V. Pagneux. Acoustic impedance measurement with grazing flow. Number 2001-2193, pages 1–9, Maastricht, Netherlands, 28 May 2001. 7th Aeroacoustics Conference, AIAA.

[158] M. Manga and H. A. Stone. Buoyancy-driven interactions between deformable drops at low Reynolds numbers. *J. Fluid Mechanics*, 256:647–683, 1994.

[159] N. N. Mansour and T. S. Lundgren. Satellite formation in capillary jet breakup. *Physics of Fluids, A*, 2:1141–1144, 1993.

[160] S. Marcuccio, A. Genovese, and M. Andrenucci. Experimental performance of field emission microthrusters. *J. Propulsion and Power*, 14(5):774–781, 1998.

[161] C. G. Marirrodriga. ESA takes another step towards the search for Earth-like planets. 2001. http://www.esa.int/esaCP/ASEKEVNW9SC_Expanding_0.html.

[162] G. M. Meesters, P. H. Vercoulen, J. C. Marijnissen, and B. Scarlett. Generation of micron-sized droplets from the Taylor cone. *J. of Aerosol Science*, 23(1):37–49, Jan. 1992.

[163] C. A. Miller and L. E. Scriven. Interfacial instability due to electrical forces in double layers 1. general considerations. *J. Colloid and Interface Science*, 33(3):360, 1970.

[164] M. L. Minion. On the stability of Godunov-projection methods for incompressible flow. *J. Computational Physics*, 123(2):435–449, 1996.

[165] N. M. Miskovsky, P. H. Cutler, and E. Kazes. Derivation of the condition for onset of instabilities of a conducting fluid surface under electrostatic stress - application to liquid metal ion sources. *J. Vacuum Science & Technology B*, 3(1):202–206, 1985.

[166] R. Misra and C. Rose. Application and Sensitivity Analysis of Process-Based Erosion Model GUEST. *European Journal of Soil Sciences*, 47:593–604, 1996.

[167] J. Mitterauer. Field emission electric propulsion - spectroscopic investigations on slit emitters. Technical Report Contract 5051/82/NL/PB (SC), ESTEC, 1985.

[168] J. Mitterauer. Indium: an alternative propellant for FEEP-thrusters. Number AIAA-2001-3792, Utah, 11 July 2001. 37th Joint Propulsion Conference.

[169] J. Mitterauer. Micropropulsion for small spacecraft: a new challenge for field effect electric propulsion and microstructured liquid metal ion sources. *Surface and Interface Analysis*, 36:380–386, 2004.

[170] H. Motulsky and A. Christopoulos. *Fitting Models to Biological Data Using Linear and Nonlinear Regression.* GraphPad Software, Inc., San Diego, CA, 2003.

[171] E. W. Müller. Field desorption. *Physical Review*, 102:618–624, 1956.

[172] K. Nabors and J. White. FastCap: a multipole accelerated 3-D capacitance extraction program. *IEEE Transactions on Computer Aided Design*, 10(11):1447–1459, Nov. 1991.

[173] S. Nagrath, K. Jansen, R. T. J. Lahey, and I. Akhatov. Hydrodynamic simulation of air bubble implosion using a level set approach. *J. Computational Physics*, 215:98–132, 2006.

[174] C. Nave. *HyperPhysics*. Dept. Physics and Astronomy, Georgia State University, Atlanta, GA 30303.

[175] C. R. Nave. Modeling the radiative cooling of a hot sphere. Technical report, Department of Physics and Astronomy, Georgia State University, http://hyperphysics.phy-astr.gsu.edu/hbase/thermo/cootime.html#c2, 2005.

[176] J. A. Nelder and R. Mead. A simplex method for function minimization. *J. Comput.*, 7(308-313), 1965.

[177] M. Nicholas. Final report on ESTEC-contract 3806/78. Technical report, ESA Report Ref. CR(P) 1395, Noordwijk, 1979.

[178] D. Nicolini, E. Chesta, and J. del Amo. Plume Characteristics of the Indium Needle Emitter (InFEEP) Thruster. Number 01–291 in IEPC 27th International Electric Propulsion Conference, pages 1–6, Pasadena, CA, October 2001.

[179] D. Nicolini, S. Marcuccio, and M. Andrenucci. 3-D Plume Characterization of a FEEP Thruster. Number 2000–3269 in AIAA 36th Joint Propulsion Conference, pages 1–4, Huntsville, AL, July 2000. Centrospazio.

[180] W. F. Noh and P. Woodward. *Lecture Notes in Physics*, volume 59. Springer-Verlag, New York/Berlin, 1976.

[181] Numerical Recipes Software, editor. *Numerical Recipes in C: the Art of Scientific Computing*. Combridge University Press, 1992.

[182] H. N. Oguz and A. Prosperetti. Bubble entrainment by the impact of drops on liquid surfaces. 203:143–179, 1990.

[183] M. Ohta, S. Haranaka, Y. Yoshida, and M. Sussman. Three-dimensional numerical simulations of the motion of a gas bubble rising in viscous liquids. *J. of Chemical Engineering of Japan*, 37(8):968–978, 2004.

[184] C. T. O'Konski and H. C. Thacher. *J. Physical Chemistry*, 57:955, 1953.

[185] S. Osher and R. Fedkiw. *Level set methods and dynamic implicit surfaces*, volume 153 of *Applied Mathematical Sciences*. Springer, 2003.

[186] S. Osher and R. P. Fedkiw. Level set methods: an overview and some recent results. Technical report, IPAM GBM Tutorials, 27 Mar. 2001.

[187] S. Osher and J. Sethian. Fronts propagating with curvature dependent speed: algorithms based on Hamilton-Jacobi formulations. *J. Computational Physics*, 79:12–49, 1988.

[188] S. Oxley. Modelling the capture theory for the origin of planetary systems. Technical report, University of York, Dept. of Physics, Dec. 1999. DPhil Thesis.

[189] M. Paine and S. Gabriel. A micro-fabricated colloidal thruster array. Number AIAA-2001-3329, Salt Lake City, Utah, 8 July 2001. 37th AIAA Joint Propulsion Conference.

[190] D. Peng, B. Merriman, S. Osher, H. K. Zhao, and M. Kang. A PDE-based fast local level set method. *J. Computational Physics*, 155:410–438, 1999.

[191] R. Peyret and T. D. Taylor. *Computational Methods for Fluid Flow*. Springer, Berlin, 1983. p. 148.

[192] J. Pezzullo. *Nonlinear least squares regression (curve fitter)*. Georgetown University Medical Center, 1711 Liggins Ave. Kissimmee, FL 34744-4091, Feb. 2006. url: http://hometown.aol.com/johnp71/.

[193] L. Rayleigh and J. W. Strutt. *Phil. Mag.*, 14:184–186, 1882.

[194] W. J. Rider and D. B. Kothe. Reconstructing volume tracking. *J. Computational Physics*, 141:112–152, 1998.

[195] V. Rokhlin. Rapid solution of integral equations of classical potential theory. *Computational Physics*, 60:187–207, 1985.

[196] I. Romero-Sanz, R. Bocanegra, and J. Fernández de la Mora. Source of heavy molecular ions based on Taylor cones of ionic liquids operating in the pure ion evaporation regime. *J. Applied Physics*, 94(5):3599–3605, 1 Sept. 2003.

[197] C. Rose. Program GUEST (Griffith University Erosion System Template). Technical Report 40, Australian Center for International Agricultural Research, 1997. p. 34-58.

[198] Y. Saad. *Iterative Methods for Sparse Linear Systems*. SIAM, 2nd edition, 2003.

[199] Y. Saad and M. Schultz. GMRes - a generalized minimal residual algorithm for solving nonsymmetric linear systems. *SIAM J. on Scientific and Statistical Computing*, 7(3):856–869, 1986.

[200] J. Sabot and H. Lauvray. *Encyclopedia of Chemical Technology*, volume 12. Kirk-Othmet, 4th edition, 1994. "Gallium and Gallium Compounds".

[201] D. Saville. Electrohydrodynamics: The Taylor-Melcher leaky dielectric model. *Annual Review Fluid Mechanics*, 29(27), 1997.

[202] G. Scatchard. The attraction of proteins for small molecules and ions. *Ann. N. Y. Acad. Sci.*, 51:660, 1949.

[203] W. Schottky. Concerning cold and hot electron discharge. *Zeitschrift fur Physik*, 14:63, 1923.

[204] J. Schwieters, E. Zehnpfenning, E. Niehuis, and A. Benninghoven. *J. Vac. Sci. Technol. A*, 8:3752, 1990.

[205] J. Scott. An Arnoldi code for computing selected eigenvalues of sparse, real, unsymmetric matricies. *ACM Transactions on Mathematical Software*, 21(4):432–475, Dec. 1995.

[206] J. A. Sethian. Fast marching methods. *SIAM Review*, 41:199–235, 1999.

[207] E. R. Setiawan and S. D. Heister. Nonlinear modeling of an infinite electrified jet. *J. Electrostatics*, 42:243–257, 1997.

[208] J. Shackelford and W. Alexander. *Materials Science and Engineering Handbook*. CRC Press LLC, Boca Raton, 2001.

[209] A. Shapiro. TOPAZ3D : A three-dimensional finite element heat transfer code. Technical report, Aug. 1985. UCID-20484. TOPAZ3D DEC VAX 11 Vesion Tape Description NESC Note 87-64 (March 24, 1987).

[210] L. Shure and B. Bonnevier. MATLAB function ellipke. Technical report, The Mathworks, Inc., 1988.

[211] W. Shyy, H. S. Udaykumar, M. M. Rao, and R. W. Smith. *Computational Fluid Dynamics with Moving Boundaries*. Taylor & Francis, Philadelphia, 1996.

[212] A. Sidi. Numerical quadrature rules for some infinite range integrals. *Math Comp*, 38(157):127–142, Jan. 1982.

[213] A. Sidi and M. Israeli. Quadrature methods for periodic singular and weakly singular Fredholm integral equations. *J. Scientific Computing*, 3(2):201–231, 1988.

[214] F. J. Sietzen. The greening of rocket propulsion. *Aerospace America*, July 2005.

[215] T. Smith. *Deconvolution of ion velocity distributions from laser-induced fluorescence spectra of xenon electrostatic thruster plumes*. PhD thesis, Department Aerospace Engineering, University of Michigan, 1320 Beal Avenue, Ann Arbor, 2003.

[216] M. Sørensen, K. Jacobsen, and H. Jónsson. Thermal Diffusion Processes in a Metal-Tip-Surface Interactions: Contact Formation and Adatom Mobility. *Physical Review Letters*, 77(25):5067–5070, 16 December 1996.

[217] V. Sossi, K. R. Buckley, P. Piccioni, A. Rahmim, M. L. Camborde, E. Strome, S. Lapi, and T. J. Ruth. Printed sources for positron emission tomography (PET). *IEEE Transactions on Nuclear Science*, 52(1):114–118, Feb. 2005.

[218] T. Spitaler. personal communication, July 2003. ARCS.

[219] D. Staack. Hall thruster electric propulsion device. Technical report, Florida State University, 16 Aug. 2006.

[220] J. Strickland and D. Amos. Fast solver for systems of axisymmetric ring vorticies. *AIAA*, 30(3):737–746, 1992.

[221] E. Stuhlinger. *Ion Propulsion For Space Flight*. McGraw-Hill, New York, NY, 1964.

[222] M. Sussman. A second order coupled level set and volume-of-fluid method for computing growth and collapse of vapor bubbles. *J. Computational Physics*, 187:110–136, 2003.

[223] M. Sussman. A parallelized, adaptive algorithm for multiphase flows in general geometries. *Computers and Structures*, 83:435–444, 2005.

[224] M. Sussman. A sharp interface method for incompressible two-phase flows. *J. Computational Physics*, page in press, 2006.

[225] M. Sussman, A. S. Almgren, J. B. Bell, P. Colella, L. H. Howell, and M. L. Welcome. An adaptive level set approach for incompressible two-phase flows. *J. Computational Physics*, 148:81–124, 1999.

[226] M. Sussman, E. Fatemi, P. Smereka, and S. Osher. An improved level set method for incompressible two-phase flows. *Computers & Fluids*, 27(5-6):663–680, June 1998.

[227] M. Sussman and E. Puckett. A coupled level set and volume-of-fluid method for computing 3D and axisymmetric incompressible two-phase flows. *J. Computational Physics*, 162:301–337, 2000.

[228] M. Sussman, P. Smereka, and S. Osher. A level set approach for computing solutions to incompressible two-phase flow. *J. Computational Physics*, 114:146–159, 1994.

[229] G. P. Sutton and O. Biblarz. *Rocket Propulsion Elements*. Wiley-Interscience. John Wiley & Sons, Inc., New York, 7th edition, 2001.

[230] V. Suvorov and E. Litvinov. Dynamic Taylor cone formation on liquid metal surface: numerical modelling. *Journal of Physics D: Applied Physics*, 33:1245–1251, 2000.

[231] V. G. Suvorov and N. M. Zubarev. Formation of the Taylor cone on the surface of liquid metal in the presence of an electric field. *J. Phys. D: Appl. Phys.*, 37:289–297, 2004.

[232] L. W. Swanson. Electron and ion emission from liquid metal surfaces. *IEEE Transactions on Plasma Science*, 19(5):746–748, Oct. 1991.

[233] M. Tajmar. *3D numerical plasma simulation and backflow contamination of a cesium field-emission-electric-propulsion (FEEP) emitter and thermionic neutralizer*. PhD thesis, Technischen Universität Wien Fakultät Elektrotechnik, Rechte Bahngasse, 1030 Wien, 12 Apr. 2001.

[234] M. Tajmar. personal communication, July 2003. ARCS.

[235] M. Tajmar. Indium capillary liquid-metal-ion-source operation in the flow resistance regime. *J. Physics D: Applied Physics*, 37:3056–3057, 2004.

[236] M. Tajmar. Development of a lifetime prediction model for indium FEEP thrusters. Number 2005-4386, pages 1–17, Tucson, AZ, July 2005. 41st Joint Propulsion Conference, AIAA.

[237] M. Tajmar. Influence of Taylor cone size on droplet generation in an indium liquid metal ion source. *Applied Physics A-Materials Science & Processing*, 81(7):1447–1450, Nov. 2005.

[238] M. Tajmar and A. Genovese. Experimental evaluation of a mass-efficiency model for an indium liquid-metal ion source. *Journal Physics A*, 76:1003–1006, 2003.

[239] M. Tajmar and A. Genovese. Critical current for droplet generation in indium LMIS. Technical report, ARC Seiborsdorf research, A-2444 Seibersdorf, Austria, May 2005.

[240] M. Tajmar, A. Genovese, N. Buldrini, and W. Steiger. Miniturized Indium-FEEP Multiemitter Design and Performance. volume AIAA 2002-5718, pages 1–7, Houston, TX, 9 September 2002. AIAA NanoTech 2002.

[241] M. Tajmar, A. Genovese, and W. Steiger. Indium Field Emission Electric Propulsion microthruster experimental characterization. *J. Propulsion and Power*, 20(2):211–218, Mar. 2004.

[242] M. Tajmar, K. Marhold, and S. Kropatschek. Three-Dimensional In-FEEP Plasmadiagnostics. IEPC 28th International Electric Propulsion Conference, pages 1–10, Toulouse, France, July 2003.

[243] M. Tajmar, W. Steiger, and A. Genovese. Indium FEEP Thruster Beam Diagnostics, Analysis and Simulation. Number 2001-3790 in JPC 37th Joint Propulsion Conference, Salt Lake City, UT, July 2001. Austrian Research Centre Seibersdorf.

[244] Y. Takao, M. Awano, Y. Kuwahara, and Y. Murase. Preparation of oxide superconductive composite by an electrostatic mixing process. *Sensors and Actuators B-Chemical*, 31(1-2):131–133, Feb. 1996.

[245] G. I. Taylor. Disintegration of water drops in an electric field. *Proceedings of the Royal Academy of London*, A280:383, 1964.

[246] S. Thompson and A. von Engel. Field emission of metal ions and microparticles. *J. Physics D*, 15:925–931, 1982.

[247] H. R. Thresh. *Met. Trans.*, 1:1531, 1970.

[248] G. Tryggvasonm, B. Bunner, D. Juric, and W. Tauber. A front tracking method for computations of multiphase flows. *J. Computational Physics*, 169:708–759, 2001.

[249] Y. H. R. Tsai, L. T. Cheng, and S. Osher. Fast sweeping algorithms for a class of Hamilton-Jacobi equations. *SIAM J. on Numerical Analysis*, 41(2):673–694, 2003.

[250] K. Tsiolkovsky. Exploration of the universe with reaction machines. *The Science Review, St. Petersburg*, 5, 1903.

[251] T. T. Tsong and E. W. Müller. Measurement of energy distribution in field ionization. *J. Chemical Physics*, 41(11):3279, 1964.

[252] M. Tsuchimoto, T. Honma, S. Yatsu, T. Kasahara, and I. Kaji. An analysis of nonlinear MHD equilibria of compact tori by using boundary element methods. *IEEE Trans. Magn.*, MAG-24(1):248–251, 1988.

[253] University of Southern California. *Vapor pressure data for selected elements*, 2003.

[254] S. Unverdi and G. Tryggvason. A front-tracking method for viscous, incompressible, multi-fluid flows. *J. Computational Physics*, 100:25–37, 1992.

[255] A. VanderWyst, A. Christlieb, M. Sussman, and I. Boyd. Boundary integral formulation of electric fields in level set simulations of charged droplets. Number 2005-4665 in 36th AIAA Plasmadynamics and Lasers Conference, Toronto, Canada, 6 June 2005. AIAA.

[256] A. Victor, T. Zurbuchen, and A. Gallimore. Development of the top hat electric propulsion plume analyzer (TOPAZ): mass analyzer design and preliminary calibration data. Number 2005-016, pages 1–11, Princeton, NJ, Nov. 2005. 29th International Electric Propulsion Conference, AIAA.

[257] V. Vladimirov, V. Badan, and V. Gorshkov. Microdroplet emission and instabilities in liquid-metal ion sources. *Surface Science*, 266:185–190, 1992.

[258] V. Vladimirov and V. Gorshkov. Stability of conducting beams in ionic sources on liquid metals. *Journal of Technical Physics*, 57(11):2155–2163, 1987.

[259] V. V. Vladimirov and V. N. Gorshkov. *J. Appl. Phys. A*, 46:131, 1988.

[260] C. Vuik. New insights in GMRes-like methods with variable preconditioners. *Computational and Applied Mathematics*, 61:189–204, 1995.

[261] A. Wagner. The hydrodynamics of liquid metal ion sources. *Appl. Phys. Letters*, 40(5):440–442, 1982.

[262] A. Wagner and T. Hall. Liquid gold ion source. *Journal Vacuum Science Technology*, 16(6):1871–1874, November 1979.

[263] J. Waltz. Analysis of a plasma tree code: short versus long-range forces. Technical report, George Mason University, Institute for Computational Sciences and Informatics, http://physics.gmu.edu/large/index.html, 1998.

[264] E. W. Washburn, editor. *International critical tables of numerical data, physics, chemistry and technology*. Knovel, 1st electronic edition, 2003.

[265] E. W. Weisstein. Fundamental theorem of Gaussian quadrature. *From MathWorld – A Wolfram Web Resource*, 1999. http://mathworld.wolfram.com/GaussianQuadrature.html.

[266] E. W. Weisstein. Green's function. *From MathWorld – A Wolfram Web Resource*, 1999. http://mathworld.wolfram.com/GreensFunction.html.

[267] E. W. Weisstein. Hessian. *From MathWorld – A Wolfram Web Resource*, 1999. http://mathworld.wolfram.com/Hessian.html.

[268] E. W. Weisstein. Nelder-Mead method. *From MathWorld – A Wolfram Web Resource*, 1999. http://mathworld.wolfram.com/Nelder-MeadMethod.html.

[269] C. White and H. Okamoto. *Phase Diagrams of Indium Alloys*. Indium Corporation of America and ASM International, USA, 1992.

[270] E. Whittaker and G. Robinson. *The calculus of observations: a treatise on numerical mathematics*. New York, 4th edition, 1967.

[271] C. T. R. Wilson and G. I. Taylor. *Proc. Cambridge Philosopical Society*, 22:728, 1925.

[272] M. Winter. *Online Periodic Table*. University of Sheffield, UK, 2003.

[273] S. Wu. *Polymer Interface and Adhesion*. Marcel Dekker, New York, 1982.

[274] A. Y. Yahiku, J. F. Mahoney, H. L. Daley, J. Perel, and A. Sherman. Experimental study of colloid annular thrusters. Number AIAA-70-1112, Stanford, California, Sept. 1970. 8th Electric Propulsion Conference.

[275] C. L. Yaws, editor. *Chemical Properties Handbook*. McGraw-Hill, 1st electronic edition, 1999. "Surface tension (live equations)".

[276] T. Ye, W. Shyy, and J. Chung. A fixed-grid, sharp-interface method for bubble dynamics and phase change. *J. Computational Physics*, 174:781–815, 2001.

[277] B. Yu. A Unified Framework for Water Erosion and Deposition Equations. *Soil Sci. Soc. Am. Journal*, 67:251–257, 2003.

[278] J. D. Yu, S. Sakai, and J. Sethian. A coupled quadrilateral grid level set projection method applied to ink jet simulation. *J. Computational Physics*, 206(1):227–251, 10 June 2005.

[279] W. S. Yue, C. L. Lin, and V. C. Patel. Large eddy simulation of turbulent open-channel flow with free surface simulated by level set method. *Physics of Fluids*, 17(2):No. 025108, Feb. 2005.

[280] G. U. Yule. On the theory of correlation. *J. Royal Statist. Society*, pages 812–854, 1897.

[281] S. Zhang, J. H. Duncan, and G. L. Chahine. The final stage of the collapse of a cavitation bubble near a rigid wall. *J. Fluid Mechanics*, 257:147–181, 1993.

[282] X. Zhang and O. A. Basaran. Dynamics of drop formation from a capillary in the presence of an electric field. *J. Fluid Mechanics*, 326:239–263, 1996.

[283] H. K. Zhao, T. Chan, B. Merriman, and S. Osher. A variational level set approach to multiphase motion. *J. Computational Physics*, 127:179–195, 1996.

INDEX

Index

ABSTRACT

FIELD EMISSION ELECTRIC PROPULSION THRUSTER MODELING AND SIMULATION

by

Anton Sivaram VanderWyst

Co-Chairpersons: Iain D. Boyd and Wei Shyy

Electric propulsion allows space rockets a much greater range of capabilities with mass efficiencies that are 1.3 to 30 times greater than chemical propulsion. Field emission electric propulsion (FEEP) thrusters provide a specific design that possesses extremely high efficiency and small impulse bits. Depending on mass flow rate, these thrusters can emit both ions and droplets. To date, fundamental experimental work has been limited in FEEP. In particular, detailed individual droplet mechanics have yet to be understood. In this thesis, theoretical and computational investigations are conducted to examine the physical characteristics associated with droplet dynamics relevant to FEEP applications.

Both asymptotic analysis and numerical simulations, based on a new approach combining level set and boundary element methods, were used to simulate 2D-planar and 2D-axisymmetric probability density functions of the droplets produced for a

given geometry and electrode potential. The combined algorithm allows the simulation of electrostatically-driven liquids up to and after detachment. Second order accuracy in space is achieved using a volume of fluid correction.

The simulations indicate that in general, (i) lowering surface tension, viscosity, and potential, or (ii) enlarging electrode rings, and needle tips reduce operational mass efficiency. Among these factors, surface tension and electrostatic potential have the largest impact. A probability density function for the mass to charge ratio (MTCR) of detached droplets is computed, with a peak around 4,000 atoms per electron. High impedance surfaces, strong electric fields, and large liquid surface tension result in a lower MTCR ratio, which governs FEEP droplet evolution via the charge on detached droplets and their corresponding acceleration. Due to the slow mass flow along a FEEP needle, viscosity is of less importance in altering the droplet velocities. The width of the needle, the composition of the propellant, the current and the mass efficiency are interrelated. The numerical simulations indicate that more electric power per Newton of thrust on a narrow needle with a thin, high surface tension fluid layer gives better performance.